TECHNISCHE UNIVERSITÄT MÜNCHEN

Lehrstuhl für Nachrichtentechnik

Multilevel Transmission and Equalization for Polymer Optical Fiber Systems

Florian Breyer

Vollständiger Abdruck der von der Fakultät für Elektrotechnik und Informationstechnik der Technischen Universität München zur Erlangung des akademischen Grades eines

Doktor–Ingenieurs

genehmigten Dissertation.

Vorsitzender:	Univ.–Prof. Dr.–Ing. habil. G. Rigoll
Prüfer der Dissertation:	1. Univ.–Prof. Dr.–Ing. N. Hanik
	2. Prof. ir. T. Koonen, Technische Universiteit Eindhoven, Niederlande

Die Dissertation wurde am 15.04.2010 bei der Technischen Universität München eingereicht und durch die Fakultät für Elektrotechnik und Informationstechnik am 02.12.2010 angenommen.

Preface

This thesis was written during my time as a research and teaching assistant at the Institute for Communications Engineering at the Technische Universität München and as an external researcher at Corporate Technology - Information&Technology at Siemens AG within a collaboration project.
First, I would like to thank my supervisor Professor Dr. Norbert Hanik, Prof. Dr. Andreas Kirstädter and Dr. Bernhard Spinnler for setting up this project in 2005, and giving me the opportunity to work towards my doctoral degree in the academic as well as in the industrial environment. Especially, I am deeply grateful to Prof. Dr. Norbert Hanik for his guidance, support and the perfect working atmosphere within the optical research group at the Institute. I am also very grateful to Prof. Ton Koonen for acting as co-supervisor.
To my colleagues at Siemens, I would like to thank Dr. Sebastian Randel for his guidance, advice, the fruitful numerous technical discussions during my time at Siemens and for acting as co-supervisor. Many thanks and a mark of respect to my research partner Dr. Jeffrey Lee, who has done an excellent job on his Ph.D. project. I think we have achieved great collaborative work together and have learned so much from each other. I will definitely miss the nearly uncountable hours together in the lab. Further, I would like to thank Dr. Joachim Walewski for involving me in his research of visible light communications. A special thanks to Dr. Daniel Cardenas for introducing me to the world of FPGA programming.
Many friends and colleagues contributed to making the years enjoyable. I would like thank all of them who are responsible for the good atmosphere at the Institute, especially my colleagues from the optical research group Stephan Hellerbrand, Bernhard Göbel, Leonardo Coelho, Oscar Gaete and Beril Inan. Another special thanks to Manfred Jürgens for the support and the production of several mechanical components for my project.
Finally, I would like to thank my family for their unique support and encouragement they provided me throughout the years, especially my brother Michael for proof-reading this thesis. Last but not least, thanks to Rebecca for her love, support, proof-reading and the patience of waiting so many times in the evenings.

München, April 2010

Florian Breyer

Contents

1 Introduction **1**

2 Polymer Optical Fiber Systems **5**

2.1 Polymer Optical Fibers 6

2.1.1 PMMA SI-POF 9

2.1.2 PMMA GI-POF 11

2.1.3 PF-GI-POF 12

2.2 Light Sources for PMMA-based POF Systems 13

3 Fiber Model for the SI-POF **17**

3.1 Modeling of Light Propagation in SI-POFs 17

3.2 Transmission impairments in SI-POFs 21

3.2.1 Mode-dependent attenuation 21

3.2.2 Modal dispersion 23

3.2.3 Mode coupling 24

3.3 Derivation of the time-dependent power flow equation 25

3.4 Solution of the time-dependent power-flow equation 28

3.5 Channel model performance 31

3.5.1 Fiber parameters and launching condition 31

3.5.2 Numerical Results 32

3.5.3 Validation with Experimental Results 36
3.6 Summary 39

4 Baseband Transmission over Polymer Optical Fibers 41
4.1 The IM/DD channel model 42
4.2 The capacity of the SI-POF IM/DD channel 46
4.2.1 Derivation of the channel capacity of the SI-POF IM/DD channel . 46
4.2.2 Numerical results for the Channel capacity 50
4.3 Modulation Formats 55
4.4 Electronic Dispersion Compensation 60
4.4.1 Symbol-spaced adaptive Equalizers 60
4.4.2 Fractionally-spaced adaptive Equalizers 63
4.5 Equalizer Coefficient Adaptation Schemes 64
4.5.1 Least-Mean-Square (LMS) Algorithm 65
4.5.2 Blind Adaptation using the Stop-and-Go algorithm 66
4.6 Performance bounds of FFE and DFE 67
4.6.1 MMSE calculation for FFE and DFE 67
4.6.2 BER performance bounds of FFE and DFE 69
4.7 Summary 72

5 POF Transmission Experiments 73
5.1 SI-POF Systems with Laser launch and receiver equalization 74
5.1.1 1.25 Gbit/s Transmission with On-Off-Keying 74
5.1.2 2 Gbit/s Transmission with On-Off-Keying 81
5.2 SI-POF Systems with LED launch and receiver equalization 84
5.2.1 500 Mbit/s Transmission with PAM-4 modulation 84

5.2.2 1.25 Gbit/s Transmission using PAM-4 modulation 88
5.3 PF-GI-POF Systems with VCSEL launch 93
5.3.1 10 Gbit/s Transmission using PAM-4 modulation 94
5.3.2 Comparison of OOK and PAM-4 for 10 Gbit/s over PF-GI-POF . . 98
5.4 Summary 104

6 Real-Time Implementation Aspects of GigE over SI-POF 107
6.1 Prototyping Platform - FPGA DSP board 108
6.2 Analog Frontend 110
6.3 DSP implementation inside the FPGA 113
6.3.1 Line Coding for PAM-4 modulation 113
6.3.2 Parallelization of FFE equalizer 116
6.3.3 Clock Recovery using Goertzel algorithm 122
6.3.4 Forward Error Correction insertion 126
6.4 Gigabit Ethernet POF Media Converter 128
6.5 Complexity Analysis of the Gigabit Ethernet POF Media Converter 130
6.6 BER performance of the Real-Time demonstrator 132
6.6.1 BER performance measurement setup 132
6.6.2 Results 132
6.7 Summary 134

7 Conclusions and Recommendations 135
7.1 Summary 135
7.2 Achievements 136
7.3 Recommendations for future research 139

A Crank-Nicolson scheme 141

B 8B10B line-code for 1000Base-X **143**

C Abbreviations and Symbols **149**

Bibliography **157**

Zusammenfassung

Diese Arbeit behandelt die Anwendung mehrstufiger Modulationsformate mit Empfängerentzerrung für optische Polymerfaser (POF) Systeme. Die Standard 1 mm Stufenindex POF wird dabei detailliert untersucht. Für diese Faser wird ein Kanalmodell entwickelt, das die drei wichtigsten Mehrmoden-Fasereffekte beinhaltet, nämlich die moden-abhängige Dämpfung, die Modendispersion und die Modenkopplung. In diesen POF Systemen kann nur Intensitätsmodulation angewendet werden. Deshalb wird eine Mehrstufen-Modulation mit empfängerseitiger Entzerrung kombiniert, um die Bandbreitenbeschränkung aufgrund von Modendispersion und den aktiven Komponenten zu kompensieren. Diese Kombination wird sowohl in theoretischen Betrachtungen der maximalen Entzerrerleistungsfähigkeit als auch in zahlreichen Experimenten untersucht. Es wird gezeigt, dass die Übertragung einer Rekord-Bitrate von bis zu 2 Gbit/s über 100 m SI-POF durch Verwendung einer Laserdiode als optisches Sendeelement und der Kombination aus Mehrstufenmodulation und Entzerrung möglich ist. Abschließend wird die Implementierung eines Medienkonverters zur Gigabit Ethernet Übertragung vorgestellt, der mit einer LED als Sendeelement arbeitet und auf einer FPGA-Plattform basiert, die folgende Signalverarbeitungsalgorithmen ausführt: PAM-4 Modulation, lineare Empfängerentzerrung, Fehlerkorrektur und Taktrückgewinnung.

Abstract

This work deals with equalized multilevel transmission schemes for polymer optical fiber (POF) systems. In particular, the standard 1 mm core diameter step-index PMMA-based POF (SI-POF) is investigated. A fiber model is developed, which includes the three major fiber effects, such as mode-dependent attenuation, modal dispersion, and mode coupling. As only intensity modulation can be applied, multi-level modulation is combined with receiver equalization schemes to overcome the bandwidth limitations due to modal dispersion and the active components. This combination is evaluated in terms of theoretical equalizer bounds and various experiments. It is shown that record bit-rates of up to 2 Gbit/s over 100 m SI-POF can be achieved by the use of this combination and a laser diode. Finally a full working Gigabit Ethernet media converter is implemented on a FPGA platform using a red LED, PAM-4 modulation, linear receiver equalization, forward error correction, and clock recovery.

1

Introduction

The rapid growth of data traffic in communication applications pushes the commonly used solutions such as copper lines and radio links to use more and more complex signal processing to achieve the required data rates. Optical communication systems, after having conquered the long-haul and medium distance connections, nowadays also migrate into short-range communication applications. Optical solutions offer the possibility of high-speed data transfer for professional as well as consumer applications. For example, the dominant access technology in Germany is today xDSL, offering up to 50 Mbit/s in the downstream. This data rate is enabled by the fact, that the optical transmission from the core network approaches the so-called last mile, which means that only the last few hundred meters are still copper-based. In the near future even these copper lines have to be replaced by optical solutions to reach data rates above a few 100 Mbit/s. For consumer electronics, Intel has announced at the Intel Developer Forum (IDF) 2009 in San Francisco the Light Peak technology, which is an optical interface combining all possible peripheral connections of a personal computer in one cable running in the first release at 10 Gbit/s. Thus, even computer peripheral connections are migrating to optical solutions in the near future.

Traditionally, all these optical connections are based on the standard single mode fiber (SSMF), which is the best transmission media for high data rate communication. However, it requires professionals for connecterization and installation. Hence, this is not a low-cost technology, which is required for the mass markets. Solutions, such as

silica-based multimode fibers (MMF), polymer optical fibers (POF), using light-emitting diodes (LED) or low-cost vertical cavity surface emitting laser diodes (VCSEL) are therefore being proposed and seem to be promising candidates for short-reach optical interconnects.

Especially the polymer optical fiber has proven the capability of being a robust, low-cost and easy-to-install transmission medium due to successful adoption in harsh environments like automotive (MOST) and industrial automation (PROFINET). However, this benefits come at the expense of less bandwidth and higher attenuation. But for short-range communication links these disadvantages can be tolerated or compensated by applying digital signal processing. For example, a copper-based Fast Ethernet link uses multilevel modulation and receiver equalization to compensate the bandwidth limitation of the twisted pair, which is approximately 3 MHz at 100 m [MDR+98]. A LED-based POF solution uses just On-Off-Keying (OOK) without digital signal processing to achieve error-free transmission of Fast Ethernet over 100 m. Thus, even the worst optical fiber in terms of bandwidth has much more bandwidth than copper-based twisted pair lines. Nevertheless, optical short-range communications is in strong competition with the traditional transmission media such as copper cables, which have already established themselves for decades, resulting in large economies of scale. After all, optical solutions have a chance in this high competitive market due to their outstanding properties in terms of robustness, bending radii, electromagnetic immunity, low power consumption and due to their ease of use.

This thesis investigates the use of digital signal processing (DSP) to overcome the bandwidth limitations of short-range optical POF-based communication systems. In particular, the combination of real-valued multilevel modulation with receiver equalization is proposed and investigated to increase the data-rate-length product of such systems. This combination is already widely employed in all copper-based Ethernet transmission systems from 100 Mbit/s up to 10 Gbit/s. To transmit these high speeds over twisted pair copper cables a huge amount of digital signal processing has to be done. For comparison, one twisted pair within a CAT-6 cable has a 3 dB bandwidth at 100 m of approximately 4 MHz, whereas a LED launched step-index POF systems has approx. 50 MHz at 100 m link length. Thus, the bandwidth of a LED based SI-POF system is 12.5 times higher than for a CAT-6 copper cable. Unfortunately, receiver noise is much higher for the LED based SI-POF system, which is an additional big distortion source. Thus, for both transmission media digital signal processing has to be done to transmit more than 100 Mbit/s. But the required complexity of the DSP algorithms for transmitting up to 1 Gbit/s over 100 m is much less for the SI-POF system.

This thesis is organized as follows:

Chapter 2 gives an introduction to optical data transmission systems based on polymer optical fibers (POF). The commonly used POF fiber types, such as the standard step-index PMMA-based POF (SI-POF), the graded-index PMMA-based POF (GI-POF), and the perfluorinated graded-index POF (PF-GI-POF) are presented. The physical parameters and differences are discussed, which make them suitable for different short-range interconnect application scenarios, such as automotive environment, industrial automation, and home networking. Finally, the characteristics of available light sources for the use in the red wavelength range are discussed and compared.

Chapter 3 presents a newly derived fiber model for the standard SI-POF. This fiber model, which is based on the time-dependent power flow equation published in the 1970s by Gloge [Glo73], includes the major multimode fiber effects, such as the mode-dependent attenuation, modal dispersion, and mode coupling. The performance of the new SI-POF model is evaluated and compared with measured transfer functions. The matching between simulation and measurement is good. Thus this fiber model can be used to simulate the real SI-POF behavior.

The fiber model of chapter 3 is extended in **chapter 4** to an intensity modulated optical communication link with direct detection (IM/DD), which is the commonly used transmitter and receiver architecture for such polymer optical fiber links. The channel capacity of the SI-POF is calculated by evaluating the newly derived IM/DD system model. Afterwards, the used modulation and equalizer schemes are presented, which are investigated throughout this thesis to increase the data-rate-length product. Finally, the performance bounds of combinations of multi-level modulation and digital receiver equalization are shown.

Chapter 5 reports on various experiments demonstrating the performance of the combination of multi-level modulation and receiver equalization. At first, a red laser diode is used to launch into a 1 mm SI-POF. It is shown that a record bit rate of 2 Gbit/s over 100 m can be achieved using On-Off-Keying (OOK) and decision feedback equalization (DFE). The second part shows, that 1.25 Gbit/s transmission is feasible using a red light-emitting diode for distances over up to 50 m enabled by PAM-4 modulation and decision feedback equalization. The last experimental part shows 10 Gbit/s transmission over up to 300 m PF-GI-POF using OOK or PAM-4 modulation, combined with receiver equalization.

Chapter 6 presents real-time implementation aspects for Gigabit Ethernet transmission over SI-POF using light emitting diodes. A Gigabit Ethernet media converter is implemented on a FPGA-based signal processing platform, showing for the first time a full-working Gigabit Ethernet link based on LEDs over up to 25 m of SI-POF. This is enabled by PAM-4 modulation, linear receiver equalization, scrambling, forward error correction, and clock recovery. The custom-made FPGA platform is introduced together with the custom-made analog front end. Certain parts of the digital signal processing algorithms were discussed with a focus on parallelization. Finally, the performance of this Gigabit Ethernet media converter is shown in terms of pre-FEC BER measurements.

Finally the achieved results are concluded in **chapter 7** and recommendations for follow-up research directions are stated.

Parts of this work have been published at conferences and in journals:

[BHC+06],[BHRS06],[BHLR07],[BLRH07b],[BMH+07],[BLRH07c],[BLRH07a], [BLRH08a],[BLRH08b],[BLRH09].

2

Polymer Optical Fiber Systems

This chapter provides an introduction to data transmission systems based on polymer optical fiber (POF). The basic block diagram of such a transmission system is depicted in Fig. 2.1. It consists of a data source, a transmitter for the electro-optical conversion, a fiber, a receiver for the opto-electrical conversion and a data sink. Typically, the optical transmission in a fiber is unidirectional. Thus, a bidirectional communication requires two fibers. The electro-optical conversion is done by a light source, i.e. a light emitting diode (LED) or a laser diode, which is discussed in detail in sub-chapter 2.2.

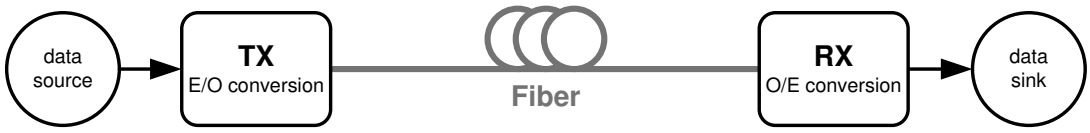

Figure 2.1: Basic Polymer Optical Fiber System block diagram.

The coupling to the fiber is done either with simple plastic lenses or even without any coupling optics. The fiber itself is connected to the active components either with simple plastic connectors or even without any connector. On the receiver side (RX), a photo diode makes the opto-electrical conversion to recover the transmitted data. In the transmission path, the only components besides the fiber can be some passive connectors. Thus, the

optical link consists mainly of three parts, namely the optical source, the fiber and the photo diode.
In the following two sub-chapters first the polymer optical fiber (POF) as transmission medium is introduced and secondly the possible light sources for the red wavelength window are discussed.

2.1 Polymer Optical Fibers

Optical data transmission is traditionally associated with high speed communication as well as long reach connections based on silica fibers, which provide large bandwidth in combination with very low attenuation. These good properties are achieved by using very thin fibers, for example the standard single mode fiber (SSMF). This fiber has a core diameter of 9 μm, which leads to a so-called single mode transmission, which means that only one configuration of an electro-magnetic field can propagate through the fiber core, actually two polarization modes. In all other fiber types, called multi mode fibers (MMFs), more than one electro-magnetic field configuration, which is called mode, is propagable. These modes travel on different paths through the fiber core with different path lengths. Hence, they arrive with different propagation delays at the fiber end. This effect is called modal dispersion and can be explained as follows: if a pulse is transmitted over all modes, it is received at different times at the receiver due to different path lengths and thus the transmitted pulse is broadened or dispersed in time. In wireless communications, this effect is called multi-path propagation.
Thus the best optical transmission media is the SSMF, because there is no modal dispersion. But this very beneficial property has to be paid by the very small fiber core diameter, which requires professionals for connecterization and installation. Another drawback of the SSMF is the fact, that the coupling between the light source and the fiber requires very tiny alignment and mechanical tolerances. Hence the SSMF is only used if no other transmission media can meet the requirements. So if the transmission distances are not too long, which means less than 1 km, and the data rate is not too high (<10 Gbit/s), fibers with more relaxed tolerances and also cheaper components can be used, such as the silica based MMFs with core diameters of 50 μm and 62.5 μm. In such short-reach application scenarios even modal dispersion can be tolerated or compensated if necessary. If even those fibers are too small and to expensive, polymer optical fibers (POFs) can be used. These POFs are made of plastic, which is a very tolerant material in terms of mechanical stress and handling. For data communication systems, POFs are used with fiber core diameters of up to 1 mm, so the coupling between a light source and a 1 mm large core is easy compared to silica fibers. This very large polymer core diameter and the

large numerical aperture have to be paid with a small bandwidth and a large attenuation. But for certain application scenarios these transmission properties are sufficient, because the common properties of optical data transmission are maintained for all fiber types, such as no electro-magnetic interference problems, no radiation, or galvanic isolation. To get a visual impression of the dimensions of these fibers, Fig. 2.2 illustrates the fiber core sizes for the investigated POFs and the commonly used silica based fibers in a relative scale. The blue region represents the fiber core and the yellow region the fiber cladding.

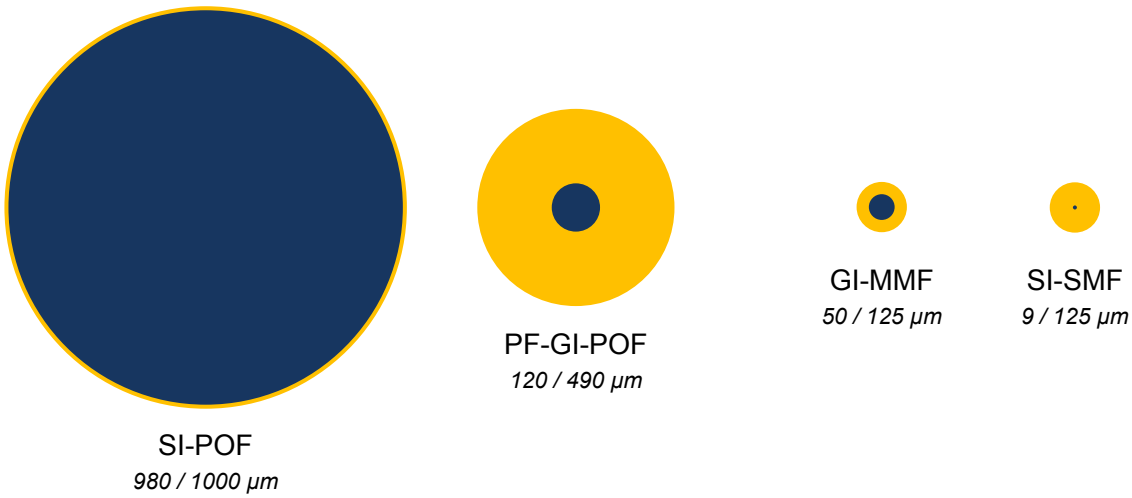

Figure 2.2: Comparison of the fiber core diameters for (left-to-right) the standard 1 mm step-index PMMA-based polymer optical fiber (SI-POF), the 120 μm perfluorinated graded-index polymer optical fiber (PF-GI-POF), the 50 μm graded-index silica based multi mode fiber (GI-MMF), and the 9 μm standard single mode fiber (SSMF).

In this thesis polymer optical fibers are investigated for short-range optical communication systems with link lengths of up to a few hundred meters. The three most common POFs are the step-index poly-methyl-methacrylate (PMMA) based POF (SI-POF), the graded-index PMMA-based POF (GI-POF), both with a core diameter of about 1 mm, and the graded-index perfluorinated POF (PF-GI-POF) with core diameters varying from 50 and 62.5 μm to up to 120 μm. Table 2.1 summarizes the properties of all aforementioned fiber types in terms of material, core diameter, numerical aperture (NA), transmission wavelength range, modal bandwidth-length product, and typical application scenarios.
The SI-POF and the GI-POF are the biggest fibers used for data communication, which are made of poly-methyl-methacrylate (PMMA), also called Plexiglas. These fibers work in the visible wavelength range, especially in the red, green and blue window. All other fibers have their attenuation minimum in the near-infrared wavelength range at 850, 1310,

or 1550 nm. As it can be seen, the PF-GI-POF is a sort of an exotic plastic fiber due to the material CYTOP, which stands for cyclic transparent optical polymer and was developed by Asahi Glass in Japan. The core sizes of this fiber type are comparable to the silica based MMFs, thus the big advantage of having a bigger core diameter than silica based fibers is not the case for this kind of fiber. But there are some benefits left, which are discussed later in sub-chapter 2.1.3. The SSMF at the right hand side is the ultimate reference fiber, due to the really impressive values in terms of attenuation. The modal bandwidth is not applicable, because there is no modal dispersion effect, besides polarization mode dispersion, which is neglected in this summary.

	SI-POF	**GI-POF**	**PF-GI-POF**	**MMF**	**SSMF**
material	PMMA	PMMA	Cytop	Silica	Silica
core diameter	1 mm	1 mm	$50 - 120\,\mu$m	$50/62.5\,\mu$m	$9\,\mu$m
NA	0.5	0.23	0.18	0.2	0.13
wavelength range	400-650 nm	650 nm	850/1310 nm	850/1310 nm	1310/1550 nm
attenuation	< 160 dB/km	< 200 dB/km	< 50 dB/km	< 3 dB/km	< 0.2 dB/km
modal bandwidth-length product	$5\,\text{MHz}\cdot\text{km}$	$> 150\,\text{MHz}\cdot\text{km}$	$> 0.3\,\text{GHz}\cdot\text{km}$	$> 0.35\,\text{GHz}\cdot\text{km}$	not applicable
target application scenarios	automotive automation home networks	home networks HDMI (HDTV)	enterprise interconnects	enterprise radio over fiber	long-haul metro access

Table 2.1: Key parameter comparison of optical fibers based on polymer and silica.

With a modal bandwidth-length product of 5 MHz$\cdot$km, the SI-POF is the worst fiber type in terms of bandwidth. But it is the mostly used POF, because it is also the most attractive fiber in terms of mechanical stress, ease of use, price, and so on. The graded-index PMMA-based POF has a higher bandwidth, but this has to be paid with a much higher attenuation and a smaller NA, which complicates the coupling between a light source and the fiber core. At the moment, this fiber is not yet available as a standard product, because in recent years the manufacturers had problems to get the fiber stable in terms of temperature stability and purity of the material. Other problems are the high bending loss and the higher attenuation. But if these problems can be solved, this fiber type is a very promising candidate for higher speed POF based data transmission systems in the Gigabit range. In the following sub-chapters a more detailed view is presented on

the characteristics and the fields of application of the three common POF types.

2.1.1 PMMA SI-POF

The SI-POF has been largely used in industrial automation for more than 20 years in applications like PROFIBUS, INTERBUS, and SERCOS, and in harsh environments. Furthermore, SI-POFs are deployed in millions of vehicles serving a multimedia oriented systems transport (MOST) bus with data rates of 25 Mbit/s and nowadays 150 Mbit/s (MOST150) [Mc]. Its main benefits are the robustness to electromagnetic interference and mechanical stress, the ease of installation and connection, the low weight, as well as the low price.

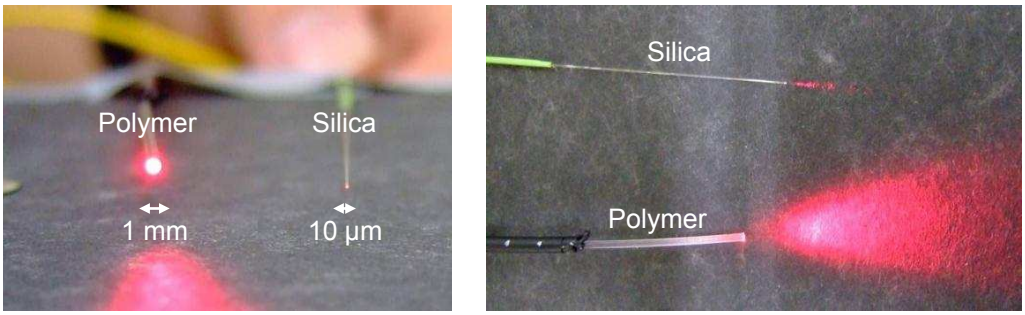

Figure 2.3: Comparison of the physical dimensions and light propagation angles for the standard step-index PMMA-based POF (SI-POF) and the standard silica single mode fiber (SSMF).

Fig. 2.3 shows a comparison of the SI-POF with a SSMF, used for long-haul transmission systems. It can be seen, that the 1 mm large diameter of the SI-POF allows easier connection and handling, and at the same time guides more light with larger angle due to the large numerical aperture (NA) of 0.5, resulting in larger tolerances for bending and alignment. However, this large numerical aperture results in a small bandwidth-length product of around 50 MHz ·100 m due to modal dispersion, which is a kind of multi-path propagation. The source of modal dispersion is illustrated in Fig. 2.4 for step-index fibers. The naming refers to the refractive index profile function $n(r)$. The step-index fiber has a refractive index step between fiber core and fiber cladding. The modal dispersion is sourced by multi-path propagation of different light modes, depicted in Fig. 2.4 as the blue solid, green dashed, and red dotted line. As the refractive index inside the fiber core is constant, the velocity of light inside the fiber core is also constant. Thus, the propagation time through a piece of fiber is different for these three depicted light rays.

The propagation time difference between the fastest (blue solid line) and the slowest (red dotted line) light path in this example is a measure of the modal dispersion in the time domain. This effect results in a low-pass behavior in the frequency domain, which limits the bandwidth-length product to the above-mentioned 50 MHz·100 m.

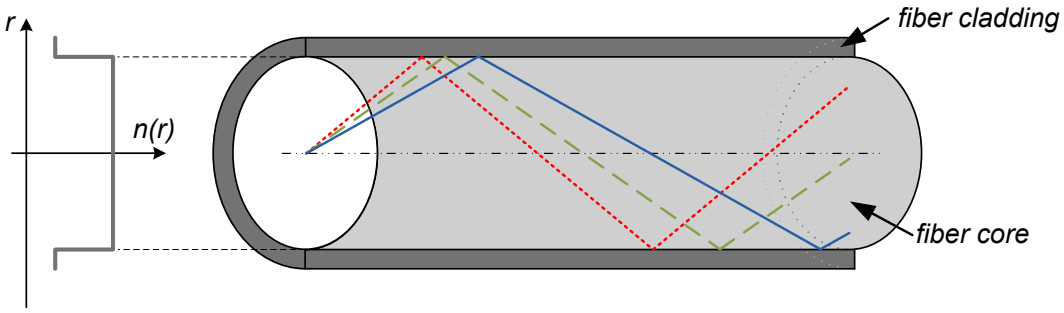

Figure 2.4: Light propagation in step-index multi-mode fibers.

Fig. 2.5 shows the spectral attenuation curve for the SI-POF, where three transmission windows in the visible spectrum can be identified, namely at 520 nm, 570 nm, and 650 nm.

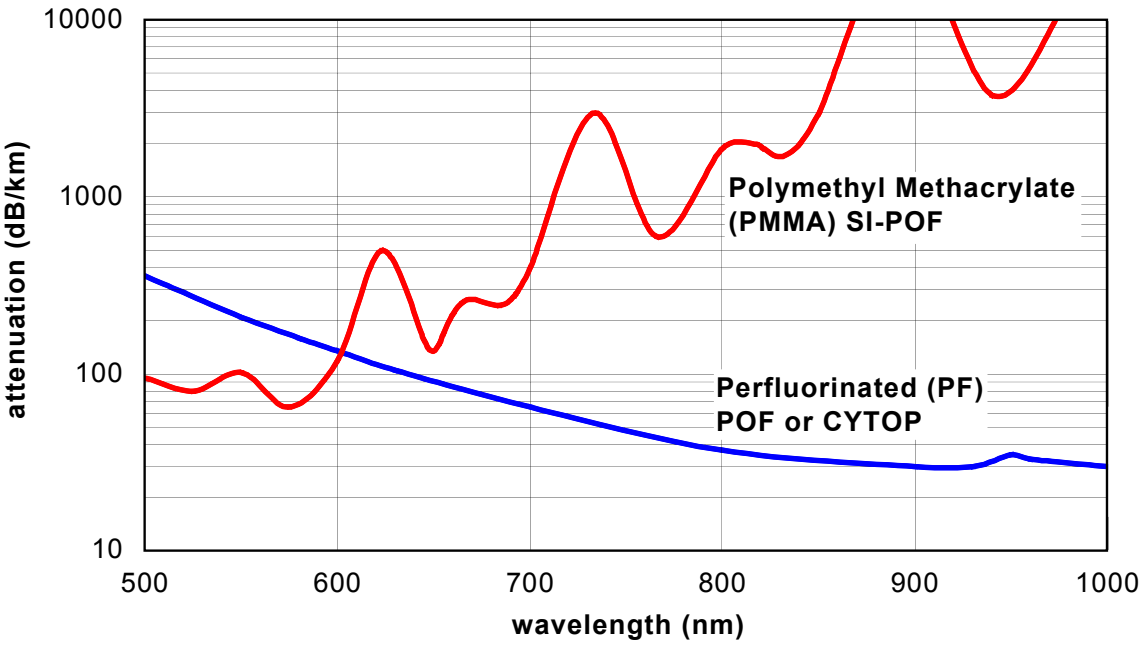

Figure 2.5: Spectral attenuation for the standard PMMA-based SI-POF and the perfluorinated graded-index POF (PF-GI-POF) [ZKZD08].

The most commonly used window for data transmission is the red wavelength window at 650 nm, just because of the good availability of light sources (light-emitting diodes (LEDs) and laser diodes) and the good responsivity of the silicon-based photo diodes. The attenuation in this window is around 150 dB/km, which restricts the application to short-range communications to a range of a few 100 m. The two other transmission windows in the green and blue spectral range have much better attenuation values, but the available transmitter components have up to now much smaller modulation bandwidths compared to the ones in the red transmission window at 650 nm. So the choice of the transmission window is a trade-off between attenuation and bandwidth.
Today's commercial systems operate at speeds of up to 100 Mbit/s over up to 100 m of SI-POF using LEDs. Next generation systems are expected to carry Gigabit Ethernet data over comparable distances. To achieve this data rate with this small bandwidth, as mentioned before, several advanced modulation techniques have been proposed recently [RLS+06, BLRH07b, LBR+09]. These proposals altogether keep the SI-POF and the LEDs as transmitter, which represent smooth upgrade scenarios for existing systems, because only the transceivers must be exchanged, while staying with the same infrastructure.

2.1.2 PMMA GI-POF

The PMMA-based graded-index POFs (GI-POFs) have similar characteristics as the SI-POF, except the gradient index profile (Fig. 2.6) [INK+95, KK09, KP08].

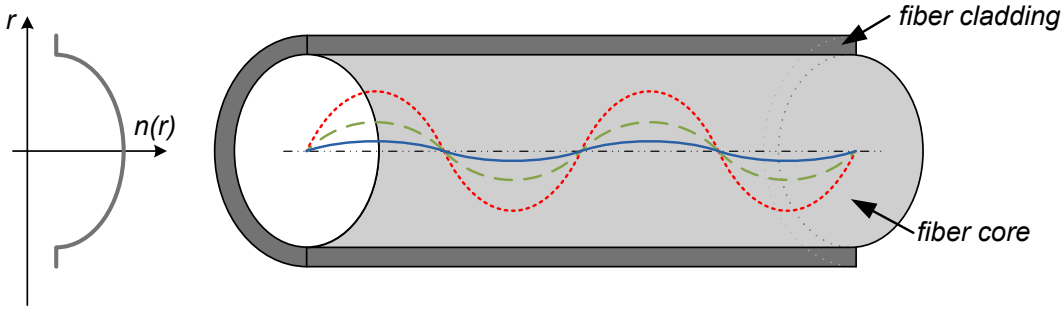

Figure 2.6: Light propagation in graded-index multi-mode fibers.

These fibers with core diameters between 0.5 mm and 1 mm have a bandwidth-length product of about 1.5 GHz ·100 m. This advantage has to be paid by a slightly higher attenuation of approximately 200 dB/km and a smaller numerical aperture (NA) of 0.23, which leads to higher bending losses. Thus this type of fiber is suitable to enable multi Gigabit transmission, but the big benefits of POF such as small bending radii and large

coupling tolerances are decreased. Another disadvantage up to now is the small specified temperature range of $-30°$ to 60°C [Opt], which is too small for e.g. automotive applications. Nevertheless, the GI-POF is a promising candidate for providing multi Gigabit communication networks in consumer applications.
The biggest difference of the graded-index POF (GI-POF) to the SI-POF is the light propagation inside the fiber core, which is illustrated in Fig. 2.6. The refractive index function $n(r)$ is continuously decreasing inside the fiber core, from the highest value at the fiber center down to value at the cladding. This results in the curved light propagation, as it is depicted in Fig. 2.6. The effect is that light modes traveling closer to the cladding have a higher velocity than those at the fiber core center. Therefore, the propagation delay difference between the fastest (blue solid line) and the slowest (red dotted line) light mode is minimized, which results directly in a smaller modal dispersion or equivalently in a higher bandwidth.
In this thesis the graded-index PMMA-based GI-POF is not investigated, because the main focus in this work is to increase the data-rate-length product by remaining with the commonly used and installed POF, which is the 1 mm standard step-index PMMA-based POF. Additionally the operation temperature range of the PMMA-based GI-POF limits the application scenarios for this fiber, whereas the SI-POF meets all the environmental requirements for nearly all application scenarios, such as automotive, industrial automation and home networks. Nevertheless, the PMMA-based GI-POF is still a promising candidate for home network applications, where the environmental requirements are not so strong.

2.1.3 PF-GI-POF

In recent years, the interest in using perfluorinated graded-index POF (PF-GI-POF) for high-speed ($\geq 10\,\text{Gbit/s}$) short-reach applications such as low-cost interconnects in data centers, local area networks (LANs), and supercomputers has increased. So far, multimode silica fibers (MMFs) are the preferred transmission media, because of the large core diameter and the large numerical aperture of 0.2 compared to standard single mode fibers (SSMFs). The PF-GI-POF has also all these advantages and additionally even more relaxed tolerances in terms of alignment, bending radii (5 mm), tensile load and stress and enables simpler connectorization. In Fig. 2.5 the spectral attenuation curve for the PF-GI-POF is shown. At 850 nm the PF-GI-POF has an attenuation of 35 dB/km, a silica MMF for comparison has 3.5 dB/km. Of course, this is a disadvantage for PF-GI-POF, but for applications with link lengths of up to 100 m, as most short interconnects are, this disadvantage can be tolerated. The bandwidth-length product at a wavelength of 850 nm

is $\geq 500\,\mathrm{MHz} \cdot \mathrm{km}$, which is in between the OM1 and OM2 MMF specifications (ISO/IEC 11801). Thus the most promising application for this fiber is the replacement of MMF for short-reach interconnects with more relaxed tolerances. So this fiber is a promising candidate for the use in the large upcoming market of active optical cables (AOC), where the distances are mostly below 100 m and the coupling and connecterization are not an issue. Especially the more relaxed tolerances to bending radii and mechanical stress are big advantages for these active optical cables.

2.2 Light Sources for PMMA-based POF Systems

As mentioned in the introduction of this chapter, the choice of the light source in PMMA-based POF systems is strongly dependent on the environmental requirements of the transmission system. The simplest and oldest form of a light source for POF transmission systems is the light emitting diode (LED). It essentially requires two layers of the same semiconductor, which form a p-n junction, which emits light through spontaneous emission, a phenomenon referred to as electro-luminescence. The emitted light is incoherent with a relatively wide spectral width (approx. 30 nm) and a relatively large angular spread, which can be modeled as a Lambertian source. The basic structure of such a LED is depicted in Fig. 2.7 on the left side.

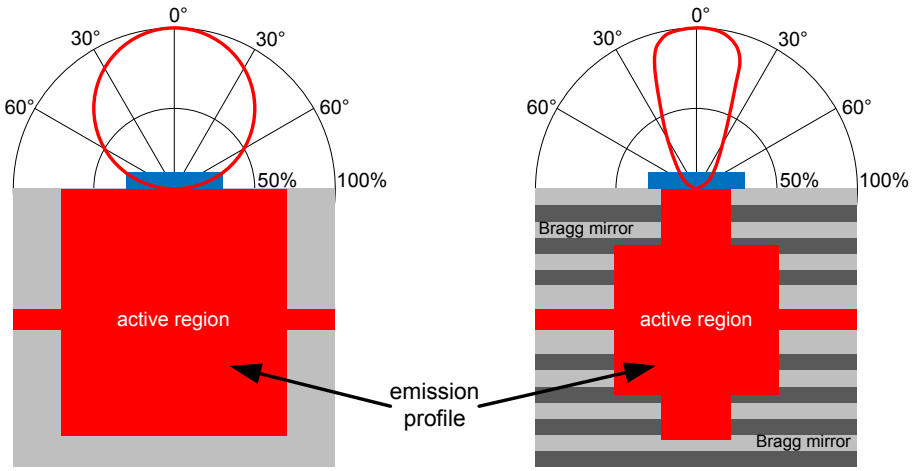

Figure 2.7: Schematic representation of a conventional LED (left) showing isotropic mode distribution with a Lambertian radiation pattern in a polar plot and a RC-LED (right) showing anisotropic mode distribution with a coil radiation pattern in a polar plot ([LMOM05]).

The typical parameters of such LEDs in the red wavelength window, which is the preferred one for PMMA-based POF systems, are summarized in Table 2.2. Up to now, the red LEDs are the most often used light sources for POF systems, because the bandwidth is high enough to transmit up to 100 Mbit/s and the temperature range is sufficient for the deployment in the automotive environment, which has one of the most stringent requirements in terms of robustness. Another big advantage of LEDs is the life cycle behavior. The output power decreases only slowly over the years, but there is no sudden death behavior. So the output power can be tracked and the optical source can be exchanged, before the output power drops below a required level.

	LED	**RC-LED**	**Laser** (edge emitting)	**VCSEL**
wavelength range	650 nm	650 nm	655 nm	665 nm
spectral width	25 nm	20 nm	1 nm	1 nm
launch NA	0.8	0.34	0.13	0.23
output power	-1.5 dBm (20 mA)	-1.5 dBm (20 mA)	4.7 dBm (30 mA)	0 dBm (5 mA)
optical 3 dB bandwidth	80 MHz	100 MHz	> 2 GHz	> 2 GHz
temperature range (operation)	$-40°C \ldots 95°C$	$-40°C \ldots 95°C$	$-10°C \ldots 60°C$	$0°C \ldots 40°C$
target application scenarios	automotive automation home networks	automotive automation home networks	home networks	home networks

Table 2.2: Key parameter comparison of optical light sources for polymer optical fiber systems in the red wavelength window (typical values at 25°C) [ZKZD08].

One property of the LED is the very broad beam characteristic. On the one hand it is an advantage in terms of coupling to the fiber, which is quite easy due to this large NA, but on the other hand the PMMA-based SI-POF only has a NA of 0.5, so a direct coupling between LED and fiber leads to a power loss due to this large NA of the LED. Therefore developments have been done to form a smaller beam. The result was the resonant-cavity LED (RC-LED), which was first proposed in 1992 [SWC+92]. The basic structure of an actual RC-LED is illustrated in Fig. 2.7 on the right side. It is formed by a thin quantum well active region sandwiched by two mirrors that form a Fabry-Perot cavity. This cavity effect produces a smaller launching beam and the modulation bandwidth is additionally increased.

The typical parameters of the red RC-LED are also summarized in table 2.2. The RC-LED has inherited all the good properties from the LED, such as the same operation temperature range, center wavelength, and output power. Furthermore the bandwidth is increased, the spectral width is decreased and the launch NA is decreased to 0.34. Thus for launching into a SI-POF with a NA of 0.5, all the excited light from the RC-LED can be coupled into the fiber. Another advantage of this smaller launch NA is the fact, that the bandwidth behavior of the SI-POF channel is also dependent on the launching power distribution, which means that the system bandwidth is increased due to the smaller launch NA.

The best light source in terms of output power and modulation bandwidth is a laser diode. In the red wavelength window, edge-emitting laser diodes are available, originally designed for DVD players. The maximum peak output power is approximately 7 dBm and the modulation bandwidth is higher than 2 GHz. The launch NA is 0.13, which additionally enhances the system bandwidth due to the smaller launch NA. Thus the use of a laser diode should be the best choice. But a laser diode has a small operating temperature range and it has a sudden death characteristic, which means that the lasing effect stops suddenly due to a bad environmental condition or a negative driving current. Further a laser is very expensive in comparison to a LED and the driving current has to be adapted to the temperature of the component, as the output power of a laser diode is strongly temperature sensitive. The only suitable application scenario is the consumer electronics market, in which the environmental requirements are much more relaxed. But still the price of a laser diode is an issue for a low-cost communication system. An alternative to the edge emitting laser diode is the use of a vertical cavity surface emitting laser diode (VCSEL). This vertical structure can be produced in a much cheaper process, but the temperature range for these devices remains the same as for a laser diode. An advantage is also that the threshold current of a VCSEL to get into the lasing effect region is much lower, thus the driving current is much smaller, as it can be seen in Table 2.2. The only differences to the red laser diode is the larger NA and the larger center wavelength of 665 nm. The first is an advantage, as it relaxes the fiber coupling tolerance, but the latter is a big disadvantage, because the spectral attenuation at 665 nm is approx. 225 dB/km, in comparison to 150 dB/km at the optimum wavelength of 650 nm in the red window (see Fig. 2.5).

To summarize, the use of a LED or a RC-LED is the preferred optical light source for PMMA-based POF systems due to the robustness of these devices. If the requirements are not so stringent, a laser diode solves more or less all problems in terms of optical power and transmitter bandwidth. The use of a VCSEL would be a very promising alternative to the laser diode, if the center wavelength could be shifted to 650 nm. To

realize Gigabit transmission over a PMMA-based POF, a laser diode and a GI-POF would be an alternative solution. Unfortunately for most application scenarios, this combination does not meet the environmental requirements.
The combination of LEDs or RC-LEDs with the SI-POF, as it is already in use, should be maintained even for moving the data rates to the Gigabit region. One approach to realize Gigabit transmission over this combination is the use of digital signal processing to overcome the bandwidth and attenuation limitations.

3

Fiber Model for the SI-POF

In this chapter, a fiber channel model is introduced based on the time-dependent power-flow equation [Glo73]. With this model all major fiber effects, such as the mode-dependent attenuation, modal dispersion and the mode-coupling or mode-mixing, can be described in one model. Especially the mode-coupling is very strong in large core PMMA-based fibers, such as the SI-POF. At the beginning of this PhD study no model could be found in the literature which combines these three fiber effects. There were only models for two out of these three effects known. By solving the time-dependent power-flow equation [Glo73] and adapting the parameters for the SI-POF, a universal solution could be found for any set of fiber parameters and launching conditions.
At first, these three major fiber effects are explained in detail, then the time-dependent power-flow equation is derived and a numerical integration method is shown using the Crank-Nicolson finite difference scheme [CN47]. Finally, numerical results of the transfer functions of SI-POFs using this model are discussed and compared to measured results.

3.1 Modeling of Light Propagation in SI-POFs

Electromagnetic propagation along optical waveguides is described exactly by Maxwell's equations. However, it is well known that the classical geometric optics provides a good approximation of light propagation in regions where the refractive index varies only slightly over a distance comparable to the wavelength of light. This is typical for multimode opti-

cal waveguides used for data communication. Thus, the most simple way to describe light propagation in multimode fibers, like the SI-POF, is to trace rays along the fiber core. A step-index fiber is often parametrized using the V parameter [Agr02], which combines the fiber characteristics like the core radius a, the core refractive index n_{core}, and the cladding refractive index n_{clad} in the following way:

$$V(\lambda) = \frac{2\pi a}{\lambda}\mathrm{NA}, \tag{3.1}$$

with

$$\mathrm{NA} = (n_{\mathrm{core}}^2 - n_{\mathrm{clad}}^2)^{1/2}, \tag{3.2}$$

where λ is the considered wavelength and NA the numerical aperture of the fiber. Because of its inverse dependence on the wavelength λ, $V(\lambda)$ is often referred to as the normalized frequency. The geometric optics can only be applied for waveguides satisfying $V \gg 1$. For the standard SI-POF, the normalized frequency at a wavelength of 650 nm and the parameters listed in Table 3.1 is approximately $V \approx 2417$, thus the condition for using geometric optics is fulfilled. Using this normalized frequency, the total number of possible propagating modes can be calculated as

$$M_{modes} = \frac{V^2}{2}. \tag{3.3}$$

So for the SI-POF the maximum number of modes propagating inside the fiber core is 2.92 Million. For comparison, in case of a single mode fiber, the normalized frequency V must be smaller than 2.405 [Agr02], which allows a maximum number of 2 modes propagating inside the fiber, one in the horizontal and one in the vertical polarization.

parameter	unit	value
core radius a	mm	0.5
refractive index core n_{core}	-	1.492
refractive index cladding n_{clad}	-	1.4057
numerical aperture NA	-	0.5
wavelength λ	nm	650

Table 3.1: Geometric parameters of the standard SI-POF.

Using geometric optics, light propagation within a uniform core of the step-index fiber of Fig. 3.1 is along straight lines. If a ray originates at Q on one core-cladding interface having an angle θ with the fiber axis, it will reach the opposite interface at R as shown.

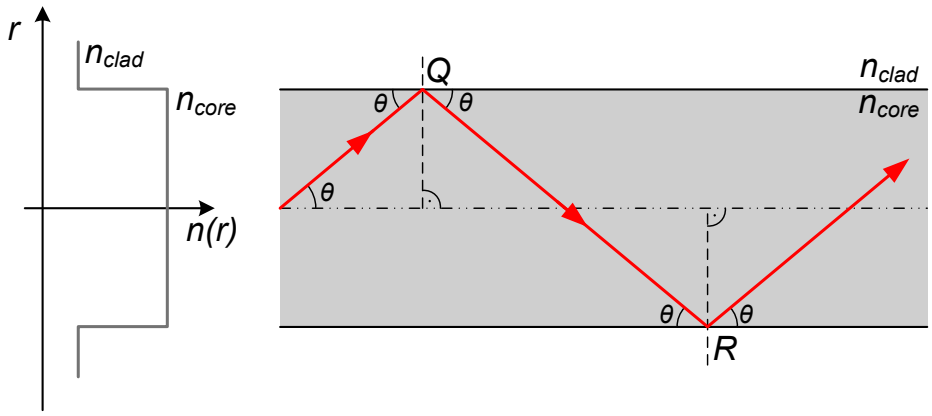

Figure 3.1: Light propagation model in a step-index polymer optical fiber based on geometric optics.

The situation at R is equivalent to the incidence at an interface between two half-spaces of refractive indices n_{core} and n_{cladd} as shown in Fig. 3.1. Reflection in this situation is governed by Snell's laws [BW70, Mar72]. These laws are usually expressed in terms of angles relative to the normal at point Q. Here the complementary angle θ relative to the fiber axis is used in the following. Thus the incident ray at Q is totally reflected if the angle θ satisfies $0 \leq \theta \leq \theta_c$, and is partly reflected and partly refracted if $\theta_c \leq \theta \leq \pi/2$, where θ_c is the complement of the critical angle inside the fiber, defined by

$$\theta_c = \arccos\left\{\frac{n_{\text{clad}}}{n_{\text{core}}}\right\} = \arcsin\left\{1 - \frac{n_{\text{clad}}^2}{n_{\text{core}}^2}\right\}^{1/2} = \arcsin\left\{\frac{\text{NA}}{n_{\text{core}}}\right\}. \tag{3.4}$$

The light rays in the two above-mentioned angle regions can be categorized by the value of θ according to

$$\text{Bound rays} \quad : \quad 0 \leq \theta \leq \theta_c, \tag{3.5}$$

$$\text{Refracting rays} \quad : \quad \theta_c \leq \theta \leq \pi/2. \tag{3.6}$$

Since the power of a bound ray is ideally totally reflected back into the core at every reflection, the ray can propagate indefinitely without any loss of power due to reflection. A refracting ray looses a small fraction of its power at each reflection and therefore attenuates as it propagates. The rays can further be categorized into rays which cross the fiber axis between reflections – known as meridional rays – and rays which never cross the fiber axis, known as skew rays. Fig. 3.2 shows these two different kinds of rays. The meridional rays (Fig 3.2a) lie in a plane of width $2a$ through the fiber axis. Consequently, these rays can also be described by the angle θ relative to the fiber axis.

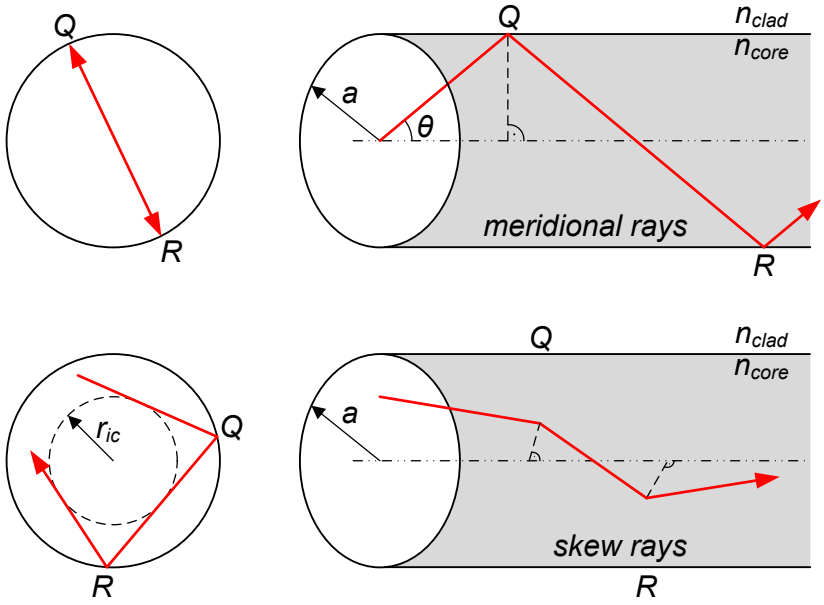

Figure 3.2: Light propagation model in a step-index polymer optical fiber based on geometric optics.

The skew rays follow a helical path, whose projection onto the cross-section is a regular polygon - not necessarily closed - as shown in Fig. 3.2b. The midpoints between reflections all touch a cylindric surface of radius r_{ic}, known as inner caustic. If such rays are projected on a plane, in which a meridional ray is traveling, the axial angle θ to the fiber axis remains constant. Thus the ray transit time is independent of the skewness [SL83], and depends only on the axial angle θ.
This angle θ can be considered as a continuous variable due to the large number of modes inside the fiber, which translates into very small differences between neighboring modes [Glo72]. So the state of power in all propagating modes inside the fiber at a spatial point z and at a time t can then be described by a continuous power distribution $p(\theta, z, t)$.

3.2 Transmission impairments in SI-POFs

In this thesis the three dominant transmission impairments for the multimode SI-POF are considered, which are the mode-dependent attenuation, the mode coupling, and the modal dispersion. All the other sources of dispersion, like chromatic and material dispersion, are neglected, because of the big dominance of modal dispersion.

3.2.1 Mode-dependent attenuation

In the SI-POF the mode-dependent attenuation can be modeled with three attenuation sources, which are depicted in Fig. 3.3. The first is due to the different path lengths of different modes (Fig. 3.3a), the second is due to reflections at the core-cladding interface (Fig. 3.3b), and the third is due to the Goos-Haenchen effect (Fig. 3.3c) [GH47].

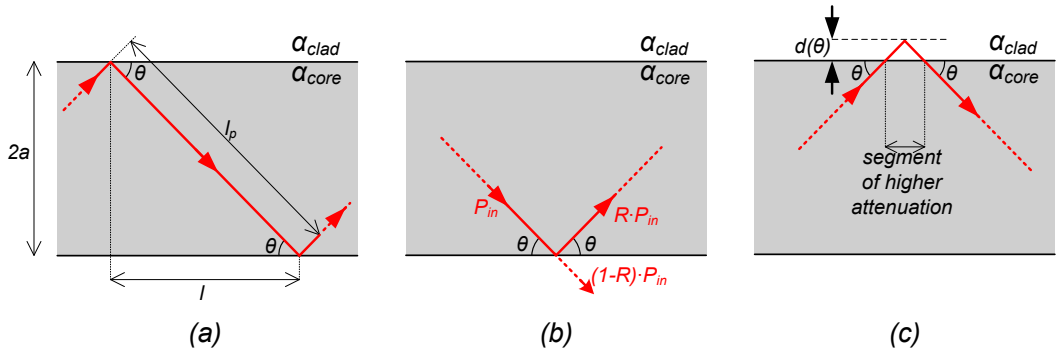

Figure 3.3: Attenuation sources in the SI-POF due to (a) path length, (b) reflection loss, and (c) Goos-Haenchen-Effect.

The mode-dependent power loss or attenuation $\alpha(\theta)$ in the SI-POF can be described dependent on the angle θ for a fiber length of L meters as

$$\begin{aligned} p(\theta, L) &= p(\theta, 0) \cdot e^{-\alpha(\theta) \cdot L} \\ &= p(\theta, 0) \cdot e^{-(\alpha_{\text{path}}(\theta) + \alpha_{\text{refl}}(\theta) + \alpha_{\text{GH}}(\theta)) \cdot L}. \end{aligned} \tag{3.7}$$

where $\alpha_{path}(\theta), \alpha_{refl}(\theta)$, and $\alpha_{GH}(\theta)$ are the three different attenuation sources, which are explained in detail in the following. As depicted in Fig. 3.3a, modes with angle θ travel on a geometric path with length l_p within a fiber segment of length l, which can be calculated as

$$l_p = \frac{l}{\cos\theta}. \tag{3.8}$$

The attenuation component due to this longer path normalized to a fiber length of 1 m

writes therefore as

$$\alpha_{\text{path}}(\theta) = \alpha_{\text{core}} \cdot l_p = \frac{\alpha_{\text{core}}}{\cos\theta} \tag{3.9}$$

where α_{core} is the attenuation coefficient of the fiber core in dB/km. This core attenuation of approximately 150 dB/km is sourced by Rayleigh scattering (12 dB/km), UV absorption (120 dB/km), and waveguide imperfections (10-40 dB/km) [KFON81]. The second source is depicted in Fig. 3.3b. The total reflection of the before mentioned bound rays at the core-cladding interface is not lossless, thus at each reflection a small amount of power is refracted into the cladding. To describe this attenuation, the number of reflections N_{refl} in fiber unit length segment of $L = 1\,\text{m}$ must be calculated. This results in

$$N_{\text{refl}} = \frac{1}{l} = \frac{\tan\theta}{2a} \tag{3.10}$$

where a is the fiber radius. To describe the power loss at each core-cladding interface reflection, a reflection factor $R_{\text{refl}} (0 \leq R_{\text{refl}} \leq 1)$ is introduced, so that after N_{refl} reflections the original power of the ray is decreased to the $R_{\text{refl}}^{N_{\text{refl}}}$ th part. This results in the second source of attenuation, which writes as

$$\alpha_{\text{refl}}(\theta) = -N_{\text{refl}} \cdot \ln R_{\text{refl}} = -\frac{\tan\theta}{2a} \cdot \ln R_{\text{refl}}. \tag{3.11}$$

The third source of attenuation is the Goos-Haenchen-Effect [GH47]. The physical explanation is, that the total reflection does not take place exactly at the core-cladding interface, but mostly inside the cladding. Thus a ray has to travel a short path inside the cladding, which has much higher attenuation. For the SI-POF this attenuation of the cladding has been measured in [PRK93] to be 50000 dB/km. The depth of penetration $d(\theta)$ into the cladding is also dependent on the angle θ and is defined in [PRK93, KB72] as

$$d(\theta) = \frac{\lambda}{2\pi\sqrt{n_{\text{core}}^2 \cos^2\theta - n_{\text{clad}}^2}}. \tag{3.12}$$

The mode-dependent attenuation of the Goos-Haenchen effect [PRK93] normalized to a fiber length of 1 m writes therefore as

$$\begin{aligned} \alpha_{\text{GH}}(\theta) &= \frac{d(\theta)}{a} \cdot \frac{\alpha_{\text{clad}}}{\cos\theta} \\ &= \frac{\lambda \cdot \alpha_{\text{clad}}}{2\pi a \cos\theta \sqrt{n_{\text{core}}^2 \cos^2\theta - n_{\text{clad}}^2}}. \end{aligned} \tag{3.13}$$

Combining the equations (3.9), (3.11), and (3.13) to the total attenuation function $\alpha(\theta)$

results in

$$\alpha(\theta) = \alpha_{\text{path}}(\theta) + \alpha_{\text{refl}}(\theta) + \alpha_{\text{GH}}(\theta) \tag{3.14}$$

$$= \frac{\alpha_{\text{core}}}{\cos\theta} - \frac{\tan\theta}{2a} \cdot \ln R_{\text{refl}} + \frac{\lambda \cdot \alpha_{\text{clad}}}{2\pi a \cos\theta \sqrt{n_{\text{core}}^2 \cos^2\theta - n_{\text{clad}}^2}}. \tag{3.15}$$

3.2.2 Modal dispersion

Modal dispersion is a distortion effect in multi-mode fibers, in which the signal is spread in time because of different transit times of different modes. This effect is similar to the multi-path propagation problem in wireless environments. In the step-index fiber, the different transit times are due to the different path lengths of different modes. So, as mentioned in the previous subsection, modes with a larger angle θ, have also a longer path, which leads to a longer transit time. The velocity of a light ray in a homogeneous fiber core is given by

$$v_{\text{core}} = \frac{c_{0,\text{light}}}{n_{\text{core}}}, \tag{3.16}$$

where $c_{0,\text{light}}$ is the speed of light in vacuum. The ray transit time for a fiber length L then follows from Eqs. (3.8) and (3.16) and Fig. 3.3 as

$$t_{\text{transit}} = \frac{L_p}{v_{\text{core}}} = \frac{L}{\cos\theta} \cdot \frac{n_{\text{core}}}{c_{0,\text{light}}}, \tag{3.17}$$

where L_p is the ray path length inside the core, from which follows that the transit time is inversely proportional to the cosine of the angle θ. In Fig. 3.4 the effect of modal dispersion is shown with three modes as a showcase. If a dirac-impulse is transmitted (left), all the three modes get power from this impulse, but each ray has a different angle θ. At the fiber end, the impulses will arrive at different times. The blue solid ray has the

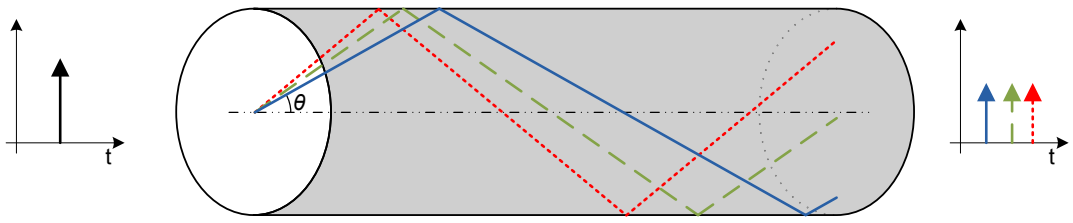

Figure 3.4: Modal Dispersion in a step-index fiber.

shortest path to travel and reaches the fiber end first, the red dotted one at last, because of the largest angle. If all possible propagating rays are considered (continuous θ), each

ray produces its own dirac-impulse at the fiber end, which results in one broadened pulse, in which no mode distinguishing can be done. This pulse broadening translates into a low-pass characteristic in the frequency domain.
The maximum pulse broadening can be calculated as the difference between the minimum and maximum transit time, which corresponds to angle values of 0 and the critical angle θ_c from Eq. (3.4). These transit times can be written as

$$\tau_{\min} = L \cdot \frac{n_{\text{core}}}{c_{0,\text{light}}} \tag{3.18}$$

$$\tau_{\max} = \frac{L}{\cos\theta_c} \cdot \frac{n_{\text{core}}}{c_{0,\text{light}}}, \tag{3.19}$$

where $\tau_{\min}$ and $\tau_{\max}$ are the minimal and maximal ray propagation times, respectively. The pulse broadening can now be calculated as

$$\begin{aligned} \Delta\tau_{\text{transit}} &= \tau_{\max} - \tau_{\min} \\ &= \frac{L\ n_{\text{core}}}{c_{0,\text{light}}} \cdot \left(\frac{1}{\cos\theta_c} - 1 \right) \\ &= \frac{L\ n_{\text{core}}}{c_{0,\text{light}}} \cdot \left(\frac{n_{\text{core}} - n_{\text{clad}}}{n_{\text{clad}}} \right). \end{aligned} \tag{3.20}$$

The first part of Eq. (3.20) is equal to the transit time of the fastest mode (see Eq. (3.19)). So the pulse broadening is proportional to this transit time $\tau_{\min}$ or to the fiber length L, of course. Thus a relative transit time difference can be defined as

$$\tau_{\text{factor}} = \frac{\Delta\tau_{\text{transit}}}{\tau_{\min}} = \left(\frac{n_{\text{core}} - n_{\text{clad}}}{n_{\text{clad}}} \right). \tag{3.21}$$

Taking the standard parameters for the SI-POF of Tab. 3.1, the relative pulse broadening factor is $\tau_{\text{factor}} = 6.14\%$, which only depends on the refractive indices of the core and cladding, and finally on the numerical aperture NA. So step-index fibers with a large NA have a large pulse broadening factor τ_{factor}, or translated into the frequency domain a much smaller bandwidth.

3.2.3 Mode coupling

Mode coupling refers to the process of transferring power between modes. This can happen, for example at scattering centers inside the fiber, which are mainly caused by density variations of the core material and Rayleigh scattering. Since light-scattering in a SI-POF generates the biggest contribution to the attenuation, this process is always present. Fig. 3.5 illustrates the mode coupling process. There are mainly two places,

where mode coupling takes place, the first one is in the fiber core itself due to material imperfections and the second at the core-cladding boundary surface. The latter can be explained by the fact that it is not possible to create an ideal surface in the sub-nanometer range, if there are these very large polymer molecules involved. Thus, mode coupling is dependent on the angle θ.

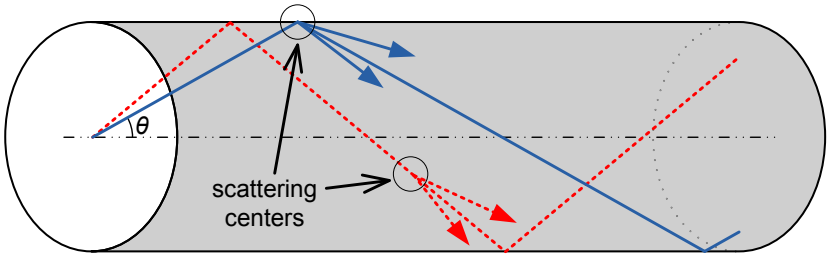

Figure 3.5: Mode Coupling inside the SI-POF at light scattering centers, which are located either at the core-cladding interface or inside the fiber core.

In the channel model, this process is modeled as a diffusion process, where only neighboring modes can exchange power with each other. The detailed introduction of this diffusion process used for the mode coupling theory in SI-POF is given in the next sub-chapter.

3.3 Derivation of the time-dependent power flow equation

In the first part of this sub-chapter, the time-independent power flow equation [Glo72] is derived to show how the mode-coupling process is modeled. Finally, this power flow model is extended by a temporal component [Glo73], which leads to the complete fiber model for all relevant fiber effects.
As mentioned in the previous chapters, the only parameter, by which a mode or ray can be identified is the angle θ relative to the fiber axis. In [Glo72] this angle is quantized for a slab waveguide as

$$\theta_m = \frac{m\lambda}{4an_{\text{core}}} \tag{3.22}$$

where m is the index of the mode under consideration and λ the considered wavelength. Thus the difference angle of neighboring modes can be written as

$$\Delta\theta = \frac{\lambda}{4an_{\text{core}}}. \tag{3.23}$$

The amount of optical power in one mode with mode number m is defined as p_m. At first, only the mode coupling (section 3.2.3) and the mode-dependent attenuation (section 3.2.1)

are considered. To model these two effects, the variation dp_m of the power p_m along a fiber axis increment dz is calculated. The variation due to dissipation and loss is represented by $-\alpha_m p_m dz$, whereas the mode coupling process is modeled using a diffusion process. In this simplified model only neighboring modes can exchange power. Thus, if c_m is the coupling coefficient between the modes with index $m+1$ and m, the variation dp_m can be written as

$$\frac{dp_m}{dz} = -\alpha_m p_m + c_m \left(p_{m+1} - p_m\right) + c_{m-1} \left(p_{m-1} - p_m\right). \tag{3.24}$$

The transition to a continuous angle θ requires the replacement of power differences by differentials, which results in

$$\frac{p_{m+1} - p_m}{\theta_{m+1} - \theta_m} = \frac{dp_m}{d\theta}. \tag{3.25}$$

With $\theta_m - \theta_{m-1} = \Delta\theta$ from Eq. (3.23), Eq. (3.24) can be rewritten as

$$\frac{dp_m}{dz} = -\alpha_m p_m + \Delta\theta \left(c_m \frac{dp_m}{d\theta} - c_{m-1} \frac{dp_{m-1}}{d\theta} \right). \tag{3.26}$$

The term in brackets can be transformed in an analog way to

$$c_m \frac{dp_m}{d\theta} - c_{m-1} \frac{dp_{m-1}}{d\theta} = \Delta\theta \frac{d}{d\theta} \left(c_m \frac{dp_m}{d\theta} \right). \tag{3.27}$$

After replacing all discrete dependencies of m by a functional dependence of θ, the power flow equation for a slab waveguide can be obtained as follows

$$\frac{\partial p(\theta, z)}{\partial z} = -\alpha(\theta) \cdot p(\theta, z) + (\Delta\theta)^2 \frac{\partial}{\partial \theta} \left(c(\theta) \frac{\partial p(\theta, z)}{\partial \theta} \right). \tag{3.28}$$

To transform this power flow equation to a cylindrical geometry, like a fiber, the index m represents now a group of m modes [Glo72]. To obtain the power flow equation for the mth mode group, Eq. (3.24) has to be summed up over all m members. The coefficients α_m and c_m depend only on m, and hence remain the same for all mode group members. However, the coupling to the lower group $(m-1)$ can occur only between $(m-1)$ members [Glo72]. This leads to a new definition of Eq. (3.24) for a cylindrical waveguide as

$$m\frac{dp_m}{dz} = -m\alpha_m p_m + mc_m \left(p_{m+1} - p_m\right) + (m-1)c_{m-1} \left(p_{m-1} - p_m\right). \tag{3.29}$$

Using Eq. (3.25) and a transformation analog to Eq. (3.27), Eq. (3.29) can be transformed to

$$\frac{\partial p_m}{\partial z} = -\alpha_m p_m + (\Delta\theta)^2 \frac{1}{m} \frac{\partial}{\partial \theta} \left(mc_m \frac{\partial p_m}{\partial \theta} \right). \tag{3.30}$$

With the help of Eq. (3.22), the power flow equation for a cylindrical waveguide is obtained as

$$\frac{\partial p(\theta, z)}{\partial z} = -\alpha(\theta) p(\theta, z) + (\Delta\theta)^2 \frac{1}{\theta} \frac{\partial}{\partial \theta} \left(\theta c(\theta) \frac{\partial p(\theta, z)}{\partial \theta} \right). \tag{3.31}$$

The diffusion process is represented by the introduction of an angle-dependent diffusion parameter $D(\theta)$, which is defined as

$$D(\theta) = (\Delta\theta)^2 \cdot c(\theta). \tag{3.32}$$

The extension of this power flow equation by a temporal component was done by Gloge [Glo73]. The starting point is here Eq. (3.31). If Eq. (3.32) is included, this can be rewritten as

$$dp(\theta, z) = -\alpha(\theta)p(\theta, z)dz + \frac{1}{\theta}\frac{\partial}{\partial\theta}\left(\theta D(\theta)\frac{\partial p(\theta, z)}{\partial\theta}\right)dz. \tag{3.33}$$

If p is a function of time t, the total variation dp can be written as

$$dp = \frac{\partial p}{\partial z}dz + \frac{\partial p}{\partial t}dt. \tag{3.34}$$

Inserting Eq. (3.34) in Eq. (3.33), and dividing the equation by dz results in

$$\frac{\partial p(\theta, z, t)}{\partial z} + \frac{dt}{dz}\frac{\partial p(\theta, z, t)}{\partial t} = -\alpha(\theta)p(\theta, z, t) + \frac{1}{\theta}\frac{\partial}{\partial\theta}\left(\theta D(\theta)\frac{\partial p(\theta, z, t)}{\partial\theta}\right). \tag{3.35}$$

The derivative dt/dz is the delay of the power $p(\theta)$ in one mode or, equivalently, the group delay of a mode with characteristic angle θ. By using the relation between characteristic angle θ and the geometrical light path length of corresponding mode, the delay dt/dz can be written as

$$\frac{dt}{dz} = \frac{n_{\text{core}}}{c_{0,\text{light}}}\frac{1}{\cos(\theta)}. \tag{3.36}$$

The equation above relates the mode delay to the vacuum light velocity $c_{0,\text{light}}$, reduced by the refractive index n_{core} of the core material, and to the cosine of the characteristic angle θ due to longer path lengths per unit length. If the delay $n_{\text{core}}/c_{0,\text{light}}$ common to all modes is neglected, a relative mode delay can be calculated as

$$\tau_{\text{rel}}(\theta) = \frac{n_{\text{core}}}{c_{0,\text{light}}}\left(\frac{1}{\cos(\theta)} - 1\right). \tag{3.37}$$

This is equivalent to the transit time (3.20) introduced in the modal dispersion subsection (3.2.2) normalized to a reference fiber length of 1 m. Inserting Eq. (3.37) into Eq. (3.35) results in the time-dependent power flow equation as

$$\frac{\partial p(\theta, z, t)}{\partial z} = -\alpha(\theta)p(\theta, z, t) - \tau_{\text{rel}}(\theta)\frac{\partial p(\theta, z, t)}{\partial t} + \frac{1}{\theta}\frac{\partial}{\partial\theta}\left[\theta D(\theta)\frac{\partial p(\theta, z, t)}{\partial\theta}\right]. \tag{3.38}$$

This equation describes the light propagation in the step-index polymer optical fiber (SI-POF) with three functions, which represent the three dominant polymer multimode fiber effects, namely mode-dependent attenuation ($\alpha(\theta)$), modal dispersion (mode delay) ($\tau_{\text{rel}}(\theta)$), and mode coupling (diffusion coefficient $D(\theta)$).

3.4 Solution of the time-dependent power-flow equation

The time-independent power-flow equation has been solved several times in literature [RJ77, DS04] with several approximations for different effects. In these cases, analytical solutions for the time-independent power-flow equation exist under special conditions and approximations [GPM75, RJ77]. The goal of this work presented in [BHLR07] was to get a universal solution for the time-dependent power-flow equation without applying any approximations, except for the ones which had to be done on the derivation path to get to the equation.
The general time-dependent power-flow equation (Eq. (3.38)) is a partial differential equation dependent on the time t, angle θ, and the location z. The first step in solving Eq. (3.38) is to get rid of the time derivation. This is done by transforming the equation from the time domain into the frequency domain with the help of the Fourier transform

$$P(\theta, z, \omega) = \mathcal{F}\{p(\theta, z, t)\}. \tag{3.39}$$

In the following, $P(\theta, z, \omega)$ is abbreviated by P for simplicity. Thus, Eq. (3.38) can be rewritten in the frequency domain as

$$\frac{\partial P}{\partial z} = -\left[\alpha(\theta) + j\omega\tau_{\mathrm{rel}}(\theta)\right] P + \frac{1}{\theta}\frac{\partial}{\partial \theta}\left[\theta D(\theta)\frac{\partial P}{\partial \theta}\right]. \tag{3.40}$$

In the frequency domain the time-derivative of Eq. (3.38) transforms in a multiplication with $j\omega$. So Eq. (3.40) contains only derivatives with respect to space and angle. Now Eq. (3.40) can be numerically integrated applying finite difference schemes, which are based on the segmentation of the θ and z axis to form a rectangular lattice. At each point (θ_n, z_m) of the grid the derivatives are approximated by difference formulas (see appendix A).Thus a set of finite difference equations with $P(\theta_n, z_m, \omega)$ replaces the differential equation (Eq. (3.40)) with $P(\theta, z, \omega)$. Commonly used explicit finite difference methods (EFDM), used for example in [DS04], have the problem of being restricted to a relation between the step sizes of the lattice to achieve convergence and stability of the numerical integration process. Thus the step sizes have to be chosen very small to get a stable solution. In this work the Crank-Nicolson implicit scheme [CN47] is applied, which is unconditionally stable and assures an excellent convergence. Furthermore the truncation error grows only with the squares of both discretization directions. For comparison the truncation error of the EFDM grows linear in one direction and with squares in the other direction. For further information about the Crank-Nicolson scheme see Appendix A.

For application of this finite difference scheme, Eq. (3.40) must be rewritten as follows

$$\frac{\partial P}{\partial z} = -\left[\alpha(\theta) + j\omega\tau_{\mathrm{rel}}(\theta)\right] P + \left[\frac{D(\theta)}{\theta} + \frac{\partial D(\theta)}{\partial \theta}\right] \frac{\partial P}{\partial \theta} + D(\theta)\frac{\partial^2 P}{\partial \theta^2}. \tag{3.41}$$

The left hand side of Eq. (3.41) is approximated by the backward space difference. The right hand side is replaced by the average of the central angle differences, according to appendix A. Thus the approximation in difference form of Eq. (3.41) writes as

$$\begin{aligned}
&\frac{P_{n,m} - P_{n,m-1}}{\Delta z} = \\
&\quad -\left[\alpha(\theta) + j\omega\tau_{\mathrm{rel}}(\theta)\right] \frac{P_{n,m} + P_{n,m-1}}{2} + \\
&\quad + \left[\frac{D_n}{\theta_n} + \frac{D_{n+1} - D_{n-1}}{2\Delta\theta}\right] \frac{(P_{n+1,m} - P_{n-1,m}) + (P_{n+1,m-1} - P_{n-1,m-1})}{2 \cdot 2\Delta\theta} + \\
&\quad + D_n \frac{(P_{n+1,m} - 2P_{n,m} + P_{n-1,m}) + (P_{n+1,m-1} - 2P_{n,m-1} + P_{n-1,m-1})}{2\Delta\theta^2}
\end{aligned} \tag{3.42}$$

where indices n and m refer to the discretization step lengths $\Delta\theta$ and Δz for angle θ and length z, respectively. In the following the solution for one frequency component is investigated. To simplify the notation, three functions $r(\theta_n)$, $s(\theta_n)$ and $t(\theta_n)$ are introduced, which are only dependent on the angle θ_n:

$$\begin{aligned}
r(\theta_n) &= -\frac{\Delta z}{2}(\alpha(\theta_n) + j\omega\tau_{\mathrm{rel}}(\theta_n)) \\
s(\theta_n) &= \frac{\Delta z}{2 \cdot 2\Delta\theta}\left(\frac{D_n}{\theta_n} + \frac{D_{n+1} - D_{n-1}}{2\Delta\theta}\right) \\
t(\theta_n) &= \frac{\Delta z D_n}{2\Delta\theta^2}.
\end{aligned} \tag{3.43}$$

Eq. (3.42) rewrites inserting these functions Eq. (3.43) as

$$\begin{aligned}
&P_{n,m} - P_{n,m-1} = \\
&\quad r(\theta_n) \cdot (P_{n,m} - P_{n,m-1}) + \\
&\quad s(\theta_n) \cdot [(P_{n+1,m} - P_{n-1,m}) + (P_{n+1,m-1} - P_{n-1,m-1})] + \\
&\quad t(\theta_n) \cdot [(P_{n+1,m} - 2P_{n,m} + P_{n-1,m}) + (P_{n+1,m-1} - 2P_{n,m-1} + P_{n-1,m-1})]\,.
\end{aligned} \tag{3.44}$$

If Eq. (3.44) is reordered in a way, that all components of the power distribution P with space index m are on the left hand side and all with space index $m-1$ are on the right hand side, further functions $a(\theta)$,.., $f(\theta)$ can be defined:

$$\begin{aligned}
&P_{n-1,m}\underbrace{(s(\theta_n) - t(\theta_n))}_{a(\theta_n)} + P_{n,m}\underbrace{(1 - r(\theta_n) + 2t(\theta_n))}_{b(\theta_n)} + P_{n+1,m}\underbrace{(-s(\theta_n) - t(\theta_n))}_{c(\theta_n)} = \\
&P_{n-1,m-1}\underbrace{(-s(\theta_n) + t(\theta_n))}_{d(\theta_n)} + P_{n,m-1}\underbrace{(1 + r(\theta_n) - 2t(\theta_n))}_{e(\theta_n)} + P_{n+1,m-1}\underbrace{(s(\theta_n) + t(\theta_n))}_{f(\theta_n)}.
\end{aligned} \tag{3.45}$$

With these new functions $a(\theta_n)$,.., $f(\theta_n)$ the linear system can be rewritten as

$$\begin{aligned} a(\theta_n)P_{n-1,m} + b(\theta_n)P_{n,m} + c(\theta_n)P_{n+1,m} = \\ d(\theta_n)P_{n-1,m-1} + e(\theta_n)P_{n,m-1} + f(\theta_n)P_{n+1,m-1}, \end{aligned} \tag{3.46}$$

or in matrix notation as

$$\begin{bmatrix} b_1 & c_1 & & 0 \\ a_2 & \ddots & \ddots & \\ & \ddots & \ddots & c_{N-1} \\ 0 & & a_N & b_N \end{bmatrix} \cdot \begin{bmatrix} P_{1,m} \\ \vdots \\ \vdots \\ P_{N,m} \end{bmatrix} = \begin{bmatrix} e_1 & f_1 & & 0 \\ d_2 & \ddots & \ddots & \\ & \ddots & \ddots & f_{N-1} \\ 0 & & d_N & e_N \end{bmatrix} \cdot \begin{bmatrix} P_{1,m-1} \\ \vdots \\ \vdots \\ P_{N,m-1} \end{bmatrix} \tag{3.47}$$

or in short hand notation

$$\underline{G}_{\mathrm{l}} \cdot \underline{P}_m = \underline{G}_{\mathrm{r}} \cdot \underline{P}_{m-1}. \tag{3.48}$$

The left hand side matrix $\underline{G}_{\mathrm{l}}$ has a tri-diagonal structure, so the inversion of the matrix $\underline{G}_{\mathrm{l}}$ is always possible. This inversion leads to the solution for the linear system (Eq. (3.48)):

$$\underline{P}_m = \underline{G}_{\mathrm{l}}^{-1} \cdot \underline{G}_{\mathrm{r}} \cdot \underline{P}_{m-1} = \underline{G}_{\mathrm{total}} \cdot \underline{P}_{m-1}. \tag{3.49}$$

The power distribution $\underline{P}_m$ can be calculated by a matrix multiplication of the mixing matrix $\underline{G}_{\mathrm{total}}$ and the power distribution $\underline{P}_{m-1}$ of the previous spatial step. This matrix $\underline{G}_{\mathrm{total}}$ can be pre-computed once for each frequency component. So the solution for the time-dependent power-flow equation (3.38) is a set of independent linear systems with respect to the frequency components, which is unconditionally stable.
The initial condition for this systems consists of two parts. The first is the launching power distribution, which is defined by the used light source. The second part is the time signal, which should be transmitted. In this thesis, the time signal is chosen to be an approximated dirac-impulse, which means that the bandwidth of the dirac-impulse is limited to the simulation bandwidth, to get the optical transfer function $H_{\mathrm{opt}}(\omega)$ or the optical impulse response $h_{\mathrm{opt}}(t)$ of the SI-POF. The input power distribution varies depending on the light source, e.g. a laser diode or a LED.

The output of the power-flow equation at a specific fiber length $z_0 = m \cdot \Delta z$ is a power distribution over the angle θ and the frequency ω. The transfer function $H_{\mathrm{opt}}(z_0 = m \cdot \Delta z, \omega)$ is then calculated by summing up all angle components of one frequency component as follows

$$H_{\mathrm{opt}}(z_0, \omega) = \sum_{\theta=0}^{\theta=\theta_c} \underline{P}_m(\theta, \omega), \tag{3.50}$$

or equivalently for the impulse response by additionally applying the inverse Fourier transform

$$h_{\mathrm{opt}}(z_0,t) = \mathcal{F}^{-1}\left\{H_{\mathrm{opt}}(z_0,\omega)\right\} = \mathcal{F}^{-1}\left\{\sum_{\theta=0}^{\theta=\theta_c} \underline{P}_m(\theta,\omega)\right\}. \tag{3.51}$$

3.5 Channel model performance

The previous sub-chapter has shown the way how to solve the power-flow equation to model the SI-POF channel. In this sub-chapter, this new channel model is used to investigate the influence of several different parameter sets, e.g. launching conditions and fiber parameters. Finally, these results are compared to measurements of the transfer function of SI-POFs launched with a laser diode and a resonant-cavity LED to evaluate the precision of the fiber model.

3.5.1 Fiber parameters and launching condition

The calculation algorithm for the impulse response or transfer function already shown in the previous chapter needs four input functions. The first is the angular power distribution of the light source at the input of the fiber. The model does not allow the definition of a beam spot size yet, because the only parameter for differentiation of light modes is the angle θ relative to the fiber axis. But by using spatial decomposition any input beam form can be decomposed into planar waves with a constant angle θ. Thus, these decompositions can be used as input for this fiber model. In this work all light sources are modeled for simplicity by a Gaussian launching beam distribution [DS00] in the form of

$$p(\theta, z=0, \omega) = \exp\left[-\frac{(\theta-\theta_0)^2}{2\sigma_{\mathrm{beam}}^2}\right] \tag{3.52}$$

with $0 \leq \theta_0 \leq \theta_c$, where θ_0 is the mean value of the incidence angle distribution, with the full width at half maximum (FWHM)

$$\mathrm{FWHM} = 2\sigma_{\mathrm{beam}}\sqrt{2\ln 2}, \tag{3.53}$$

which can be approximated depending on the numerical aperture in the following way

$$\mathrm{FWHM} \approx 2\arcsin(\mathrm{NA}). \tag{3.54}$$

Combining Eqs. (3.54) and (3.53) and inserting them into Eq. (3.52) results in

$$p(\theta, z=0, \omega) = exp\left[-\ln 2\left(\frac{\theta-\theta_0}{\arcsin(\mathrm{NA})}\right)^2\right]. \tag{3.55}$$

To characterize the fiber itself, the three fiber parameter functions $\alpha(\theta)$, $\tau_{\text{rel}}(\theta)$, and $D(\theta)$ are needed. The relative delay of a mode $\tau_{\text{rel}}(\theta)$ can be calculated by using Eq. 3.37. The other two functions strongly depend on the manufacturing process, e.g. the roughness of the core cladding interface or the purity of the core material. Unfortunately, the only parameters given by the manufacturers are the total attenuation and some numbers about the numerical aperture, but nothing about desired information to calculate the mode-dependent attenuation according to sub-chapter 3.2.1. Also for the diffusion coefficient, there is no information about it from the manufacturer side.
So all the further studies in this work rely on measured data. Mateo et. al. [MLGZ06] have done a very good job in measuring and approximating these two functions by using a far field measurement and bi-sigmoid approximation fits. In Fig. 3.6 the results for $\alpha(\theta)$ and $D(\theta)$ for two fibers (Mitsubishi Eska GH and Toray PGU) are shown.

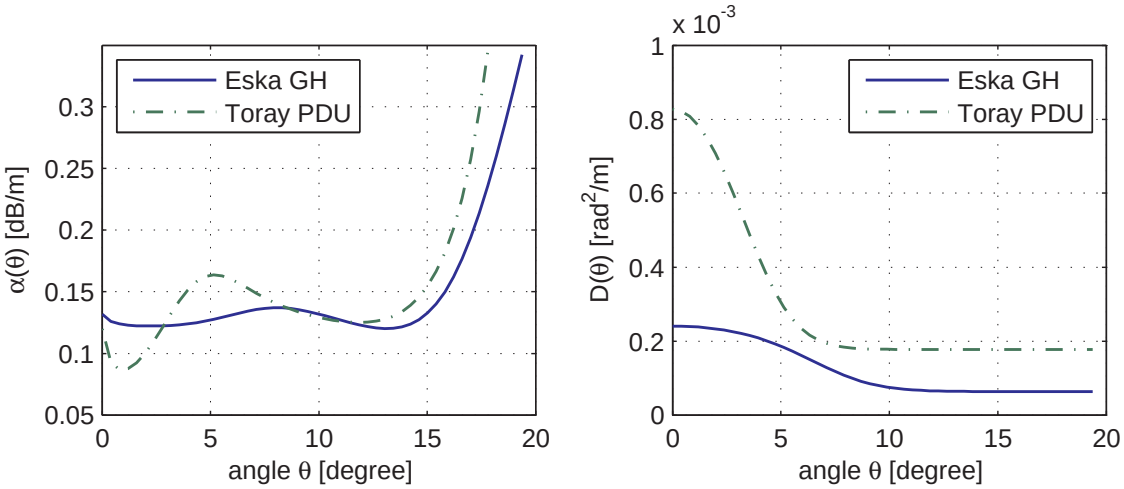

Figure 3.6: Fiber functions: left: mode-dependent attenuation, right: mode-dependent diffusion coefficient for Mitsubishi Eska GH and Toray PGU fiber [MLGZ06].

3.5.2 Numerical Results

Fig. 3.7 shows a typical result of the SI-POF channel model, on the left side the impulse response and on the right side the transfer function. For this plot, a Mitsubishi Eska GH SI-POF and a light source with a numerical aperture of NA = 0.17 was used. This simulation and all following ones have been carried out with an angular step size of $\Delta\theta = 0.4°$, a length step of $\Delta z = 0.25\,\text{m}$, and a time step of $\Delta t = 20\,\text{ps}$.

At a fiber length of 100 m the model predicts an overall attenuation of about 14.7 dB and a 3 dB bandwidth of around 48 MHz, which agrees well with measured results for this

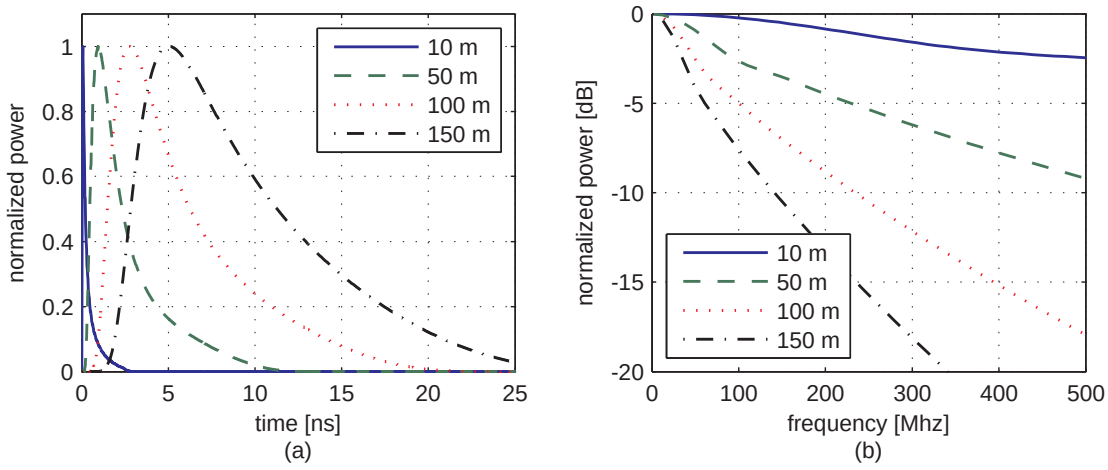

Figure 3.7: Numerical results for Mitsubishi Eska GH fiber:(a) impulse responses, (b) transfer functions for fiber length of 10, 50, 100 and 150 m.

kind of fiber. At shorter length (10 m) the shape of the impulse response in Fig. 3.7 is predominantely influenced by the mode-dependent attenuation, whereas with increasing fiber length the mode-coupling process interacts more and more with the attenuation, which leads to a more gaussian-like shape with a decentralized maximum, shifted to the left side, which means the tail of the impulse is much longer. The transfer function depicted in Fig. 3.7b shows low-pass characteristics with a smooth decrease.
In the following, SI-POFs from two manufacturers are investigated, which represent the most common used fibers. These are the Mitsubishi Eska Premium GH-4001 (Eska) and the Toray PGU-FB1000 (Toray).

Influence of the launching Numerical Aperture

All modeled fiber effects depend on the incident angle θ and on the initial power distribution, which models the light source. Combining these effects should result in a dependence of the behavior of the fiber on the inital condition. Fig. 3.8 shows the optical 3 dB bandwidth and the overall attenuation plotted versus the fiber length for the Eska fiber (3.8a,b) and the Toray fiber (3.8c,d) for different launching numerical apertures with a mean incident angle of $\theta_0 = 0°$.

As can be seen in Fig. 3.8 a and c, the bandwidth is strongly dependent on the initial power distribution, which means that an optical source with a small numerical aperture like a laser diode leads to a higher bandwidth than a source with a large numerical aperture (e.g. LED). For example, the calculated optical 3 dB bandwidth is doubled if a source with a NA = 0.17 is used instead of a NA = 0.8 for the Eska fiber at a fiber length

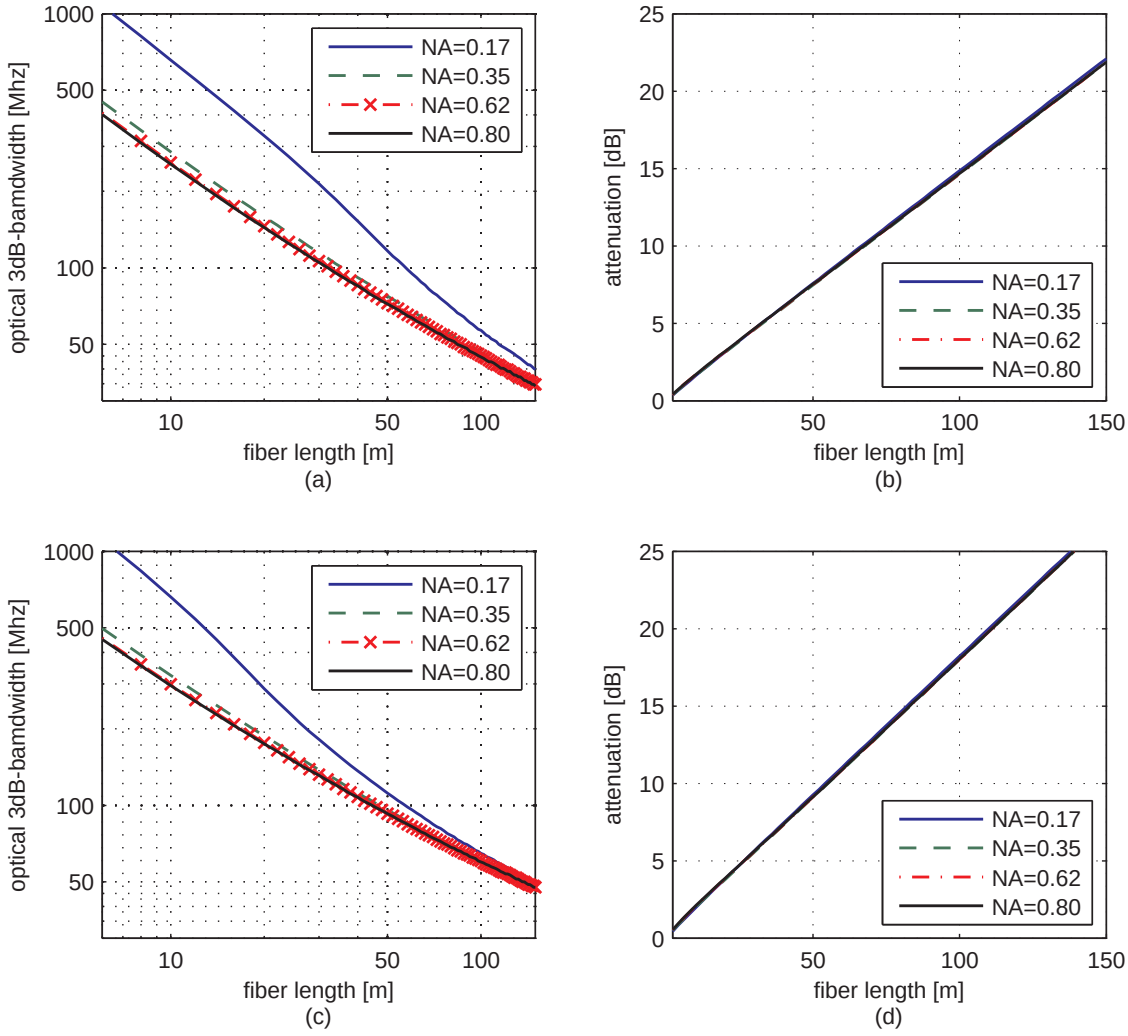

Figure 3.8: Optical 3db-bandwidth and attenuation vs. fiber length for different launch NA : (a) Eska bandwidth, (b) Eska attenuation, (c) Toray bandwidth, and (d) Toray attenuation.

of 30 m. However, at a certain fiber length the bandwidth will converge to a launch independent behavior. This effect can be explained by the equilibrium mode distribution (EMD), which means that the power distribution over the angle θ has reached a steady state, remaining unchanged if the light propagates further. This convergence of the power distribution is done by the mode-coupling process and the mode-dependent attenuation. These two effects interact with each other, and at some point this steady state is reached. The overall attenuation (Fig. 3.8 b and d) is independent of the launching condition and increases linearly with the fiber length. This figure shows also the difference of the two

fibers. The Toray fiber has a larger attenuation of approx. 3 dB at a fiber length of 100 m. The bandwidth behavior is also different. Due to the fact that the mode-coupling is stronger in the Toray fiber (see Fig. 3.6b), the steady state or EMD is reached earlier, which means the impact of the launching condition decreases faster with increasing fiber length. But at shorter fiber length the bandwidth is more or less the same for both fiber types, if a numerical aperture of NA = 0.17 is used. For larger launching numerical apertures the Toray fiber has a larger bandwidth.
To summarize, if a laser diode is used as optical source, which has a small numerical aperture, the system will benefit twice in terms of bandwidth. The first advantage is the large bandwidth of the laser diode itself, and the second is due to the smaller launch NA, which generates a larger modal bandwidth.

Influence of main incident angle

The second parameter of the launching condition which can be modified is the main incident angle θ_0, which represents the angle offset of the optical source to the fiber core axis. In Fig. 3.9 the optical 3 dB bandwidth is plotted vs. the fiber length for the two types of fiber and different main incident angles. These results show the angle alignment tolerance of different launch NAs.

The upper two plots in Fig. 3.9 show a dependence of the bandwidth for changing the main incident angle for a launch NA= 0.17. In this case the bandwidth strongly depends on the main angle. Only in the case of an incident angle of $\theta_0 = 0°$, the bandwidth enhancement of a low NA launch is maintained compared to the case with a large launch numerical aperture. If the main incident angle is increased, the bandwidth decreases. Already at an incident angle of 15° the effect of bandwidth increase due to smaller launching NA vanishes. In case of a launch NA of 0.8, no dependence on the main incident angle is observed, thus the bandwidth-length relation remains the same independent of the incident angle.
To conclude, optical sources with large numerical apertures are completely tolerant to angle alignment mismatches into the SI-POF, whereas sources with small NAs allow only small alignment mismatches, if the larger modal bandwidth shall be maintained. Thus, the benefit of using laser diodes in terms of bandwidth has to be paid by losing alignment tolerance, which is one of the big advantages of using POF in low cost applications, in which the tolerances should be not very stringent.

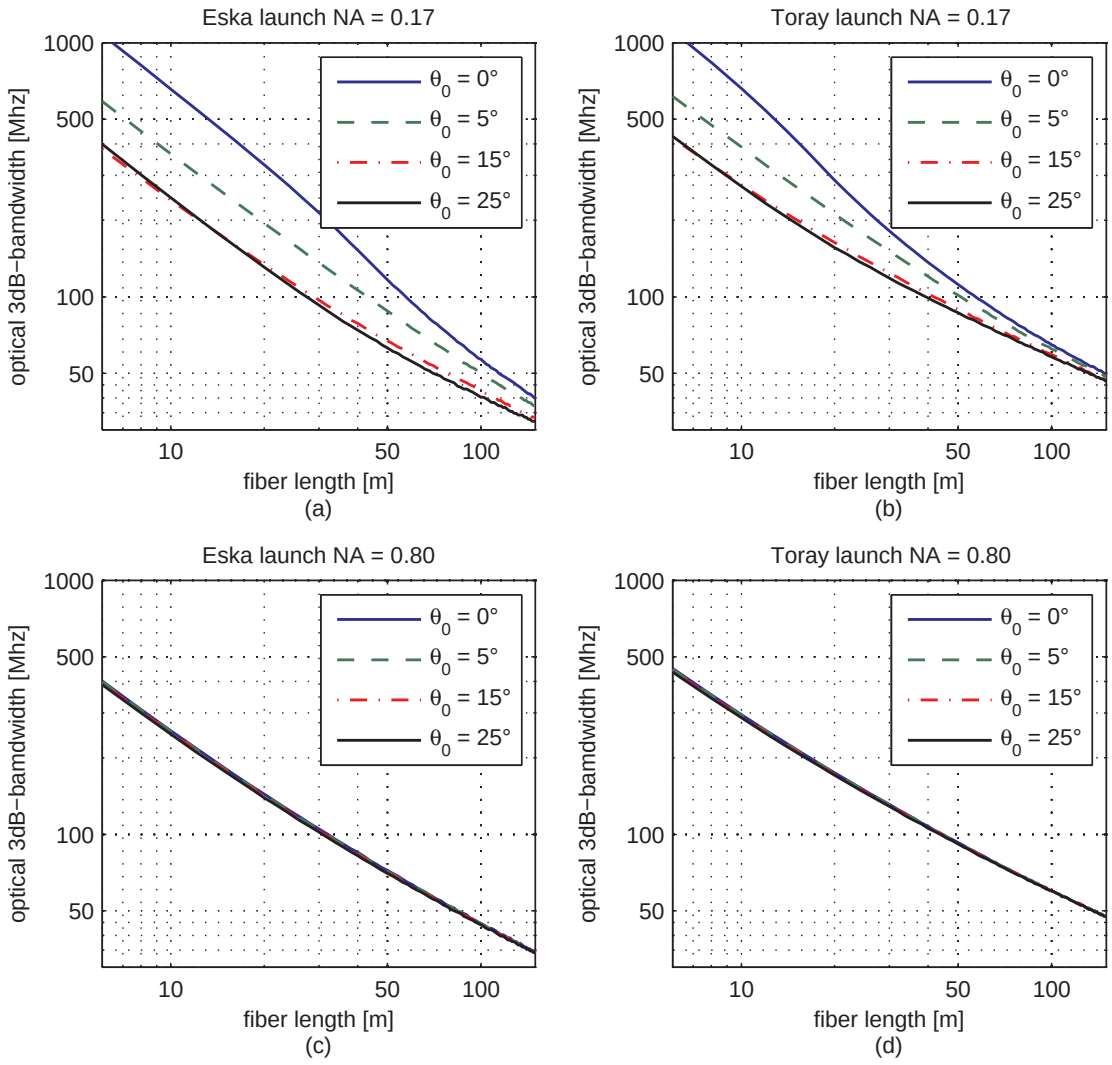

Figure 3.9: Optical 3dB-bandwidth vs. fiber length at varying main incident angles : (a) Eska with launch NA= 0.17, (b) Toray with launch NA= 0.17, (c) Eska with launch NA= 0.8, and (d) Toray with launch NA= 0.8.

3.5.3 Validation with Experimental Results

To get a figure of merit of the quality and the accuracy of the introduced SI-POF model, the results are compared to measured results. In Fig. 3.10 the simulated and measured transfer functions are plotted for a POF system consisting of a laser diode as optical source with a launching NA of 0.17, an Eska GH 4001 SI-POF, and a silicon photo diode with integrated trans-impedance amplifier.

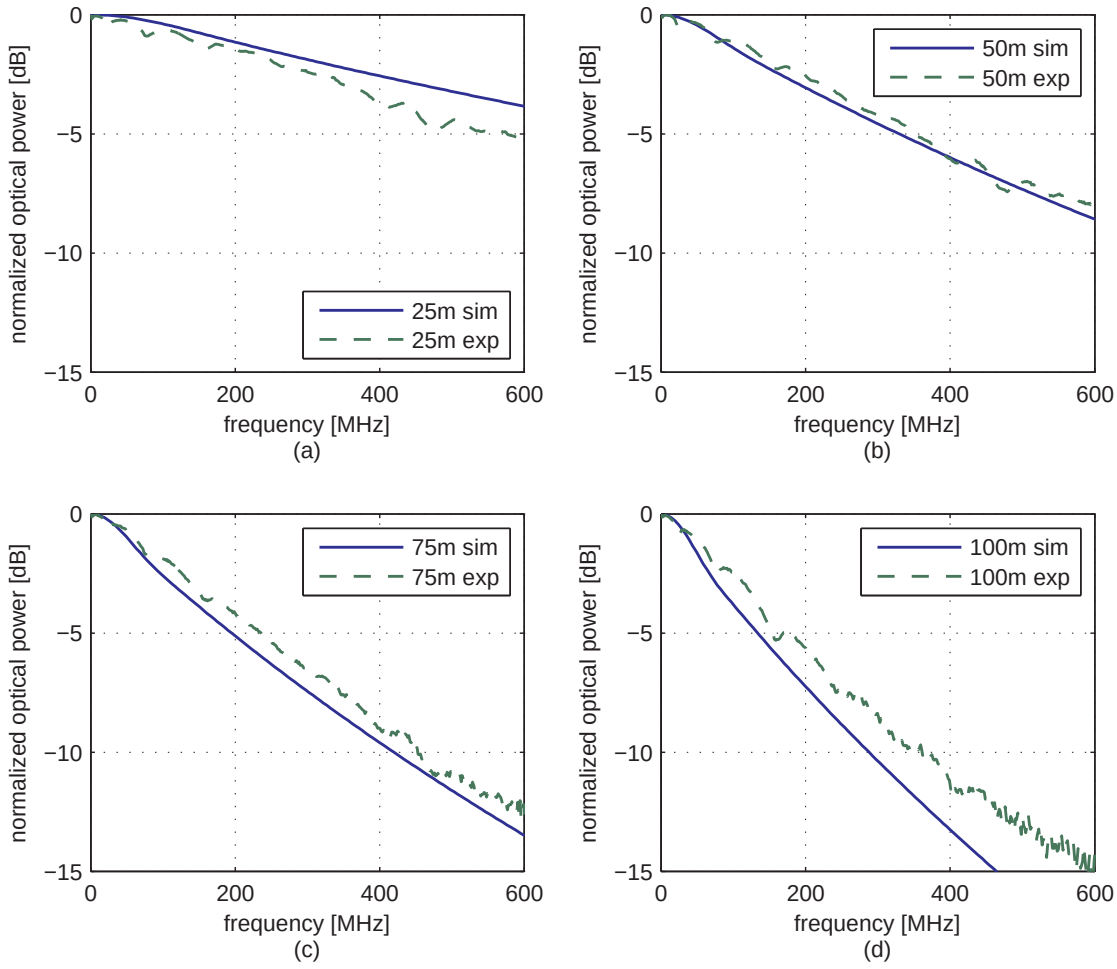

Figure 3.10: Measured (green dashed line) and simulated (blue solid line) optical transfer functions with Laser launching (NA=0.17) for fiber lengths of (a) 25 m, (b) 50 m, (c) 75 m, (d) 100 m of Eska GH4001 SI-POF.

To get the optical transfer function of the fiber itself, a reference measurement with a fiber length of 1 m was done. For all fiber lengths this reference transfer function is used to normalize the transfer functions, resulting in the optical transfer function of the fiber itself. The measured curves all have some dips and small oscillations at higher frequencies. These are not due to the SI-POF channel, but induced by some reflections in the measurement setup, due to electrical cables and impedance mismatches. Therefore, in a well designed transmitter and receiver, these dips and ripples will disappear, resulting in a smooth transfer function, similar to the simulated one. Unfortunately, well-designed and impedance matched transmitters and receivers were not available at the time of the

measurements.
For this measurement a Union Optronics SLD-650-P10-RG05 laser diode is used with a full width at half maximum (FWHM) of 8° and 30° in the parallel and perpendicular plane, respectively. This angular beam distribution is approximated with an NA of 0.17 in the simulation. For all fiber lengths, the measured and simulated transfer functions match well. In the transfer function plots a trend can be observed, that the measured transfer function is first lying under the simulated one (for 25 m) and then with increasing fiber length lying above the simulated one (for 75 m and 100 m). Reasons for this behavior could be coupling mismatches, the missing spot-size definition in the model or the receiver electronics. As the used TIA has an automatic gain control (AGC), the bandwidth of the TIA changes for different received optical powers. Thus the calibration function does not remain constant for all fiber lengths. The received optical power could not be adjusted to a constant value due to the lack of a variable optical attenuator. In the cases of 75 m and 100 m the simulations are lower bounds of the performance of the real laser launched SI-POF channels. For a fiber length of 50 m the simulated optical 3 dB bandwidth is 200 MHz and the measured 230 MHz. Taking all the imperfections in the measurement setup into account, these results match very well.

In Fig. 3.11 the same comparison is shown for a resonant-cavity LED (RC-LED) as optical source with a launching NA of 0.34 (Firecomms FC-300R-120) for fiber lengths of 25 m, 50 m, and 75 m.

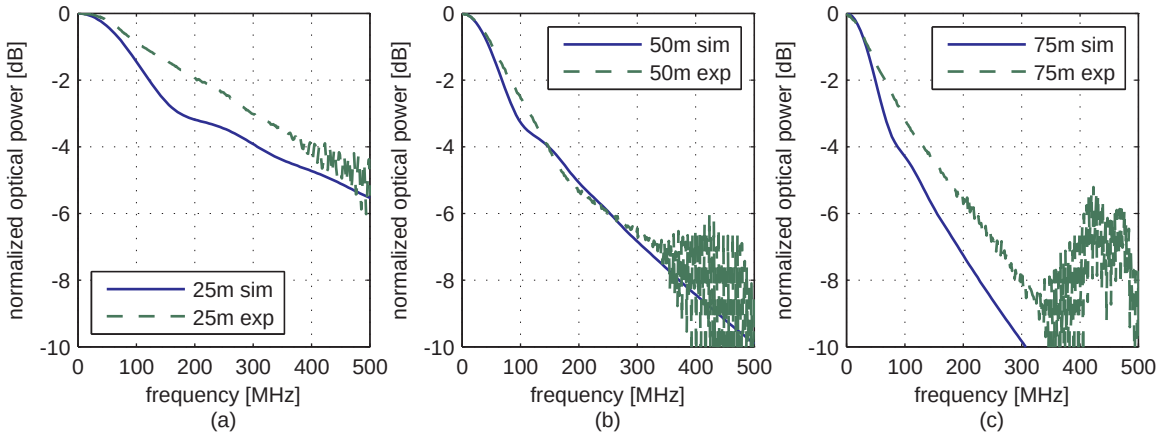

Figure 3.11: Measured (green dashed line) and simulated (blue solid line) optical transfer functions with LED launching for fiber lengths of (a) 25 m, (b) 50 m, (c) 75 m of Eska GH4001 SI-POF.

In this measurement a reference measurement with a fiber length of 1 m was carried out to normalize the other transfer functions, resulting in the optical transfer functions for RC-LED launch.
As can be seen in Fig. 3.11, the simulated transfer function does match very well for a fiber length of 50 m. For the two other fiber lengths, however, the simulated transfer functions are a bit too pessimistic. The oscillations in the measured transfer function result from reflections in the measurement setup. The optical 3 dB bandwidth at a fiber length of 50 m is 93 MHz for the simulation model and 117 MHz for the measurement. Hence either, the fiber model is too pessimistic for a RC-LED launch or the calibration measurement is not valid for all fiber lengths. A second reason could be that the receiver electronics, especially the TIA and its AGC, have a different behavior for the three fiber lengths. The latter reason is the most probable one, because the uncalibrated measured transfer functions, which are depicted in chapter 5 in Fig. 5.12 for 50 m and 75 m, have more or less the same 10 dB bandwidth. Thus, this measurement is not perfect for evaluating the fiber model performance, but it gives a first guess. In summary, this fiber model can be used as a lower bound for the system performance. Thus a new evaluation measurement should be done.

3.6 Summary

A general numerical method to solve the time-dependent power-flow equation was derived, which allows the modeling of all three dominant multimode fiber effects, such as mode-dependent attenuation, modal dispersion and mode coupling, in one differential equation. This fiber model accepts arbitrary input functions for the launching condition, the mode-dependent attenuation, the modal delay and the mode-coupling. Furthermore, the solution scheme is unconditionally stable, which allows large grid steps. This leads to very low computation time in the range of minutes for fiber lengths of 100 m on a contemporary personal computer.
The simulations in sub-chapter 3.5.2 show that the bandwidth of the SI-POF strongly depends on the launch condition (see Fig. 3.8), and for small launch NA also on the main incident angle θ_0. This means for a LED launch, that the bandwidth is independent of the main incident launching angle, which results in a very large alignment tolerance. For a laser launch, the big advantage is the larger bandwidth due to the smaller launch NA, but this has to be paid by a smaller angle alignment tolerance.

4

Baseband Transmission over Polymer Optical Fibers

Short-range multimode optical communication systems like POF systems typically employ direct intensity modulation and direct detection (IM/DD). This has mainly two reasons. The first is the cost factor. By using direct modulation, no other components are needed and the driving current of an optical source can be directly modulated. The second is that the bandwidth provided by a directly modulated optical source is sufficient for data rates up to the 10 Gbit/s range. This leads to the fact, that only the intensity of the light can be modulated, so no phase modulation can be done. On the receiver side only the intensity has to be detected, so a single photo diode is sufficient to capture all the transmitted information. This combination of transmitter modulation and receiver detection is called Intensity Modulation and Direct Detection (IM/DD).

In the previous chapter a channel model for the SI-POF was derived, in this chapter the system performance of a complete communication link is analyzed. For this purpose, the SI-POF channel model is extended to a full system simulation model to evaluate the performance of baseband modulation schemes in combination with receiver equalization. Therefore, the SI-POF channel model is extended to the IM/DD system model. Subsequently, the channel capacity of this model is evaluated for different launching conditions. Finally, the performance bounds of digital equalizers in combination with multilevel modulation, such as pulse amplitude modulation (PAM), are calculated and discussed.

4.1 The IM/DD channel model

In Fig. 4.1 the block diagram of the IM/DD channel is shown. This model is the basis for all theoretical investigations in this thesis. All these blocks are replaced step by step throughout this thesis by real devices until the fully working real-time demonstrator is shown in chapter 6.

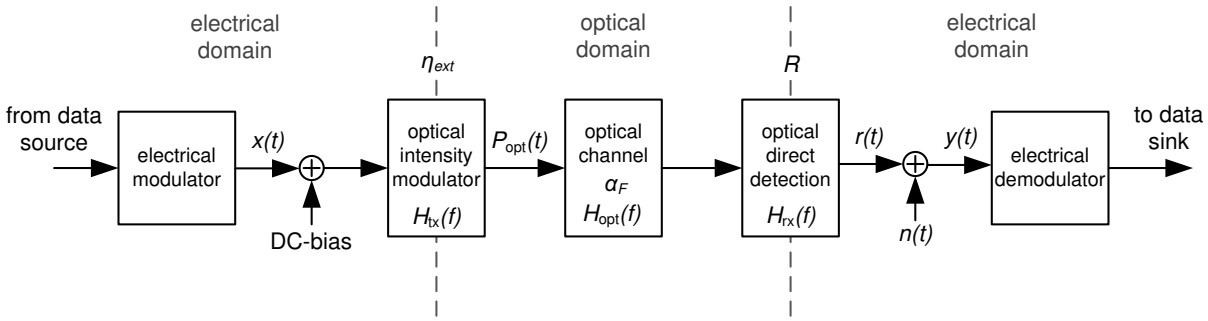

Figure 4.1: The optical IM/DD channel model.

At first, an electrical modulator block is used to modulate the incoming binary data stream using an appropriate modulation format, which can be a simple On-Off-Keying (OOK) or a multilevel baseband modulation scheme or a more sophisticated multi-carrier modulation scheme such as Discrete Multitone Modulation (DMT). This block can also contain all kinds of channel encoders, scramblers, or interleavers. This electrical transmitter signal processing results in a bipolar electrical current signal $x(t)$, which is used to drive an optical intensity-modulated biased source such as an LED or a laser diode.
The real-valued signal current $x(t)$ is peak limited with a maximum peak value of

$$x_{\text{peak}} = \max\left(|x(t)|\right). \tag{4.1}$$

Furthermore, it is defined that the mean value is $E\{x(t)\} = \langle x(t)\rangle = 0$ and the mean power (normalized on 1Ω) of $x(t)$ is $E\{x^2(t)\} = \langle x^2(t)\rangle$. To relate the peak value x_{peak} with the mean power $\langle x^2(t)\rangle$, the crest factor μ is introduced, which is defined as

$$\mu = \frac{x_{\text{peak}}}{x_{\text{RMS}}} = \frac{x_{\text{peak}}}{\sqrt{\langle x^2(t)\rangle}} \tag{4.2}$$

where x_{RMS} is the root mean-squared value of $x(t)$. An optical intensity-modulated light source can only be modulated with an unipolar signal, so the bipolar output signal $x(t)$

has to be shifted into a unipolar regime. This is achieved by adding a DC bias current I_{bias} appropriately. So the unipolar driving current signal $I_{\text{drive}}(t)$ writes as

$$I_{\text{drive}}(t) = I_{\text{bias}} + x(t) \tag{4.3}$$

where the minimum peak value of $x(t)$ has to be smaller than the bias current I_{bias}

$$x_{\text{peak}} \leq I_{\text{bias}}. \tag{4.4}$$

The ratio between the maximum absolute value x_{peak} of $x(t)$ and the bias current I_{bias} is defined as the modulation index η_{mod}

$$\eta_{\text{mod}} = \frac{x_{\text{peak}}}{I_{\text{bias}} - I_{\text{th}}} \qquad \text{with} \qquad 0 \leq \eta_{\text{mod}} \leq 1. \tag{4.5}$$

The optical intensity modulator is modeled as an ideally linear modulator, as depicted in Fig. 4.2. Using this model, it is assumed that no optical power is emitted when the driving current $I_{\text{drive}}(t)$ is below a certain threshold current I_{th} and is linearly increasing in proportion to the driving current $I_{\text{drive}}(t)$ for currents larger than I_{th}. Another assumption of the model is that there is no saturation effect for larger driving currents at least until $2 \cdot I_{\text{bias}}$.

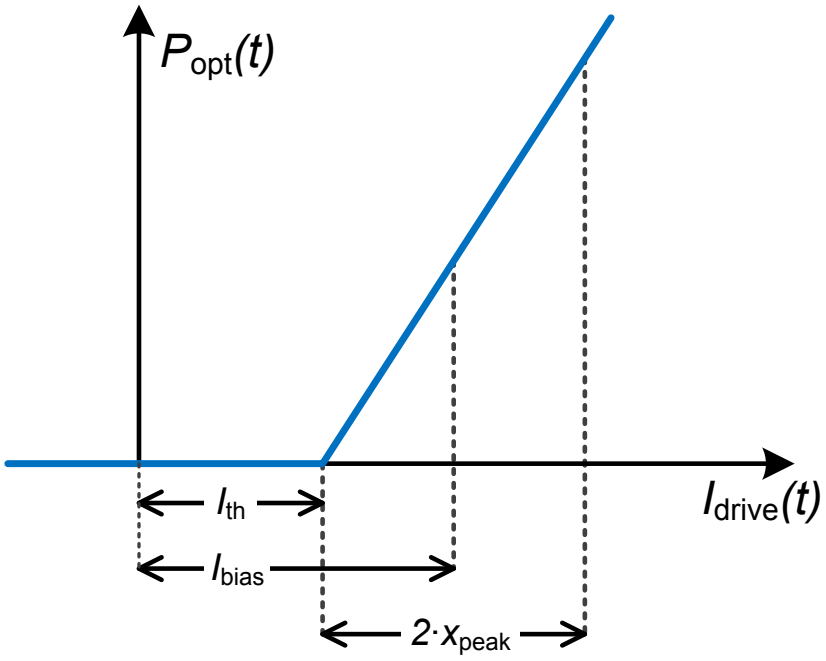

Figure 4.2: Ideal optical intensity modulator model.

The relation between the optical output power of the optical intensity modulator and the driving current $I_{\text{drive}}(t)$ is defined by a proportionality constant η_{ext}, which is the external

efficiency of the electrical current-to-optical conversion given in W_o/A. Although I_{th} is depicted in Fig. 4.2 with a non-zero value, it will, for convenience, be assumed to be 0 in the following. The resulting instantaneous transmitted power $P_{opt}(t)$ in W_o can then be written as a function of the driving current I_{drive} combining Eqs. (4.2), (4.3), and (4.5) to

$$\begin{aligned} P_{opt}(t) &= \eta_{ext} \cdot I_{drive} \\ &= \eta_{ext} \left[I_{bias} + x(t) \right] \\ &= \eta_{ext} \left[\frac{x_{peak}}{\eta_{mod}} + x(t) \right] \\ &= \eta_{ext} \left[\frac{\mu \cdot x_{RMS}}{\eta_{mod}} + x(t) \right] \\ &= \eta_{ext} \left[\frac{\mu}{\eta_{mod}} \sqrt{\langle x^2(t) \rangle} + x(t) \right]. \end{aligned} \tag{4.6}$$

This equation does not yet include the dynamic behavior of the optical source, because the model of the optical intensity modulator relies on a static current-to-optical power transfer characteristic. To take also the dynamic behavior into account, the modulation response of the optical source is modeled as a 1st order RC-lowpass with 3 dB frequency f_{3dB}^{tx} and a transfer function $H_{tx}(f)$ or equivalently an impulse response $h_{tx}(t)$ with $\int_{-\infty}^{\infty} h_{tx}^2(t)dt = 1$. Thus the complete description of the instantaneous transmitted power $P_{opt}(t)$ is given by the convolution of Eq. (4.6) and $h_{tx}(t)$, which writes as

$$P_{opt}(t) = \eta_{ext} \left[\frac{\mu}{\eta_{mod}} \sqrt{\langle x^2(t) \rangle} + x(t) \right] * h_{tx}(t) \tag{4.7}$$

where $*$ stands for the linear convolution. This optical power modulated signal is transmitted over the fiber, which is modeled using the SI-POF channel model derived in chapter 3. This model consists of a static fiber length dependent attenuation α_F and an optical transfer function $H_{opt}(f)$ corresponding to an impulse response $h_{opt}(t)$ with $\int_{-\infty}^{\infty} h_{opt}^2(t)dt = 1$. Thus the received optical instantaneous signal $P_{opt}^{rx}(t)$ can be written as

$$\begin{aligned} P_{opt}^{rx}(t) &= P_{opt}(t) * (\alpha_F \cdot h_{opt}(t)) \\ &= \eta_{ext}\alpha_F \left[\frac{\mu}{\eta_{mod}} \sqrt{\langle x^2(t) \rangle} + x(t) \right] * h_{tx}(t) * h_{opt}(t). \end{aligned} \tag{4.8}$$

On the receive side, the optical direct detection block consists of a photo diode and a trans-impedance amplifier. The photo diode can be modeled as a linear transformation of the received optical power to the photo diode current via the responsivity R, which is given in A/W_o. The dynamic response of the photo diode is modeled as a 1st order RC-lowpass with a 3 dB frequency f_{3dB}^{rx}, which defines the transfer function $H_{rx}(f)$ with

the corresponding impulse response $h_{\mathrm{rx}}(t)$ with $\int_{-\infty}^{\infty} h_{\mathrm{rx}}^2(t)dt = 1$. Thus the input current into the trans-impedance amplifier I_{photo} can be written as

$$\begin{aligned} I_{\mathrm{photo}}(t) &= P_{\mathrm{opt}}^{\mathrm{rx}}(t) * (R \cdot h_{\mathrm{rx}}(t)) \\ &= \eta_{\mathrm{ext}}\alpha_{\mathrm{F}} R \left[\frac{\mu}{\eta_{\mathrm{mod}}} \sqrt{\langle x^2(t) \rangle} + x(t) \right] * h_{\mathrm{tx}}(t) * h_{\mathrm{opt}}(t) * h_{\mathrm{rx}}(t). \end{aligned} \tag{4.9}$$

The trans-impedance amplifier (TIA) acts as a linear amplifier, which subtracts the DC component of the input signal to get a bipolar or AC-coupled signal at the output, because there is no information in the DC component. In the following it is assumed, that dynamic response of the TIA is included in the transfer function of the photo diode $H_{\mathrm{rx}}(f)$. This leads to the output signal $r(t)$ of the optical direct detection block as

$$\begin{aligned} r(t) &= I_{\mathrm{photo}}(t) - \langle I_{\mathrm{photo}}(t) \rangle \\ &= \eta_{\mathrm{ext}}\alpha_{\mathrm{F}} R \cdot x(t) * h_{\mathrm{tx}}(t) * h_{\mathrm{opt}}(t) * h_{\mathrm{rx}}(t). \end{aligned} \tag{4.10}$$

Unfortunately, an amplifier always adds noise, in this case it is just amplified thermal noise, which can be modeled as additive white gaussian noise (AWGN) $n(t)$ with zero mean and single-sided power-spectral density N_0. All other noise sources (shot noise, etc.) are neglected throughout this thesis due to the dominance of thermal noise. This leads to the input signal $y(t)$ of the electrical demodulator, which writes as

$$y(t) = r(t) + n(t). \tag{4.11}$$

The signal-to-noise power ratio SNR of the signal $y(t)$ can therefore be defined as

$$\begin{aligned} \mathrm{SNR} &= \frac{P_{\mathrm{signal}}}{P_{\mathrm{noise}}} = \frac{r_{\mathrm{RMS}}^2}{n_{\mathrm{RMS}}^2} \\ &= \frac{\eta_{\mathrm{ext}}^2 \alpha_{\mathrm{F}}^2 R^2 \cdot x_{\mathrm{RMS}}^2}{N_0 \cdot \Delta f_{\mathrm{noise}}} \end{aligned} \tag{4.12}$$

where $\Delta f_{\mathrm{noise}}$ is the equivalent noise bandwidth. With the introduction of the noise equivalent power (NEP), which is the equivalent optical noise power spectral density of the electrical thermal noise generated by the amplifier transformed to the optical input of the photo diode, the noise power-spectral density N_0 can be written as

$$N_0 = (R \cdot \mathrm{NEP})^2 \tag{4.13}$$

where the NEP is given in $\mathrm{W_o}/\sqrt{\mathrm{Hz}}$. This is a commonly used figure of merit to characterize the noise performance of photo-detectors, which includes the photo diode and the TIA. Inserting Eqs. (4.2), (4.5), and (4.13) into Eq. (4.12) results in

$$\mathrm{SNR} = \frac{\left(\eta_{\mathrm{ext}}\alpha_{\mathrm{F}} R \cdot \frac{\eta_{\mathrm{mod}}}{\mu} I_{\mathrm{bias}} \right)^2}{(R \cdot \mathrm{NEP})^2 \cdot \Delta f_{\mathrm{noise}}}. \tag{4.14}$$

This can be modified to depend on the mean optical transmit power P_{mean} by using $P_{\text{mean}} = \eta_{\text{ext}} \cdot I_{\text{bias}}$, so the electrical SNR writes as

$$\text{SNR} = \frac{\alpha_{\text{F}}^2 \eta_{\text{mod}}^2 P_{\text{mean}}^2}{\mu^2 \text{NEP}^2 \cdot \Delta f_{\text{noise}}}. \tag{4.15}$$

4.2 The capacity of the SI-POF IM/DD channel

Using the channel model derived in the previous chapter, the channel capacity for the SI-POF IM/DD channel will be analyzed in this section by making use of the well-known water-filling method described in [Gal68, Pro01]. The idea of this SI-POF IM/DD channel analysis has first been presented by Gaudino et. al. in [GBB+07], which forms the basis of the derivation given in subsection 4.2.1. These results were extended by Lee et al. [LBR+09], but only for the assumption that the SI-POF channel transfer function can be modeled with a gaussian low-pass characteristic, which is a very pessimistic approximation of a SI-POF system. In this thesis, the channel capacity is calculated with the new SI-POF channel model given in chapter 3 and compared to the two mainly used approximations for the SI-POF, such as a gaussian low-pass characteristics or a 1st order low-pass characteristics [LBR+09].

4.2.1 Derivation of the channel capacity of the SI-POF IM/DD channel

As mentioned in the previous chapter, only the intensity of the light can be modulated, so the channel capacity has to be calculated for a real valued input. Thus the channel capacity C in bits/s [Sha48, Gal68] is given by maximizing the quantity

$$C \leq \frac{1}{2} \int_{-\infty}^{\infty} \log_2 \left(1 + \frac{G_{\text{sig}}(f)}{G_{\text{noise}}(f)} \right) df \tag{4.16}$$

under the average receive power constraint

$$P_{\text{sig}} = \int_{-\infty}^{\infty} G_{\text{sig}}(f) df \tag{4.17}$$

where $G_{\text{sig}}(f)$ is the power spectral density of the receive signal, P_{sig} is its total power, and $G_{\text{noise}}(f)$ is the noise power spectral density of the additive white Gaussian noise source. The power spectral density $G_{\text{sig}}(f)$ has to be found, which maximizes the capacity C. The solution for this optimization problem is based on Lagrange multipliers and given in [Gal68, Pro01]. It can be expressed by

$$G_{\text{sig}}(f) = (\nu - G_{\text{noise}}(f))^+ \tag{4.18}$$

where ν is a constant value to be selected such that

$$\int_{-\infty}^{\infty} (\nu - G_{\text{noise}}(f))^{+} = P_{\text{sig}}. \tag{4.19}$$

The function $(\ldots)^{+}$ delivers the positive part of its argument, defined as

$$(z)^{+} = \begin{cases} z & \text{if} \quad z \geq 0 \\ 0 & \text{if} \quad z < 0 \end{cases}. \tag{4.20}$$

This method is known in the literature as water-filling [Gal68], the idea of it is depicted in Fig. 4.3.

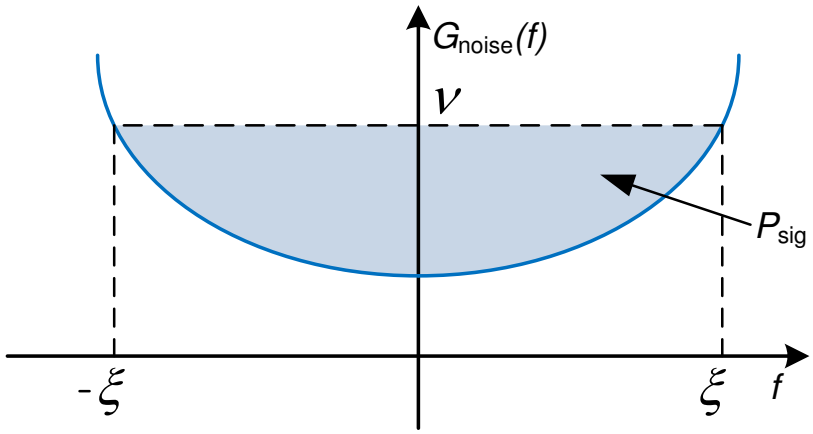

Figure 4.3: Water-filling method.

For a given $G_{\text{noise}}(f)$, finding ν in Eq. (4.18) means finding the "water-level" ν, so that the grey area, which is surrounded by $G_{\text{noise}}(f)$ and ν, in the figure is exactly equal to P_{sig}. The resulting optimal $G_{\text{sig}}(f)$ is then defined by inverting $G_{\text{noise}}(f)$ and using the ν level as reference level. Hence the solution allocates most of the power in frequency ranges where the noise is least. In particular, no power is allocated outside the "critical frequency" ξ, which satisfies the equation $G_{\text{noise}}(\xi) = \nu$.
In case of the channel model derived in chapter 4.1, the power spectral density of the ac-coupled received signal $r(t)$ (Eq. (4.10)) after photo detection writes as

$$G_{\text{r}}(f) = R^2 \alpha_{\text{F}}^2 \left|H_{\text{total}}(f)\right|^2 \eta_{\text{ext}}^2 G_{\text{x}}(f) \tag{4.21}$$

where $H_{\text{total}}(f) = H_{\text{tx}}(f) \cdot H_{\text{opt}}(f) \cdot H_{\text{rx}}(f)$ and $G_{\text{x}}(f)$ is the power spectral density of the DC-free transmitted signal $x(t)$ (defined by Eqs. (4.1) and (4.2)). The additive white

gaussian noise has a flat power spectral density function

$$G_{\mathrm{n}}(f) = \frac{N_0}{2} = \frac{R^2 \mathrm{NEP}^2}{2}. \tag{4.22}$$

The capacity of the SI-POF channel can now be calculated by inserting Eqs. (4.21) and (4.22) in Eq. (4.16), and by setting $G_{\mathrm{sig}} = G_{\mathrm{r}}$ and $G_{\mathrm{noise}} = G_{\mathrm{n}}$, which results in

$$C \leq \frac{1}{2} \int_{-\infty}^{\infty} \log_2 \left(1 + \frac{2R^2 \alpha_{\mathrm{F}}^2 \left| H_{\mathrm{total}}(f) \right|^2 \eta_{\mathrm{ext}}^2 G_{\mathrm{x}}(f)}{R^2 \mathrm{NEP}^2} \right) df. \tag{4.23}$$

The two functions $G_{\mathrm{sig}}(f)$ and $G_{\mathrm{noise}}(f)$ of the general optimization problem formulated in Eqs. (4.18) and (4.19) can be redefined in a way that all distortions are parts of the noise function $G_{\mathrm{noise}}(f)$. Applying this redefinition results in

$$G_{\mathrm{noise}}(f) = \frac{\mathrm{NEP}^2}{2\alpha_{\mathrm{F}}^2 \left| H_{\mathrm{total}}(f) \right|^2 \eta_{\mathrm{ext}}^2}. \tag{4.24}$$

Thus the signal function $G_{\mathrm{sig}}(f)$ consists only of the power spectral density of the ac-coupled modulation current $x(t)$, which writes as

$$G_{\mathrm{sig}}(f) = G_x(f). \tag{4.25}$$

The power constraint (Eq. (4.17)) can now be calculated dependent on the mean optical transmit power P_{mean}, the crest factor μ of $x(t)$, the modulation index η_{mod}, and the external quantum efficiency η_{ext} as follows

$$P_{\mathrm{sig}} = P_x = x_{\mathrm{RMS}}^2 = \frac{\eta_{\mathrm{mod}}^2}{\mu^2} \cdot I_{\mathrm{bias}}^2 = \frac{\eta_{\mathrm{mod}}^2}{\mu^2} \frac{P_{\mathrm{mean}}^2}{\eta_{\mathrm{ext}}^2}. \tag{4.26}$$

Now the power spectral density $G_x(f)$ of the modulation current $x(t)$ is unknown in the optimization problem and must satisfy the power constraint set by Eq. (4.17). Combining Eqs. (4.18), (4.19), and (4.26) results in

$$\int_{-\xi}^{\xi} (\nu - G_{\mathrm{noise}}(f)) df = P_x \tag{4.27}$$

with

$$\nu = G_{\mathrm{noise}}(\xi). \tag{4.28}$$

By inserting Eqs. (4.24) and (4.26) in Eq. (4.27), the final optimization problem can be written as

$$\begin{aligned}
\int_{-\xi}^{\xi} \left(G_{\text{noise}}(\xi) - G_{\text{noise}}(f)\right) df &= P_x \\
\int_{-\xi}^{\xi} \frac{\text{NEP}^2}{2\alpha_{\text{F}}^2 \eta_{\text{ext}}^2} \left(\frac{1}{|H_{\text{total}}(\xi)|^2} - \frac{1}{|H_{\text{total}}(f)|^2} \right) df &= \frac{\eta_{\text{mod}}^2}{\mu^2} \frac{P_{\text{mean}}^2}{\eta_{\text{ext}}^2} \\
\int_{0}^{\xi} \left(\frac{1}{|H_{\text{total}}(\xi)|^2} - \frac{1}{|H_{\text{total}}(f)|^2} \right) df &= \frac{\eta_{\text{mod}}^2 \alpha_{\text{F}}^2 P_{\text{mean}}^2}{\mu^2 \text{NEP}^2}.
\end{aligned} \tag{4.29}$$

If the signal to noise power ratio (SNR), defined in Eq. (4.15), is inserted in the above equation, the optimization problem in ξ simplifies to

$$\int_{0}^{\xi} \left(\frac{1}{|H_{\text{total}}(\xi)|^2} - \frac{1}{|H_{\text{total}}(f)|^2} \right) df = \text{SNR} \cdot \Delta f_{\text{noise}}. \tag{4.30}$$

This turns out to be a nonlinear problem in the unknown ξ, which can be solved numerically. If an appropriate ξ has been found, the capacity of the SI-POF channel can be calculated as

$$C \leq \int_{0}^{\xi} \log_2 \left(1 + \frac{\nu - G_{\text{noise}}(f)}{G_{\text{noise}}(f)} \right) df \tag{4.31}$$

which can be reformulated as

$$C \leq \int_{0}^{\xi} \log_2 \left(\frac{\nu}{G_{\text{noise}}(f)} \right) df. \tag{4.32}$$

Inserting Eq. (4.28) in Eq. (4.32) results in

$$C \leq \int_{0}^{\xi} \log_2 \left(\frac{G_{\text{noise}}(\xi)}{G_{\text{noise}}(f)} \right) df. \tag{4.33}$$

Finally, Eq. (4.24) can be inserted in the above equation to get the dependence on the system transfer function $H_{\text{total}}(f)$, which writes as

$$C \leq \int_{0}^{\xi} \log_2 \left(\frac{|H_{\text{total}}(f)|^2}{|H_{\text{total}}(\xi)|^2} \right) df. \tag{4.34}$$

4.2.2 Numerical results for the Channel capacity

In sub-chapter 4.2.1, the channel capacity was derived for an arbitrary transfer function. At first the channel capacity of the optical channel itself without any limitation induced by transmitter or receiver devices is considered. Therefore, the transfer functions $H_{\mathrm{tx}}(f)$ and $H_{\mathrm{rx}}(f)$ are set to 1. The launching power distribution (chapter 3.5.1) is investigated for two different numerical apertures (NA). Fig. 4.4 shows the channel capacities for laser launch with a NA= 0.1 for fiber lengths of 25 m, 50 m, 75 m and 100 m.

The capacity is given in Gbit/s and the equivalent noise bandwidth $\Delta f_{\mathrm{noise}}$ is chosen to be 1 GHz. For comparison there are also capacity curves for the gaussian low-pass

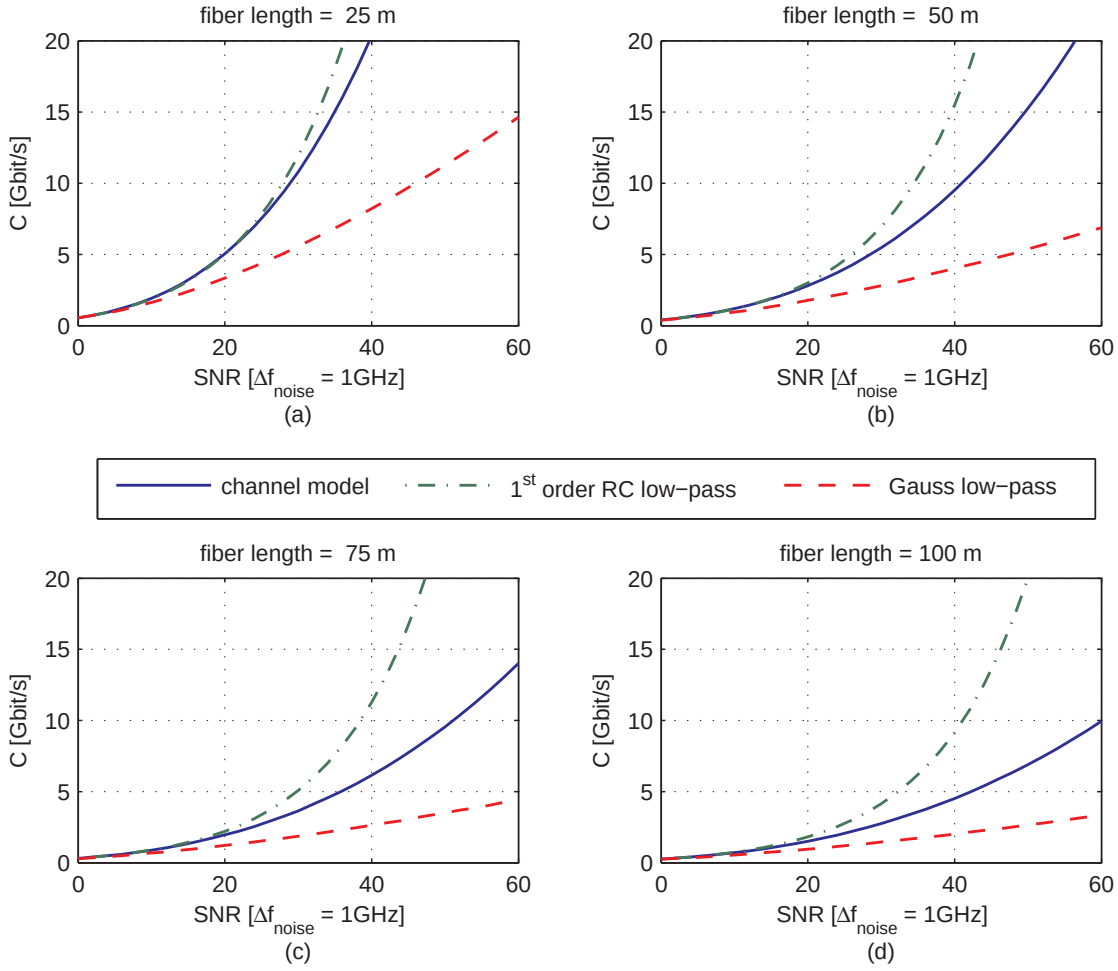

Figure 4.4: Channel capacity of the SI-POF channel (Eska GH fiber) for a launching NA of 0.1 as a function the signal to noise power ratio (SNR) for fiber lengths of 25, 50, 75 and 100 m (for comparison, capacities of a gaussian low-pass and a 1st order RC-low-pass channel are evaluated).

and 1st order low-pass approximations of the total channel transfer function. The 3 dB frequencies of these two approximations are given by the fiber transfer function of the SI-POF model. It can be seen that the two approximations are a lower and an upper bound for the real channel capacity of the SI-POF channel derived in chapter 3. For short distances the channel model capacity matches quite well with the 1st order low-pass approximation. With increasing fiber length the channel model capacity moves down to the lower bound, which is the gaussian low-pass approximation. This behavior confirms very well the conclusions done in [Lee09], in which the 1st order approximation is used for fiber lengths up to 100 m and the gaussian approximation for fiber lengths $\geq$200 m.

In Fig. 4.5 the channel capacity calculations were done for an LED launch with a launching NA of 0.78. The same behavior as for the laser launch can be observed. The two low-pass approximations act as upper and lower bound of the capacity.

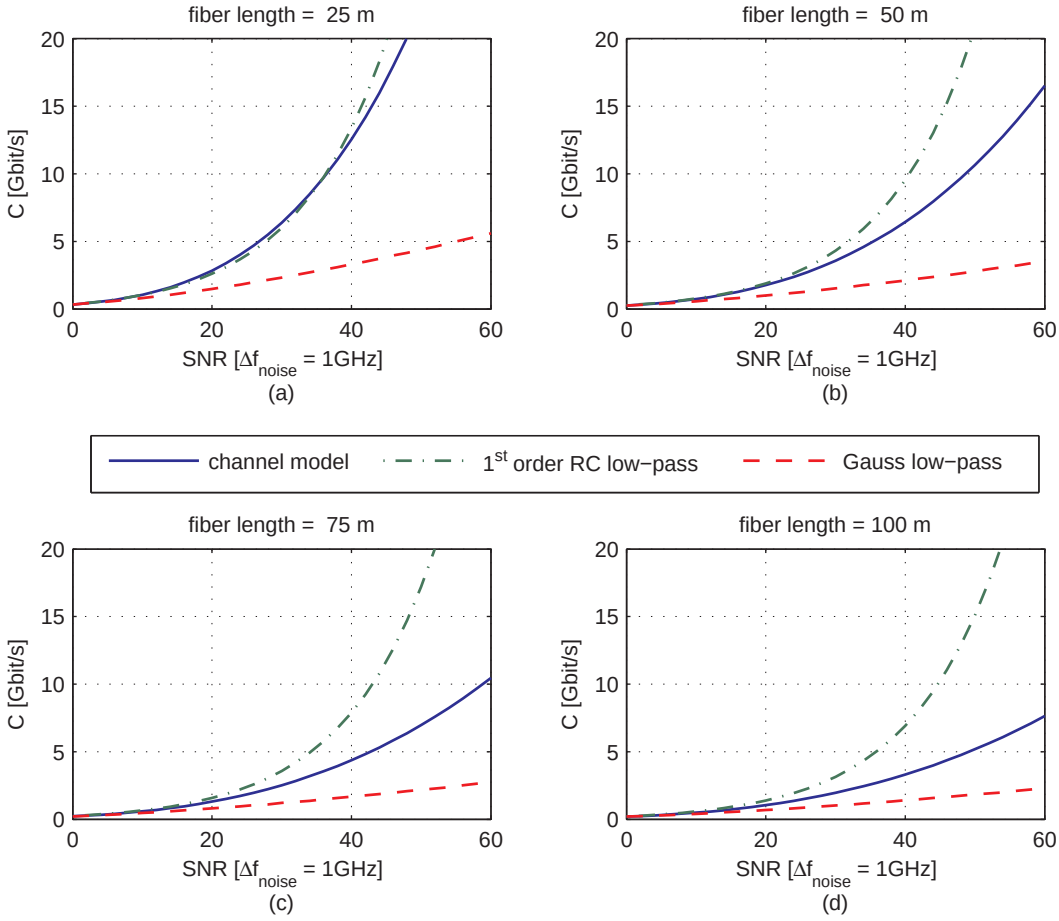

Figure 4.5: Channel capacity of the SI-POF channel for a launch NA of 0.78 vs. the signal to noise ratio (SNR) for fiber lengths of 25, 50, 75 and 100 m.

Of course the capacities are much smaller compared to the ones with laser launch, but this is quite obvious due to the smaller bandwidth induced by the larger numerical aperture (see section 3). For example for an SNR of 40 dB and a fiber length of 100 m the capacity is 4.52 Gbit/s and 3.31 Gbit/s for laser and LED launch, respectively. So the capacity gain just due to the smaller launch NA is 27 %.
So far, only the bandwidth limitations due to the fiber itself are taken into account. Now the low-pass characteristics of the electro-optical conversion component (LED or Laser) is included in the calculation. This component is modeled as a 1st order low-pass with a 3dB frequency bw_{el}. The laser diode used is modeled with a numerical aperture of 0.1 and an electrical bandwidth bw_{el} of 1 GHz. The resonant-cavity LED (RC-LED) has a numerical aperture of 0.34 and an electrical bandwidth bw_{el} of 150 MHz. These parameters represent commonly used light sources for SI-POF systems. These values and all other relevant parameters are listed in Tab. 4.1.

Parameter	Value		Unit
	Laser launch	RC-LED launch	
P_{mean}	2.5	-3	dBm
NA	0.1	0.34	
bw_{el}	1000	150	MHz
α_{F}	140		dB/km
NEP	16		$\mathrm{pW}/\sqrt{\mathrm{Hz}}$
$\Delta f_{\mathrm{noise}}$	1000		MHz

Table 4.1: System Parameters for channel capacity simulations.

In Fig. 4.6 the capacity curves for these light sources are illustrated. With the inclusion of the transmitter bandwidth, capacity values of 4.42 Gbit/s, and 2.78 Gbit/s can be observed at a SNR of 40 dB, a fiber length of 100 m and laser or RC-LED launch, respectively. If these values are compared to the values without transmitter bandwidth limitation, it can be observed that the capacity value for laser launch is decreased only by 0.1 Gbit/s. Thus for laser launch the fiber low-pass characteristic is the predominant effect. This is different for the case with RC-LED. Here the capacity value without transmitter limitation is 3.46 Gbit/s, so the decrease in capacity is 0.68 Gbit/s or 20 %. The difference between laser launch and RC-LED launch is 1.64 Gbit/s or 37 %.

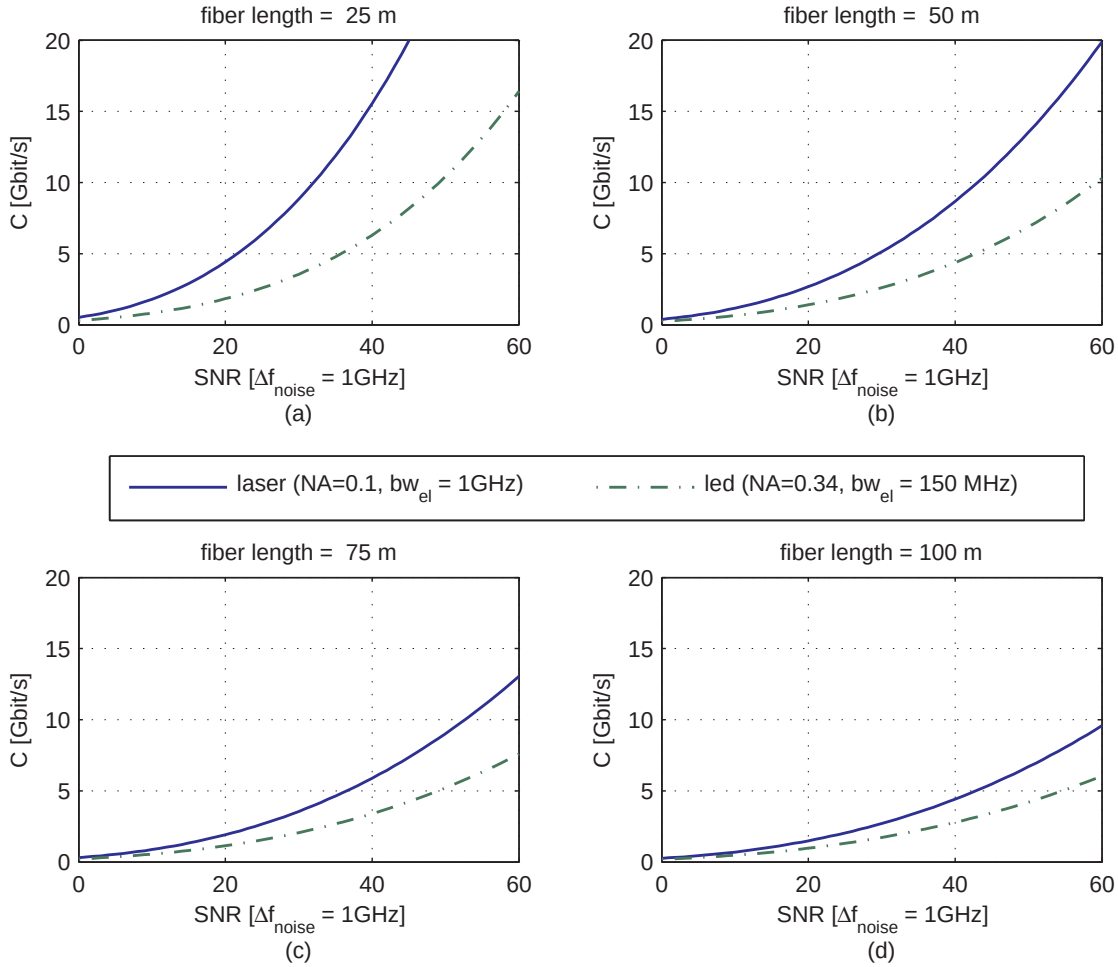

Figure 4.6: Channel capacity of the SI-POF channel with laser and RC-LED, including transmitter bandwidth limitations, as a function of the signal to noise power ratio (SNR) for fiber lengths of 25, 50, 75 and 100 m.

To evaluate the capacity of a SI-POF system with contemporary components, the system parameters listed in Tab. 4.1 are used. Additionally the modulation index η_{mod} is set to 1. The only free parameter in the SNR definition is now the crest factor μ, which depends on the applied modulation scheme. The highest SNR value is achieved by setting the crest factor to 1, but this implies the use of On-Off-Keying (OOK) to reach the channel capacity. However, this is only true under the assumption that transmission over the IM/DD channel does not cause inter-symbol interference. Thus, higher modulation formats or spectral shaping in terms of transmitter filtering have to be used, these techniques all increasing the crest factor. To include all these effects into the crest factor, it is chosen to be $\mu = 3$, which is just a reasonable guess and is also used in [Lee09]. With all these assumptions, SNR values for all fiber lengths can be calculated. Hence a capacity value

can be extracted from the curves in Fig. 4.6. The results are listed in Tab. 4.2. For an RC-LED system and a fiber length of 100 m, the SNR is 22 dB and thus the capacity value is approx. 1 Gbit/s. For laser launch at the same length, the SNR is 33 dB, which results in a capacity value of 3.17 Gbit/s. Of course these capacity values strongly depend on the system parameters, for example if the noise equivalent power could be decreased, the capacity will increase quadratically.

	LED launch (NA= 0.34, $bw_{\mathrm{el}} = 150\,\mathrm{MHz}$)		LASER launch (NA= 0.1, $bw_{\mathrm{el}} = 1\,\mathrm{GHz}$)	
length [m]	$SNR_{1\,\mathrm{GHz}}$ [dB]	Capacity [Gbit/s]	$SNR_{1\,\mathrm{GHz}}$ [dB]	Capacity [Gbit/s]
25	43	7.37	54	30.0
50	36	3.59	47	11.91
75	29	1.96	40	5.89
100	22	1.09	33	3.17

Table 4.2: Channel capacity values for Laser or RC-LED launched SI-POF system with a crest factor of $\mu = 3$ and the system parameters of Tab. 4.1.

4.3 Modulation Formats

This sub-chapter shortly introduces the modulation formats used in this thesis. The IM/DD channel can only be modulated in the intensity, which is linear dependent on the driving current of the optical light source. This driving current is therefore modulated in amplitude only. To overcome the bandwidth limitation induced by the channel or the transmitter, a combination of multilevel modulation and receiver equalization, which will be described in the next sub-chapter, is applied in this thesis. This combination is used to push the data rates to the direction of the channel capacity. Another way to reach channel capacity, is applying orthogonal frequency division multiplexing (OFDM) or derivations like discrete multitone modulation (DMT). But these schemes introduce a much higher complexity than the proposed multilevel schemes with receiver equalization, which is discussed later in sub-chapter 6.5. For further information about the application and the performance of multi carrier schemes it is referred to the doctoral thesis of Jeffrey Lee [Lee09].

In commercial optical transmission systems with directly modulated light sources, the only modulation scheme is On-Off-Keying (OOK) so far. This modulation scheme makes the transmitter electronics quite easy, because only two levels have to be generated. Linearity of the driving circuitry is not an issue in that case. First proposals for using something different than OOK have been submitted for the standardization process of the 10Gbit-Ethernet standard over legacy silica multimode fiber [iee06], but these proposals have been rejected, unfortunately. One of these proposals suggests the use of a 4-level amplitude modulation scheme to counteract the bandwidth limitations due to modal dispersion.
In this thesis, the use of multilevel modulation is proposed to reduce the required symbol rates, because of the severe inter-symbol interference (ISI) induced by the transmitter and the POF channel. Therefore M-ary pulse amplitude modulation (PAM-M) with M levels is introduced, realized as a bipolar amplitude modulation scheme. The optical transmitter element requires a uni-polar signal, so the bipolar PAM signal has to be biased with a DC component, resulting in a positive driving current I_{drive} (see Eq. 4.6). Therefore groups of $\log_2(M)$ bits are mapped on one PAM-M symbol of the alphabet $\{\pm 1, \pm 3, \ldots, \pm(M-1)\}$. The benefit of using PAM is that the symbol rate for a constant bit rate is reduced by a factor of $log_2(M)$ and thus the required receiver bandwidth is divided by this factor also, which leads to less noise at the receiver. The drawback is that the receiver has to detect M different levels. In Fig. 4.7 the eye diagrams of a two-level and a four-level PAM-signal are shown in a bipolar peak amplitude limited system (normalized to ± 1), as it is the case

for an optical IM/DD channel. The peak amplitude limit for the bipolar driving current is the DC-bias current, because an optical light source would be destroyed if a negative current is applied.

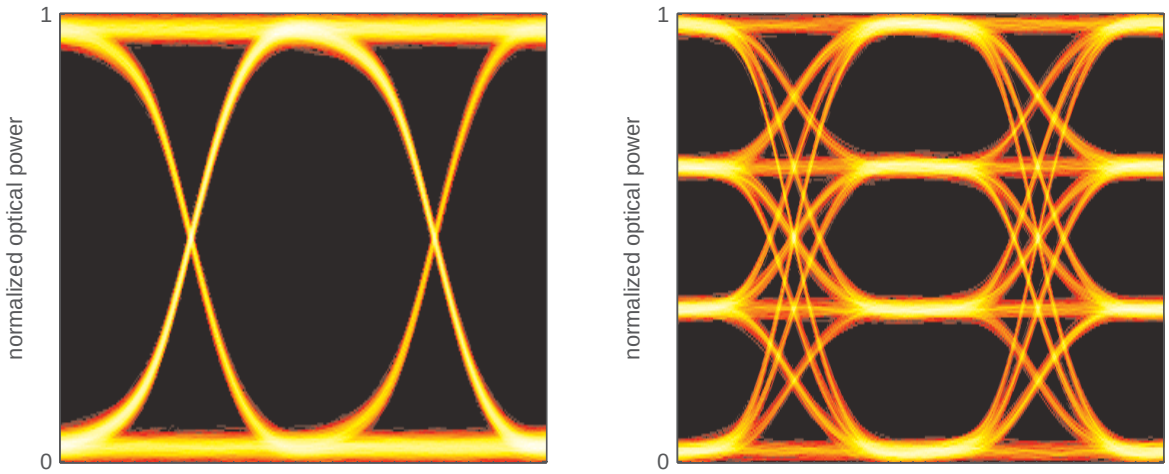

(a) OOK or biased bipolar PAM-2 (b) 4-ASK or biased bipolar PAM-4

Figure 4.7: Eye diagrams of OOK and PAM-4 for the optical power limited IM/DD channel.

In such an optical peak power limited system, the transition from OOK (left side) to PAM-4 (right side) results in a eye opening penalty of 1/3, which can be transformed to an optical power penalty of 4.77 dB. However, the PAM-4 signal needs half the bandwidth due to the smaller symbol rate only. Thus the electrical noise bandwidth is reduced by a factor of two, or 3 dB in the electrical domain, which translate into 1.5 dB in the optical domain. Thus, the theoretical optical receiver sensitivity penalty for using PAM-4 instead of OOK is 3.27 dB. Nevertheless, the use of PAM-4 has some advantages. For example, the decreased symbol rate leads to a slower signal processing clock if digital signal processing is used. Further, real transmitter components are not ideal and of course bandwidth limited, which decreases the power penalty of 3.27 dB additionally.
This power penalty can be derived elsewise by estimating the BER performance of the modulation schemes. For the case of a M-ary bipolar PAM modulation scheme, the BER can be calculated as follows (referred to [Pro01, LM94])

$$\mathrm{BER} = \frac{2(M-1)}{M \cdot \log_2(M)} \cdot Q\left(\sqrt{\frac{6}{M^2-1}\frac{E_s}{N_0}}\right). \tag{4.35}$$

Here, E_s is the energy per symbol and the $Q(\ldots)$ function is the complementary cumulative density function for AWGN, which is related to the complementary gaussian error function erfc$(\ldots)$ as

$$Q(x) = \frac{1}{2}\text{erfc}\left(\frac{x}{\sqrt{2}}\right). \tag{4.36}$$

Eq. (4.35) uses the E_s/N_0 as input parameter. Here, this relation has to be reformulated by use of the SNR definition in Eq. (4.15) in the following way:

$$\frac{E_s}{N_0} = \frac{P_{\text{signal}} \cdot T_{\text{symbol}}}{N_0} = \frac{P_{\text{signal}} \cdot \log_2(M) \cdot T_{\text{bit}}}{N_0}. \tag{4.37}$$

P_{signal} is the received signal power (see Eq. (4.12)) and T_{symbol} and T_{bit} are the length of one symbol and one bit, respectively. With Eq. (4.15) the signal power can be written as

$$P_{\text{signal}} = \left(\alpha_F \cdot R \cdot \frac{\eta_{\text{mod}}}{\mu} \cdot P_{\text{mean}}\right)^2 \tag{4.38}$$

and the noise power spectral density N_0 as

$$N_0 = (R \cdot \text{NEP})^2. \tag{4.39}$$

Thus Eq. (4.37) can be rewritten as

$$\frac{E_s}{N_0} = \frac{\alpha_F^2 \eta_{\text{mod}}^2 P_{\text{mean}}^2 \cdot T_{\text{bit}}}{\text{NEP}^2} \cdot \frac{\log_2(M)}{\mu_{\text{PAM}}^2(M)}. \tag{4.40}$$

For M-ary PAM the crest factor can be written dependent on the number of levels M as

$$\mu_{\text{PAM}}(M) = \sqrt{3 \cdot \frac{M-1}{M+1}}. \tag{4.41}$$

Inserting Eq. (4.41) into Eq. (4.40) leads to

$$\frac{E_s}{N_0} = \frac{\alpha_F^2 \eta_{\text{mod}}^2 P_{\text{mean}}^2 \cdot T_{\text{bit}}}{\text{NEP}^2} \cdot \frac{\log_2(M) \cdot (M+1)}{3(M-1)}. \tag{4.42}$$

This definition of the E_s/N_0 can be split into two parts. The first includes all the transmission system parameters, such as the modulation index η_{mod}, mean transmit power P_{mean}, fiber attenuation α_F, equivalent receiver noise NEP and the bit length T_{bit}. The second part contains the relationship to the number of levels M. In the following this first part is defined as the normalized signal-to-noise ratio SNR_{norm}, thus Eq. (4.42) writes as

$$\frac{E_s}{N_0} = \text{SNR}_{\text{norm}} \cdot \frac{\log_2(M) \cdot (M+1)}{3(M-1)}. \tag{4.43}$$

Inserting the above equation in the BER estimation formula (Eq. (4.35)) results in a BER estimation only dependent on the number of levels and the normalized SNR:

$$\mathrm{BER} = \frac{2(M-1)}{M \cdot \log_2(M)} \cdot Q\left(\sqrt{\frac{2 \cdot \log_2(M)}{(M-1)^2}\mathrm{SNR}_{\mathrm{norm}}}\right). \tag{4.44}$$

Fig. 4.8 shows BER curves evaluated with Eq. (4.44) for two (OOK) and four (PAM-4) levels.

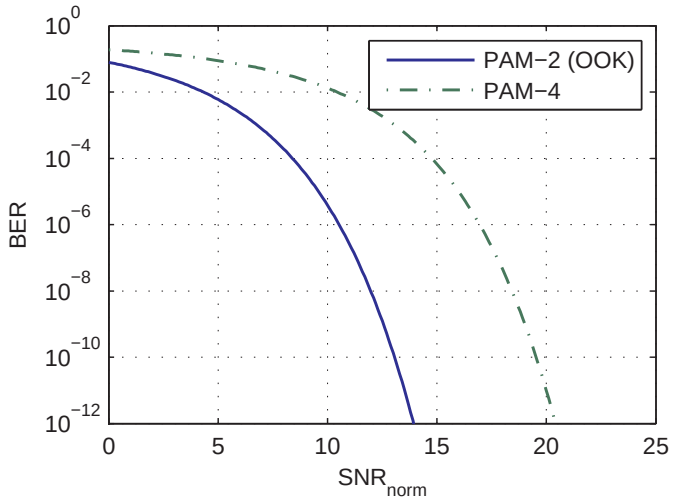

Figure 4.8: BER performance vs. $\mathrm{SNR}_{\mathrm{norm}}$ for PAM-2 (OOK) and PAM-4 and ideal conditions of the optical IM/DD channel.

The $\mathrm{SNR}_{\mathrm{norm}}$ penalty is approx. 6.5 dB in the electrical domain, which, translated back into optical receiver sensitivity penalty, gives 3.25 dB according to the equivalent optical signal-to-noise power ratio $\mathrm{oSNR}_{\mathrm{eq}}$

$$\begin{aligned} \mathrm{oSNR}_{\mathrm{eq}} &= \frac{P^{\mathrm{o-eq}}_{\mathrm{signal}}}{P^{\mathrm{o-eq}}_{\mathrm{noise}}} = \frac{I^{\mathrm{RMS}}_{\mathrm{signal}}/R}{I^{\mathrm{RMS}}_{\mathrm{noise}}/R} = \sqrt{\frac{(I^{\mathrm{RMS}}_{\mathrm{signal}})^2}{(I^{\mathrm{RMS}}_{\mathrm{noise}})^2}} = \sqrt{\mathrm{SNR}} \\ \mathrm{oSNR}_{\mathrm{eq}}|_{dB} &= 1/2 \cdot \mathrm{SNR}|_{dB}\,. \end{aligned} \tag{4.45}$$

Here, $P^{\mathrm{o-eq}}_{\mathrm{signal}}$ and $P^{\mathrm{o-eq}}_{\mathrm{noise}}$ are the equivalent optical powers for the electrical signal and noise RMS currents related through the responsivity R, respectively. Hence the $\mathrm{oSNR}_{\mathrm{eq}}$ is half the SNR in the electrical domain. Thus the value of the optical receiver sensitivity penalty of 3.25 dB is the same value as calculated before from the eye opening and the noise bandwidth considerations.

This optical receiver sensitivity penalty represents the maximum penalty, if PAM-4 is compared with OOK for a flat channel. For example, if a LED is used as transmitter, which has already a bandwidth limitation, this optical receiver sensitivity penalty decreases. In Fig. 4.9 eye diagrams for both modulation schemes are shown with a bandwidth limitation of an LED of 250 MHz (3 dB frequency).

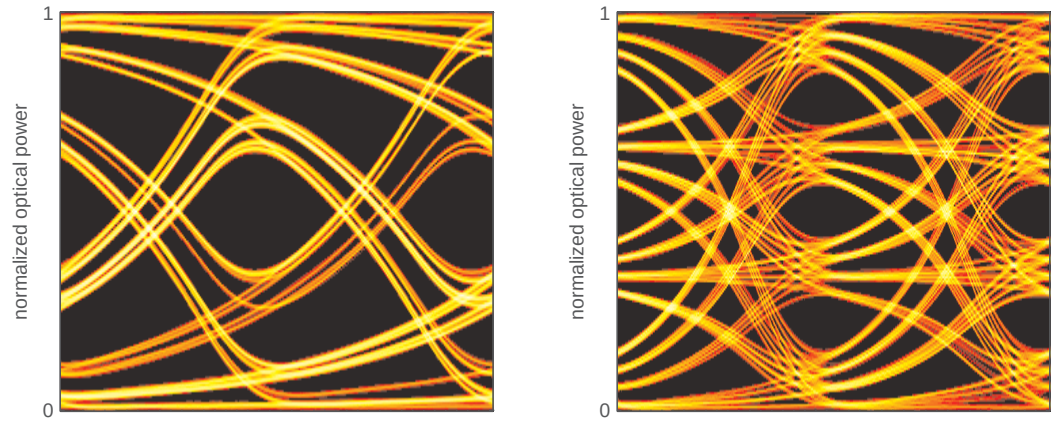

(a) OOK with LED (b) PAM-4 with LED

Figure 4.9: Eye diagrams of OOK and PAM-4 for the optical peak power limited IM/DD channel at a data rate of 1.25 Gbit/s and an electrical LED bandwidth of 250 MHz (back-to-back case).

For this case the optical receiver sensitivity penalty decreases to 1.97 dB, which is still a significant penalty, but this penalty can be tolerated or even reduced further, as soon as the highly bandwidth limited channel of the SI-POF is considered. Another point is the fact, that commercial TIAs with smaller bandwidths show reduced noise power densities, which is also in favor of PAM-4.

4.4 Electronic Dispersion Compensation

The electronic dispersion compensation (EDC) technique proposes to mitigate the bandwidth limitation of POF systems due to modal dispersion or due to bandwidth limited transmitter components by means of electronic signal processing. In this thesis two types of equalizers are used as EDC, such as the feed-forward equalizer (FFE), which is in principle a finite impulse response (FIR) filter with adjustable coefficients and the decision feedback equalizer (DFE), which is a combination of a FFE and an adjustable threshold detector. This is realized by feeding weighted decisions back to the input of the decision device, which has also a FIR filter structure. These two equalization schemes are the most simple ones, but it is shown in chapter 4.6, that the performance of these schemes is a good choice in terms of trade off between complexity and performance.
This chapter gives a brief introduction to the symbol-spaced and fractionally-spaced implementations of the FFE and DFE. For detailed information about these equalization schemes, it is referred to the literature [GHW92, Hay02, Pro01, LM94]. Throughout this thesis the following naming conventions are applied:

FFE m	feed-forward equalizer with m taps
DFE (m, n)	decision feedback equalizer with m forward taps and n feedback taps

Table 4.3: Equalizer naming conventions.

4.4.1 Symbol-spaced adaptive Equalizers

Both equalization schemes, the FFE and DFE, can be further differentiated by the number of samples per information symbol at which they operate. First the symbol-spaced equalization schemes are considered, which means that the incoming signal has to be sampled once every information symbol at the ideal sampling instance, which is typically in the center of a symbol duration. The basic structure of a FFE with coefficient adaptation is shown in Fig. 4.10.

The distorted signal $y(t)$ is the output of the IM/DD channel model (see Fig. 4.1) and the input to the electrical demodulator. This signal is filtered in the front-end filter to reduce aliasing products after the sampling device [LM94], which samples the signal at multiples of T, where T represents the symbol duration. Ideally, this front-end filter is a matched filter, resulting in the maximum SNR, which can be achieved.
The equalization process is achieved by summing up weighted delayed copies of the sampled input signal. This is realized by a tapped-delay line for the delayed copies, and by

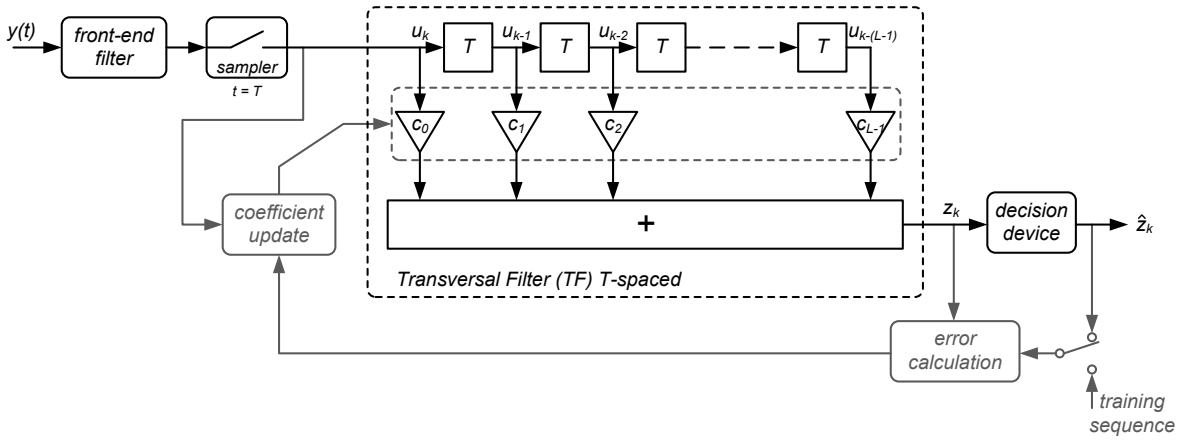

Figure 4.10: Structure of a symbol-spaced adaptive Feed Forward Equalizer (FFE).

multiplications with the equalizer coefficients **c** for weighting. So the structure of the FFE is in principle a digital FIR filter.

The difference between an adaptive FFE and a digital FIR filter is the adaptation process for calculating the filter coefficients **c**. This adaptation process can pursue different goals. The zero-forcing (ZF) equalization has the goal to invert the channel transfer function, resulting in a complete elimination of inter-symbol interference by the equalizer. Thus frequencies with high attenuation are strongly amplified, which can lead to large noise amplification, if the transfer function has zeros or is below the noise floor.

To avoid this large noise enhancement, the minimum mean square error (MMSE) equalization strategy can be used, which targets to minimize the mean square error, which is calculated as the squared difference between signal before and after the decision device. Thus it wants to make a trade-off between channel inversion and noise amplification.

For both equalization strategies the optimal equalizer coefficients $\mathbf{c} = [c_0, c_1, \ldots, c_{L-1}]$ can be calculated, if the transfer function of the system and the noise power spectral density are known. Normally, this is not the case, so the equalizer has to train and adapt its coefficients automatically dependent on the instantaneous channel transfer function and the actual noise power.

The structure in Fig. 4.10 uses this adaptive MMSE strategy. The error calculation box calculates an error signal between the signal before the decision device and a reference signal, which is used in the coefficient update box to adjust the equalizer coefficients **c**. The reference signal can be either the decided signal, which is then called decision-directed (DD) mode, or a training signal, which is a known sequence given to the receiver to train the equalizer coefficients. This training has to be done in the case of strong ISI,

because the decision directed mode is only capable to track channel variation and not to find blindly the optimal equalizer coefficients. Thus, equalizers have to be trained in the startup phase of a transmission system and can then be switched, if convergence is reached, to the DD mode for tracking the channel variations.
The requirement for this training phase is a bidirectional communication link, because the transmitter has to send the training sequence first and then switch to the real data signal, if the equalizer has reached convergence. If this bidirectional communication is not possible, equalizers could also reach the convergence region by applying so called "blind" adaptation algorithms, which are able to find the optimal coefficients or at least get into the direction of these without knowledge about the actual system condition (transfer function and noise power). How these blind adaption algorithms work, is considered in the next sub-chapter 4.5.

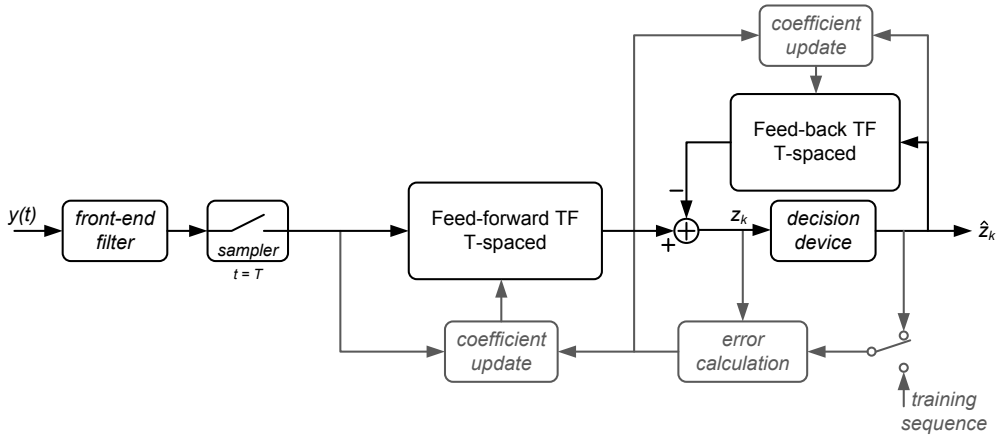

Figure 4.11: Structure of a symbol-spaced adaptive Decision Feedback Equalizer (DFE).

The structure of an adaptive symbol-spaced DFE is shown in Fig. 4.11. The basic idea of a DFE is that if decisions on the past symbols have been made, the past-symbol-induced ISI on the current symbol can be canceled before a decision is made on the current symbol. The typical structure of a DFE consists of a feed-forward equalizer (FFE) followed by a nonlinear feedback equalizer. The feed-forward equalizer is used to minimize the ISI induced by future symbols (pre-cursors). The nonlinear feedback equalizer adjusts the input level to the decision device symbol by symbol based on known past symbols (post-cursors). Thus, a DFE can remove ISI from past symbols without any noise amplification, which can be a big advantage. Of course this holds only, if the decided symbols are correct, which is a drawback of a DFE, but this effect of error propagation can be neglected if the

SNR is high enough.
The components used are more or less the same as for the FFE shown in Fig. 4.10. At the beginning a front-end filter with a following sampling device is needed, then a feed-forward transversal filter (TF) is used. It has the same structure as the dashed box in Fig. 4.10. From its output the fed back symbols, which are weighted by the feedback transversal filter (TF), are subtracted before the decision is made. The coefficient update works in the same manner as it works for the symbol-spaced FFE. The error signal and the instantaneous samples or decided symbols inside the TFs are used for the update algorithm of the coefficients of the feed-forward or the feedback TFs.

4.4.2 Fractionally-spaced adaptive Equalizers

For the optimal performance of a symbol-spaced equalizer an analog matched filter has to be used as front-end filter, and the sampling has to take place at the ideal sampling point. Both requirements are hard to implement for an unknown channel. So to get rid of these requirements, fractionally-spaced equalizers (FSE) could be used [GHW92, Pro01, LM94]. The result is, that the matched filter merges into the adaptive equalizer, thus the optimal equalizer can be realized. Further the equalizer gets independent of the sampling instance, because the FSE can compensate for any delay distortion or sampling phase without noise enhancement. For detailed information about these fractionally spaced equalizers it is referred to the literature, for example [GHW92, Pro01, LM94].

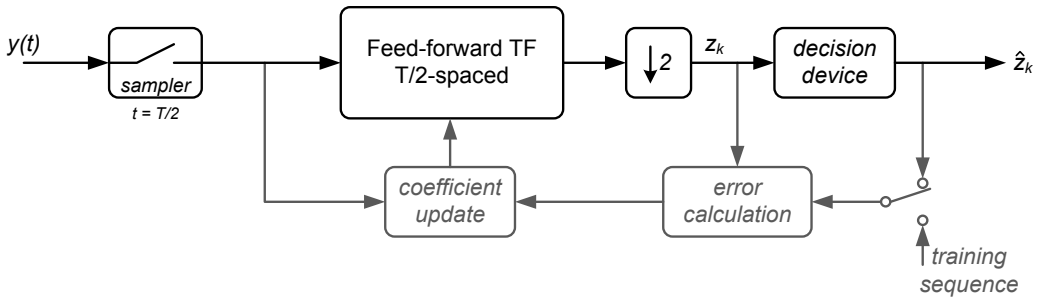

Figure 4.12: Structure of a fractionally spaced Feed-Forward Equalizer (FFE).

Fig. 4.12 shows the structure of the $T/2$-fractionally spaced FFE, which means that 2 samples per information symbol are used to equalize the channel. The front-end filter has merged into the transversal filter (TF) and the sampling has to be done twice in each symbol time T. There is no requirement anymore on the position of the sampling within the symbol time T. The adaptation process is the same as for symbol-spaced

equalizers. The output of the FSE is down sampled by a factor of 2, resulting in samples at the symbol rate $1/T$, thus the output behavior is the same as for the symbol-spaced FFE. The structure of the $T/2$-fractionally-spaced decision feedback equalizer is shown in Fig. 4.13, the difference to the symbol-spaced DFE is just in the feed-forward part. This transversal filter works at twice the symbol rate $1/T$, the feed-back filter works still at the symbol rate, because it just removes the ISI at the sampling point of one symbol. Thus it is in principle only a fractionally spaced FFE with an additional feedback transversal filter.

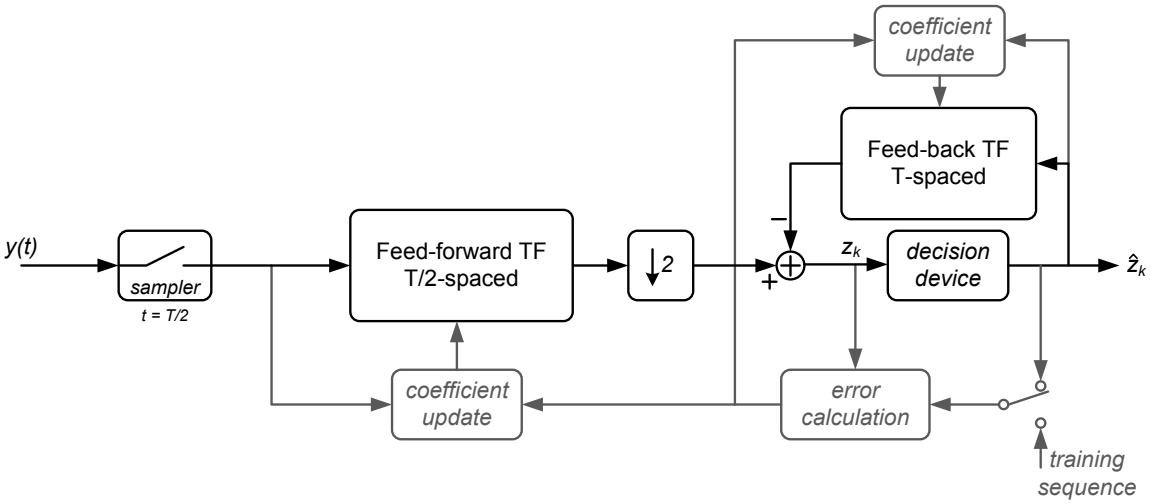

Figure 4.13: Structure of a fractionally spaced Decision Feedback Equalizer (DFE).

4.5 Equalizer Coefficient Adaptation Schemes

The equalizer coefficients of the before mentioned electronic dispersion compensation schemes can be calculated in an optimal way solving the Wiener-Hopf equations [WH31], also known as the Minimum Mean Square Error method (MMSE). But this requires correlations and matrix inversions and perfect knowledge about the channel transfer function and the noise power. The focus in this thesis is to apply this scheme in real-time implementations, thus the coefficients have to be calculated adaptively.

In this sub-chapter a short summary for two adaptation algorithms used in this thesis is given, the least-mean-square (LMS) algorithm [WH60] for decision directed (DD) and trained adaptation and the Stop-and-Go algorithm [PP87] for blind adaptation. The cost function J of the optimization problem for both adaptation schemes is the mean square error (MSE), which has to be minimized. The MSE is the average of the squared difference

between the equalizer output z_k and the decided symbol $\hat{z}_k$ and can be written as

$$J = \text{MSE} = E\left[z_k - \hat{z}_k\right]^2, \tag{4.46}$$

where E denotes the ensemble average over the data sequence and the additive noise.

4.5.1 Least-Mean-Square (LMS) Algorithm

The least-mean-square (LMS) error adaptive filtering algorithm proposed by Widrow and Hoff [WH60] is an important member of the family of stochastic gradient algorithms. The term "stochastic gradient" is intended to distinguish the LMS from the method of steepest descent, which uses a deterministic gradient in a recursive computation of the Wiener filter for stochastic inputs. A significant feature of the LMS algorithm is its simplicity. It does not require any correlations or matrix inversions. Thus the LMS is one of the most simple adaptation algorithms in terms of complexity and also one of the best in terms of performance. Referred to the symbol-spaced FFE in Fig. 4.10, the output z_k can be written as

$$z_k = \mathbf{c}^T(k) \cdot \mathbf{u}(k) \tag{4.47}$$

where $\mathbf{c}^T(k)$ is the transposed coefficient vector at the time instance k, and $\mathbf{u}(k)$ contains the samples inside the tapped delay line. The LMS error in tracking mode can therefore be calculated by the difference of the filter output z_k and the decided symbol $\hat{z}_k$, thus e_{LMS} at time instant k is calculated as

$$e_{\text{LMS}}(k) = z_k - \hat{z}_k. \tag{4.48}$$

In the training mode, the estimated decided symbol $\hat{z}_k$ is exchanged by the known symbol of the training sequence. The coefficient adaptation is done by the following equation

$$\mathbf{c}(k+1) = \mathbf{c}(k) + \beta \cdot e_{\text{LMS}}(k) \cdot \mathbf{u}(k). \tag{4.49}$$

Here, β is the step size parameter.
The complexity in terms of multiplications and additions can easily be calculated. For each adaptation step the error signal is calculated by one subtraction, then for each equalizer coefficient two multiplications and one addition have to be done. Even those numbers of required arithmetic calculations can be decreased using simplifications of the LMS algorithm. For more information about the LMS and all the different simplifications and options, it is referred to the literature [Hay02, BC02].

4.5.2 Blind Adaptation using the Stop-and-Go algorithm

The blind or self-training equalization in multilevel communications systems has been firstly proposed by Sato [Sat75]. According to [Hay02], the Sato algorithm consists of minimizing a nonconvex cost function

$$J_{\text{Sato}} = E\left[(\hat{x}_k - z_k)^2\right] \tag{4.50}$$

where z_k is the output of the equalizer defined in Eq. (4.47) and $\hat{x}_k$ is an estimate of the transmitted symbol x_k. This estimate is obtained by a zero-memory nonlinearity described by the formula

$$\hat{x}_k = \gamma_{\text{Sato}} \cdot \text{sgn}\left(z_k\right). \tag{4.51}$$

The constant

$$\gamma_{\text{Sato}} = \frac{E\left[\hat{x}_k^2\right]}{E\left[|\hat{x}_k|\right]}. \tag{4.52}$$

sets the gain of the equalizer. Minimizing this cost function J_{Sato} using a stochastic gradient algorithm leads to the LMS algorithm defined in Eq. (4.49) just by exchanging the error expression. The error signal for the Sato algorithm writes therefore as

$$e_{\text{Sato}}(k) = \gamma_{\text{Sato}} \cdot \text{sgn}\left(z_k\right) - z_k. \tag{4.53}$$

The Sato algorithm for blind equalization was introduced to deal with one-dimensional multilevel (M-ary PAM) signals, with the objective of being more robust than a decision directed algorithm. Initially, the algorithm treats such a digital signal as a binary signal by estimating the most significant bit. The remaining bits of the signal are treated as additive noise for the blind adaptation part. The algorithm then uses the results of this preliminary step to modify the error signal obtained from a conventional decision-directed algorithm defined in Eq. (4.48). The critical point is the correct switching time between blind and decision-directed adaptation, because right after the switching process a complete different error signal is used to adapt the equalizer coefficients, which can lead to instabilities.

The Stop-and-Go algorithm proposed by Picchi and Prati [PP87] can be seen as variant of the Sato algorithm combined with the performance of the decision-directed LMS algorithm. This algorithm uses both error signals instantaneously to adapt the equalizer coefficients. The coefficient update equation is the same as for the LMS algorithm defined in Eq. (4.49). The Stop-and-Go algorithm only controls the error calculation in the following way

$$e_{\text{SaG}}(k) = \begin{cases} e_{\text{LMS}}(k) & \text{if} \quad \text{sgn}\left(e_{\text{LMS}}(k)\right) = \text{sgn}\left(e_{\text{Sato}}(k)\right) \\ 0 & \text{otherwise} \end{cases} \tag{4.54}$$

where $e_{\text{Sato}}(k)$ is the Sato error given by Eq. (4.53), and $e_{\text{LMS}}(k)$ is the error used in the decision directed mode of the LMS algorithm given by Eq. (4.48). The basic idea is that the algorithm converges if the updating of the equalizer coefficients is turned off with sufficiently high probability every time the sign of the DD error differs from the Sato error. This results in a blind start-up phase and the same convergence behavior as the DD-LMS algorithm, because the same error signal is used to adapt the coefficients. It just turns off the adaptation, when it is too uncertain. Since no switching between different error signals has to be done, no problems with instabilities are left. Hence there is a smooth transition from blind adaptation to the decision directed mode.

4.6 Performance bounds of FFE and DFE

In this sub-chapter the performance of different combinations of multilevel modulation (PAM) (section 4.3) and optimal equalizers (FFE or DFE) (section 4.4) is presented. Therefore, the performance bounds of equalizers with an infinite number of taps are calculated in terms of the minimum mean square error (MMSE) $J_{\min}$.

4.6.1 MMSE calculation for FFE and DFE

The optimum linear equalizer in theory is a continuous-time matched filter followed by a symbol-spaced FFE. The minimum mean squared error $J_{\min}^{\text{FFE}}$ at the equalizer output is given by [LM94, Pro01, GHW92]

$$J_{\min}^{\text{FFE}} = \frac{T}{2\pi} \int_{-\pi/T}^{\pi/T} \frac{1}{Y(\omega)} d\omega \tag{4.55}$$

with

$$Y(\omega) = 1 + \frac{2E_s}{N_0} \cdot \sum_{k=-\infty}^{\infty} \left| H_{\text{total}} \left(\omega - \frac{2\pi k}{T} \right) \right|^2 \tag{4.56}$$

where T is the symbol duration, E_s the symbol energy, and $|H_{\text{total}}(\omega)|^2$ the power transfer function at the matched filter's output of the total system (see Eq. (4.21)). The minimum mean squared error for the symbol-spaced DFE was calculated by J. Salz [Sal73] and is given by

$$J_{\min}^{\text{DFE}} = \exp\left\{ -\frac{T}{2\pi} \int_{-\pi/T}^{\pi/T} \ln\left[Y(\omega)\right] d\omega \right\}. \tag{4.57}$$

The signal-to-noise power ratio for infinite long equalizers (γ_∞) can be calculated accord-

ing to [Pro01] dependent on the minimum mean square error $J_{\min}$ as

$$\gamma_\infty = \frac{1 - J_{\min}}{J_{\min}}. \tag{4.58}$$

This relation between γ_∞ and $J_{\min}$ also holds when there is residual inter-symbol interference in addition to the noise [Pro01].
Without inter-symbol interference, the folded power transfer function of the total system at the matched filter's output results in

$$\sum_{k=-\infty}^{\infty} \left| H_{\text{total}} \left(\omega - \frac{2\pi k}{T} \right) \right|^2 = 1, \qquad |\omega| \leq \pi/T. \tag{4.59}$$

Thus the minimum mean square errors for both equalizers achieve their minimum value, namely

$$J_{\min}^{\text{FFE}} = J_{\min}^{\text{DFE}} = \left(1 + \frac{2E_s}{N_0} \right)^{-1}. \tag{4.60}$$

This translates in a signal to noise power ratio of

$$\gamma_\infty^{\text{FFE}} = \gamma_\infty^{\text{DFE}} = \frac{2E_s}{N_0}, \tag{4.61}$$

which is the matched filter performance for a single pulse transmission. This matched filter output signal-to-noise power ratio $\gamma_\infty^{\text{MF}}$ for an analog implementation is given by [Pro01, LM94]

$$\gamma_\infty^{\text{MF}} = \frac{2E_s}{N_0}, \tag{4.62}$$

which is the maximum SNR for detecting a single isolated pulse among noise. To get a performance measure in terms of BER, the dependence of the symbol-energy-to-noise-density ratio E_s/N_0 on the signal-to-noise power ratio γ_∞ has to be calculated for all three cases (FFE, DFE, MF) to

$$\frac{2E_s}{N_0} = \begin{cases} \gamma_\infty^{\text{MF}} & \text{for matched filter} \\ \gamma_\infty^{\text{FFE}} = 1/J_{\min}^{\text{FFE}} - 1 & \text{for FFE} \\ \gamma_\infty^{\text{DFE}} = 1/J_{\min}^{\text{DFE}} - 1 & \text{for DFE.} \end{cases} \tag{4.63}$$

This symbol-energy-to-noise-density ratio E_s/N_0 can be inserted in Eq. (4.35) to calculate the BER, if it is assumed that the combination of the gaussian receiver noise and the residual inter-symbol interference at the output of the equalizers can be roughly approximated by a gaussian noise process [BC02]. Thus the BER approximation writes as

$$\text{BER} \approx \frac{2(M-1)}{M \cdot \log_2(M)} \cdot Q\left(\sqrt{\frac{3}{M^2 - 1} \cdot \frac{2E_s}{N_0}} \right). \tag{4.64}$$

For the equalizers this equation is an approximation, whereas for the matched filter it is the exact result, which is the so-called matched filter bound [Pro01, LM94]. This bound can not be exceeded by an equalizer, even if a maximum likelihood sequence estimation (MLSE) is applied.

4.6.2 BER performance bounds of FFE and DFE

For the BER performance simulations, the IM/DD channel model derived in chapter 4.1 is used with the system parameters of Tab. 4.1. The two commonly used light sources for SI-POF systems are investigated, namely the laser diode and the RC-LED. As modulation schemes, OOK and PAM-4 were evaluated. The calculation of the BER values is done according to chapter 4.6.1.
Fig. 4.14 shows the BER performance over the link length for a data rate of 1.25 Gbit/s for these four cases.
The blue solid lines represent the matched filter bounds, which are the ultimate performance bounds for all equalization schemes (see chapter 4.6.1). The green dashed dotted lines are the BER curves of the FFE and the red dashed lines represent the performance of the DFE. The matched filter bounds for OOK can reach a longer link length in comparison to the matched filter bounds of PAM-4. But if more realistic equalization schemes are used, always the PAM-4 modulation outperforms the OOK in terms of link length and of course the DFE outperforms the FFE. These plots show also that by using a laser diode the transmission of Gigabit Ethernet over 100 m is possible with both modulation schemes, which will be verified later in the experiments (chapter 5.1). With a RC-LED as optical source, this goal of error-free transmission ($< 10^{-12}$) without FEC of Gigabit Ethernet over 100 m could not be reached without changing the system parameters, particularly the receiver noise.
Fig. 4.15 shows the BER performance plots for a data rate of 2.5 Gbit/s. The behavior is similar, as the PAM-4 combination outperforms always the OOK. The penalties in terms of link length to the matched filter bound for the FFE and DFE are much bigger than for the 1.25 Gbit/s case, but even the RC-LED system can reach a link length of 50 m with the PAM-4 and DFE combination. A link length of 100 m at this data rate can be achieved by using a laser diode in combination with PAM-4 modulation and FFE or DFE. The DFE performs better than the FFE, because it can remove the post cursor inter symbol interference without noise amplification. The reason for the big penalties with respect to the matched filter bound can be explained by the fact that the severe low-pass characteristic of the channel at the considered data rate pushes the higher frequency

components below the noise floor. Thus, even a DFE can not counteract against such a distortion, which is mainly noise. One of the alternatives to get nearer to the matched filter bound is to use a sequence estimation like a MLSE or to optimize the transmit spectrum.

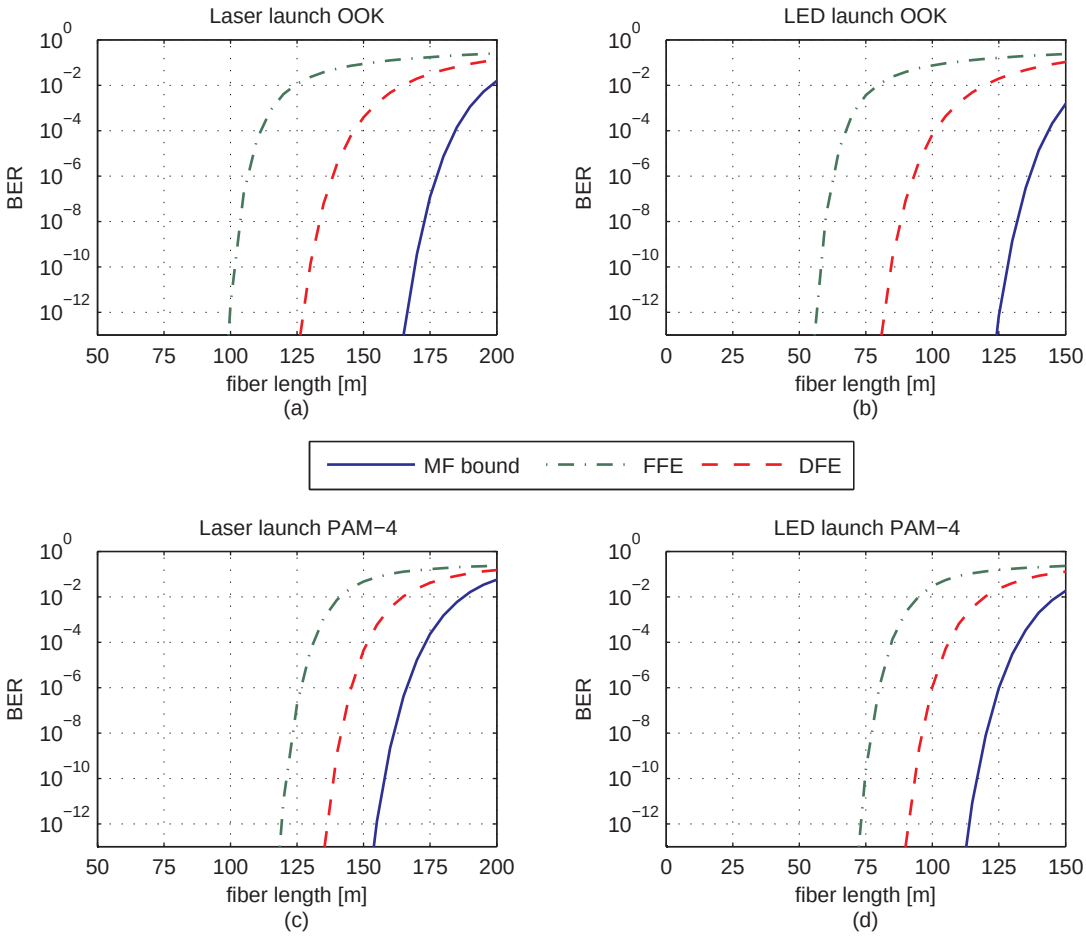

Figure 4.14: BER performance bounds for a data rate of 1.25 Gbit/s: blue solid - matched filter bound, green dashed dotted - FFE with an infinite number of taps, red dashed - DFE with an infinite number of taps; for different scenarios: laser launch with OOK (a), RC-LED launch with OOK (b), laser launch with PAM-4 (c), and RC-LED launch with PAM-4 (d).

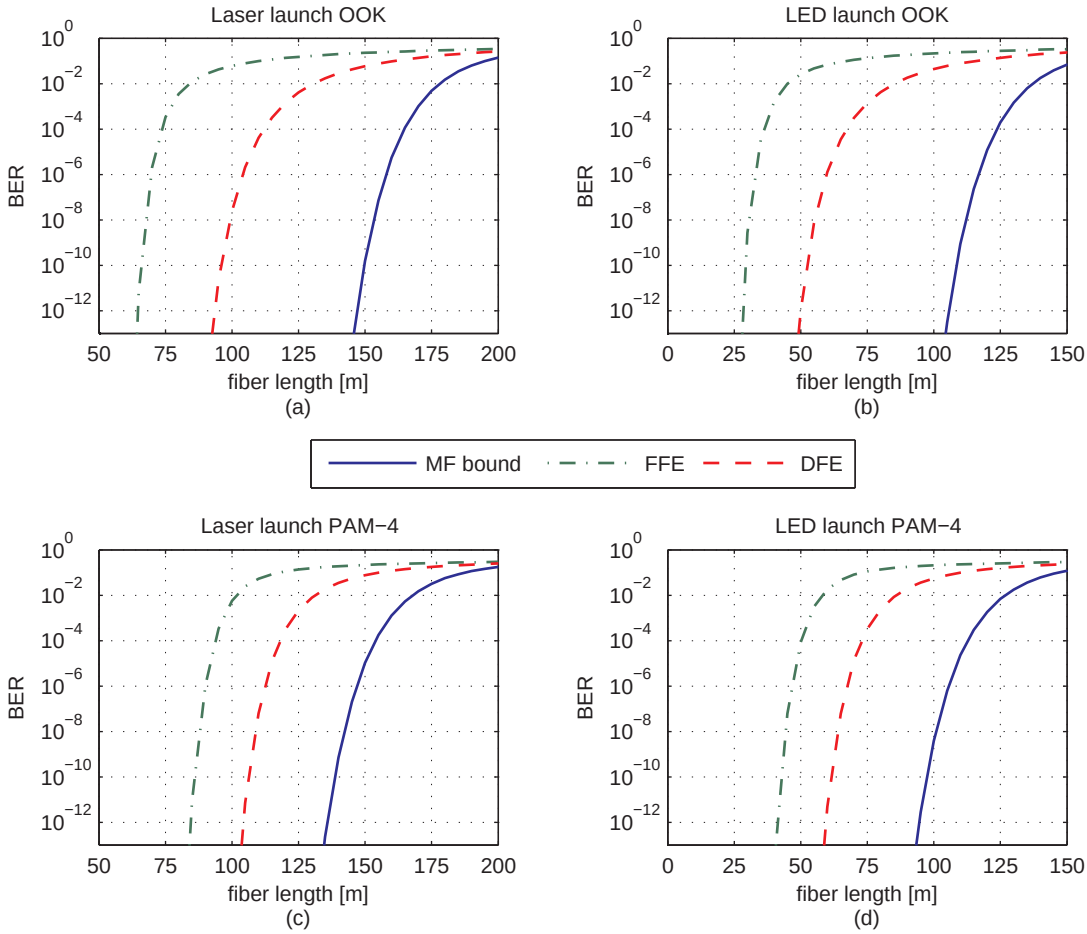

Figure 4.15: BER performance bounds for a data rate of 2.5 Gbit/s: blue solid - matched filter bound, green dashed dotted - FFE with an infinite number of taps, red dashed - DFE with an infinite number of taps; for different scenarios: laser launch with OOK (a), RC-LED launch with OOK (b), laser launch with PAM-4 (c), and RC-LED launch with PAM-4 (d).

4.7 Summary

In this chapter the optical IM/DD channel for the SI-POF has been introduced. The channel capacity was calculated for the two commonly used approximations, the Gaussian and the 1st order low-pass characteristic, and for the newly derived SI-POF channel model (see chapter 3). The results confirm the observations of recently published work [Lee09, LBR+09], that for short fiber length (< 25 m) the 1st order approximation can be used and for longer fiber length (> 150 m) the Gaussian approximation can be applied. But for the range in between (25 m $<$ fiber length $<$ 150 m) none of these two approximations represent the real SI-POF channel very well. The introduced SI-POF channel model, described in chapter 3, fits very well for all fiber lengths, from 0 m to 200 m.
Subsequently, the modulation formats used in this thesis were introduced, namely the On-Off-Keying (OOK) and the 4 level pulse amplitude modulation (PAM-4). In an optical peak power limited IM/DD channel the optical receiver sensitivity penalty of PAM-4 with respect to OOK is 3.25 dB, in theory. But if bandwidth limited transmitters are used, such as RC-LEDs, this penalty decreases very fast. In combination with one of the two receiver equalization schemes introduced, this penalty can even get negative, as shown in sub-chapter 4.6.2. Hence, for all combinations of the optical transmitter components and receiver equalization schemes, the PAM-4 modulation wins the performance comparison in terms of maximum transmission link length for error-free transmission ($< 10^{-12}$).
Apart form the performance gain, if PAM-4 signaling is used, also the complexity, especially the clock rate of the digital signal processing parts in the transmitter and receiver will be decreased, because of the lower symbol rate (in this case a factor of 2). The only drawback of using PAM-4 signaling is the need of a linear driving circuitry at the transmitter, but this should not be a big problem as only 4 different levels have to be generated [CBZ+06].

5

POF Transmission Experiments

This chapter gives an overview of the realistically achievable performance of amplitude modulation schemes in combination with receiver equalization in terms of experimental results. Depending on the application scenarios, different combinations of optical sources and polymer optical fibers are used.
Therefore three commonly used combinations as summarized in Tab. 5.1 are investigated. The first is the use of a laser diode to launch into a SI-POF for data rates up to 2 Gbit/s over 100 m, the second is the use of a LED to launch into a SI-POF for data rates up to 1.25 Gbit/s over up to 100 m, and the last one is the use of a VCSEL to launch into a PF-GI-POF for a data rate of 10 Gbit/s over up to 300 m.

sub chapter	fiber type	light source	modulation format	max. data rate	max. link length
5.1.1	SI-POF	laser	OOK	1.25 Gbit/s	100 m
5.1.2				2 Gbit/s	100 m
5.2.1	SI-POF	LED	PAM-4	500 Mbit/s	50 m
5.2.2				1.25 Gbit/s	75 m
5.3.1	PF-GI-POF	VCSEL	PAM-4	10 Gbit/s	220 m
5.3.2			OOK / PAM-4	10 Gbit/s	300 m

Table 5.1: Overview POF transmission experiments: combinations of fiber types, light sources and modulation formats.

5.1 SI-POF Systems with Laser launch and receiver equalization

A laser diode can only be used for certain application scenarios, in which the problems of a laser diode, such as operation temperature range and sudden death characteristic is not an issue. So, for example, this combination could be used for in-building communication systems, because the requirements are not so strict as in the automotive environment. Thus the optical transmitter element is not limiting the system bandwidth, but the SI-POF channel does. Due to it's large core diameter, modal dispersion limits the bandwidth to approximately 35 MHz at 100 m.
Recently, several efforts have been undertaken to counteract such bandwidth limitations [MJG+09]. While some efforts concentrate on the development of novel fibers and components such as the 1 mm graded-index PMMA based plastic optical fiber (GI-POF) [KK09, INK+95, KP08] and VCSELs in the red wavelength range [WMH+08], other approaches focus on advanced receiver electronics [GVZL08] or novel transmission schemes in combination with transmitter and receiver digital signal processing. Examples for these innovations are multi-carrier techniques including OFDM and DMT [LBR+08b, RLS+06] and multilevel signaling in combination with adaptive receiver equalization [BLRH07b, CLNC+09, BLRH08b, BLRH09]. For comparison, the highest bit rate ever reported for a SI-POF at the starting point of this work was an On-Off-Keying (OOK) transmission experiment with analog equalization, achieving a bit-rate of 531 Mbit/s [YWB93].
In this sub-chapter (5.1) two experiments are presented. The first shows the feasibility and the requirements for transmitting Gigabit Ethernet with a data rate of 1.25 Gbit/s over up to 100 m SI-POF, and the second is a proof of concept and an extension to 2 Gbit/s transmission over 100 m of SI-POF.

5.1.1 1.25 Gbit/s Transmission with On-Off-Keying

The goal of this experiment was the transmission of Gigabit Ethernet with a line data rate of 1.25 Gbit/s over up to 100 m of SI-POF using a laser diode and the simple OOK modulation scheme. This goal is achieved by using digital receiver equalization. Simple equalizer structures are used, such as the symbol-spaced linear feed forward equalizer (FFE) and the symbol-spaced nonlinear decision feedback equalizer (DFE). Parts of this experiment were presented at the ECOC 2007 in Berlin [BLRH07b].

System Setup

Fig. 5.1 depicts the experimental setup of the transmission system. A directly modulated lensed 650 nm laser diode (LD), originally designed for DVD players, is used as the transmitter with an average output power of 5 dBm. This laser is modulated by a non return-to-zero $2^7 - 1$ pseudo-random binary sequence (PRBS) at 1.25 Gbit/s. The output light is efficiently coupled into the SI-POF (Eska GH) with a numerical aperture of 0.5, a diameter of 1 mm, and an optical loss of 140 dB/km with fiber lengths of 25 m, 50 m, 75 m and 100 m. At the receiver the output light is coupled into a GaAs-PIN photodiode with an active area of 100 μm followed by an integrated trans-impedance amplifier (TIA) with a 3-dB bandwidth of 1.5 GHz.

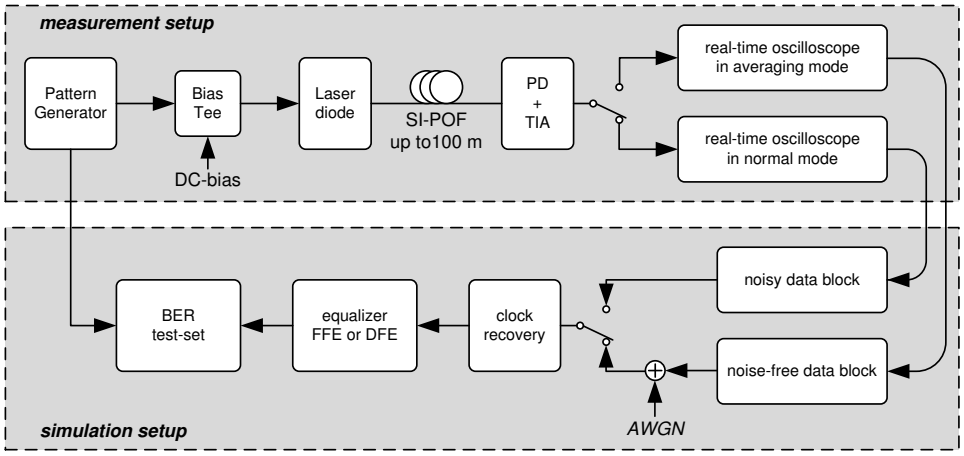

Figure 5.1: Experimental and Simulation Setup for 1.25 Gbit/s transmission with laser and OOK modulation in combination with symbol-spaced receiver equalization.

The measured electrical transfer functions of the system for the considered fiber lengths are depicted in Fig. 5.2. For a fiber length of 100 m the whole system has a 3-dB bandwidth of 60 MHz, which is mainly dominated by the bandwidth limitation of the SI-POF.
The ripples in the measured transfer functions are induced by impedance mismatching and reflections at the measurement device interface. The received electrical signal is captured by a Lecroy Wavemaster 8500A real-time digital sampling oscilloscope at a sampling rate of 20 GSamples/s. The oscilloscope operates in two different modes (see Fig. 5.1): In the "averaging mode" 1000 waveforms are averaged in the oscilloscope itself and then stored to be processed afterwards, resulting in a nearly noise-free signal (noise-free data block). In the "normal mode" the oscilloscope takes just one shot to get a noisy signal, with which the real performance of the system can be evaluated (noisy data block). These two

data blocks are used as input for the simulation environment depicted in the lower part of Fig. 5.1. Monte-Carlo simulations were carried out by numerically adding additive white Gaussian noise (AWGN) to the noise-free data block, thus the performance can be evaluated versus the elecrical signal-to-noise power ratio ($\mathrm{SNR}_{\mathrm{el}}$), which is defined as $\mathrm{SNR}_{\mathrm{el}} = E_s/N_0$, by varying the amount of added noise.

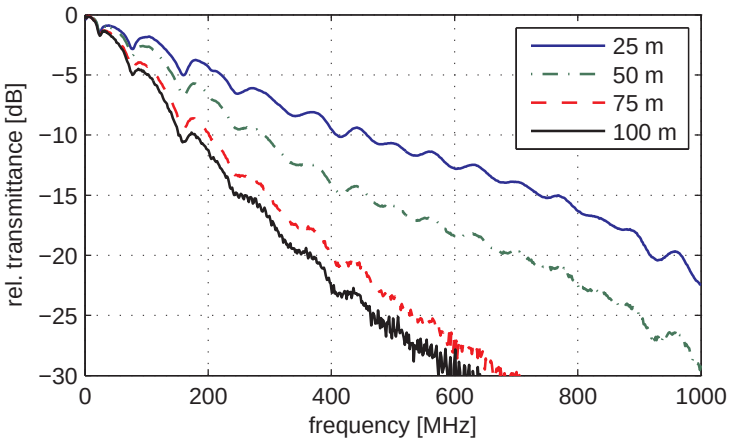

Figure 5.2: Transfer functions of the 1.25 Gbit/s OOK modulated experiment over SI-POF for fiber length of up to 100 m.

The noisy data block is used to calculate the actual performance of the measurement setup. So, the noisy distorted signal (with either natural or numerical noise) is fed into the receiver digital signal processing stage. First the clock is recovered by using the non-linear spectral line method. For details about this method see [LM94, Pro01]. Afterwards the signal is downsampled to the symbol rate (1.25 Gbaud) and equalized, either by a symbol-spaced feed-forward equalizer (FFE) or a decision feedback equalizer (DFE). For more details about the equalizers see chapter 4.4. The equalizer coefficients are trained initially and afterwards adapted using the least mean squares (LMS) algorithm (see chapter 4.5). Finally the decided bits are compared to the transmitted PRBS and the bit error ratio (BER) is calculated.

Results and Discussion

To get the optimum number of required equalizer taps, the longest fiber length of 100 m is considered first. In Fig. 5.3, the BER performance vs. $\mathrm{SNR}_{\mathrm{el}} = E_s/N_0$ is depicted for different numbers of filter taps. On the left side the curves for the symbol-spaced FFE are plotted. Except the FFE with 5 taps, all other equalizers have nearly the same performance. So the minimum number of required equalizer taps is 7 for this system. In

the following results a FFE with 15 taps is used, to get in any case the best performance of a symbol-spaced FFE.

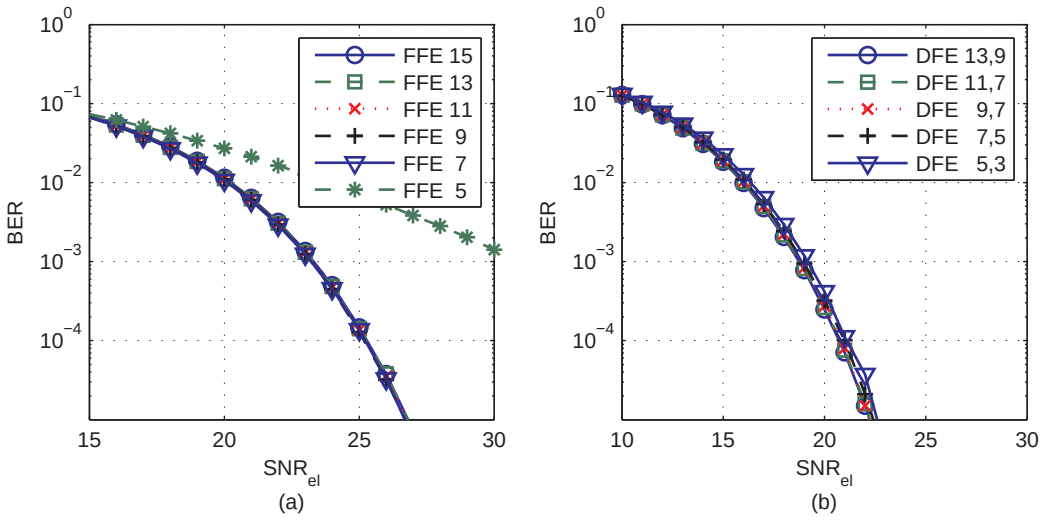

Figure 5.3: BER performance for 1.25 Gbit/s over 100 m SI-POF for different numbers of equalizer taps: on the left side for FFE (a) and on the right side for DFE (b).

On the right side the comparison of BER performance curves for the symbol-spaced DFE are plotted. In this case all tested equalizer parameterizations lead to the same performance, thus even a DFE with only 5 forward and 3 backward taps is sufficient to get the maximum performance for this setup, as the larger equalizers do not perform better in terms of BER. So in the following a DFE with 9 forward and 7 feedback taps is used throughout the following experiment.
The bit error ratio (BER) performance simulations were done by transmitting 20 million bits, so a BER value of $5 \cdot 10^{-6}$ is achieved by counting 100 errors, which is sufficient to get a statistically stable result. The parameter sweep was done over the electrical signal-to-noise power ratio (SNR_{el}) within a range of 10 to 30 dB. In Fig. 5.4 the BER performance curves are depicted for fiber lengths of 25 m (a), 50 m (b), 75 m (c) and 100 m (d). For comparison the matched filter bound (MF bound), introduced in chapter 4.6.1, is included in all subplots in Fig. 5.4 (blue solid line with dots). This reference curve is completely based on simulations and represent the upper performance bound for all equalization schemes. The green dashed-dotted line represents the case without equalization. Even for the shortest considered fiber length of 25 m an error-free transmission is never possible. This is due to the bandwidth limitation of the SI-POF induced by modal dispersion (compare Fig. 5.2).

At a fiber length of 25 m, the required SNR_{el} for a target BER of 10^{-6} with the FFE is 16.3 dB. The equalization gain of the DFE with respect to the FFE is only 0.2 dB. This small difference can be explained by the fact that the ISI is not too strong at this fiber length, and the noise amplification of the linear equalizer is not so high. For a fiber length of 50 m, the required SNR_{el} for the FFE increases to 19 dB, here the equalization gain of the DFE increases to 1 dB.

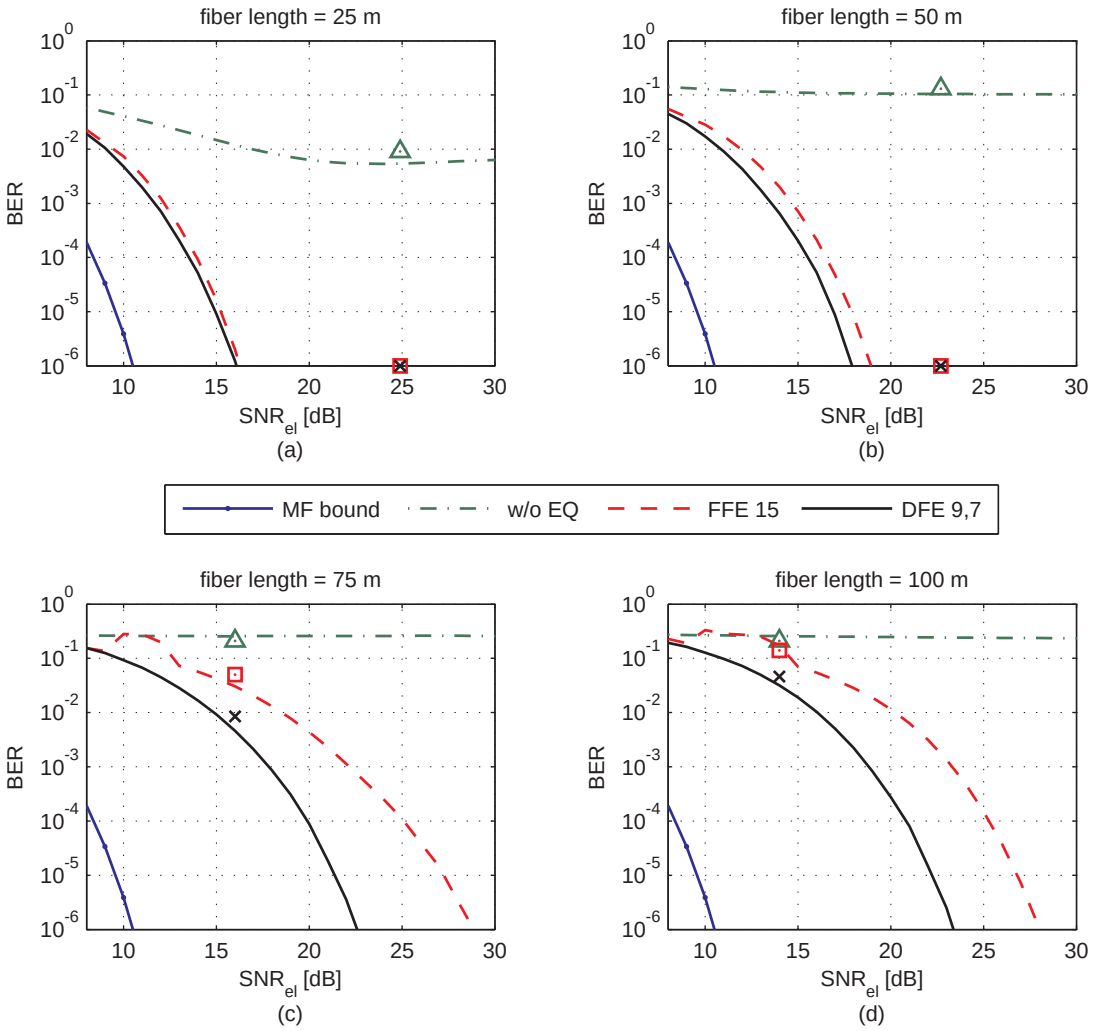

Figure 5.4: BER results for the four cases: matched filter bound (MF bound), without equalization (w/o EQ), with FFE 15, and with DFE (9,7) for fiber length of: 25 m (a), 50 m (b), 75 m (c) and 100 m (d). Markers represent the values with noisy captured data.

For fiber lengths of 75 m and 100 m, the required SNR_{el} values for FFE increase to 28.9 dB

and 28 dB, respectively. The equalization gain of the DFE grows up to 6.3 dB and 4.6 dB for 75 m and 100 m.
The strange behavior, that the equalizer performances for these two lengths are nearly the same, can be explained by the transfer functions depicted in Fig. 5.2. For these fiber lengths the transfer functions are nearly identical, so the equalizer performances should not be far away from each other. The reason for this behavior can be explained by the used trans-impedance amplifier (TIA) with integrated automatic gain control (AGC) with peak detection. In case of strong ISI, the signal levels do not remain long time at the highest signal level, so the AGC always carries out some gain adjustments. The transfer function and the noise performance of a TIA also depend on this gain factor, so this peak detection can be the reason for this strange behavior. However, the benefit of using a DFE instead of a FFE can clearly be seen at this fiber length. The DFE equalization gain reaches values of up to 6.3 dB, which is mainly due to the fact that the DFE removes post-cursor ISI without amplifying noise. At longer fiber lengths the receiver noise is more and more the dominant distortion effect.
Up to now only the noise-free data blocks are used to evaluate the performance of the equalizer schemes versus SNR_{el}. If noisy data blocks are used and processed with the same equalizers, the real system performance of the measurement setup can be evaluated. The measured SNR_{el} values and the corresponding BER values for the two considered equalizers and without equalization are listed in table 5.2. Additionally, these values are plotted in Fig. 5.4 as markers: triangles for without equalization, squares for FFE, and crosses for DFE.

	25 m	50 m	75 m	100 m
SNR_{el}[dB]	24.9	22.7	16	14
BER [w/o EQ]	$9 \cdot 10^{-3}$	$1.3 \cdot 10^{-1}$	$2.1 \cdot 10^{-1}$	$2.1 \cdot 10^{-1}$
BER [FFE 15]	$< 10^{-5}$	$< 10^{-5}$	$5.0 \cdot 10^{-2}$	$1.4 \cdot 10^{-1}$
BER [DFE (9,7)]	$< 10^{-5}$	$< 10^{-5}$	$8.5 \cdot 10^{-3}$	$4.6 \cdot 10^{-2}$

Table 5.2: BER values without equalization (w/o EQ) and after equalization (FFE 15 and DFE 9,7) with noisy data.

For fiber lengths of 25 m and 50 m both equalizers perform well and no errors could be detected within a noisy data block length of $2.4 \cdot 10^5$ bits, which translates in a BER smaller than 10^{-5}. For 75 m and 100 m errors are detected for both equalizers. These values fit well with the results of the numerical noise addition in Fig. 5.4. In Fig. 5.5

interpolated eye diagrams (40 samples/symbol) at the equalizer output are plotted for the DFE equalizer to get a more visual impression of the equalizer performance.

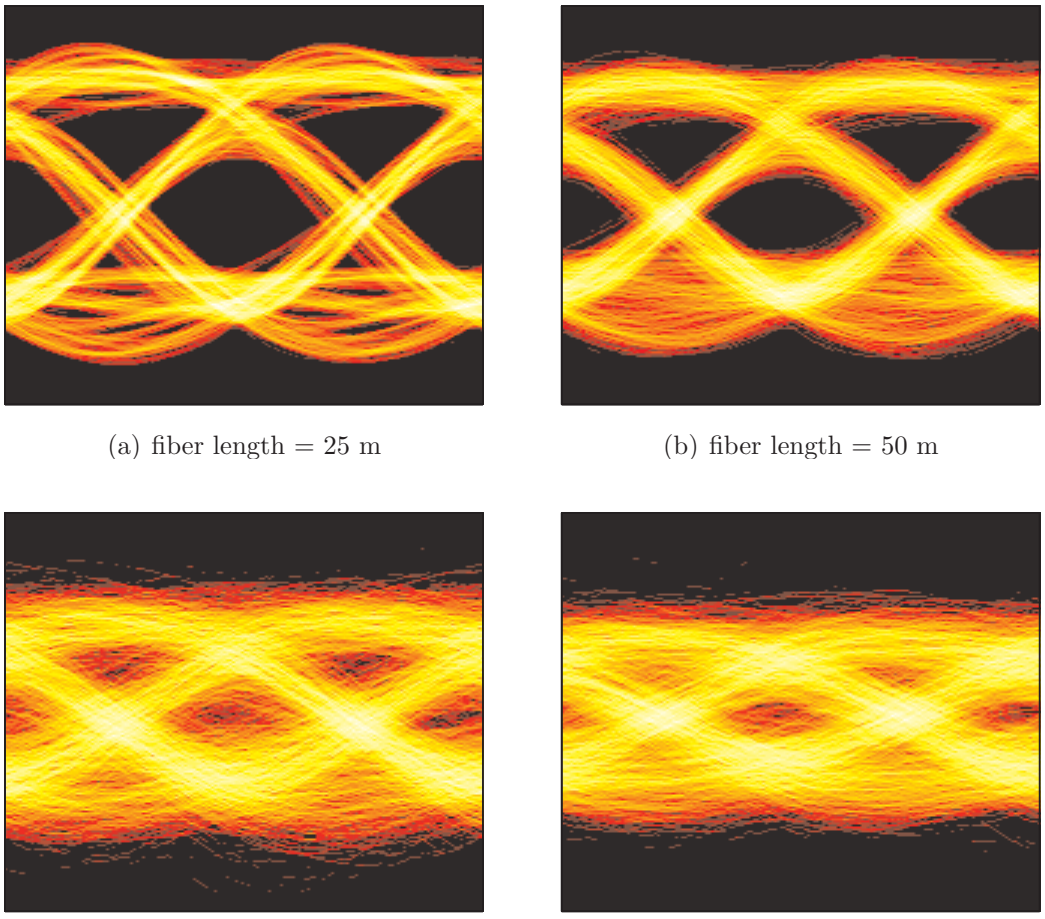

(a) fiber length = 25 m

(b) fiber length = 50 m

(c) fiber length = 75 m

(d) fiber length = 100 m

Figure 5.5: Eye diagrams (interpolated) after equalization (DFE 9,7) with noisy sampled data (no numerical noise addition, noise induced by the system itself) for fiber length of 25 m (a), 50 m (b),75 m (c) and 100 m (d).

In the first eye diagram (Fig. 5.5a) for 25 m, noise is not a problem. Only some residual ISI is left, but a clear open eye can be detected. For 50 m, the ISI can be mostly mitigated, but the increasing influence of the noise can be observed. The two eyes for 75 m and 100 m are completely closed, but predominantly due to noise, as there is a soft shape of an eye. This result is also proven by the simulations vs. the SNR_{el}, in which error-free transmission is possible if the SNR_{el} is high enough.

Conclusion

The bandwidth limitation of a SI-POF based transmission system can be counteracted by using digital symbol-spaced equalizers. At a fiber length of 100 m the DFE performs best with a required SNR_{el} of 23.4 dB for a target BER of $1 \cdot 10^{-6}$. At this fiber length the SNR_{el} penalty with respect to the matched filter bound is 13 dB. Therefore, one way to get a smaller penalty is to apply a better equalization scheme, for example Maximum Likelihood Sequence Estimation (MLSE) [Vit67]. Nevertheless, the results demonstrate the potential of SI-POF-based systems permitting Gigabit Ethernet transmission over distances of up to 100 m, enabled by digital symbol-spaced decision feedback equalization. This approach shows the feasibility of an upgrade scenario by inserting digital signal processing at the receiver, leaving the transmitter side unchanged.

5.1.2 2 Gbit/s Transmission with On-Off-Keying

In the previous sub-chapter it has been shown that 1.25 Gbit/s transmission over 100 m SI-POF should be possible, if the receiver noise can be decreased. The receiver used in the previous experiment is optimized for a silica multi-mode fiber system, which operates at a wavelength of 850 nm and a fiber core diameter of 50 μm or 62.5 μm. Thus the effective area of the photo diode (100 μm) used before is sufficiently large to receive nearly all the light out of the fiber core. For the SI-POF case, with a fiber core diameter of 1 mm and an operating wavelength of 650 nm, this detector has to work under sub-optimal conditions, resulting in a high power loss.

System Setup

In this sub-chapter, the same experimental and simulation setup is used as in the previous sub-chapter (see Fig. 5.1), except of some minor modifications, which are explained in the following. First, a silicon based PIN photo diode is used with an active area diameter of 540 μm and a responsivity of around 0.4 A/W_o. Thus much more light out of the SI-POF can be detected and converted into a current. Directly after the photo diode, a discrete TIA (TZA-3023) is used as first stage amplifier with a 3-dB bandwidth of 650 MHz. The second change is that the overall analog setup was optimized, which can be seen in the transfer function depicted in Fig. 5.6(a).
The 3-dB frequency has increased in this setup to 101 MHz in comparison to 60 MHz in the previous experiment, but the 3-dB bandwidth of the TIA has decreased to 650 MHz, thus for higher frequencies the transfer function is worse. The third difference is in the digital

signal processing part. The equalizers changed here to fractionally spaced operation and the number of taps was significantly increased.

Results and Discussion

This experiment was carried out only for a fiber length of 100 m of SI-POF and two data rates: 1.25 Gbit/s and 2 Gbit/s.

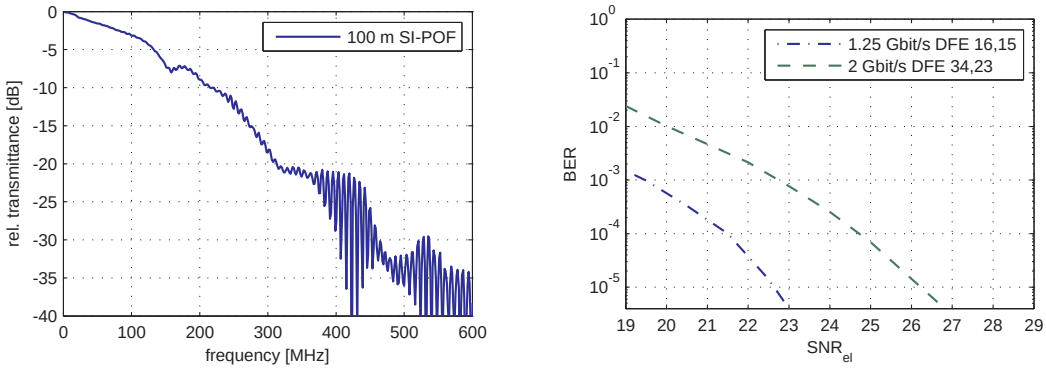

(a) transfer function for 100 m SI-POF

(b) BER performance for 1.25 and 2 Gbit/s over 100 m SI-POF

Figure 5.6: (a) Transfer function for 100 m SI-POF with laser launch and photo diode with 540 μm active area diameter. (b) BER performance for a data rate of 1.25 Gbit/s and $T/2$-spaced DFE(16,15), and data rate of 2 Gbit/s and $T/2$-spaced DFE(34,23) versus the electrical $\mathrm{SNR}_{\mathrm{el}} = E_s/N_0$ with numerically added noise for a fiber length of 100 m.

As equalizer, a fractionally-spaced decision feedback equalizer was applied with 34 or 16 forward and 23 or 15 backward taps for 2 Gbit/s or 1.25 Gbit/s, respectively. The number of taps was optimized to get the best performance.
At a data rate of 1.25 Gbit/s the required electrical $\mathrm{SNR}_{\mathrm{el}}$ at a BER of 10^{-4} is approx. 21.4 dB, which is approximately the same value as in the previous experiment. Note that more taps are needed in comparison to the results in chapter 5.1.1 due to smaller TIA bandwidth of 650 MHz. In Fig. 5.7 on the left side the eye diagram is depicted for 1.25 Gbit/s over 100 m at the equalizer output with measured noisy data. The eye is clearly open and no error could be detected in the simulation. So error-free transmission of Gigabit Ethernet over 100 m SI-POF is possible by using digital DFE equalization.

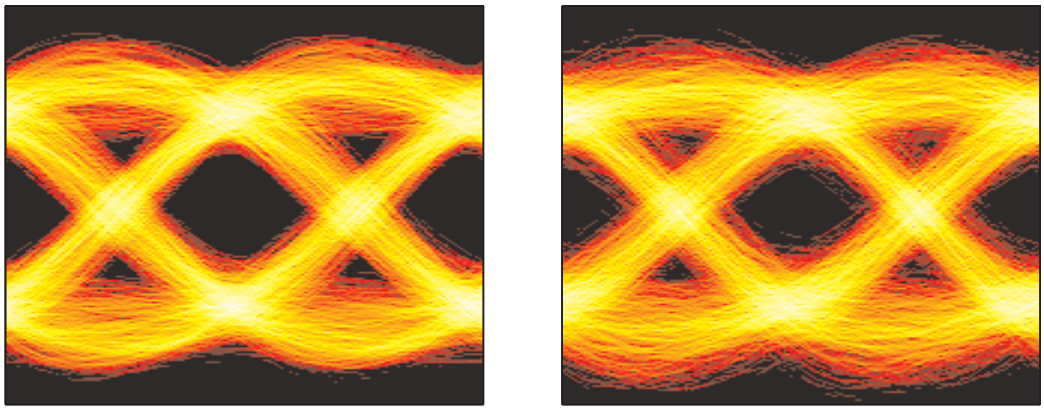

(a) 100 m, data rate 1.25 Gbit/s (b) 100 m, data rate 2 Gbit/s

Figure 5.7: Eye diagrams (interpolated) after equalization for: (a) a data rate of 1.25 Gbit/s and $T/2$-spaced DFE(16,15), and (b) a data rate of 2 Gbit/s and $T/2$-spaced DFE(34,23) with noisy sampled data (no numerical noise addition, noise induced by the system itself) for a fiber length of 100 m.

With the same system setup, the data rate is increased to 2 Gbit/s and the equalizer size is increased to 34 forward and 23 backward taps. The BER versus $\mathrm{SNR}_{\mathrm{el}}$ curve is depicted in Fig. 5.6(b), the required $\mathrm{SNR}_{\mathrm{el}}$ for a BER of 10^{-4} is increased to 24.7 dB, which is only 3.3 dB more than for 1.25 Gbit/s. In Fig. 5.7 on the right side the eye diagram at the equalizer output for a data rate of 2 Gbit/s over 100 m SI-POF is shown. The BER for the noisy data block was calculated to $1 \cdot 10^{-5}$.

Conclusion

This experiment shows the capability of a laser launched SI-POF system to transmit Gigabit Ethernet (1.25 Gbit/s) and beyond over 100 m of fiber. This is achieved by using conventional transmitter circuitries for digital OOK modulation and digital receiver equalization. The 2 Gbit/s experiment shows, that even data rates higher than 1.25 Gbit/s can be transmitted with this system architecture. Thus, reliable and relaxed transmission should be possible for Gigabit Ethernet over 100 m SI-POF.

5.2 SI-POF Systems with LED launch and receiver equalization

The use of LEDs as light sources in a SI-POF transmission system has significant advantages such as high reliability and robustness, longer lifetime, lower cost, less sensitivity to temperature variation, larger working temperature range, and relaxed eye safety regulations. Thus the application of SI-POF systems in environments like automotive and industrial is possible. Recently, several approaches have been reported to overcome the additional bandwidth limitation introduced by the LED itself, by either using multi-carrier modulation DMT [LBR+08b, RLB07] or by using multilevel modulation in combination with receiver equalization [LBR+08a, BLRH08b]. The LED used in these experiments is a resonant-cavity type [Fir], which is denoted here as RC-LED.
In this sub-chapter two experiments are presented. The first is a transmission of 500 Mbit/s over 50 m SI-POF, which addresses the IEEE1394b S400 standard [iee02] for a net data rate of 400 Mbit/s. The second experiment is a 1.25 Gbit/s transmission over up to 75 m to realize a Gigabit Ethernet link.

5.2.1 500 Mbit/s Transmission with PAM-4 modulation

This experiment was the first step towards Gigabit transmission using LEDs. To compensate for the additional bandwidth limitation of the RC-LED, the bandwidth of the data signal is divided by a factor of two using a 4-level pulse amplitude modulation (PAM-4). This modulation carries 2 bits per symbol, so that the symbol rate decreases by a factor of 2 compared to the bit rate. In combination with receiver equalization, the transmission of 500 Mbit/s over 50 m SI-POF could be demonstrated. Parts of the experimental results were presented at the EphotonONe Summer School 2007 [BLRH07c].

System Setup

Figure 5.8 shows the experimental and simulation setup of the transmission system. The PAM-4 signal is precomputed with a software tool by encoding a pseudo random binary sequence (PRBS 9) into a 4-level signal with Gray coding. A rectangular impulse shaper is used to generate the bipolar driving signal. The analog waveform is generated using an arbitrary waveform generator (AWG) with 625 MSamples/s (N8241A) and an amplitude resolution of 15 bits. For the electro-optical conversion a biased commercial 650 nm RC-LED with an average output power of about -2 dBm and a numerical launch aperture (NA) of 0.35 is used. After transmission over 50 m of standard 1 mm SI-POF, the signal

is received by a PIN photo diode with an active area of 0.8 mm^2 followed by an amplifier stage. The received electrical signal is captured by a Lecroy Wavemaster 8500A real-time digital sampling oscilloscope at a sampling rate of 10 GSamples/s. The scope is used in averaging mode, which means that 1000 waveforms are evaluated within the scope to compute the mean value of the waveform. This leads to a nearly noise-free signal, which is stored in a data block called "noise-free data block".

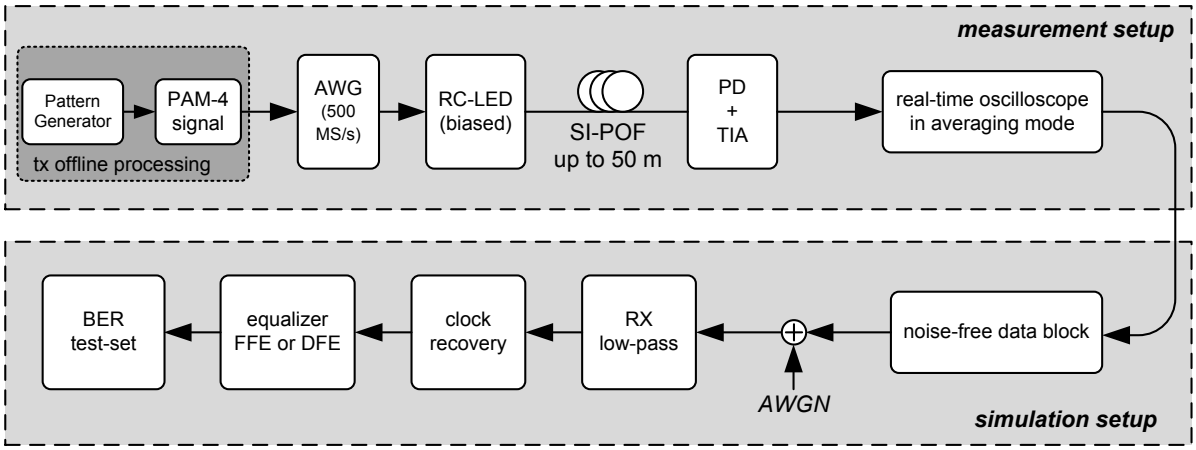

Figure 5.8: Experimental and Simulation setup for 500 Mbit/s transmission with RC-LED and PAM-4 modulation in combination with symbol-spaced receiver equalization.

This "noise-free data block" is used as input data for the simulation setup depicted in the lower block in Fig. 5.8. By varying the numerically added additive white Gaussian noise (AWGN), the BER performance is evaluated using the Monte Carlo approach. The noise power added is defined by the electrical signal-to-noise power ratio $\mathrm{SNR}_{\mathrm{el}} = E_s/N_0$. The noisy distorted signal is filtered using a 5th order Bessel low-pass (LP) filter with a 3-dB bandwidth of 177 MHz (symbol rate/$\sqrt{2}$). Afterwards a clock recovery is used to sample the noisy signal at the baud rate (250 Mbaud/s). This is done by choosing the nearest sample to the optimum calculated sampling point, which is the result of a non-linear spectral line method [LM94, Pro01]. This sampled symbol-spaced signal is fed into either a symbol-spaced feed-forward equalizer (FFE) with 5 taps or a symbol-spaced decision feedback equalizer (DFE) with 5 forward and 2 backward taps. The equalizer coefficients are trained using a training sequence and adapted using the least-mean squares (LMS) algorithm. The BER is evaluated by demodulating the equalized signal and comparing it to the transmitted PRBS sequence.

Results and discussion

Figure 5.9 shows the electrical transfer function of the transmission system in the optical back-to-back (btb) case and with a piece of 50 m SI-POF. In the back-to-back case, which means a fiber length of 1 m, the system has a 3-dB bandwidth of 71 MHz, which reduces to 51 MHz with the 50 m piece of SI-POF. But, as it can be seen in Fig. 5.9, the transfer functions decrease slowly, with a 10-dB bandwidth of about 279 MHz and 139 MHz, respectively. The ripples in these measured transfer functions are artifacts of impedance mismatching and reflections at the measurement device and not a result of the transmission system.

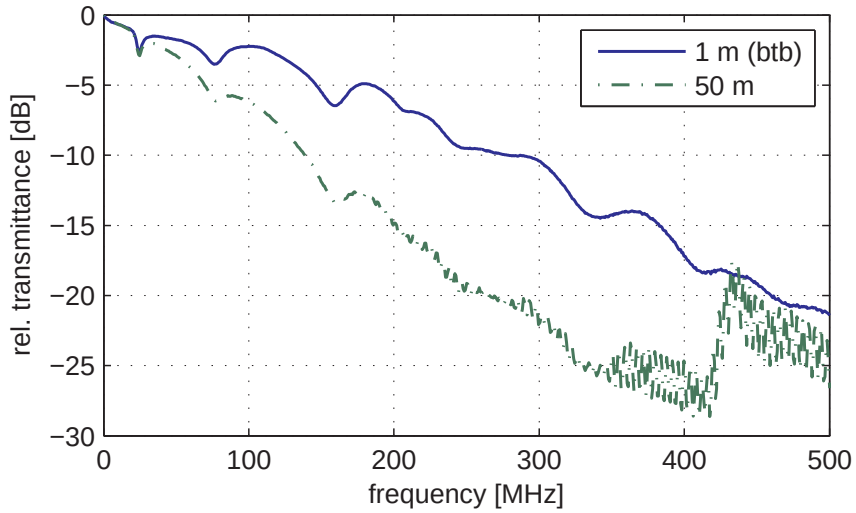

Figure 5.9: Transfer functions for the 500 Mbit/s experiment with RC-LED launched fiber of a length of 1 m and 50 m.

The BER performance versus SNR_{el} is plotted in Fig. 5.10, on the left side for the back-to-back (btb) case and on the right side for a fiber length of 50 m. The blue solid line represents the BER performance of the matched filter bound (see chapter 4.6.1). The green dashed-dotted line represents the performance without equalization. For the back-to-back case an error-free transmission is possible, if the SNR_{el} is high enough. This behavior changes for a fiber length of 50 m. Here no error free transmission is possible, because of the inter symbol interference (ISI) due to modal dispersion and the bandwidth limitation of the transmitter device. The red dashed line is the BER curve for the FFE 5 and the black solid line for the DFE 5,2. Both equalizers can compensate the bandwidth limitation for both fiber lengths. In the back-to-back case the equalizers can compensate the transmitter bandwidth limitation with a SNR_{el} penalty of about 5 dB at a target BER

of $1 \cdot 10^{-4}$ with respect to the matched filter bound. For the 50 m long fiber this penalty increases to 6.8 dB and 7.0 dB for the DFE and FFE, respectively. Thus, the transmission over 50 m SI-POF has only 3 dB electrical SNR_{el} penalty for both equalizers. The 2 additional feedback taps of the DFE do not increase the system performance, because the ISI not too strong and the noise floor is far below the transfer function. Thus, the noise enhancement of the FFE does not affect the performance.

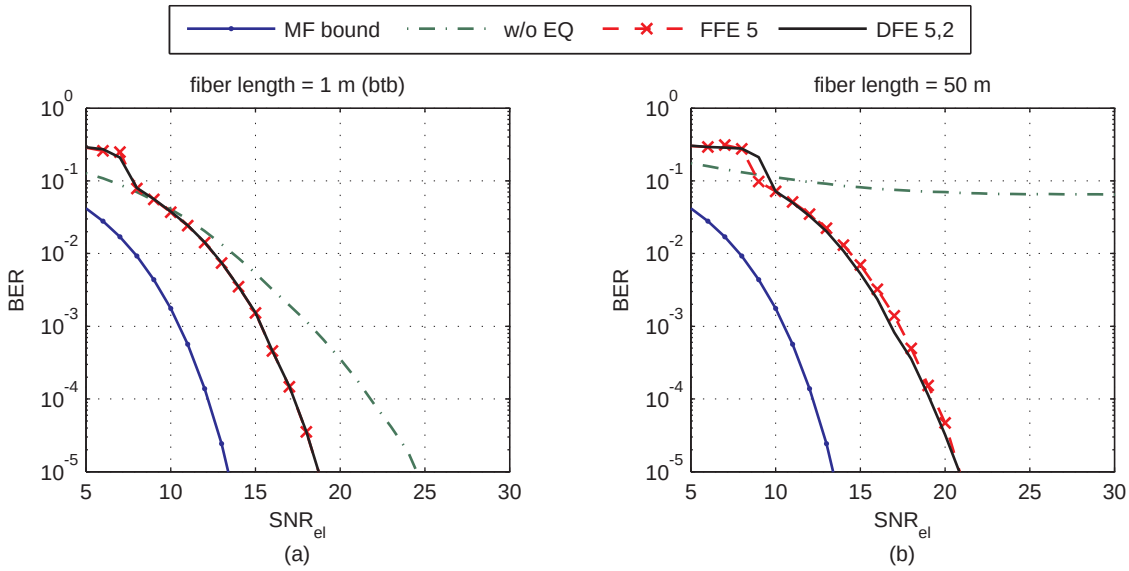

Figure 5.10: BER results for the four cases: matched filter bound (MF bound), without equalization (w/o EQ), with FFE 5, and with DFE 5,2 for fiber length of 1 m (a) and 50 m (b).

Conclusion

In this experiment it has been shown that 500 Mbit/s transmission over 50 m SI-POF with 650 nm RC-LED was enabled by using PAM-4 modulation in combination with simple receiver equalization. Even the simple symbol-spaced feed-forward equalizer with 5 taps is sufficient to combat the inter-symbol interference due to modal dispersion and the bandwidth limitations of the active components. This result shows the capability of a low-cost implementation of an optical IEEE1394b2002-S400 [iee02] communication link using a RC-LED and a FFE with 5 taps.

5.2.2 1.25 Gbit/s Transmission using PAM-4 modulation

This experiment is the proof of concept that Gigabit Ethernet transmission using a red RC-LED over 50 m of SI-POF is possible. Therefore, a predistorted PAM-4 signal with a symbol rate of 625 MSymbol/s is used in combination with digital fractionally-spaced receiver equalization. These results were partly presented at the ECOC 2008 [BLRH08b].

System Setup

The experimental setup is shown in Fig. 5.11 in the upper box. The PAM-4 signal is generated inside a computer using a pseudo-random quaternary sequence [MS76] of order 5, which is Gray-encoded into a four-level sequence. A digital symbol-spaced pre-filter is used to predistort the digital driving signal (TX pre-filter). With an arbitrary waveform generator (AWG) with a sampling rate of 625 MSample/s the pre-distorted sequence is digital-to-analog converted with 1 sample per symbol, which results in a data rate of 1250 Mbit/s. This signal drives a resonant-cavity LED (RC-LED) with a bias current of 20 mA, an average coupled optical power of -1.4 dBm and optical modulation amplitude (OMA) of approx. 0 dBm. The optical signal is butt-coupled (without connector or coupling optics) into bare fibers (Mitsubishi GH4001) of different length (1 m, 25 m, 50 m and 75 m) cut with a low-cost cutting tool (razor blade) and fixed with a bare fiber lock.

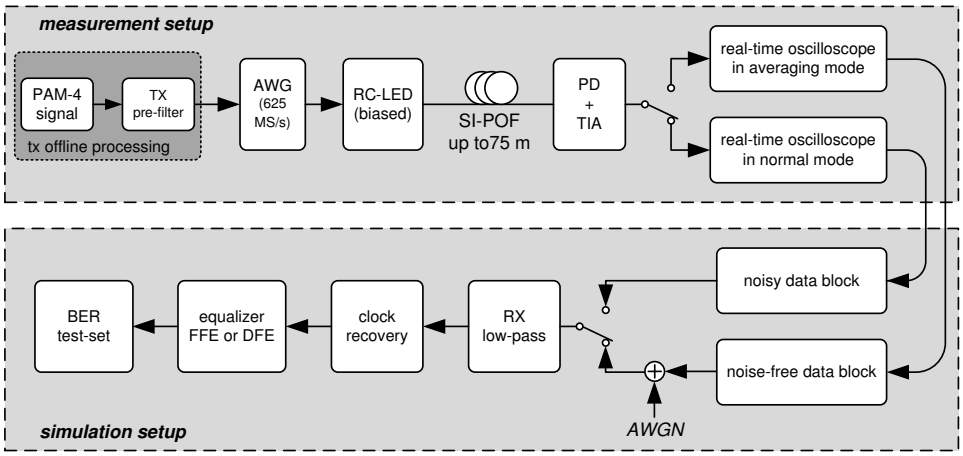

Figure 5.11: Experimental and Simulation setup for the 1.25 Gbit/s transmission with RC-LED and PAM-4 modulation in combination with fractionally-spaced receiver equalization.

At the receiver side, a silicon PIN photo diode (PD) with a 540 μm diameter active area is connected to an external trans-impedance amplifier (TIA:TZA-3023) with integrated

automatic-gain control (AGC). The analog system transfer functions are depicted in Fig. 5.12(a).

The analog signal is post-amplified and captured using a real-time digital sampling oscilloscope with a sampling rate of 10 GSample/s. The sampling is done in two ways: the averaging mode averages 100 waveforms to get a nearly noise-free signal, the normal mode captures the noisy signal once. These two signals are used to do performance simulations in a computer. As input data for the simulations, additive white Gaussian noise (AWGN) is added numerically to the noise-free signal, or the noisy captured data is used directly. The digital receiver part consists of a Bessel low-pass filter of order 4 with a 3-dB bandwidth of 0.7 · symbol rate (RX low-pass), a downsample stage with internal clock recovery (clock recovery) followed by a fractionally-spaced equalizer (FFE or DFE). At the end a bit error evaluation is done.

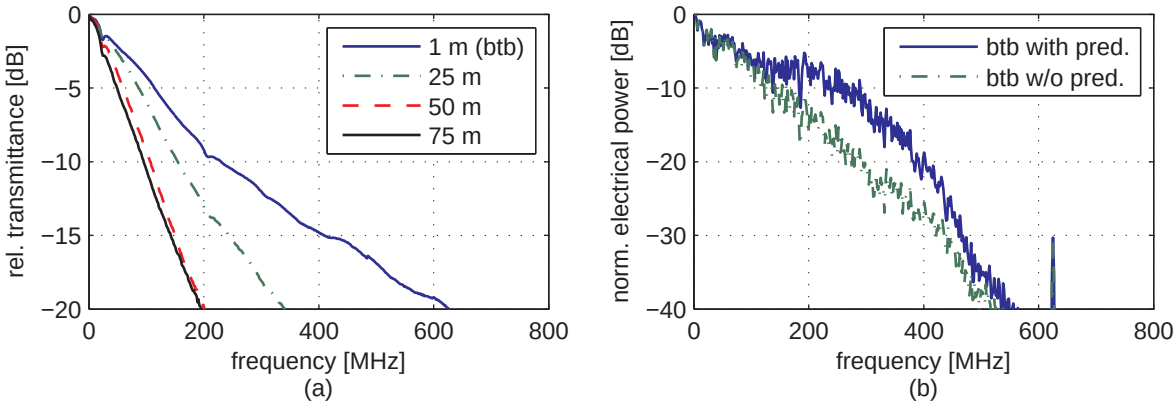

Figure 5.12: Transfer functions for RC-LED launched fiber length of 1 m, 25 m, 50 m and 75 m (a), and electrical spectra of the received signal for the optical back-to-back case with and without predistortion (b).

The predistortion filter (TX pre-filt) is implemented as digital symbol-spaced finite impulse response (FIR) high-pass filter. The spectra with and without predistortion in the back-to-back case is shown in Fig. 5.12(b). The green dashed dotted line represents the transmitter spectrum without predistortion in the optical back-to-back case (fiber length 1 m). The blue solid line is the predistorted transmitter spectrum. The high-pass characteristic of the filter boosts up the higher frequencies, but also decreases the SNR_{el} at the receiver. This is due to the generation of large peaks in the LED driving signal (higher crest factor), so the major energy of this signal is concentrated in a smaller modulation amplitude. For both cases, there is a spectral line at the symbol rate of 625 MHz, this is

just the sampling clock itself due to crosstalk in the AWG.
At the receiver a feed forward equalizer (FFE) with 12 taps and a decision feedback equalizer (DFE) with 8 forward and 3 feedback taps are investigated. Both equalizers are fractionally-spaced with half the symbol rate ($T/2$). The equalizer coefficients are adapted blindly using the Stop-and-Go algorithm [PP87].

Results and Discussion

For the bit-error ratio (BER) performance simulations approximately 10 million bits are transmitted and the electrical $\mathrm{SNR_{el}} = E_s/N_0$ is varied from 14 to 32 dB. In Fig. 5.13 the BER performance curves are plotted for fiber lengths of 1 m (a), 25 m (b), 50 m (c) and 75 m (d).
For comparison the BER curve of the matched filter bound (MF bound) is plotted with the solid blue line with dots. The green dashed dotted line represents the case without equalization. Even in the back-to-back case (1 m) an error-free transmission is impossible. This is due to the bandwidth limitation of the RC-LED. For longer fiber lengths the bandwidth limitation due to modal dispersion reduces the total bandwidth additionally. The dashed red lines represent the FFE 12 and the black solid lines the DFE 8,3 for the different fiber lengths. The $\mathrm{SNR_{el}}$ penalty of the FFE at a target BER of 10^{-4} is increased by approx. 4 dB every 25 m compared to the back-to-back case (1 m). For the DFE the $\mathrm{SNR_{el}}$ penalty compared to the back-to-back case is 3.2, 7.4 and 9.4 dB for fiber lengths of 25 m, 50 m and 75 m, respectively.
The simulated BER results for the noisy captured data are shown in Tab. 5.3. Additionally the BER values for the two equalizers are depicted in Fig. 5.13 as markers: red squares for the FFE and black crosses for the DFE.

	1 m	25 m	50 m	75 m
RxPower [dBm]	-1.4	-5.4	-9.2	-13
$\mathrm{SNR_{el}}$[dB]	28.6	28.2	26.3	21.6
BER [FFE 12]	$< 10^{-5}$	$< 10^{-5}$	$2.3 \cdot 10^{-4}$	$2.5 \cdot 10^{-2}$
BER [DFE 8,3]	$< 10^{-5}$	$< 10^{-5}$	$2.1 \cdot 10^{-5}$	$1.05 \cdot 10^{-2}$

Table 5.3: BER values after equalization with noisy data.

The measured received optical power (RxPower) confirms the fiber attenuation of approximately 160 dB/km. The $\mathrm{SNR_{el}}$ values are not proportional to the received electrical power because of the automatic gain control (AGC) in the TIA. The markers

are not perfectly matching with the simulated curves, because of the averaging process in the oscilloscope. This process averages also other transmission and system impairments, like i.e. baseline wander and transient effects of the active components. Furthermore, the sampling clock of the oscilloscope is not synchronized with the transmitter clock, which leads to a clock drift for long sampling shots in the oscilloscope. But the mismatch between the markers and the curves is very small, so all these impairments can be neglected.

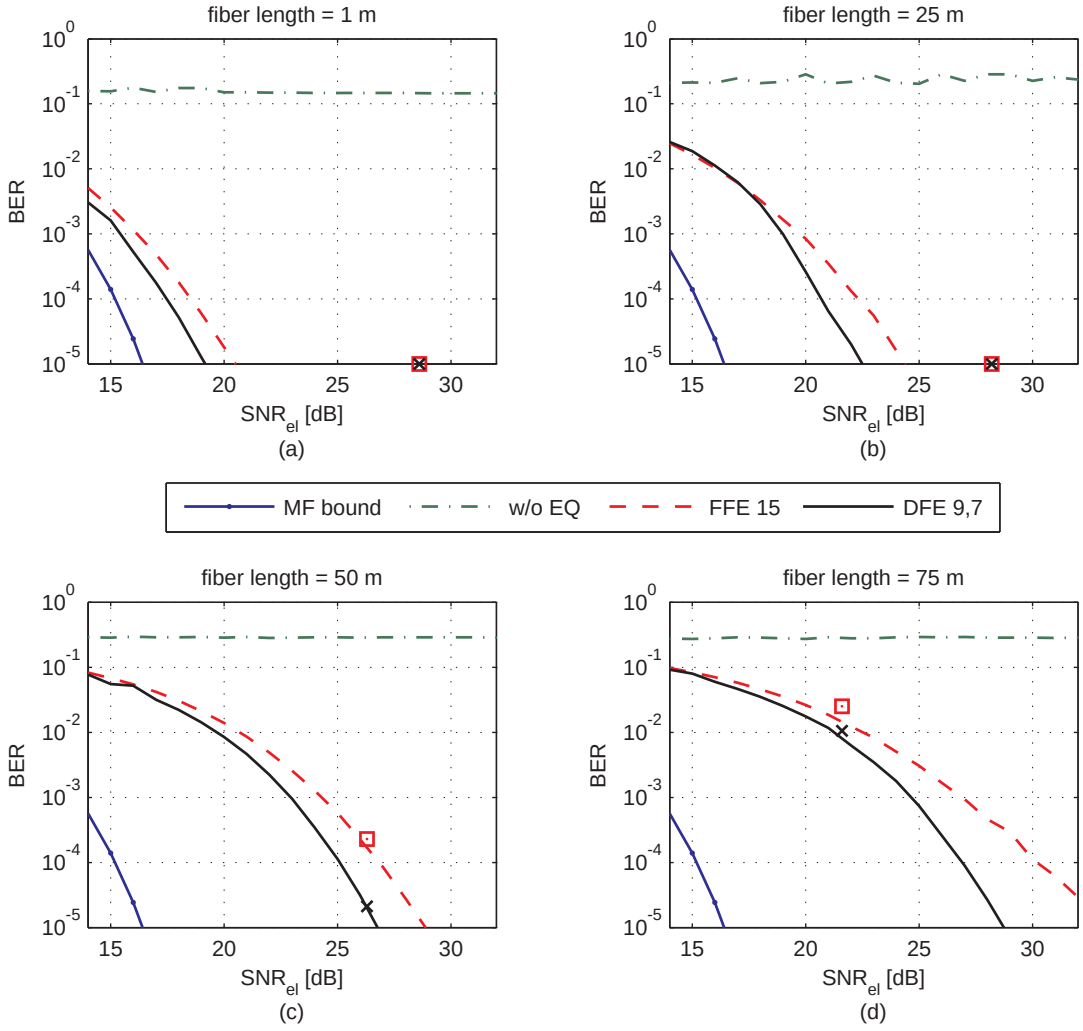

Figure 5.13: BER performance for a data rate of 1.25 Gbit/s and PAM-4 modulation $T/2$-spaced FFE 12 and DFE(8,3) versus $\mathrm{SNR_{el}}$ with numerically added noise for a fiber length of 1 m (a), 25 m (b), 50 m (c) and 75 m (d). Markers represent the values with noisy captured data.

For both equalizer schemes no error could be detected within 5 million transmitted bits for fiber lengths of 1 m (btb) and 25 m. For fiber lengths of 50 m and 75 m the DFE 8,3 has output BER values of $2.1 \cdot 10^{-5}$ and $1.05 \cdot 10^{-2}$, respectively. To visualize the equalizer performance, the interpolated eye diagrams of the DFE output are plotted in Fig. 5.14 for all fiber lengths. For 1 m and 25 m the eyes are clearly open, which must be the case because no errors are detected for these two fiber lengths.
For a fiber length of 50 m, the eye is still open, but smaller, which results in a higher BER. The eye at 75 m is completely closed, but only due to noise. Because the shape of the three eyes can still be identified, transmission is possible, if the receiver noise is decreased.

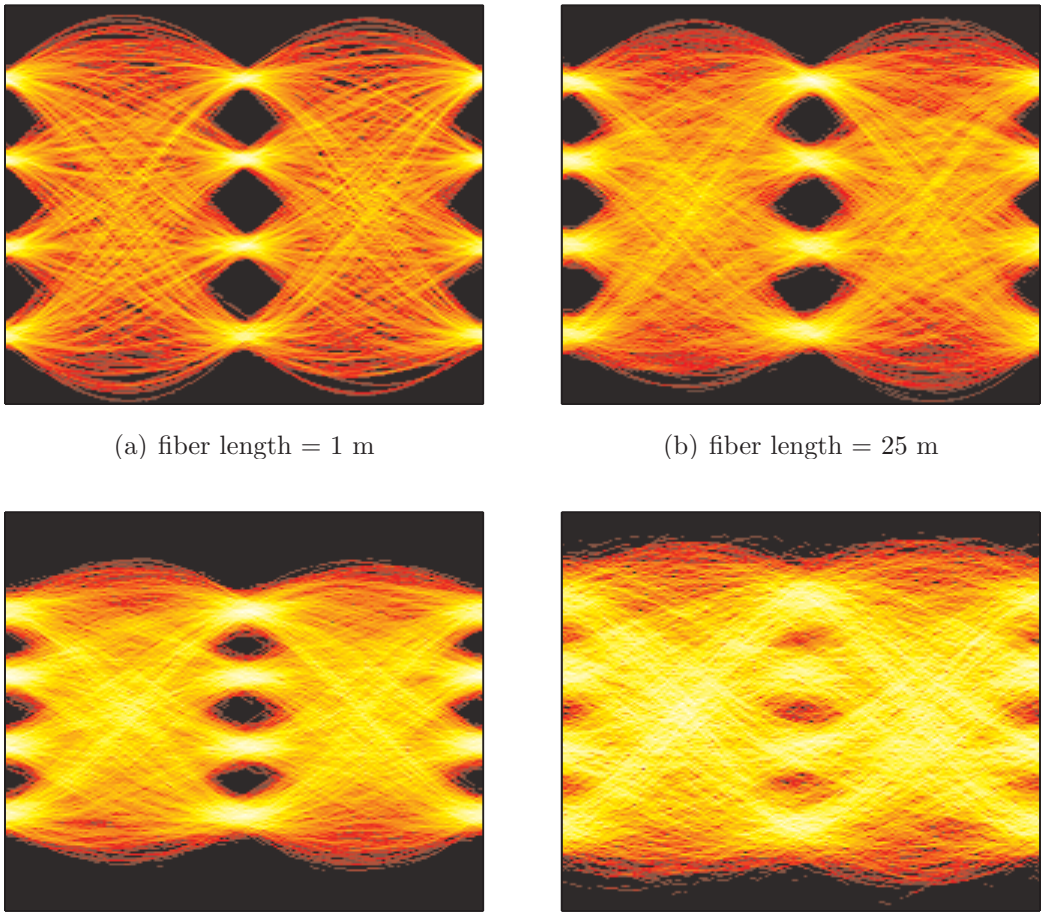

(a) fiber length = 1 m

(b) fiber length = 25 m

(c) fiber length = 50 m

(d) fiber length = 75 m

Figure 5.14: Eye diagrams (interpolated) after equalization (DFE 8,3) with noisy sampled data (no numerical noise addition, noise induced by the system itself) for fiber length of 1 m (a), 25 m (b), 50 m (c) and 75 m (d).

Conclusion

This experiment shows that 1.25 Gbit/s transmission over a LED based SI-POF system up to 75 m is possible using pre-distorted PAM-4 modulation and decision feedback equalization. For a fiber length of 50 m, the experimental setup has a BER after equalization of $2.1 \cdot 10^{-5}$. Hence error-free transmission over longer fiber lengths requires optimized receivers in terms of thermal noise or high-power transmitters. The required SNR_{el} values can be approximated by extrapolation of the BER curves in Fig. 5.13.
This experiment also represents a first step for the implementation of a fully working Gigabit Ethernet media converter demonstrator, which will be introduced in chapter 6.

5.3 PF-GI-POF Systems with VCSEL launch

The rapid growth of data traffic in data communications applications in local area networks (LAN), such as enterprise or datacenter backbones, has pushed the demand for high-speed and low-cost photonic networks [DeC05]. The use of 10 Gigabit Ethernet (10GbE) in such environments will often require new installations, because the commonly used CAT-5 copper cables are not applicable. A feasible solution is the use of fiber optic cables. In comparison to multimode silica fibers, the perfluorinated graded-index polymer optical fiber (PF-GI-POF) with core diameters of 50 μm, 62.5 μm, or 120 μm is a promising alternative due to ease of use and installation with clip-on connectors requiring minimal training. The PF-GI-POF cable itself is extremely flexible, offering bending radii of 5 mm compared with 25 mm for silica fiber cables and 30 mm for CAT-6A copper cables, which are required to transmit 10 Gigabit Ethernet.
Over such a PF-GI-POF 10 Gbit/s on-off keying (OOK) modulated data transmission has been limited to distances not longer than 100 m [GWW+99], because of the bandwidth limitation due to modal dispersion in the multimode fiber. Recent experiments have shown OOK modulated transmission of 10 Gbit/s over 220 m PF-GI-POF using a maximum likelihood sequence estimation (MLSE) and forward error correction (FEC) [LBR+07a]. But this equalizer has a large complexity and a huge power consumption, furthermore it is not really a low-cost solution.
In this chapter two experiments are presented enabling 10 Gbit/s transmission over up to 300 m of PF-GI-POF. The first experiment shows the capability of using PAM-4 modulation with simple receiver equalization to reach the required fiber length of 220 m of the 10Gbase-LRM standard [iee06]. The second is a comparison between OOK and PAM-4 modulation for a 10 Gbit/s link of 300 m using receiver equalization.

5.3.1 10 Gbit/s Transmission using PAM-4 modulation

The goal of this experiment was the proof of concept of 10 Gbit/s transmission over 220 m of PF-GI-POF by use of PAM-4 modulation and digital receiver equalization. This experiment shows that a commercially available VCSEL can be driven in a linear way, which is required for multilevel modulation. The good linearity of this VCSEL is also shown by transmitting DMT over the same experimental setup [LBR+07b]. The results of this experiment were presented at the International POF Conference (IC-POF) 2007 [BLRH07a].

System Setup

The setup of the experiment, depicted in Fig. 5.15, is divided into two parts. In the experimental part (upper box) the transmission of the PAM-4 modulated signal is measured and captured using a real-time digital sampling oscilloscope. The stored data blocks are used as input data in the simulation part (lower box). There the BER performances of two equalizer schemes are evaluated in a computer based simulation environment.

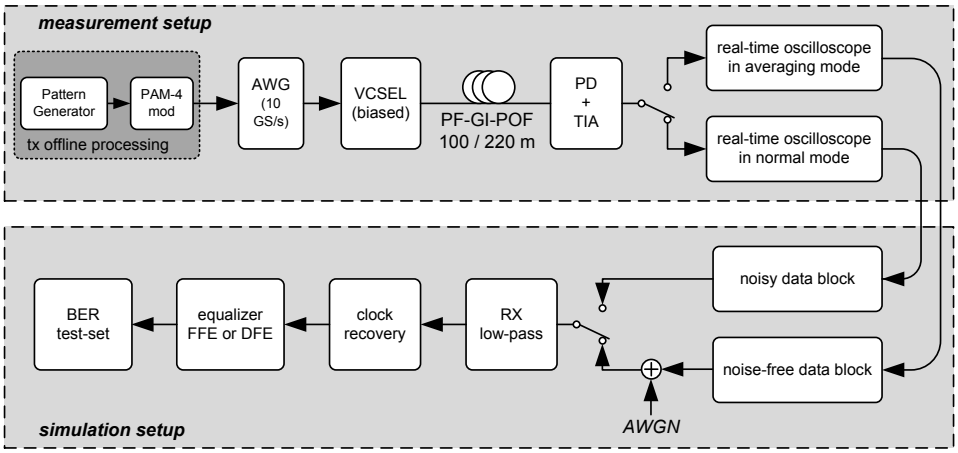

Figure 5.15: Experimental and simulation setup for the 10 Gbit/s experiment with VCSEL and PAM-4 modulation in combination with symbol-spaced receiver equalization.

In the experimental part, the PAM-4 signal is pre-computed with a software tool. A pseudo-random binary sequence of order 11 (PRBS 11) is encoded into a 4-level signal with gray encoding. A rectangular impulse shaper is used to compute the two times oversampled driving signal, which results just in one repetition of each data sample. This signal is digital-to-analog converted using an arbitrary waveform generator (AWG) with

a sampling rate of 10 GSample/s. The result is an analog waveform with a symbol rate of 5 GSymbol/s and a bitrate of 10 Gbit/s.
For electro-optical conversion, a directly-modulated commercial 850 nm multimode vertical cavity surface emitting laser (VCSEL) with an average output power of -1 dBm is used. This optical signal is launched into different lengths of the perfluorinated graded-index polymer optical fiber (PF-GI-POF), which is a commercially available fiber with a core diameter of 120 μm and a total diameter of 500 μm including cladding. The attenuation is approximately 40 dB/km at 850 nm and the numerical aperture (NA) is 0.185. First a 50 μm silica multimode fiber (MMF) patch cord is used to connect the VCSEL and the 120 μm PF-GI-POF.
At the receiver side, a 62.5 μm silica multimode fiber (MMF) pigtailed GaAs PIN detector with integrated trans-impedance amplifier (TIA) is used, leading to a 2.9 dB coupling loss due to core size mismatch between the PF-GI-POF (120 μm) and the silica MMF patch cord (62.5 μm). With this fiber coupling mismatch, no modal noise effects could be observed. A possible explanation for this could be that the (120 μm) PF-GI-POF guides most of the light within the lower order modes and higher order modes are strongly attenuated.
The received electrical signal is captured using a real-time digital sampling oscilloscope. The oscilloscope operates in two different modes. The average mode is used to get a nearly noise-free signal by averaging 2000 waveforms inside the oscilloscope. In normal mode the oscilloscope captures one shot of the electrical received signal.
The lower box in Fig. 5.15 shows the simulation setup for the BER performance evaluation of the transmission system using the Monte Carlo approach. Additive white Gaussian noise (AWGN) is added to the nearly noise-free signal captured by the oscilloscope. The noise power added is defined by the signal-to-noise power ratio $\mathrm{SNR}_{\mathrm{el}} = E_s/N_0$. The noisy signal is filtered using a 5th order Bessel low-pass (LP) filter with a 3-dB bandwidth of symbol rate/$\sqrt{2}$ (3.535 GHz). A clock recovery and a down sampling stage is used to sample the noisy signal at the symbol rate (5 GSample/s). The symbol-spaced sampled signal is fed into the feed-forward (FFE) or the decision-feedback equalizer (DFE). At the end, the equalized sequence is demodulated and compared with the transmitted bit sequence to get the BER. To evaluate the BER performance of the measured noisy signal (normal capture mode in the oscilloscope), the same setup is used, except the addition of noise.

Results and Discussion

Figure 5.16 shows the BER performance versus $\mathrm{SNR}_{\mathrm{el}}$ for a fiber length of 100 m (left) and 220 m (right). For the BER performance evaluation five million bits are transmitted

and evaluated. For comparison, the BER curve of the matched filter bound (MF bound) is depicted in both plots with the blue solid line with dots. The green dashed dotted line represents the case without equalization. For a fiber length of 100 m error-free transmission is possible, if the SNR_{el} is high enough. For 220 m the BER curve never reaches an error-free region because of inter-symbol interference due to modal dispersion. Thus for a target BER of $1 \cdot 10^{-5}$ the required SNR_{el} is 25.8 dB for 100 m and not applicable for 220 m. The penalty in terms of SNR_{el} with respect to the matched filter bound is 9.4 dB for 100 m and also not applicable for 220 m.
The red dashed line represents the BER curve for a feed-forward equalizer (FFE) with 5 taps and the black solid line for a decision feedback equalizer (DFE) with 5 forward and 2 additional feedback taps. For a fiber length of 100 m, the FFE and DFE can reduce the SNR_{el} penalty of 9.4 dB without equalization to 2.2 dB and 2.0 dB, respectively. Hence the inter-symbol interference introduced by the transmitter and the fiber can be mostly compensated. For the 220 m long fiber the penalties of these equalizers increase only by 0.2 dB. Thus even the very simple FFE with 5 taps can mitigate the introduced ISI in this transmission system.

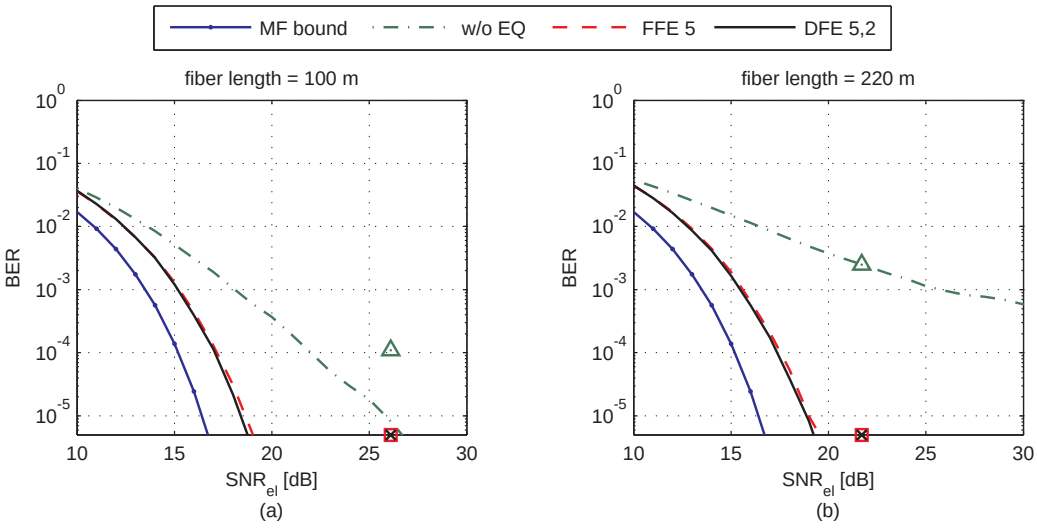

Figure 5.16: BER performance for a data rate of 10 Gbit/s and PAM-4 modulation versus the electrical SNR_{el} with numerically added noise for a fiber length of 100 m (a) and 220 m (b). Markers denote the performance with the noisy captured data.

Figure 5.17 shows the performance in terms of eye diagrams for the normal capture mode in the oscilloscope, which represents the actual performance of the experimental setup. Here a single shot with 10 MSamples was made, which translates into 2.5 million symbols.

In Fig. 5.17(a) the measured eye diagram for 100 m is shown. The eyes are still open, with some small lines, crossing the lower eye. This eye without equalization leads to a detected BER of $1.1 \cdot 10^{-4}$.

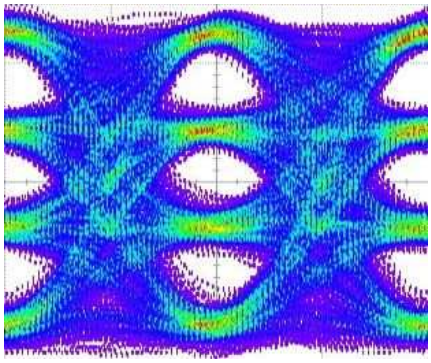

(a) before equalizer at a fiber length of 100 m (measured)

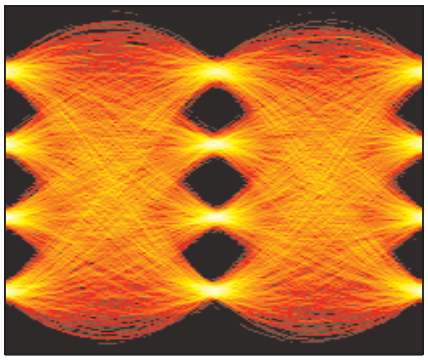

(b) after equalizer at a fiber length of 100 m (interpolated)

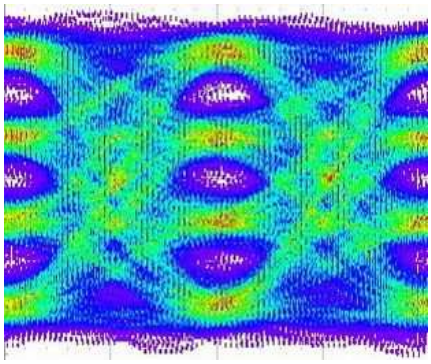

(c) before equalizer at a fiber length of 220 m (measured)

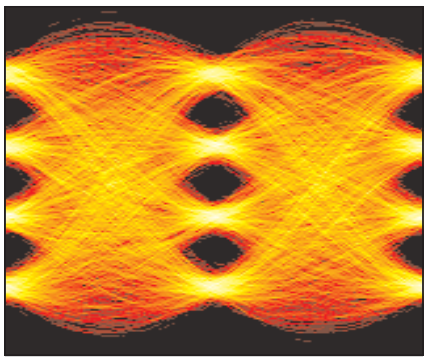

(d) after equalizer at a fiber length of 220 m (interpolated)

Figure 5.17: Measured eye diagrams at the receiver amplifier output for fiber lengths of 100 m (a) and 220 m (c) and simulated interpolated eye diagrams at the equalizer output (DFE 5,2) for fiber lengths of 100 m (b) and 220 m (d).

In Fig. 5.17(b) the interpolated eye diagram at the output of the DFE is depicted. Here, the eyes are much more open. In this equalized sequence no error could be counted for both equalizers. Fig. 5.17(c) shows the measured eye for 220 m. The eye is more or less closed, which results in a detected BER of $2.5 \cdot 10^{-3}$. In the last eye diagram (Fig. 5.17(d)), the interpolated equalizer output eyes for the DFE are plotted. The eyes are all quite open. Of course a little bit smaller than for 100 m, but still no error could be counted for both equalizers. This means that the BER is less than $1 \cdot 10^{-5}$. These BER

values are also depicted as markers in Fig. 5.16. The triangles represent the case without equalization, the squares the FFE, and the crosses the DFE, respectively. For the BER markers, which are plotted on the SNR_{el} axis, no error could be detected. The mismatch between the markers and the simulated curves can be due to the capture process within the oscilloscope. The clock of the transmitter and the sampling clock of the oscilloscope are not synchronized. This leads to a clock drift in the measured large data block. Another reason can be the averaging process, because it averages more than only the receiver noise. Nevertheless, the mismatches are not too big, except one point. Unfortunately, the experiment could not be repeated, because the measurement devices were not available any more.

Conclusion

Data transmission of 10 Gbit/s over 220 m PF-GI-POF with PAM-4 modulation and symbol-spaced equalization has been demonstrated. Even with a simple FFE with 5 taps, error-free transmission over 220 m is feasible. The reached fiber length corresponds to the required length in the new 10 Gbit-Ethernet standard 10GBase-LRM [iee06] for legacy multimode fiber links. Hence, this solution has the potential for low-cost implementation using a commercial VCSEL at 850 nm and a simple feed-forward equalizer with 5 taps. Additionally, this equalizer scheme can be implemented in the analog domain [Inc03], so no analog-to-digital conversion at the receiver is needed.

5.3.2 Comparison of OOK and PAM-4 for 10 Gbit/s over PF-GI-POF

This experiment makes a fair comparison between OOK and PAM-4 modulation for 10 Gbit/s transmission over 300 m PF-GI-POF. For this purpose, the analog transmission system setup of the previous sub-chapter (5.3) is used, which consists of a VCSEL, the PF-GI-POF and the analog receiver. This means that it is a peak driving current limited optical transmission system. Parts of this experiment were presented at the Optical Fiber Conference (OFC) 2008 [BLRH08a].

System Setup

The system setup is divided into two parts. In the experimental part the transmission of the PAM-4 or OOK modulated signal is measured and captured using a real-time digital sampling oscilloscope. The stored signals are used as input data for the simulation

part. There the BER performances of the two different modulation schemes and two equalization schemes are evaluated in a computer based simulation environment.
In Fig. 5.18 the experimental setup of the PF-GI-POF transmission system is depicted in the upper box. For the OOK signal generation a bit pattern generator produces a pseudo-random binary sequence of order 11 (PRBS 11). For the PAM-4 case, the driving signal is generated by an arbitrary waveform generator (AWG) with a sampling rate of 10 GSample/s. The waveform is pre-computed with a software tool. The PRBS 11 sequence is encoded in a 4-level signal with gray-coding. A rectangular impulse shaper is used to calculate the waveform, which is digital-to-analog converted inside the AWG with a symbol rate of 5 GSymbol/s and a bit rate of 10 Gbit/s.

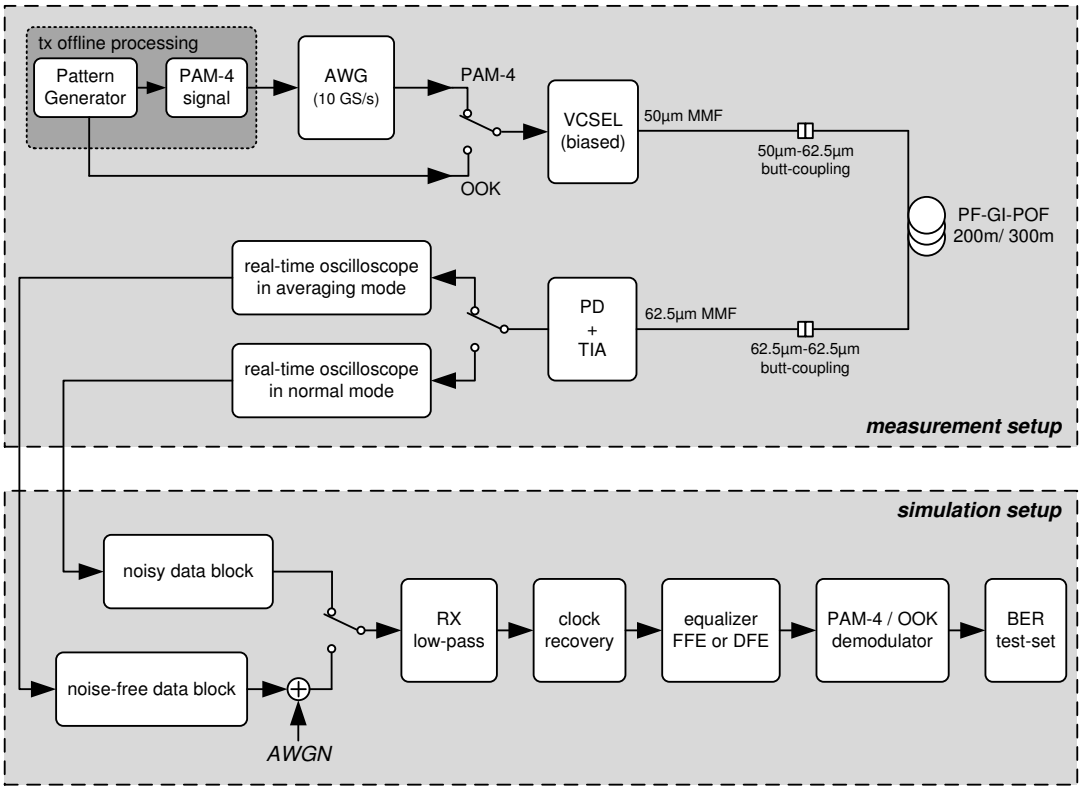

Figure 5.18: Experimental and Simulation setup for the 10 Gbit/s experiment with VCSEL and OOK or PAM-4 modulation in combination with fractionally-spaced receiver equalization.

A directly-modulated commercial 850 nm multimode vertical cavity surface emitting laser (VCSEL) with an average optical output power of 1 dBm and an extinction ratio of 4.5 dB is used for electro-optical conversion. This optical signal is launched into a 50 μm silica

multi-mode fiber (MMF) patch cord. The PF-GI-POF is butt-coupled to this patch cord. The PF-GI-POFs used in this experiment are commercial fibers with 62.5 μm core-diameter and 500 μm total diameter including cladding. The attenuation of this fiber at a wavelength of 850 nm is approximately 40 dB/km. At the receiver side a 62.5 μm silica MMF patch cord is used to couple the light into a 62.5 μm pigtailed GaAs-PIN detector with integrated trans-impedance amplifier (TIA) with a noise-equivalent power (NEP) of 60 pW/$\sqrt{\text{Hz}}$.
The electrical signal is captured using a real-time digital sampling oscilloscope with a sampling rate of 20 GSample/s. This oscilloscope operates in two different modes. The averaging mode is used to get a nearly noise-free signal (noise-free data block) by averaging 1000 waveforms. This is possible because the transmitted sequences are cyclic ones. The normal mode captures one shot of the received electrical signal (noisy data block).
The lower box in Fig. 5.18 shows the simulation setup for the BER performance evaluation of the transmission system. The nearly noise-free captured data is used to do Monte Carlo simulations. Therefore the signal-to-noise power ratio $\text{SNR}_{\text{el}} = E_s/N_0$ is varied by adding numerically additive white Gaussian noise (AWGN). To verify the simulations and to get the real performance of the experimental setup the noisy captured data is used.
For both cases the identical receiver structure is used. First the signal is filtered using a 5th order Bessel low-pass with a 3 dB bandwidth of 0.75·symbol rate. Afterwards a clock recovery and down sampling stage is used to sample the signal at twice the symbol rate. The down sampled signal is fed into the fractionally-spaced feed-forward equalizer (FFE) or decision-feedback equalizer (DFE). In this experiment, the FFE has 24 $T/2$-spaced taps and the DFE has 18 $T/2$-spaced forward and 3 T-spaced feedback taps. The equalizer coefficients are calculated with the least-mean square (LMS) adaptation algorithm. The equalizers are first trained with a training sequence and afterwards they are switched to the decision-directed mode (see chapter 4.5).

Results and Discussion

The BER performance simulation is carried out by applying the Monte Carlo approach and by transmitting 5 million bits. Therefore, the measured signal captured in average mode is used. The results are shown in Fig. 5.19 for OOK with fiber lengths of 200 m (a) and 300 m (b), and for PAM-4 with fiber lengths of 200 m (c) and 300 m (d). The optical received power is -7.4 dBm and -11.7 dBm for 200 m and 300 m, respectively.
The blue solid lines with dots represent the matched filter bounds for OOK and PAM-4 modulation. The green dashed dotted lines stand for the case without equalization. For all four cases no error-free transmission is possible without equalization because of the bandwidth limitation due to modal dispersion.

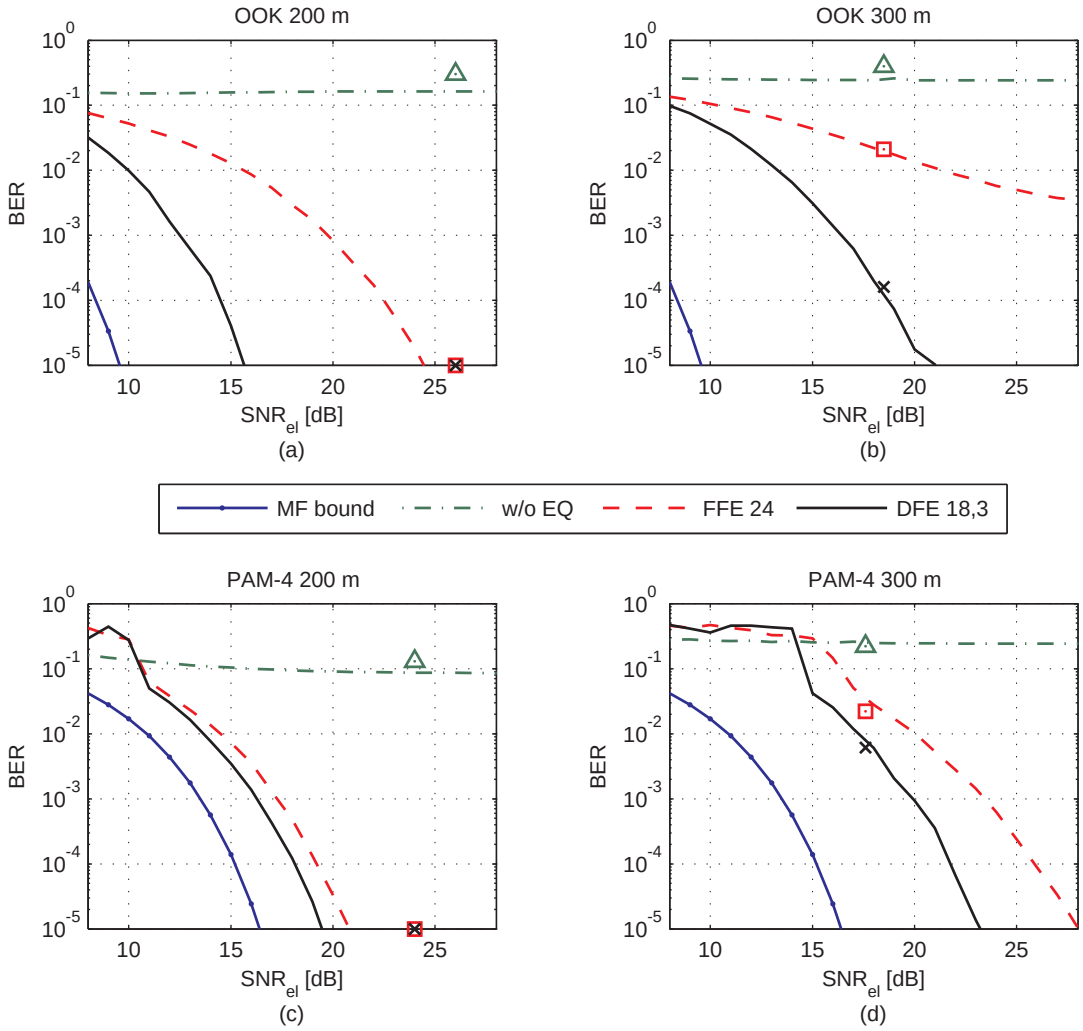

Figure 5.19: BER performance for a data rate of 10 Gbit/s and $T/2$-spaced FFE 24 and DFE(18,3) versus $\mathrm{SNR_{el}}$ with numerically added noise for OOK and fiber lengths of 200 m (a) and 300 m (b), and for PAM-4 and fiber lengths of 200 m (c) and 300 m (d). Markers denote the performance with the noisy captured data.

The performance of the FFE with 24 $T/2$-spaced taps is represented with the red dashed lines. The black solid lines stand for the DFE with 18 $T/2$-spaced forward and 3 feedback taps.

For a target BER of $1 \cdot 10^{-4}$, the $\mathrm{SNR_{el}}$ penalty with respect to the matched filter bound for OOK and a fiber length of 200 m is 14.1 dB and 6.1 dB for the FFE and the DFE, respectively. For 300 m the FFE is not able to reach the target BER. The DFE has a

SNR_{el} penalty of 10.3 dB. In the PAM-4 case the SNR_{el} penalties are 4 dB and 2.9 dB, and 10.6 dB and 6.5 dB for FFE and DFE at fiber lengths of 200 m and 300 m, respectively. Thus the inter-symbol interference (ISI) of the PAM-4 signal can be better compensated than the ISI from OOK, due to the smaller bandwidth demand of the PAM-4 signal.
Comparing the modulation formats, PAM-4 has a SNR_{el} penalty of approx. 3 dB at target BER of $1 \cdot 10^{-4}$ to OOK. If this penalty is transferred in an equivalent optical receiver sensitivity penalty, it is 1.5 dB. The theoretically derived optical penalty of PAM-4 to OOK is 3.27 dB, which was derived in chapter 4.3. Thus, this penalty has been decreased to approx. half. Nevertheless, OOK outperforms PAM-4 modulation for this system setup running at 10 Gbit/s.
To verify the simulation results and to get figures of merit of the actual performance of the experimental setup with noisy data, the BER values and the corresponding SNR_{el} values for the two equalizers are summarized in Tab. 5.4.

	OOK 200 m	OOK 300 m	PAM-4 200 m	PAM-4 300 m
SNR_{el}[dB]	26	18.5	24	17.6
BER [FFE 24]	$< 10^{-5}$	$2.1 \cdot 10^{-2}$	$< 10^{-5}$	$2.2 \cdot 10^{-2}$
BER [DFE 18,3]	$< 10^{-5}$	$1.6 \cdot 10^{-4}$	$< 10^{-5}$	$6.1 \cdot 10^{-3}$

Table 5.4: BER values after equalization with noisy data.

The performance of the DFE is visualized with interpolated eye diagrams at the equalizer output. In Fig. 5.20 interpolated eye diagrams for the four cases are plotted as follows: OOK at 200 m (a), OOK at 300 m (b), PAM-4 at 200 m (c), and PAM-4 at 300 m (d). Additionally the BER values, calculated with the noisy data, are depicted in Fig. 5.19 as markers: triangles for without equalization, squares for FFE, and crosses for DFE.
At a fiber length of 200 m the equalized eyes for OOK and PAM-4 are clearly open and no errors could be counted within 2.5 million transmitted bits. At 300 m with OOK and DFE, a BER of $1.6 \cdot 10^{-4}$ was detected. With PAM-4 and DFE, the BER was $6.1 \cdot 10^{-3}$. The measured SNR_{el} values of the two modulation formats differ by 2 dB and 0.9 dB for 200 m and 300 m, respectively. This is due to the higher crest factor of PAM-4, which is 2.55 dB higher in theory than the crest factor of OOK. In the transmitter the optical modulation amplitude (OMA) is the same for both modulations, but the electrical power of the DC-free driving signal in the PAM-4 case is 2.55 dB lower than the power of the OOK signal.

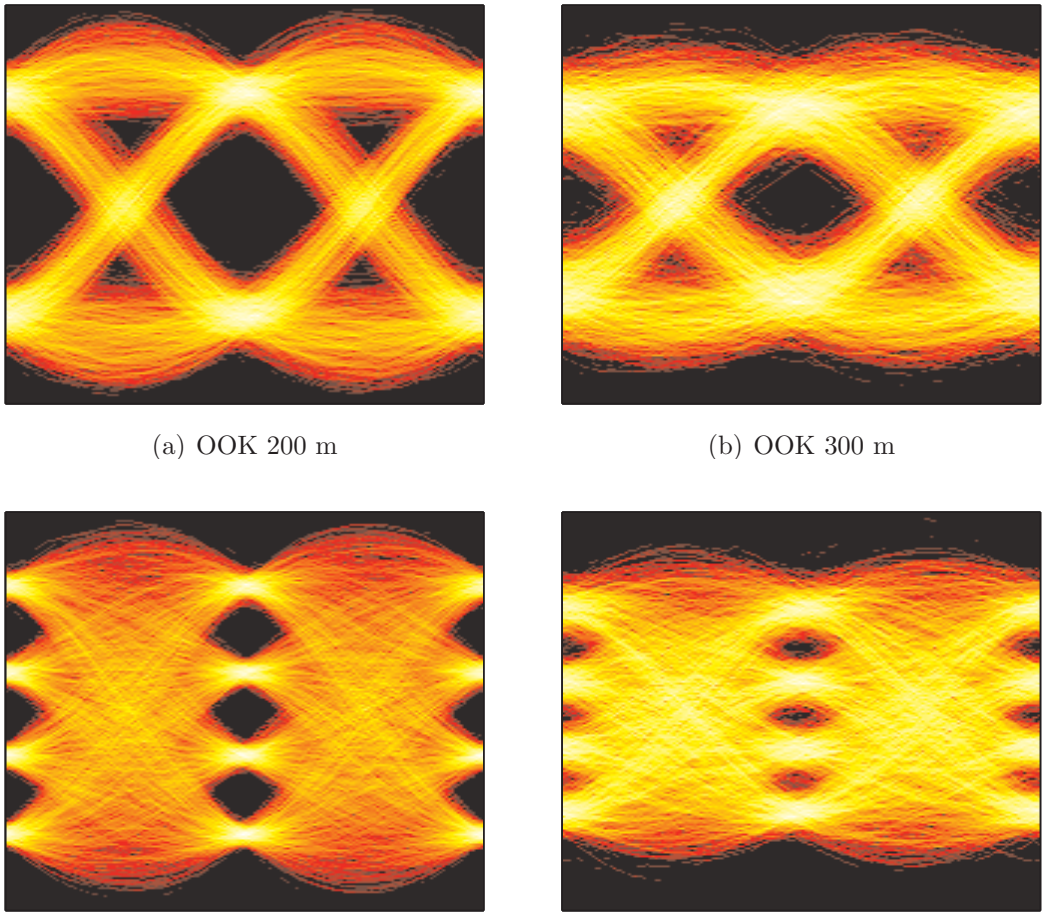

(a) OOK 200 m (b) OOK 300 m

(c) PAM-4 200 m (d) PAM-4 300 m

Figure 5.20: Eye diagrams (interpolated) after equalization (DFE 18,3) with noisy sampled data (no numerical noise addition) for fiber lengths of 200 m and OOK (a), 300 m and OOK (b), 200 m and PAM-4 (c) and 300 m and PAM-4 (d).

Conclusion

10 Gbit/s transmission over up to 300 m PF-GI-POF has been demonstrated using OOK and PAM-4 modulation in combination with decision-feedback equalization. The OOK modulation has a larger noise tolerance compared to PAM-4 modulation at the expense of a higher bandwidth demand in the active components and the analog-to-digital (ADC) converter in the receiver. To realize an error-free transmission over 300 m PF-GI-POF, both modulation schemes need a receiver with better sensitivity than the used one in the experiment (see Tab. 5.4). PAM-4 is attractive due to the more relaxed requirements on the bandwidth (active components) and the speed of receiver electronics, but a linear

driving circuitry in the transmitter is required. Thus, a trade-off has to be made between a linear transmitter for PAM-4 or double the speed of the receiver electronics for OOK. To summarize these results, both modulation formats have benefits. A decision for the better one can only be done if more information about the active components and the environmental specifications, such as power consumption or maximum footprint size, is available.

5.4 Summary

In this chapter it was demonstrated that multilevel PAM in combination with digital receiver equalization can be used to compensate both the bandwidth limitation of the POF channel due to modal dispersion and the bandwidth limitations of the transmitter components, e.g. of RC-LEDs.
With a laser launched SI-POF system, it was experimentally demonstrated that error-free 1.25 Gbit/s transmission over 100 m of PMMA SI-POF is possible with OOK and a decision feedback equalization at the receiver. Further, it has been shown that the transmission of 2 Gbit/s over 100 m SI-POF is also possible using a very large DFE. All these results are achieved using a low-cost DVD laser diode at a wavelength of 655 nm.
Even by using a low-cost resonant-cavity LED at 650 nm, error-free transmission of 1.25 Gbit/s over up to 50 m SI-POF was demonstrated by using PAM-4 modulation in combination with a blindly adapted fractionally-spaced decision feedback equalizer. Even for longer fiber lengths, error-free transmission is feasible, if the receiver noise is decreased. Recent results have shown, that this is possible by designing new Opto-Electronic Integrated Circuits (OEIC), in which the photo diode and the trans-impedance amplifier (TIA) are integrated on the same wafer [AGSZ09, ASZ09], which results in a much better matching between photo diode and amplifier stage and finally leads to less receiver noise. Concluding so far, the combination of PAM-4 and receiver equalization is a promising solution for low-cost Gigabit-Ethernet transmission over SI-POF based on LED technology. Of course, if the environment can handle the requirements of using a laser diode, error-free Gigabit-Ethernet transmission can be achieved using OOK and receiver equalization. Hence, simple state-of-the art digital driving circuitry can be used.
For transmission of 10 Gbit/s over longer distances of up to 300 m, the PF-GI-POF is a promising alternative to the commonly used silica multimode fibers. The benefits are the easier handling and the robustness in terms of bending radii and mechanical stress. 10 Gbit/s transmission was demonstrated using PAM-4 and OOK as modulation scheme in combination with decision feedback equalization for the 300 m long fiber.
The question which modulation format should be used for the 10 Gbit/s PF-GI-POF

system, can not be answered directly. The performance of both modulation formats is very similar, so a trade-off between complexity in the transmitter for PAM-4 or even higher complexity in the receiver for OOK has to be found, based on implementation requirements. As silica based MMF links according to the IEEE 10Gbase-LRM standard [iee06] have an electronic dispersion compensation element at the receiver, the complexity of a PF-GI-POF solution is not much higher. But the transmission medium is much more robust, as mentioned before. Therefore, the PF-GI-POF could become a promising alternative to silica based MMFs.

6

Real-Time Implementation Aspects of Gigabit Ethernet over SI-POF

This chapter gives a final overview about the implementation of a fully working real-time Gigabit-Ethernet SI-POF based media converter. It was realized by using a field programmable gate array (FPGA) platform for the digital signal processing and appropriate analog driving and receiving circuitries. This demonstrator applies the foregoing chapters of this thesis, in which theoretical investigations were followed by the proof of concept based on experiments applying offline processing, by realizing a full working Gigabit Ethernet media converter, which can be plugged into any Gigabit Ethernet connection.
This chapter is organized as follows: first the custom made FPGA platform and the analog front-end are described. Then some implementation issues are discussed concerning the realization of the digital signal processing algorithms on the FPGA platform. Afterwards the complexity of these algorithms are discussed in terms of usage of resources. Finally measurement results in terms of BER performance of the transmission system are presented.

6.1 Prototyping Platform - FPGA DSP board

At the time the decision was made to construct a real-time demonstrator for the transmission of Gigabit Ethernet over SI-POF using LEDs, no FPGA based evaluation board was available which satisfied the requirements. One special feature of the platform should be a tunable clock source on the receiver side to implement a clock recovery. However, conventional FPGA boards provide only one central reference clock source, which all different chips on the board use as reference clock. Thus a clock recovery or in other words the tracking of another reference clock source could not be implemented on such a FPGA board.
Therefore, a custom-made FPGA board was designed for this demonstrator. The basic components, which are needed to construct the demonstrator with the approach of using multilevel modulation in combination with receiver equalization, are depicted in Fig. 6.1.

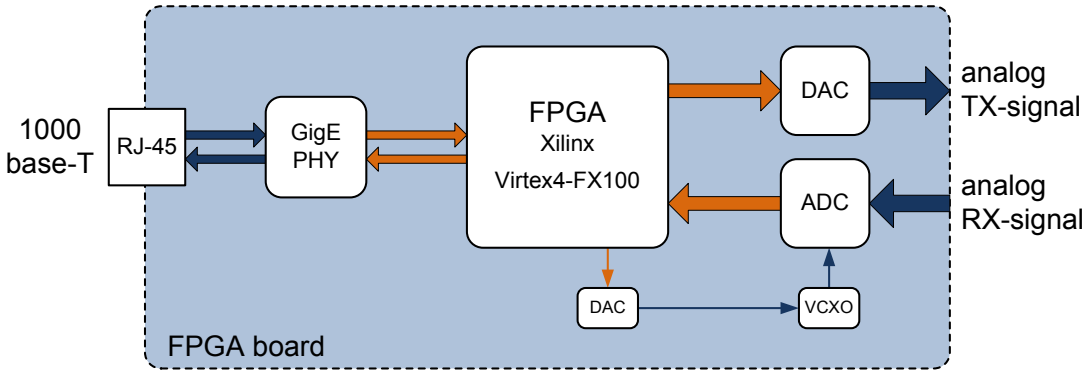

Figure 6.1: Block diagram of the custom made FPGA board.

On the left side a RJ-45 connector connects the board to a conventional copper based Gigabit Ethernet interface (1000base-T). A Gigabit Ethernet physical layer chip (GigE PHY) from Marvell (MV88E1111) terminates the copper based interface and converts the Gigabit Ethernet signal into a 8B10B coded continuous serial stream with a data rate of 1.25 Gbit/s (1000base-X). This serial stream is terminated inside the FPGA in the so-called RocketIO, which is a serial transceiver supporting a variety of communication standards. Within the FPGA, which is a Xilinx Virtex-4FX100, all the signal processing for the transmitter and receiver chains is done, including forward error correction, modulation, equalization, clock recovery and all kinds of required signal conditioning to guarantee an error-free transmission. On the transmitter side an Analog Devices AD9736 DAC is used, with a maximum sampling rate of 1200 MHz and a vertical resolution of 14 bits, to

produce the analog bipolar modulation signal (analog TX-signal). On the receiver side a National Semiconductor ADC08D1500 ADC is used with a maximum sampling rate of 3000 MHz and a vertical resolution of 8 bits to capture the received signal. For the clock recovery, which is built as a hybrid phase-locked-loop (PLL), a slow DAC with a sampling rate of 1 MSample/s is used to produce the tuning voltage for a voltage-controlled crystal oscillator (VCXO), which generates the sampling frequency of the ADC. In this block diagram all orange arrows represent digital interfaces, whereas the dark blue ones represent analog interfaces.

Fig. 6.2 shows a picture of the custom-made FPGA board. In the center the Virtex-4FX100 is placed, two DACs (AD9736) are placed to the right and the ADC (ADC08D1500) is placed next to the upper left corner of the FPGA. The Gigabit Ethernet PHY chip (MV88E1111) is located next to the lower left corner of the FPGA. All the other components are supplementary, for example power supply, configuration switches, and debugging interfaces.

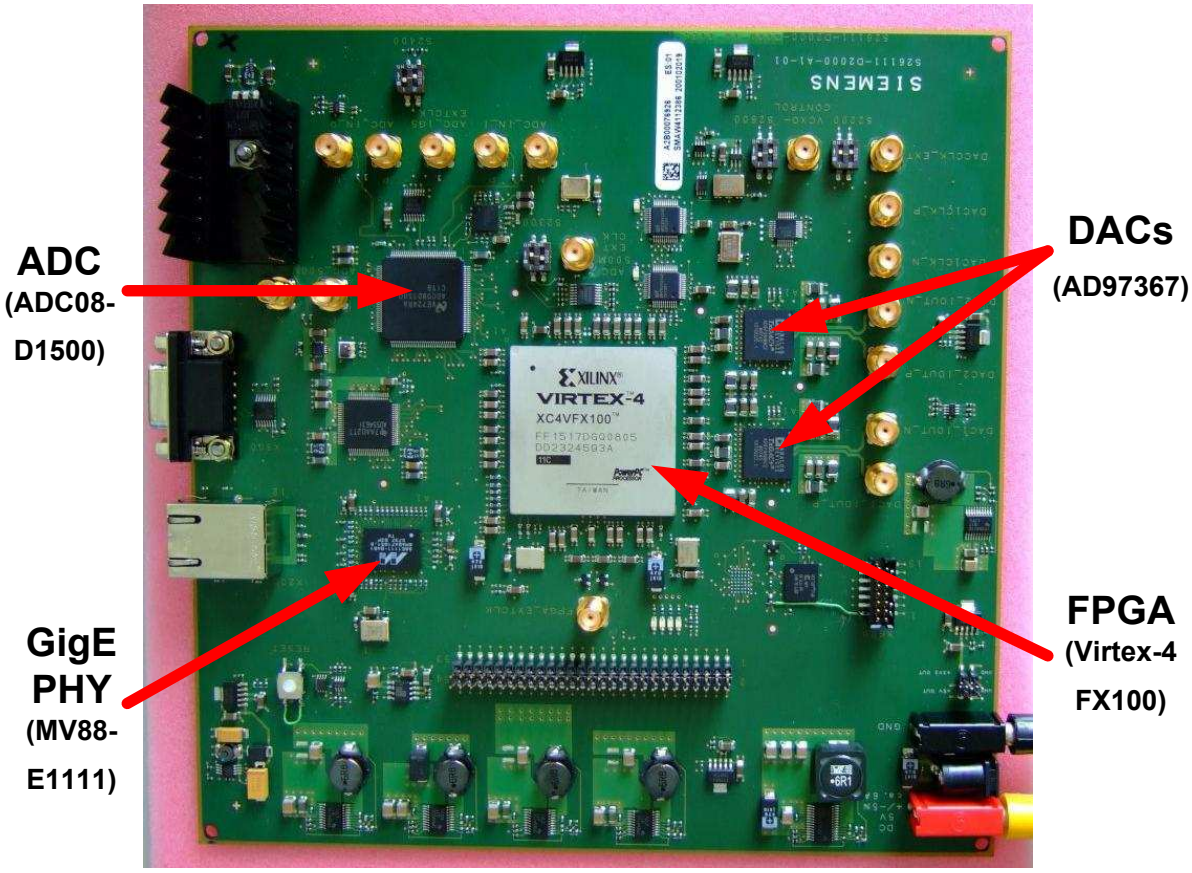

Figure 6.2: FPGA based Digital Signal Processing evaluation board.

6.2 Analog Frontend

As no linear driver circuits were available to drive a LED in the required way and no receiver circuitry was available to receive the analog signal and amplify it to a level, which met the special requirements for the FPGA board introduced in chapter 6.1, also a custom made analog front-end board was designed. Fig. 6.3 shows the third version of the analog front-end, which was developed in the framework of this thesis. The upper part is the receiver chain (RX-path), the transmitter chain is in the middle (TX-path), and the circuitry in the lower part of the AFE is just for power supply. On this version of the AFE the optical components are mounted in a standard MOST housing (depicted on the right side).

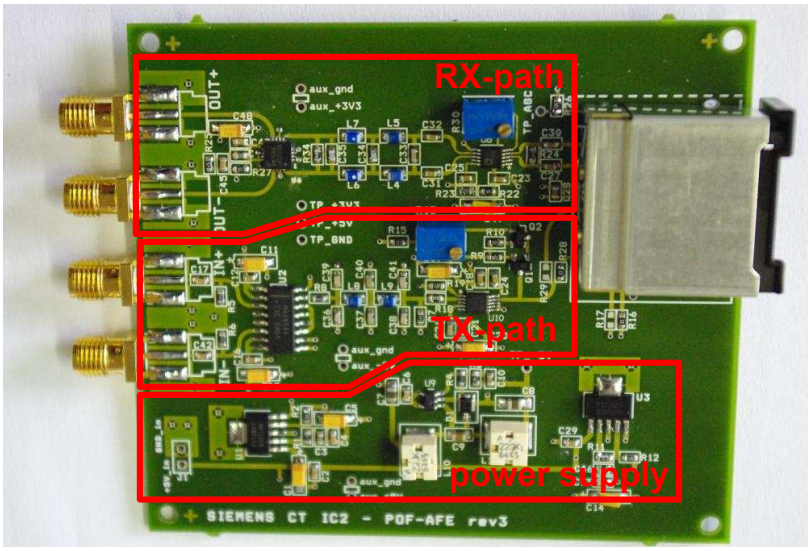

Figure 6.3: Analog front-end PCB board.

The conceptual schematic of the linear LED driving circuit is shown in Fig. 6.4. The driving current I_{drive} is generated separately for the modulation and the bias current. The bias current is controlled by bipolar transistors and can be adjusted with a current mirror (upper part of the schematic). The modulation current is generated from the output signal of the DAC of the FPGA board. Therefore, it first has to be converted into a voltage signal and then from its differential signaling to a single-ended voltage signal. For simplicity reasons, these components are not depicted in the conceptual schematic below. The analog single-ended modulation voltage signal has to be converted once more into a bipolar current signal. Using an operational transconductance amplifier (OTA - OPA615), which is sometimes also called "ideal transistor", this linear bipolar voltage-

to-current conversion could be realized. This OTA is called ideal transistor, because it can source and sink the same amount of current by maintaining a high impedance, which approximates the ideal current source very well. Thus the sum of the modulation current and the bias current flow through the LED, because both current sources have a high impedance, whereas the LED has a low impedance.

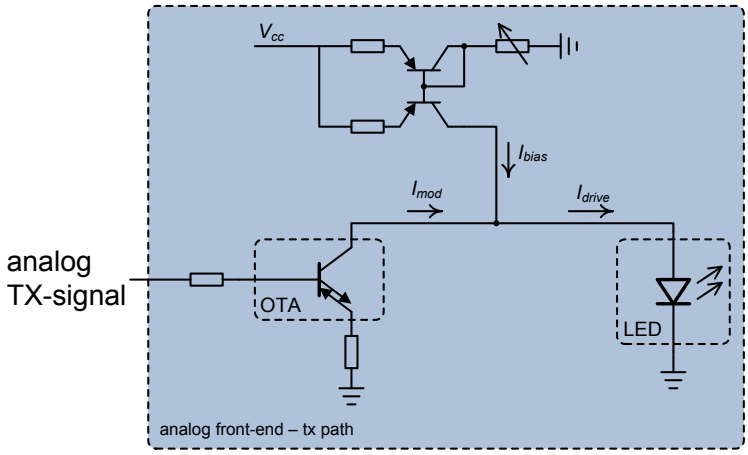

Figure 6.4: Conceptual schematic of the LED driver on the analog front end.

The LED itself has a more or less linear current-to-optical power conversion characteristic, so the linearity of this driving circuitry was achieved by driving the LED with a current signal. This means that the OTA pushes the modulation current through the LED, because the OTA approximates a voltage-controlled ideal bipolar current source. This behavior results in a kind of peaking and clamping of the LED, which is a commonly used method to decrease the rise and fall times of a digital optical modulator.
In Fig. 6.5 the conceptual schematic of the receiver chain is shown. A silicon photo diode with an active area diameter of 540 μm captures the optical signal. The trans-impedance amplifier (TIA - TZA3026) is integrated into an optical subassembly. The TIA has an automatic gain control (AGC) with peak detector, thus it is optimized for the transmission of OOK.

The TIA output signal is differential and has to be amplified once more, because the output level of the TIA is not high enough. Further the integrated AGC in the TIA does not provide a really constant output level, especially if a distorted PAM-4 signal is the input. Thus, the second amplifier stage has to be a variable gain amplifier (VGA - AD8351) to control manually the output peak-to-peak level, which is finally amplified with a buffer amplifier (BA - LMH6555). This buffer amplifier is the preferred input amplifier stage of the used ADC08D1500 on the FPGA board. Thus the output signal of

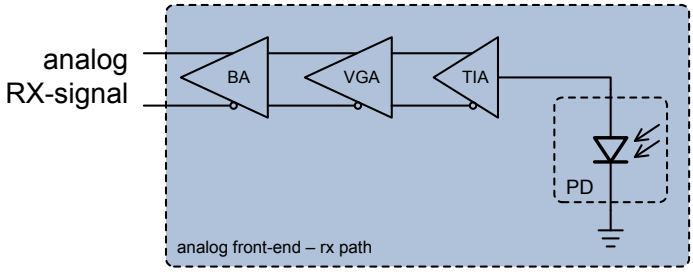

Figure 6.5: RX amplifier stages - analog front end.

the LMH6555 is the analog input RX-signal (see Fig. 6.1).
In Fig. 6.6 the performance of the analog front-end is depicted in terms of the transfer function and of the eyediagram of a 900 Mbit/s OOK-modulated signal, transmitted by using the AFE and a fiber length of 1 m. The transfer function has a 6-dB attenuation frequency of approx. 400 MHz, which is the result of the good current driving capabilities of the OTA. If the LED is driven with a voltage signal, then the 6-dB frequency is only 117 MHz for comparison, so the designed LED driver does really a very good job.

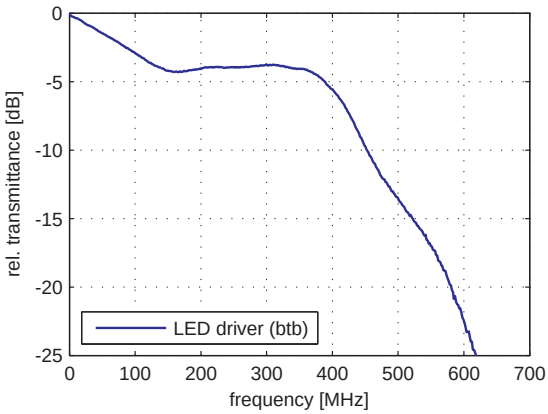

(a) Transfer function of the optical back-to-back setup

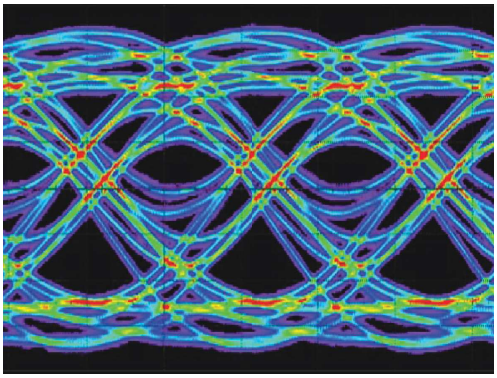

(b) Eye diagram for 900 Mbit/s OOK for the optical back-to-back case

Figure 6.6: Transfer function of the analog front-end (LED driver and receiver) in the optical btb case (1 m fiber) (a); Eye diagram for 900 Mbit/s transmission using OOK and the analog front-end (b).

The steep decay of the transfer function is due to the bandwidth limitations of the used amplifiers on both sides, the transmitter and receiver side. But this effect is intended, because this AFE is designed for the transmission of a PAM-4 signal with a symbol rate

of 625 MSymbol/s, thus this bandwidth is sufficient to recover the signal and is beneficial to limit the noise contribution.
On the right side of Fig. 6.6 an eye diagram is shown for a test transmission of 900 Mbit/s using OOK-modulation and the analog front-end with a fiber length of 1 m. The bandwidth limitation of the transfer function can be seen as a large number of inter-symbol interference lines in the eye diagram. However, these lines are thin and each of them can be differentiated, which is an indication of the good signal-to-noise ratio (SNR).

6.3 DSP implementation inside the FPGA

This chapter deals with implementation issues of the proposed digital signal processing, which was described in the previous chapters, such as PAM-4 modulation, receiver equalization, and clock recovery. One of the challenging facts is that with a maximum achievable DSP clock speed of 450 MHz, a bitrate of 1.25 Gbit/s and a PAM-4 symbol rate of 625 MSymbol/s, almost all of the functionalities have to be parallelized. Further, additional signal processing has to be done if a real data traffic has to be transmitted, because transmission of Gigabit Ethernet (1000base-X) is something completely different than transmitting just a PRBS sequence. The solution for this problem is discussed in the next sub-chapter. Afterwards the equalizer implementation is discussed. A parallelization of factor 4 and register pipelining is applied to realize the required signal processing speed. Then one of the most critical components in a real-time system is introduced, the clock recovery. This is implemented by using a hybrid PLL structure. Finally, the inclusion of forward error correction (FEC) is presented, which does not require additional redundancy, because the overhead of the FEC can be inserted in the overall redundancy of the line code.

6.3.1 Line Coding for PAM-4 modulation

Line Coding is normally used for certain purposes such as spectral shaping characteristics, DC-balancing, error detection, limitation of the number of same symbols and so on. The input data stream for the FPGA demonstrator is a 8B10B encoded [WF83] Gigabit-Ethernet stream. This code is based on look-up tables and has the comfortable properties of being DC-balanced and digital run-length limited, i.e. the number of successive identical symbols is limited. Furthermore, the side-band information for Ethernet, such as ”start of packet”, ”end of packet”, ”idle symbols”, and ”inter-frame gaps” is included in this serial stream. Thus, from a physical layer perspective, only a bit stream has to be transmitted because the sideband informations of the GMII interface are included in the

serial stream.
The first approach to the line coding for the PAM-4 transmission was a simple mapping of 2-bit groups of one 10-bit word into 5 PAM-4 symbols, resulting in a symbol stream of 625 MSymbol/s. Thus the benefit of the inclusion of the side band information can be maintained. The DC-balancing can be roughly conserved as well as the digital run-length limitation. Thus, this line coding looks very good, but the adaptive MMSE-based equalizer does not converge. This is due to the fact that if the Gigabit Ethernet medium access (MAC) layer detects no connection only the auto negotiation sequence is transmitted, which is a repetitive sequence of 80 bits. For details about this sequence and the 8B10B code, it is referred to appendix B.
Thus at the beginning, when the equalizer has not converged yet, the data input signal consists of 80 bits or 40 symbols, which are repeated. As a blindly adapted equalizer needs ideally a white random sequence as input for convergence, this idle sequence has definitely not the required randomness for the convergence.
In order to get this required randomness, even if only "idle symbols" or the auto negotiation sequence are transmitted, a scrambler on symbol level is applied. Therefore a self-synchronizing scrambler is used to avoid any synchronization efforts in the descrambler of the receiver part. Fig. 6.7 shows the parallel implementation of a scrambler on PAM-4 symbol level, which is in principle the addition of taps of a shift register.

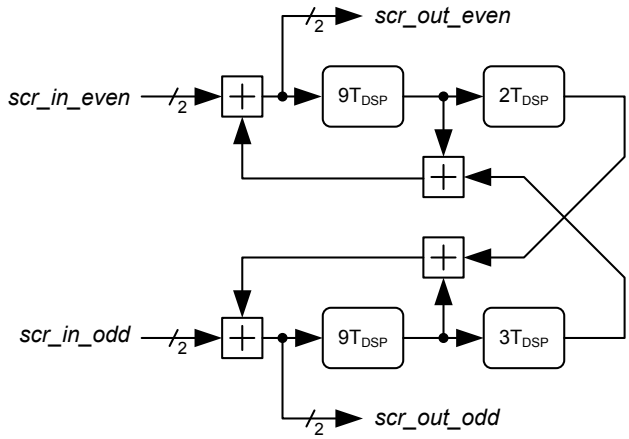

Figure 6.7: Implementation of a self-synchronizing scrambler with parallelization of 2, running at T_{DSP} =3.2 ns (312.5 MHz) with the scrambling polynom $1 + x^{18} + x^{23}$. The additions are modulo-4 additions.

The taps, which are summed up, can be described with primitive polynomials. In this case the scrambling polynomial is $1 + x^{18} + x^{23}$, thus three taps are added to calculate

the output symbol. All the additions are modulo-4 additions and the DSP clock period is T_{DSP} =3.2 ns (312.5 MHz). Thus, these boxes named for example $9T_{\mathrm{DSP}}$ are delay elements with a delay of multiples of T_{DSP}. In this example the data is delayed by nine clock cycles. The In- and Output ports are named with suffixes 'even' and 'odd', which represent the two parallel processed symbols, which are transmitted serially.
The result of the scrambling process is a DC-balanced signal, which has sufficient randomness for the convergence of the equalizer at the receiver.
On the receiver side, a descrambler has to be established to get the original 10bit words back. The parallelized self-synchronizing descrambler is depicted in Fig. 6.8.

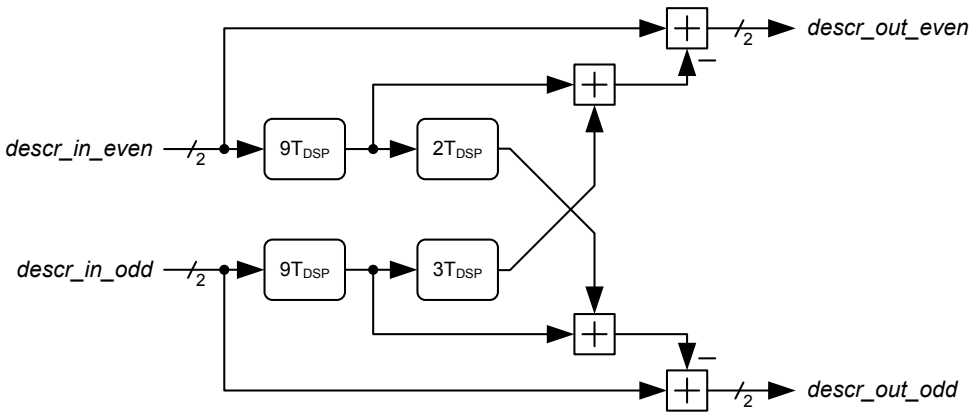

Figure 6.8: Implementation of a self-synchronizing descrambler with parallelization of 2, running at T_{DSP} =3.2 ns (312.5 MHz) with the scrambling polynom $1 + x^{18} + x^{23}$. The additions are modulo-4 additions.

All additions and subtractions used for descrambling are modulo-4 operations. This descrambling algorithm does not need any start phase or synchronization, which is very beneficial in terms of simplicity for the implementation. Further no additional overhead has to be transmitted. However, the big disadvantage of such a self-synchronizing descrambler scheme is the error multiplication. When an error occurs on the input of this descrambler, three symbols at the output are affected, because the descrambler has to invert the scrambler operation, which is the modulo-4 addition of three taps. Thus each error at the input of the descrambler leads to three errors at the output. This error multiplication property can be avoided, if an additive scrambling scheme is used. However, this scheme is not self-synchronizing and has therefore not been used in this demonstrator.

6.3.2 Parallelization of FFE equalizer

As mentioned before, the digital signal processing clock runs at 312.5 MHz or with a clock period of T_{DSP} =3.2 ns. The implemented equalization scheme is a $T/2$ fractionally-spaced FFE, which means that the input sample rate is 1.25 GSample/s. As a result, the equalizer structure has to process 4 input samples in each clock cycle. To achieve this, the equalizer is parallelized by a factor of 4. Additionally the complete DSP structure has to be pipelined. These two implementation related mechanisms are explained in the following sub-chapter. This parallelized and highly pipelined equalizer core structure also affects the coefficient adaption process, which is discussed afterwards.

Parallelization of the FFE filter core

To derive the parallel FFE architecture according to [ES07], first the output z_k of the non-parallel FFE with L coefficients and the coefficient vector $[c_0, c_1, \ldots, c_{L-1}]$ is considered, which writes as

$$z_k = \sum_{i=0}^{L-1} c_i \cdot y_{k-i}, \tag{6.1}$$

where y_k is the input data with time index k. Fig. 6.9 shows the structure of a non-parallel FIR structure with 4 taps as an example.

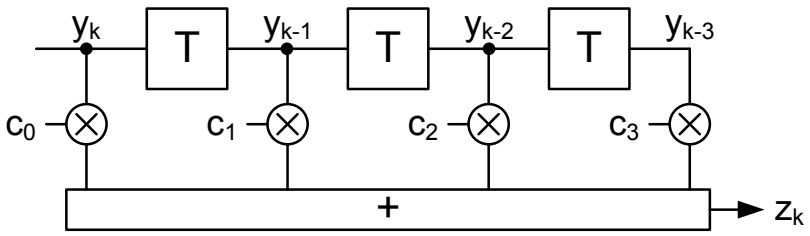

Figure 6.9: Serial FIR structure with 4 taps.

The first step to decrease the hardware clock speed by a factor of M is to split up the in- and output stream y_k and z_k into M different substreams y_{Ml-m} and z_{Ml-m} in the temporal grid $M \cdot T$ with $m = 0, \ldots, M-1$ being the substream index. Thus, the in- and outputs are becoming a vector of samples with length M. A new index l is introduced, which is related to the former index k by $l = k/M$. l, k, and M must be integer values.

Thus, the output substream with index m of the parallel filter can be written as

$$z_{Ml-m} = \sum_{i=0}^{L-1} c_i \cdot y_{Ml-m-i} \quad \text{for} \quad m = 0, \ldots, M-1. \tag{6.2}$$

Fig. 6.10 shows the first step for the parallelization by a factor M of the FIR filter in Fig. 6.9, according to Eq. (6.2).

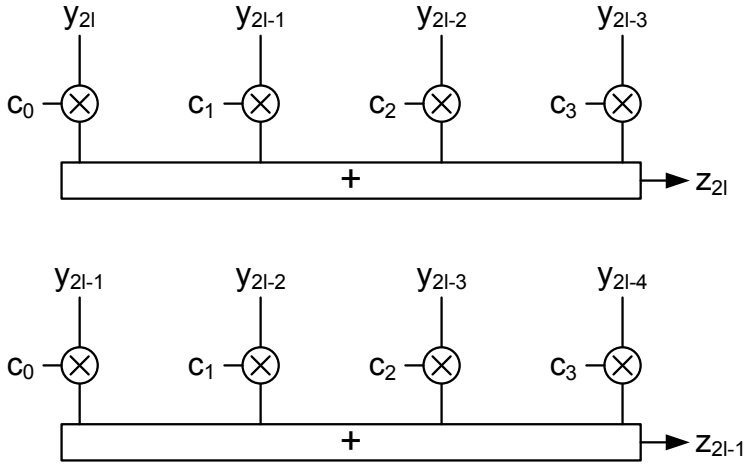

Figure 6.10: First step for the parallelization of a FIR structure with 4 taps and $M = 2$.

A parallelization by a factor of M results in the minimum delay of a delay element being $M \cdot T$. As it is depicted in Fig. 6.10, no delay elements are there anymore. Thus, to get back to tapped delay lines as basic elements in a FIR filter, the right-hand side of Eq. (6.2) can be rearranged by replacing the sum index i by $Mj - n$. This leads to the convolution being split up into M parts with respect to the M input substreams $y_{Ml-m-Mj-n}$ for $(m, n = 0, \ldots, M-1)$. Inserting these new indices into Eq. (6.2) results in

$$\begin{aligned} z_{Ml-m} &= \sum_{n=0}^{M-1} \sum_{j=0}^{L_n-1} c_{Mj+n} \cdot y_{Ml-m-Mj-n} \\ &= \sum_{j=0}^{L_0-1} c_{Mj+0} \cdot y_{Ml-m-Mj-0} + \sum_{j=0}^{L_1-1} c_{Mj+1} \cdot y_{Ml-m-Mj-1} + \ldots \\ &+ \sum_{j=0}^{L_{M-1}-1} c_{Mj+(M-1)} \cdot y_{Ml-m-Mj-(M-1)} \\ &\text{for} \quad m = 0, \ldots, M-1 \quad \text{and} \quad n = 0, \ldots, M-1 \\ &\text{with} \quad L_n = L \; div \; M + \begin{cases} 1 & \text{if} \quad n < (L \bmod M) \\ 0 & \text{if} \quad n \geq (L \bmod M) \end{cases} . \end{aligned} \tag{6.3}$$

The *div* function is an integer division and the *mod* function means the modulo function. The final parallelized structure for the FIR filter depicted in Fig. 6.9 for a parallelization factor of $M = 2$ is shown in Fig. 6.11.

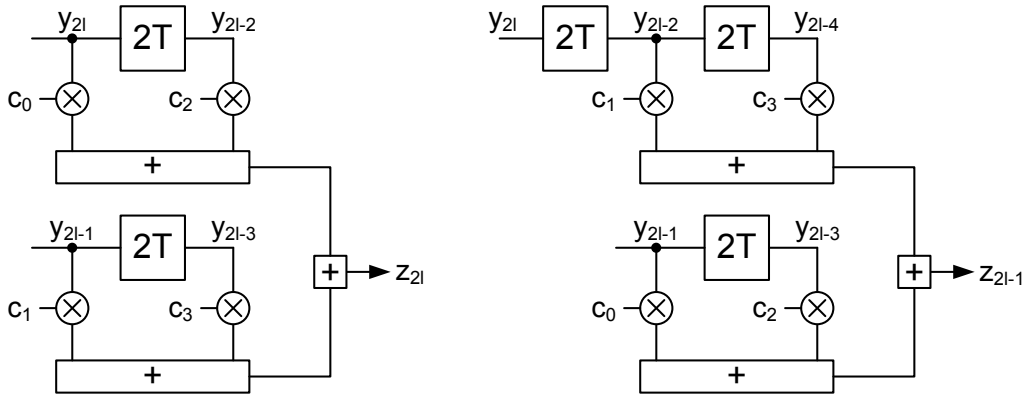

Figure 6.11: Final step for the parallelization of a FIR structure with 4 taps and $M = 2$.

Eq. (6.3) can be transferred to a compact vector notation:

$$z_{Ml-m} = \vec{c}_0^T \cdot \vec{y}_{Ml-m,0} + \vec{c}_1^T \cdot \vec{y}_{Ml-m,1} + \ldots + \vec{c}_{M-1}^T \cdot \vec{y}_{Ml-m,(M-1)}$$

$$\text{with} \quad \begin{aligned} \vec{c}_n &= [c_n, c_{M+n}, \ldots, c_{M(L_n-1)+n}]^T \\ \vec{y}_{Ml-m,n} &= [y_{Ml-m-n}, y_{Ml-m-M-n}, \ldots, y_{Ml-m-M(L_n-1)-n}]^T. \end{aligned} \tag{6.4}$$

Eq. (6.4) and Fig. 6.11 give further insight into the real structure of a parallel FIR filter implementation. Each vector multiplication in Eq. (6.4) represents a small subfilter in Fig. 6.11. Thus one output substream can be calculated by adding the outputs of subfilters, which use parallel input vectors $\vec{y}_{Ml-m,n}$. If all these input vectors are available at one specific time instance, all parallel output substreams can be calculated. Thus, this parallel structure of the FIR filter is identical to the serial structure differing only in the smaller signal processing clock speed.

For the POF media converter, a fractionally-spaced 16 tap FFE should be realized with a symbol rate of 625 MSymbol/s and two samples per symbol. Thus, the equalizer input sample rate is 1.25 GSamples/s. The maximum clock speed for the used FPGA is 450 MHz. So the degree of parallelization is set to 4, which leads to a DSP clock of 312.5 MHz. The parallel equalizer has therefore 4 input substreams and 2 output substreams, due to the nature of a fractionally-spaced equalizer with 2 samples/symbol input

rate and 1 sample/symbol output rate. Inserting this information in Eq. (6.4) results in

$$
\begin{aligned}
z_{4l} &= [c_0, c_4, c_8, c_{12}] \begin{bmatrix} y_{4l} \\ y_{4l-4} \\ y_{4l-8} \\ y_{4l-12} \end{bmatrix} + [c_1, c_5, c_9, c_{13}] \begin{bmatrix} y_{4l-1} \\ y_{4l-5} \\ y_{4l-9} \\ y_{4l-13} \end{bmatrix} + \\
&\quad + [c_2, c_6, c_{10}, c_{14}] \begin{bmatrix} y_{4l-2} \\ y_{4l-6} \\ y_{4l-10} \\ y_{4l-14} \end{bmatrix} + [c_3, c_7, c_{11}, c_{15}] \begin{bmatrix} y_{4l-3} \\ y_{4l-7} \\ y_{4l-11} \\ y_{4l-15} \end{bmatrix} \\
z_{4l-2} &= [c_0, c_4, c_8, c_{12}] \begin{bmatrix} y_{4l-2} \\ y_{4l-6} \\ y_{4l-10} \\ y_{4l-14} \end{bmatrix} + [c_1, c_5, c_9, c_{13}] \begin{bmatrix} y_{4l-3} \\ y_{4l-7} \\ y_{4l-11} \\ y_{4l-15} \end{bmatrix} + \\
&\quad + [c_2, c_6, c_{10}, c_{14}] \begin{bmatrix} y_{4l-4} \\ y_{4l-8} \\ y_{4l-12} \\ y_{4l-16} \end{bmatrix} + [c_3, c_7, c_{11}, c_{15}] \begin{bmatrix} y_{4l-5} \\ y_{4l-9} \\ y_{4l-13} \\ y_{4l-17} \end{bmatrix} . \qquad (6.5)
\end{aligned}
$$

These two output substreams z_{4l} and z_{4l-2} consist each of 4 subfilters, which are simple 4-tap FIR filters running at a DSP clock of 312.5 MHz. The first step to implement such a 4-tap FIR filter is the FIR direct form type I, which is depicted in Fig. 6.12. For notation simplicity, only the 4-tap FIR filter depicted in Fig. 6.9 is considered. The subfilters in Eq. (6.5) can be implemented in the same manner, just by exchanging the indices.

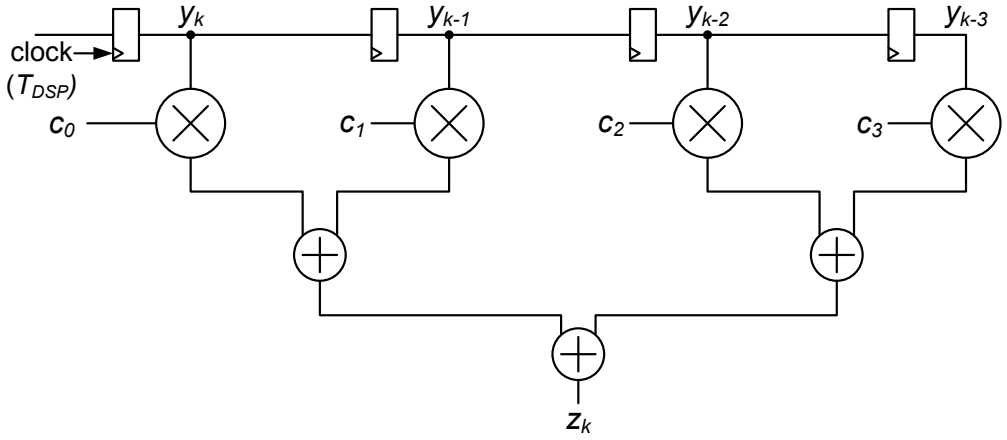

Figure 6.12: FIR direct form type I.

This structure is called direct form I, because it is the direct implementation of the formula of one subfilter in Eq. (6.5). The clocked boxes are D-FlipFlops, which delay the input data for one clock cycle. Unfortunately, this structure does not work at high speeds, because all the arithmetic functions (here 1 multiplication and 2 additions) can not be done within one clock cycle. Thus, pipelining has to be used to get rid of timing problems, which means that after each arithmetic functionality a clocked memory element, such as a Flip-Flop, should be used. This pipelining can fix the timing problems, when it is implemented in a free configurable hardware.
In the case of FPGAs, special hardware blocks have to be used for such high speed signal processing. In the Virtex-4 device, so called DSP48 elements are available, which consist in principle of a multiplier and an adder. The best way to connect them is to build chains of DSP48 cells. Fig. 6.13 shows the implementation of the 4-tap FIR filter using Virtex-4 DSP48 slices in a highly pipelined systolic filter structure.

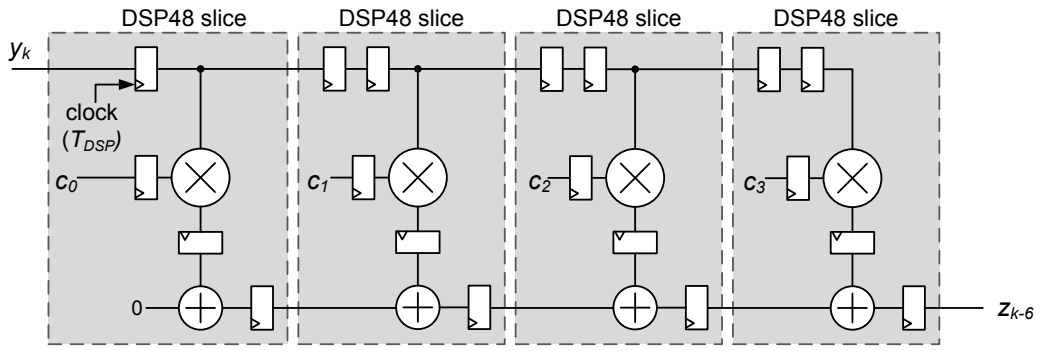

Figure 6.13: Systolic FIR implementation using Xilinx Virtex-4 DSP48 slices.

Thus the direct form FIR filter (Fig. 6.12), which uses an adder-tree structure, has changed to a systolic FIR filter with an adder chain structure. The advantage is that the DSP48 slices can be used very efficiently and only one DSP48 slice has to be used for one filter tap. The only disadvantage is the higher latency of this filter due to pipelining and due to the systolic structure. But only this filter structure can be clocked with 312.5 MHz. Fig. 6.14 shows the parallelized FFE structure for the first output substream z_{4l} of the applied 16-tap $T/2$ fractionally-spaced equalizer for the demonstrator. The latency of this structure is 11 DSP clock cycles or 44 input sample clock cycles due to the pipelining stages inside the filter. The red dashed-dotted line in Fig. 6.14 shows the path for the latency calculation.

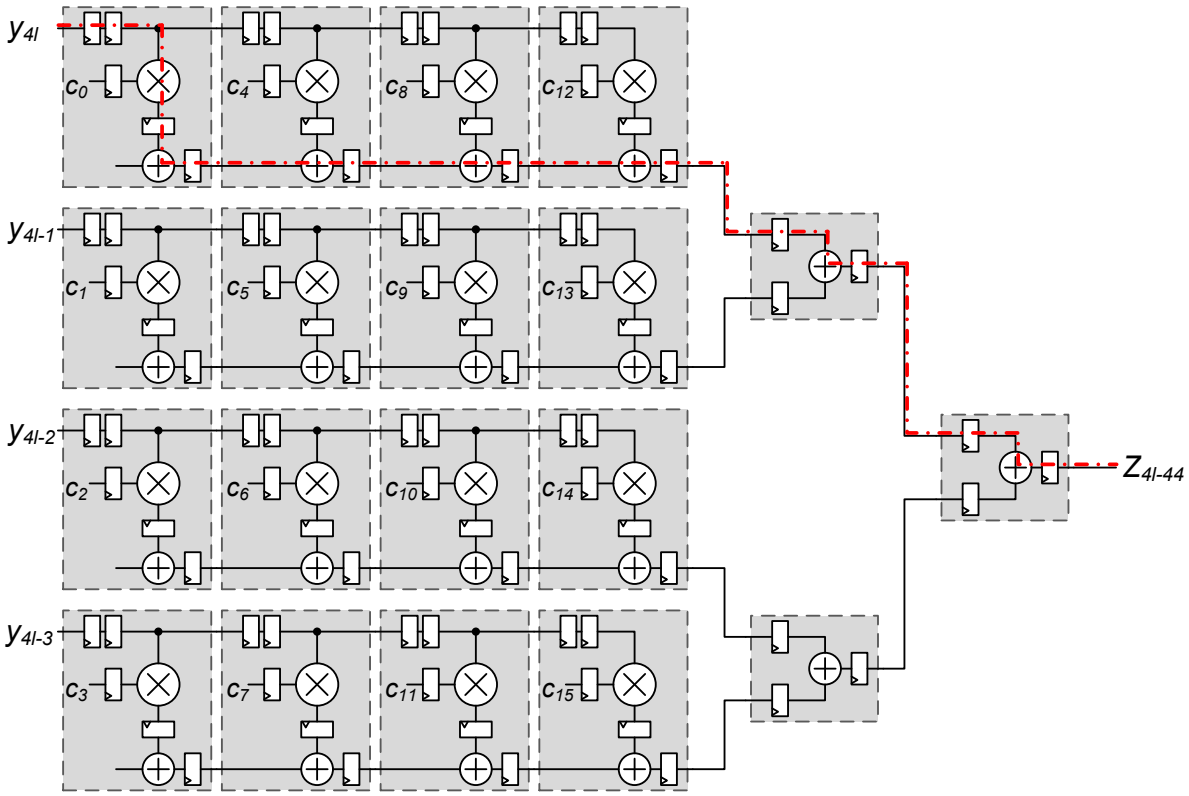

Figure 6.14: Parallel implementation for one of two output substreams of the fractionally-spaced 16 tap FFE, using the Xilinx Virtex-4 DSP48 slices.

The second output substream z_{4l-2} is implemented by a second instance of the filter structure depicted in Fig. 6.14. So the implemented parallel FFE has the same behavior as the offline processed ones in chapter 5, except of the latency provided by the pipelining stages. Thus the parallel implementation has only an impact on the filter adaption algorithm, which is discussed in the following sub-section.

Filter coefficient update implementation

For the coefficient adaptation, the Stop-and-Go algorithm introduced in chapter 4.5.2 should be implemented. Unfortunately, not all the required information is available at the right time inside the FPGA due to the parallel and pipelined implementation of the FFE filter core. Especially the pipelining results in latency of the filter core. By using the delayed LMS (DLMS) algorithm [Kab83], the problem can be solved. This algorithm just uses delayed updates for the equalizer coefficients, which can be written in the LMS coefficient update formula as

$$c_i(k+1) = c_i(k) + \beta \cdot e(k - M_{\text{filt}}) \cdot y(k - i - M_{\text{filt}}) \tag{6.6}$$

where $y(k - M_{\text{filt}})$ is the equalizer input signal delayed by M_{filt} clock periods. M_{filt} is the latency introduced by the FFE filter core. Thus for the LMS case, the error can be calculated as

$$e(k - M_{\text{filt}}) = z_{\text{odd}}((k - M_{\text{filt}})) - \hat{z}_{\text{odd}}((k - M_{\text{filt}})). \tag{6.7}$$

How this delayed LMS is applied to the parallelized FFE is shown in Fig. 6.15. Due to the parallelization, each clock cycle produces two output samples. Thus, for simplicity and due to the time-invariant channel, the coefficients are only updated each second symbol. The outputs of the FFE filter core are denoted as $z_{\text{even}}(k - M_{\text{filt}})$ and $z_{\text{odd}}(k - M_{\text{filt}})$. For the adaption process only the z_{odd} symbols are used.

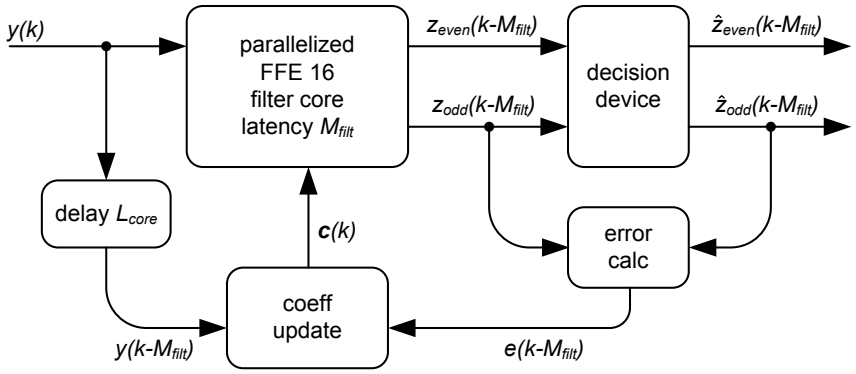

Figure 6.15: Block diagram of the delayed least mean square (DLMS) coefficient update algorithm.

After the error calculation $e(k - M_{\text{filt}})$, the update process is done by adapting each coefficient according to Eq. (6.6). Each equalizer coefficient c_i is updated with the delayed version of the error signal $e(k-M_{\text{filt}})$ and the corresponding input sample $y(k-i-M_{\text{filt}})$. It has been shown in [Kab83], that the steady-state performance of the DLMS can reach the level of the non-delayed LMS, if the channel does only change slowly. The convergence process of the DLMS to reach the steady-state needs more time. However, as the SI-POF channel is a time-invariant channel, this constraint does not affect the steady-state performance of the transmission system.

6.3.3 Clock Recovery using Goertzel algorithm

One of the most critical parts in a transmission system is the recovery of the transmitter clock at the receiver. In this demonstrator a hybrid phase-locked loop (PLL) is used to lock to the transmitter clock, which can be extracted from the received signal. In

Fig. 6.16 the block diagram of such a hybrid PLL is shown. The word hybrid means, that parts of the PLL are realized in the analog domain and parts are implemented in the digital domain in the FPGA. Here, the ADC running at a sampling frequency of $f_{\text{sample}} = 2.5$ GHz, the VCXO for generation of this sampling clock and the small DAC for producing the tuning voltage V_{tune} for the VCXO are the analog components.

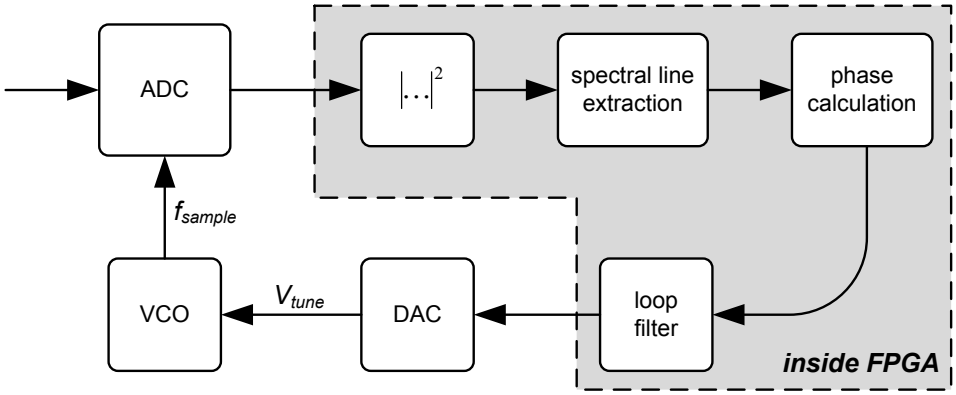

Figure 6.16: Hybrid Clock recovery PLL.

Inside the FPGA, the phase detector is implemented as a nonlinearity (square function) and a spectral line extraction followed by a CORDIC algorithm block for calculating the phase of this spectral line. This phase signal is low-pass filtered with a 2nd order digital loop filter, which results in the control signal for the VCXO. For detailed information about the nonlinear spectral line method for clock recovery issues, it is referred to the literature [GHW92, LM94].

The crucial part in terms of signal processing complexity is the spectral line extraction. The most popular method to calculate spectral components of a time signal in the digital domain is the Fast Fourier Transformation (FFT). However, the only relevant spectral component, is the one at the symbol rate, which is 625 MHz for this demonstrator. Using a FFT to calculate this spectral component is very inefficient. Thus, a different algorithm to calculate spectral components is proposed, which is the so-called Goertzel-algorithm [Goe58]. This algorithm is explained in the following. All other components in Fig. 6.16 are standard DSP components, like the squarer, the phase calculation with the help of the CORDIC algorithm [Vol59] and the 2nd order digital loop filter. For further information about these components it is referred to the literature, e.g. [MMR98].

The Goertzel Algorithm for spectral line extraction

The Goertzel-algorithm calculates spectral components by a recursive difference equation. The considered block size of the time or frequency vector is N. The spectral component $X[k]$ with frequency index k can be efficiently calculated using an infinite impulse response (IIR) filter structure depicted in Fig. 6.17.

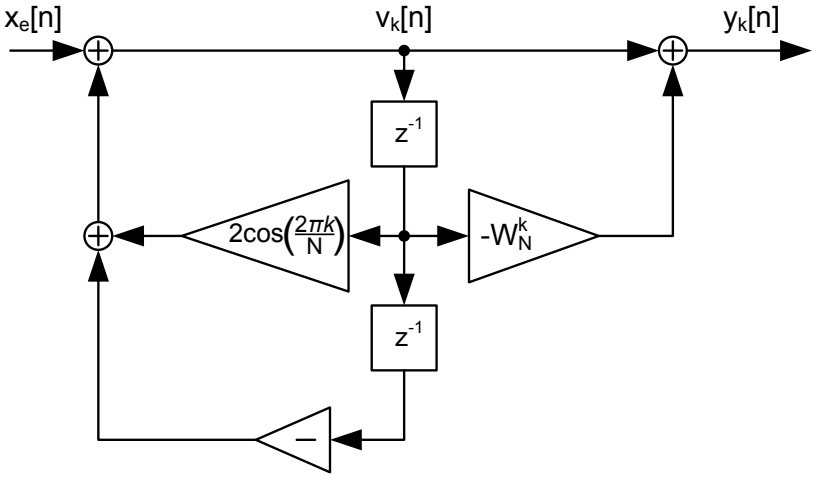

Figure 6.17: The general Goertzel Filter.

Mathematically this filter can be described by its transfer function in the z-Domain as

$$H_k(z) = \frac{y_k[z]}{x_e[z]} = \frac{1 - W_N^k z^{-1}}{1 - 2\cos(2\pi k/N)z^{-1} + z^{-2}} \tag{6.8}$$

where $W_N^k = e^{-j\frac{2\pi k}{N}}$. The desired spectral component is calculated by filtering the input data block $x[n]$ with the above IIR and evaluating the output at $n = N$. Thus, the FIR filter part in Eq. (6.8) must only be calculated once for every data block. The recursive part of the filter has an output signal $v_k[n]$, which can be written as

$$v_k[n] = x_e[n] + 2\cos(2\pi k/N)v_k[n-1] - v_k[n-2] \tag{6.9}$$

with

$$x_e[n] = \begin{cases} x[n] & \text{if} \quad 0 \leq n \leq N-1 \\ 0 & \text{if} \quad n < 0 \ , \ n \geq N \end{cases} \tag{6.10}$$

Finally, the FIR filter part has to be calculated to get the desired spectral component $X[k]$ to

$$X[k] = y_k[N] = v_k[N] - W_N^k v_k[N-1] \tag{6.11}$$

So the final result is just a weighted linear combination of two consecutive output values of the recursive part.

The Goertzel algorithm applied for the Clock recovery

Now this scheme is applied to calculate the frequency component at the symbol rate of 625 MHz with an input sampling rate of 2.5 GSample/s. Applying these two values to Eq. (6.8) results in the evaluation at the frequency index $k = N/4$. This leads to tap weights $W_N^{N/4} = -j$ and $2\cos((2\pi(N/4)/N)) = 0$. Thus, the transfer function of the filter $H_{N/4}(z)$ simplifies to

$$H_{N/4}(z) = \frac{1 + jz^{-1}}{1 + z^{-2}} \tag{6.12}$$

It can be seen that no multiplication is needed in the above equation anymore. The recursive part is only a subtraction of the value delayed by two clock cycles and the output is separated in terms of real and imaginary parts of the spectral component. Thus the spectral line extraction circuit simplifies to the following structure:

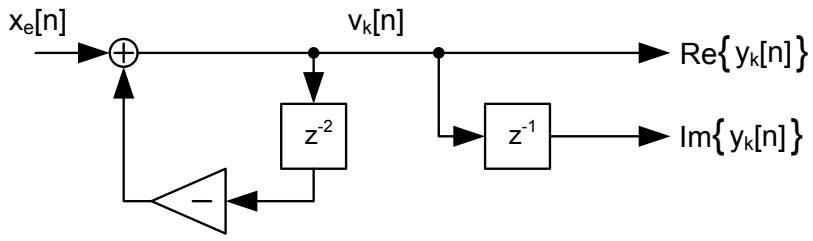

Figure 6.18: Clock recovery with goertzel with an oversampling factor of 4.

The algorithm works as follows: first the block of N samples is passed through the recursive part, which is just one subtraction. Then the output is evaluated at the time index $n = N$. The spectral component writes as

$$X[k] = y_k[N] = v_k[N] + j \cdot v_k[N-1]. \tag{6.13}$$

The processing speed of the Goertzel algorithm is also limited to the DSP clock speed of 312.5 MHz. Thus, the update rate of the phase detector is defined by this clock speed and the block size N for the spectral line extraction. In the demonstrator the block size was chosen to 2048. Thus the sampling phase estimate update rate is approx. 153 kHz, which should be sufficient for tracking the clock drift of the reference clock crystals, which normally have drift speeds in the low kHz range.

6.3.4 Forward Error Correction insertion

Forward error correction (FEC) is a commonly used instrument to correct decision errors in a data transmission system due to AWGN. To achieve this, an encoder adds a small coding overhead to be able to correct a certain amount of errors in a received data block. In this demonstrator, a Reed-Solomon FEC is used to achieve the required BER of $< 10^{-12}$ of Gigabit Ethernet. As mentioned before, an overhead has to be added to the payload data to be transmitted. For the demonstrator this should be achieved without changing the data line rate in the SI-POF. In Fig. 6.19 the block diagram for the FEC insertion is depicted. Until now the FEC bypass is used (gray dotted line), which encodes the 8B10B coded 1.25 Gbit/s serial stream directly into scrambled PAM-4 symbols.
Initially, this 8B10B coding is used to get a serial stream with in-line sideband signaling (Start of Packet, End of Packet, Idle,...) and to get a DC-balanced and digital run-length limited transmission. For more details about the 8B10B code it is referred to appendix B. The only required feature of this coding for the demonstrator is the in-line sideband signaling. Thus, the overhead of 25% can be reduced to 12.5% by decoding the serial stream. The output of the decoder in Fig. 6.19 is a 9 bit wide bus, one bit for the indication of user data or control information and the 8 bit wide user data bus running at 125 MHz. Thus, all 9 bits must be transmitted to guarantee a proper Ethernet connection with all the required sideband information.
The reduction of the overhead by 12.5% can now be used to insert the FEC overhead data. To stay with the same line rate on the SI-POF channel, the FEC overhead should be 1/9. Due to implementation issues the word length of the used Reed Solomon (RS) FEC is chosen to be 10 bits. This leads to a RS(270,300), which means that 270 data words in a block are used to calcuate the 30 check words, which are added to the data block for transmission.
The block diagram of the insertion of this RS(270,300) FEC code is shown in Fig. 6.19. There the input is a 10bit wide bus running at 125 MHz, which is the serial-to-parallel converted 1.25 Gbit/s serial stream from the GigE PHY. Then the 8B10B decoder decodes these words to a data bus of 9 bit at 125 MHz (control information and user data). In front of the RS(270,300) encoder, the data has be reordered to get 10 bit words for the RS encoder. The FEC encoded data bus is then 10 bits wide at 125 Mhz, which is again a 1.25 Gbit/s data stream with inserted FEC overhead. This data stream is fed into the scrambler to achieve the requirements for the transmission and the convergence of the equalizer at the receiver.

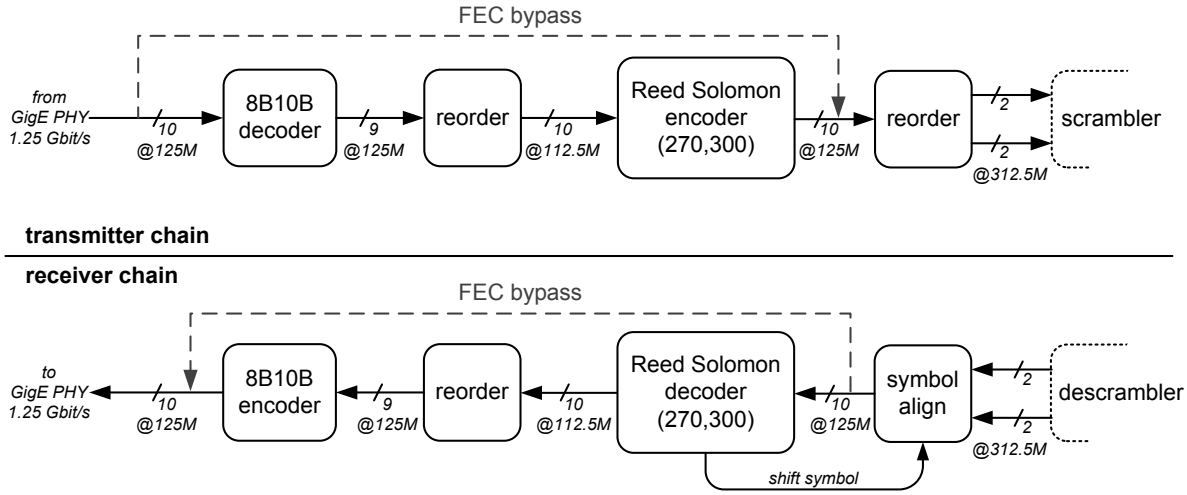

Figure 6.19: Block diagram FEC insertion without additional overhead.

On the receiver side the descrambled data has to be reordered to a 10 bit wide data bus at 125 MHz, which is the input stream to the RS(270,300) decoder. The big challenge at the receiver side is the FEC block synchronization, which has to be done without any synchronization overhead. The synchronization process is done with a PAM-4 symbol shifter and the FEC decoder block. First the decoder decodes one block and indicates if the block could be corrected or if the correction process has failed. If it has failed, the decoder activates the feedback signal 'shift symbol', which leads to a symbol shift in the symbol align block. Thus, the FEC block borders are shifted by one PAM-4 symbol. The shifting process is done until the decoder is able to correct a certain amount of data blocks in a row. This searching process can lead to a longer starting or synchronization phase. But if the synchronization is found, the FEC block borders do not change anymore and the transmission can be established. In the worst case, this initial synchronization process needs 14.4 ms. It takes into account that the decoder works at 125 MHz and needs 1200 clock cycles to get a decoder fail signal due to implementation issues. One FEC block consists of 1500 PAM-4 symbols. Thus, the maximum search time is $1200 \cdot 1/(125\ \text{MHz}) \cdot 1500 = 14.4\,\text{ms}$. After the block synchronization has been found, the decoded data is 8B10B encoded again and transmitted to the GigE PHY.
The FEC insertion does not affect any other DSP component in the transmitter and receiver paths, because the interface at the scrambler and descrambler is the same with FEC or without FEC (FEC bypass). This good property can be used for test purposes to measure the difference between transmission with and without FEC. For BER performance measurements, which are presented in sub-chapter 6.6, the FEC is bypassed to get pre-FEC BER values.

6.4 Gigabit Ethernet POF Media Converter

In Figure 6.20 the block diagram of the Gigabit Ethernet POF transceiver is shown, which is built as a media converter from 1000Base-TX to Gigabit POF. It consists of an analog front-end PCB (AFE, see subsection 6.2) and a FPGA board with a high-speed ADC and DAC (see 6.1). The block diagram is passed on the transmitter side from left to right and on the receiver side from right to left. The Gigabit Ethernet PHY converts the input 1000base-T data into a serial 8B10B-coded signal with 1.25 Gbit/s (1000base-X), which is fed into the FPGA with the help of the RocketIO serial transceiver. This data is stored in an elastic buffer to compensate for clock differences between the PHY chip reference clock and the FPGA transmit clock. Then the 8B10B coded signal is decoded and FEC encoded (RS(270,300)) according to sub-chapter 6.3.4. Afterwards the data is scrambled with a multiplying scrambler (sub-chapter 6.3.1) to get an almost DC-free signal after PAM4-modulation with a symbol rate of 625 MSymbol/s, which is done with gray-coding. The scrambler is also necessary to get enough transitions between the amplitude values for the adaptation algorithm of the receiver equalizer. After the modulation, a digital symbol-spaced pre-filter is applied to compensate partly for the $\sin(x)/x$-frequency characteristic of the DAC. For test purposes, a pseudo-random quaternary sequence (PRQS) of order 5 [MS76] can be inserted instead of the Ethernet data. The DAC realizes the digital-to-analog conversion with only one sample per symbol. On the analog front-end PCB (sub chapter 6.2), the LED driver circuit converts the differential DAC output signal to a suitable current to drive a DC-biased commercially available red LED with a fiber-coupled output power of -1.4 dBm (after 1 m SI-POF). The achieved modulation index is approximately $\eta_{\mathrm{mod}} = 0.6$. On the receiver side, the optical signal is detected using a PIN

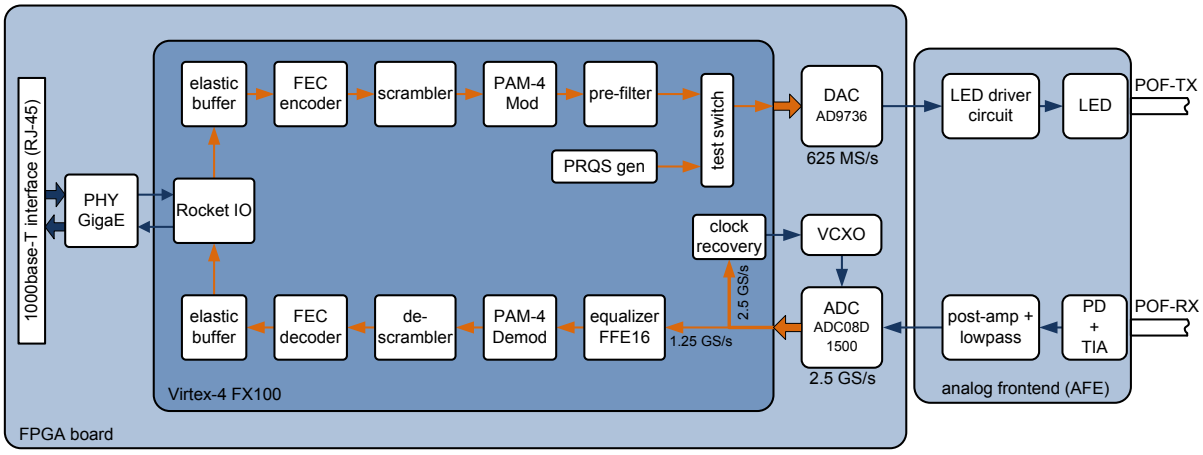

Figure 6.20: Transceiver block diagram.

photo diode with an active-area diameter of 540 μm with integrated trans-impedance amplifier. On the AFE this signal is post-amplified and filtered using an analogue 5th order Bessel filter with a 3 dB bandwidth of 440 MHz. The ADC runs at a sampling rate of 2.5 GSample/s (GS/s). Inside the FPGA the sampled signal is split into a data stream at 2.5 GS/s and one at 1.25 GS/s. The first is used to perform the clock recovery by applying the nonlinear spectral line method to get phase information of the clock signal at the symbol rate (see sub-chapter 6.3.3). This signal is used to control a voltage controlled crystal oscillator (VCXO), which is the clock source for the ADC. The 1.25 GS/s data signal is fed to the adaptive 16-tap fractionally-spaced linear equalizer (2 samples per symbol) (see sub-chapter 6.3.2). The coefficients are blindly adapted using the stop-and-go algorithm [PP87]. Afterwards the equalized PAM-4 signal is demodulated, descrambled, and decoded in the FEC decoder. At this point also the synchronization is done to the following 8B10B encoder, to pass the encoded signal to the RocketIO, which makes the connection to the Gigabit Ethernet PHY. The Gigabit Ethernet PHY converts the serial data stream back to the 1000base-T signal. Fig. 6.21 shows a picture of the Media converter in a housing.

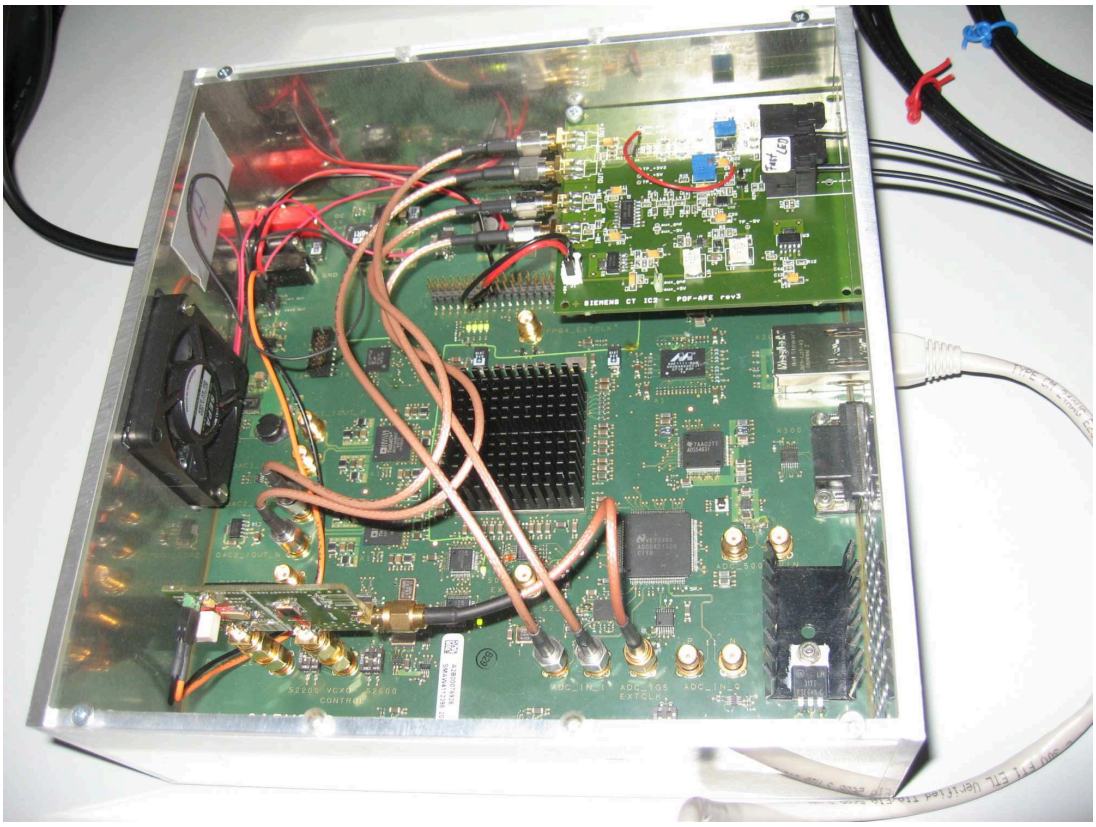

Figure 6.21: Gigabit Ethernet media converter.

6.5 Complexity Analysis of the Gigabit Ethernet POF Media Converter

To get a figure of merit of the implementation complexity of the different signal processing blocks inside the FPGA, the resource allocation of all functional blocks is evaluated and plotted in Fig. 6.22. All functional blocks are implemented using logic cells in the Virtex-4, which are called slices. A Virtex-4 slice consists of two 4-input look-up-tables and two D-Flip-Flops. All embedded hardware, such as the DSP-48 slices, is not used, to get a better comparison to the real resource demand in terms of look-up-tables and Flip-Flops. The total number of slices needed to build the POF media converter is 16162. The portion of each functional block is denoted in percentage.

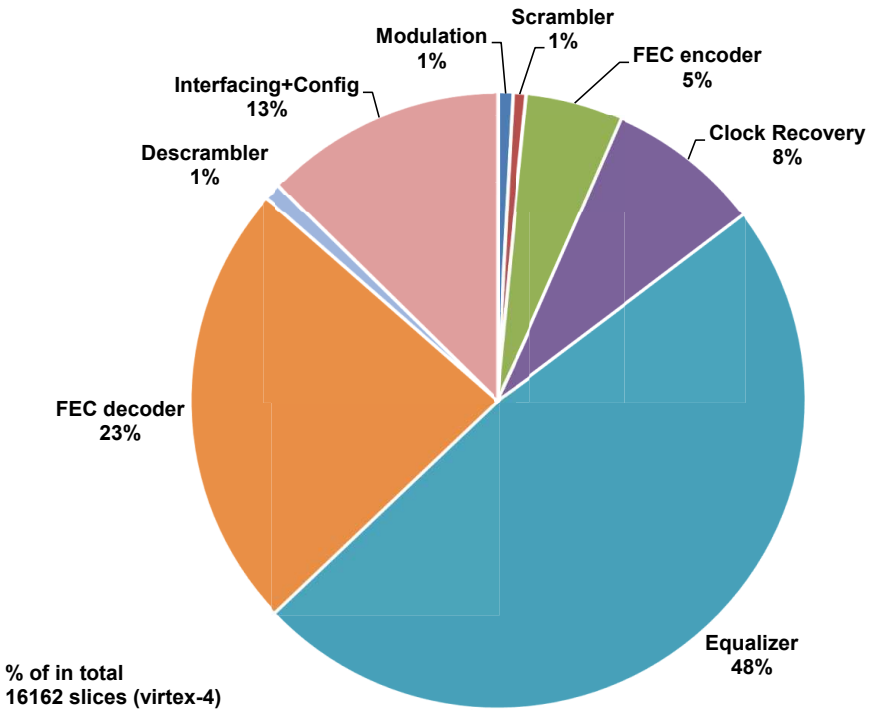

Figure 6.22: Virtex-4 FPGA slices utilized for the full working Gigabit Ethernet Media converter according to functionality (normalized).

The equalizer needs almost 50% of the complete logic, this is mainly due to the parallelization by a factor of 4. The second biggest part (23 %) is the FEC decoder. This block is that big because this functionality too has to be parallelized by a factor of 2, due

to the large latency of the applied RS(270,300) decoder. The FEC encoder needs just 5 %, because no parallelization has to be done and the functionality is not that big as compared to the decoding process. The clock recovery needs also a big part of 8 %, which is mainly occupied by the CORDIC phase calculation algorithm. Modulation, scrambling, and descrambling are not that big, because these parts just work on data buses which are only 2 bits wide and all the arithmetical operations are modulo-4 operations. A big part is also used for the interfacing logic and the chip configuration logic. Most of this logic can be discarded, because flexibility for chip configuration is no longer necessary.
Of course, if the embedded hardware like the DSP-48 slices, is used, the picture changes completely. Using 61 DSP-48 slices, which are mainly used in the equalizer, the total amount of required logic slices can be decreased to 9330. This number shows how the signal processing tasks could be efficiently implemented using these embedded hardware slices.
In a recently published work, the number of slices needed for implementing only the transmitter part of a DMT system for the same data rate on the identical hardware platform was calculated to be approx. 8400 slices [LBC+09]. Hence, for a DMT system the required slices for the transmitter and receiver demodulation without FEC and equalization can be approximated to 16800. This number is sufficient to implement the complete media converter with FEC and interfacing, if the approach introduced in this thesis is used. The number of slices required to implement the modulation, scrambling and equalization is approx. 8208. Thus, the use of DMT requires twice the amount of logic needed for the use of PAM-4 in combination with linear receiver equalization.

6.6 BER performance of the Real-Time demonstrator

In this chapter the BER performance of the Gigabit Ethernet media converter is shown. Here the FEC is not used, which results in a pre-FEC BER performance. Therefore the FEC blocks are just bypassed, so that the BER could be measured. Parts of these results were presented at the ECOC 2009 [BLRH09].

6.6.1 BER performance measurement setup

To evaluate the BER performance of the POF media converter, the setup shown in Fig. 6.23 is used.

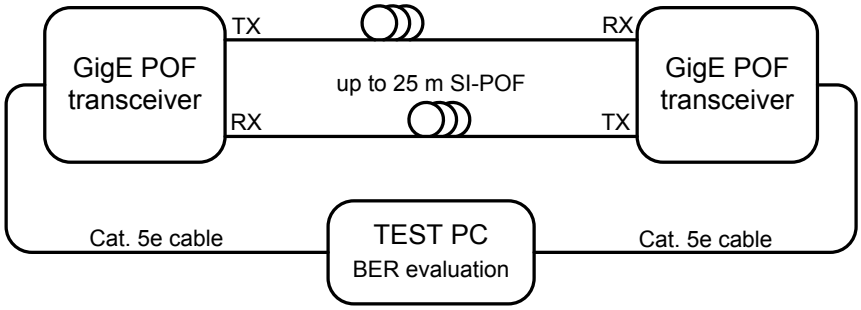

Figure 6.23: Test setup block diagram.

Two Gigabit Ethernet POF media converters are connected to each other to build a bidirectional link, which consists of up to 25 m SI-POF. The media converters themselves are connected to a PC to calculate the BER performance. For link lengths of 5 and 10 m the BER is calculated by transmitting 4.2 million Ethernet packets with a packet size of 1500 bytes, whereas for link lengths of 15 to 25 m the PRQS sequence is transmitted and compared. This is due to Ethernet packet synchronization problems at higher BER values in the serial data signal. The evaluated PRQS sequence length is 10 million bits.

6.6.2 Results

In Fig. 6.24 on the left side the BER curve versus link length is depicted. The blue solid line (circles) represents the performance with the recovered clock. The green dashed line (squares) represents the performance with synchronized clock, which means an external

synchronized clock source for transmitter and receiver. The performance penalty due to clock recovery is about 2 m link length, which is equal to an optical power penalty of 0.3 dB. In Fig. 6.24 on the right side the interpolated eye diagram at the equalizer output is plotted for a fiber length of 25 m. The BER for this fiber length is $7.4 \cdot 10^{-4}$, which is below the FEC limit of the used RS(270,300). Thus, if the FEC blocks are included in the transmitter and receiver chains, error-free transmission is possible even for a fiber length of 25 m.

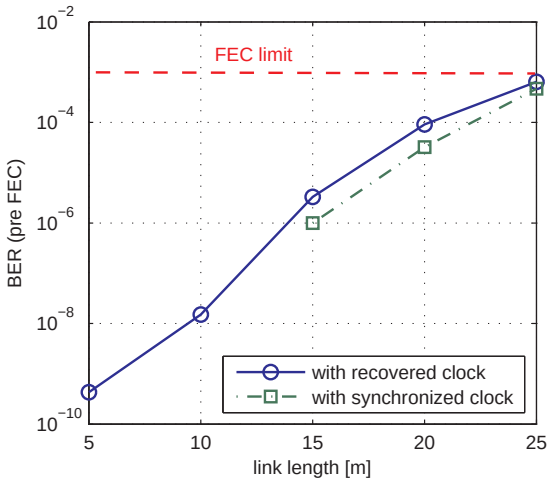

(a) BER performance

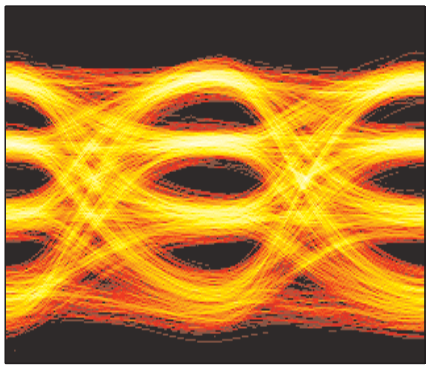

(b) Eye diagram for a fiber length of 25 m

Figure 6.24: BER performance before FEC of the Gigabit Ethernet media converter for fiber lengths of up to 25 m, with synchronized clocks (green dashed dotted) and with the recovered clock (blue solid) (a); Eye diagram at the equalizer output (interpolated) for a fiber length of 25 m (b).

6.7 Summary

The implementation of a complete working Gigabit Ethernet media converter for the 1 mm core diameter PMMA SI-POF for fiber lengths of up to 25 m has been demonstrated. This was achieved by building a custom made FPGA-based DSP board as well as a custom made analog front-end PCB. The digital signal processing was implemented inside the FPGA and consists of the following key features:

- ▷ PAM-4 modulation
- ▷ Scrambler and Descrambler
- ▷ 16-tap T/2 fractionally-spaced feed-forward equalizer
- ▷ Forward Error correction implementation : RS(270,300)
- ▷ Clock recovery using the nonlinear spectral line method
- ▷ Elastic buffers to compensate reference clock differences

The experimental results show that error-free transmission ($< 10^{-12}$) is possible by using this demonstrator with enabled FEC for transmission distances of up to 25 m of SI-POF. Experimental results in chapter 5.2 show that the transmission distance can easily be increased by decreasing the receiver noise. This can be achieved by optimizing the analog front-end, which means for example using Opto-Electronic Integrated Circuits (OEIC), in which the photo diode and the trans-impedance amplifier are integrated on the same die [AGSZ09, ASZ09], which results in a much better noise performance. Additionally the equalizing performance could be improved applying decision feedback equalization.

7

Conclusions and Recommendations

This thesis dealt with the application of digital signal processing to increase the data-rate-length product of polymer optical fiber (POF) based communication systems. Especially the combination of multilevel modulation and digital receiver equalization was investigated in theory and in various experiments for different combinations of light sources and fiber types. Finally a fully working Gigabit Ethernet media converter using a red LED and a PIN photodiode was built on a FPGA platform.

7.1 Summary

First an introductory chapter detailed the basic characteristics and differences of optical communication systems based on polymer optical fibers. The big differences compared to silica based fiber were pointed out, which are mainly the core diameter and the material, which lead to high attenuation and small bandwidth. Even within the family of polymer optical fibers, big differences arise when the PMMA-based POFs are compared with the perfluorinated ones. The first is a low-cost fiber with a core diameter of 1 mm and the second is a competitor to the silica based MMF with core diameters of up to 120 μm.
In the third chapter a channel model for the SI-POF was developed based on the time-dependent power-flow equation, introduced in the 1970s by Gloge [Glo73]. This

model combines the three major multimode fiber effects, such as mode-dependent attenuation, modal dispersion and mode coupling. The channel model was evaluated with measured transfer functions. The matching between simulation and experiment was quite good, so that this channel model can be used to represent a real SI-POF.
This channel model was extended to a complete communication link model for an optical IM/DD channel in chapter 4. The channel capacity was calculated for the new channel model and as a reference, for the two commonly used approximations of a SI-POF, namely a Gaussian low-pass or a 1st order low-pass approximation. The new channel model was also used for the evaluation of different combinations of M-ary PAM modulation and digital receiver equalization in terms of the BER with respect to the link length.
Chapter 5 presented experimental results for the application of M-ary PAM and digital receiver equalization, which were carried out offline on a personal computer. Here, three different combinations of light sources and fiber types were evaluated. Firstly, a laser diode was used to launch into a SI-POF, secondly a RC-LED was used to launch into a SI-POF, and last a VCSEL was used to launch into a PF-GI-POF. For all the combinations the performance was measured in terms of the BER for certain link lengths.
The last chapter dealt with the real-time implementation of a Gigabit Ethernet media converter using a LED as light source. Therefore a custom-made FPGA board as well as an analog frontend were designed. The digital signal processing algorithms were implemented inside the FPGA. One of the biggest problems was the parallelization of the algorithms, which had to be done due to the high speed input data rate. The complexity of such a full working media converter was discussed and compared to an approach, which uses DMT as modulation format. Finally the performance was evaluated in terms of pre-FEC BER measurements.

7.2 Achievements

The following main results were achieved for the modeling of the SI-POF channel, the channel capacity calculations, and the equalizer performance bounds:

- ▷ A general method to solve the time-dependent power-flow equation was derived. This solution algorithm accepts arbitrary input functions for the launching condition, the mode-dependent attenuation, the modal delay and the mode-coupling. Furthermore, the solution scheme is unconditionally stable, which allows large grid steps. This leads to very low computation time in the range of minutes for fiber

lengths of 100 m on a contemporary personal computer.

- ▷ Bandwidth simulations showed that the bandwidth of the SI-POF is strongly dependent on the launching condition (see Fig. 3.8) and for small launching NA also dependent on the main incident angle θ_0.
  This means for a LED launch that the bandwidth is independent of the main incident launching angle, which results in a very large alignment tolerance. For a laser launch this behavior is different. The bandwidth increases for smaller launch NA, but decreases as the main incident angle θ_0 increases. Thus the benefit of having a higher modal bandwidth has to be paid by a smaller angle alignment tolerance.

- ▷ The channel model was evaluated with measured transfer functions. The result is a very good matching between simulation and measurement. Thus this channel model represents the real SI-POF channel very well.

- ▷ The channel capacity was calculated for the two commonly used approximations, the Gaussian and the 1st order low-pass characteristic, and for the newly derived SI-POF channel model (see chapter 3). The results confirm the observations of recently published work [Lee09, LBR+09], that for short fiber length (< 25 m) the 1st order approximation can be used roughly and for longer fiber length (> 150 m) the Gaussian approximation can be applied. But for the range in between (25 m $<$ fiber length < 150 m) none of these two approximations represent the real SI-POF channel very well. Whereas the introduced SI-POF channel model, described in chapter 3, fits very well for all fiber lengths from 0 m to 200 m.

- ▷ The use of PAM-4 as modulation scheme outperforms the OOK modulation format in terms of achievable link length, if it is used in combination with digital receiver equalization. This holds for all investigated light sources. Thus multilevel modulation is a promising candidate for increasing the data-rate-length product.

At the beginning of this work the largest measured data-rate-length product for a laser launched SI-POF system was 531 MBit/s·100 m [YWB93]. This value could be increased in this thesis for every combination of light source and fiber type. The main achieved results with offline receiver signal processing are summarized as follows:

- ▷ With a laser launched SI-POF system, it was experimentally demonstrated that error-free 1.25 Gbit/s transmission over 100 m of PMMA-based SI-POF is possible with OOK and a decision feedback equalization. Further it has been shown for the first time that the transmission of 2 Gbit/s over 100 m SI-POF is also possible using

a very large DFE. All these results are achieved by using a low-cost DVD laser diode at a wavelength of 655 nm.

- ▷ Even by using a low-cost resonant-cavity LED at 650 nm, error-free transmission of 1.25 Gbit/s over 50 m SI-POF was demonstrated by using PAM-4 modulation in combination with a blindly adapted fractionally-spaced decision feedback equalizer. For longer fiber lengths, error-free transmission is feasible, if the receiver noise can be decreased.

- ▷ For transmission of 10 Gbit/s over longer distances of up to 300 m, the PF-GI-POF is a promising alternative to the commonly used silica multimode fiber. The benefits are the easier handling and the robustness in terms of bending radii and mechanical stress. 10 Gbit/s transmission was demonstrated using PAM-4 or OOK as modulation scheme in combination with decision feedback equalization for a 300 m long fiber.

Finally, the implementation of a fully working LED based Gigabit Ethernet media converter for SI-POF lengths of up to 25 m has been demonstrated. In Fig. 7.1 two media converters are shown in a testbed environment, connected with each other and with two PCs to evaluate the Ethernet performance. The media converter was implemented by building a custom made FPGA-based DSP board as well as a custom made analog front-end printed circuit board (PCB). The digital signal processing was implemented inside the FPGA and consists of the following key parts:

- ▷ PAM-4 modulation and demodulation
- ▷ Scrambler and Descrambler
- ▷ 16-tap $T/2$ fractionally-spaced feed-forward equalizer (blindly adapted)
- ▷ Forward Error correction: RS(270,300)
- ▷ Clock recovery using the nonlinear spectral line method (implemented using the Goertzel algorithm)
- ▷ Elastic buffers to compensate reference clock differences

The experimental results demonstrated that error-free transmission ($< 10^{-12}$) is possible by using this demonstrator with enabled FEC for transmission distances of up to 25 m of SI-POF. The offline processed results in chapter 5.2 showed that the transmission distance can easily be increased by decreasing the receiver noise, which can be achieved by optimizing the analog front-end. Additionally the equalizer performance could be improved applying decision feedback equalization. Thus the performance of the demonstrator could be increased, if the analog frontend is optimized.

Figure 7.1: Test bed of two connected Gigabit Ethernet media converters with a fiber length of 10 m.

7.3 Recommendations for future research

In this thesis the use of multilevel modulation in combination with receiver equalization achieved very good results in terms of data rate and link length. But as the channel capacity calculations showed, there is enough space for performance improvement in terms of data-rate-length porduct. Here are some ideas, with which this data-rate-length product could be increased in the direction of the channel capacity:

- ▷ In this thesis modulation and equalization and channel coding are considered separately. To improve the performance, these three parts should be investigated together, e.g. trellis coded modulation could give up to 6 dB coding gain, just by adding an extra level in the modulation alphabet, like it is done for the copper-based Gigabit Ethernet transmission.

- ▷ As the SI-POF is a low-pass channel, the symbol rate should be as small as possible, thus for transmitting Gigabit Ethernet a different kind of line coding should be used to get rid of this large overhead of up to 25%, as it is the case for the used 8B10B coding.

- ▷ For LED based SI-POF systems, a huge amount of bandwidth limitation is due to the LED itself, thus the use of predistortion could compensate for the limitations of the transmitter. For example, the feedback part of a DFE at the receiver could be transferred to the transmitter, which results in the so-called "Tomlinson-Harashima precoding".

In summary, all the efforts done for copper-based communication links, like Ethernet, could also be applied for the POF communication with the big differences of having much more bandwidth in the channel and no crosstalk at the transmitter and receiver. Unfortunately, the receiver noise is much higher for the POF system. Hence a different balance between modulation, equalization, and coding should be used to achieve the best performance. A promising solution for LED-based SI-POF systems could be the use of coded modulation in combination with equalization, to be more robust against receiver noise.

A

Crank-Nicolson scheme

In this appendix the Crank-Nicolson scheme [CN47] is explained by means of a simplified version of the time-dependent power-flow equation (3.38), which writes as

$$\frac{\partial p}{\partial z} = \frac{\partial^2 p}{\partial \theta^2} \qquad \text{for} \qquad 0 \leq \theta \leq \theta_c, \qquad z \geq 0. \tag{A.1}$$

To solve this partial differential equation, the numerical finite difference method is applied. Therefore, a grid is used, which consists of a direction in space z and angle θ with discrete step sizes Δz and $\Delta\theta$, respectively. For further calculations the indices m and n are introduced in the following way:

$$z = m \cdot \Delta z, \qquad \theta = n \cdot \Delta\theta. \tag{A.2}$$

For the finite difference method, three major schemes exist: the forward space centered angle (FSCA), the backward space centered angle (BSCA) and the Crank-Nicolson scheme. All three schemes operate on this grid. In Fig. A.1 the used neighboring points to calculate the new point (black, solid) are depicted for all three schemes.

In this work, the Crank-Nicolson scheme is used. It is an implicit method, like the BSCA scheme, which means it is unconditionally stable [Ame92]. Another advantage is the smaller truncation error in the space direction m. The Crank-Nicolson scheme uses two difference schemes to represent the derivatives: the backward difference for derivatives in

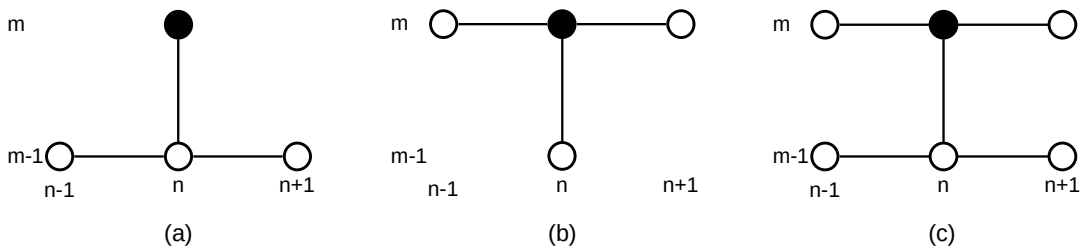

Figure A.1: Finite difference schemes (black point : considered point): (a) Forward space, centered angle; (b) backward space, centered angle; (c) Crank-Nicolson.

z and the central difference for derivatives in θ. The applied differences for Eq. (A.1) are shown in Eq. (A.3) and (A.4).

$$\frac{\partial p}{\partial z} = \frac{p_m - p_{m-1}}{\Delta z} \tag{A.3}$$

$$\frac{\partial^2 p}{\partial \theta^2} = \frac{p_{n+1,m} - 2p_{n,m} + p_{n-1,m}}{\Delta \theta^2} \tag{A.4}$$

Using the Crank-Nicolson scheme, the left hand side of Eq. (A.1) is approximated with the backward space difference (Eq. A.3). The right hand side of Eq. (A.1) is approximated with the average of the central differences (Eq. A.4) evaluated at the current and the previous space point. Thus, Eq. (A.1) is approximated with

$$\frac{p_{n,m} - p_{n,m-1}}{\Delta z} = \frac{1}{2}\left(\frac{p_{n+1,m} - 2p_{n,m} + p_{n-1,m}}{\Delta \theta^2} + \frac{p_{n+1,m-1} - 2p_{n,m-1} + p_{n-1,m-1}}{\Delta \theta^2}\right). \tag{A.5}$$

This scheme has only a truncation error of $\mathcal{O}(\Delta z^2) + \mathcal{O}(\Delta \theta^2)$ in comparison to $\mathcal{O}(\Delta z) + \mathcal{O}(\Delta \theta^2)$ for both other schemes (FSCA, BSCA) due to the averaging on the right hand side.

B

8B10B line-code for 1000Base-X

This review of the 8B10B encoding for Gigabit Ethernet is a summary of [Sei98]. 1000Base-X or the serial version of Gigabit Ethernet uses an 8B10B block code [WF83]. 8 bits of data (1 byte) are encoded into 10 code bits. The coding scheme was developed and patented by IBM Coperation and licensed for use in both Fiber Channel and Gigabit Ethernet [FWrp]. This particular code provides a number of important characteristics:

- ▷ The coding ensures sufficient signal transitions for clock recovery at the receiver.
- ▷ The code space allows control signals to be encoded in the serial data stream.
- ▷ Some of the encodings (used for control signals) contain a unique, easy recognizable code-bit pattern (known as "comma symbols").

To make it easier to deal with 256 possible data values and 1024 theoretically possible code-words, a shorthand notation was developed for the 8B/10B code. The code space is divided into two groups of code:

1. the "D" group, used to encode data bytes
2. the "K" group, used to encode special control characters

The entire coding table is provided in Tab. B.2 for the data bytes and in Tab. B.3 for the control symbols. The 8 bits of the data byte are denoted A,B,C,D,E,F,G, and H (least-significant bit to most significant bit). The encoder translates these 8 bits into a 10 bit code, denoted as a,b,c,d,e,i,f,g,h, and j. The code-word is treated as two subgroups, one containing 6 code bits (a,b,c,d,e, and i) and one containing 4 code bits (f,g,h, and

j). A given code is referred to by the shorthand /Dx.y/ (for data codes) or /Kx.y/ (for special codes), where x is the decimal value of EDCBA and y the decimal value of HGF. In order to ensure that the 10B-encoded signal can be AC-coupled onto the medium, the number of ones and zeros in the encoded stream must be equal over time for any arbitrary data transmission. Thus the code-words are carefully chosen. The code-words used for data codes never

- ▷ generate more than 4 consecutive ones or zeros, or
- ▷ have an imbalance of greater than one.

In addition to selecting only the most balanced codes, two 10B encodings for every 8B group are defined. If the chosen 10B encoding for a given value has the same number of ones and zeros, then the two 10B encodings may be the same. If the 10B encoding has more ones than zeros, than the alternate encoding uses the inverse of the bits within the subgroups [abcdei] or [fghj] (or both) in which the imbalance occurs.
The transmitter keeps a running tally, on a code-word by code-word basis, of whether there have been more ones than zeros transmitted or more zeros than ones. Since a code-word can compromise (at most) an imbalance of only one additional one or zero, only a single bit of information is required for running the tally. This is called "running disparity" (RD). RD is a measure of whether the patterns are "leaning" toward too many ones(RD+ or positive disparity) or toward too many zeros (RD- or negative disparity). The encoder selects one of the two possible codes for each transmitted byte depending on whether the current running disparity is positive or negative. As a result, the running disparity will either invert (flip) or be left the same.
Control information (as opposed to data) is communicated through the transmission of ordered sets. An ordered set is a string of one or more code-words, always beginning with a code from the special group (K-group). The use of special codes makes ordered sets easily distinguishable from data. This distinction allows the system to unambiguously pass both data and control information across the same communications channel; that is, ordered sets provide an "out-of-band" signaling method. Thus the input data of an encoder consists of nine bits, 8 bits (1 byte) for the data and one bit to distinguish whether this byte is a data byte ("D"-group) or whether it is a control character ("K"-group). On the receive side, its the same only in the opposite direction.
Gigabit Ethernet defines and uses eight such ordered sets, given in Table B.1. The configuration sets are used for Auto-Negotiation of link characteristics, the idle sets are used between transmissions. The /S/ and /T/ sets are used as delimiters that indicate the beginning and the end of each transmitted frame, respectively.
These ordered sets are summarized in Tab. B.1.

Name	Description	Number of Code-Words in Set	Encoding
/C1/	Configuration 1	4	/K28.5/D21.5/config-message
/C2/	Configuration 2	4	/K28.5/D2.2/config-message
/I1/	Idle 1	2	/K28.5/D5.6/
/I2/	Idle 2	2	/K28.5/D16.2/
/R/	Carrier Extend	1	/K23.7/
/S/	Start of Packet	1	/K27.7/
/T/	End of Packet	1	/K29.7/
/V/	Error Propagation	1	/K30.7/

Table B.1: Ordered Sets of 1000Base-X.

Data Byte	bits HGFEDCBA	RD- abcdeifghj	RD+ abcdeifghj	Data Byte	bits HGFEDCBA	RD- abcdeifghj	RD+ abcdeifghj
D0.0	00000000	1001110100	0110001011	D0.4	10000000	1001110010	0110001101
D1.0	00000001	0111010100	1000101011	D1.4	10000001	0111010010	1000101101
D2.0	00000010	1011010100	0100101011	D2.4	10000010	1011010010	0100101101
D3.0	00000011	1100011011	1100010100	D3.4	10000011	1100011101	1100010010
D4.0	00000100	1101010100	0010101011	D4.4	10000100	1101010010	0010101101
D5.0	00000101	1010011011	1010010100	D5.4	10000101	1010011101	1010010010
D6.0	00000110	0110011011	0110010100	D6.4	10000110	0110011101	0110010010
D7.0	00000111	1110001011	0001110100	D7.4	10000111	1110001101	0001110010
D8.0	00001000	1110010100	0001101011	D8.4	10001000	1110010010	0001101101
D9.0	00001001	1001011011	1001010100	D9.4	10001001	1001011101	1001010010
D10.0	00001010	0101011011	0101010100	D10.4	10001010	0101011101	0101010010
D11.0	00001011	1101001011	1101000100	D11.4	10001011	1101001101	1101000010
D12.0	00001100	0011011011	0011010100	D12.4	10001100	0011011101	0011010010
D13.0	00001101	1011001011	1011000100	D13.4	10001101	1011001101	1011000010
D14.0	00001110	0111001011	0111000100	D14.4	10001110	0111001101	0111000010
D15.0	00001111	0101110100	1010001011	D15.4	10001111	0101110010	1010001101
D16.0	00010000	0110110100	1001001011	D16.4	10010000	0110110010	1001001101
D17.0	00010001	1000111011	1000110100	D17.4	10010001	1000111101	1000110010
D18.0	00010010	0100111011	0100110100	D18.4	10010010	0100111101	0100110010
D19.0	00010011	1100101011	1100100100	D19.4	10010011	1100101101	1100100010
D20.0	00010100	0010111011	0010110100	D20.4	10010100	0010111101	0010110010
D21.0	00010101	1010101011	1010100100	D21.4	10010101	1010101101	1010100010
D22.0	00010110	0110101011	0110100100	D22.4	10010110	0110101101	0110100010
D23.0	00010111	1110100100	0001011011	D23.4	10010111	1110100010	0001011101
D24.0	00011000	1100110100	0011001011	D24.4	10011000	1100110010	0011001101
D25.0	00011001	1001101011	1001100100	D25.4	10011001	1001101101	1001100010
D26.0	00011010	0101101011	0101100100	D26.4	10011010	0101101101	0101100010

Data Byte	bits HGFEDCBA	RD- abcdeifghj	RD+ abcdeifghj	Data Byte	bits HGFEDCBA	RD- abcdeifghj	RD+ abcdeifghj
D27.0	00011011	1101100100	0010011011	D27.4	10011011	1101100010	0010011101
D28.0	00011100	0011101011	0011100100	D28.4	10011100	0011101101	0011100010
D29.0	00011101	1011100100	0100011011	D29.4	10011101	1011100010	0100011101
D30.0	00011110	0111100100	1000011011	D30.4	10011110	0111100010	1000011101
D31.0	00011111	1010110100	0101001011	D31.4	10011111	1010110010	0101001101
D0.1	00100000	1001111001	0110001001	D0.5	10100000	1001111010	0110001010
D1.1	00100001	0111011001	1000101001	D1.5	10100001	0111011010	1000101010
D2.1	00100010	1011011001	0100101001	D2.5	10100010	1011011010	0100101010
D3.1	00100011	1100011001	1100011001	D3.5	10100011	1100011010	1100011010
D4.1	00100100	1101011001	0010101001	D4.5	10100100	1101011010	0010101010
D5.1	00100101	1010011001	1010011001	D5.5	10100101	1010011010	1010011010
D6.1	00100110	0110011001	0110011001	D6.5	10100110	0110011010	0110011010
D7.1	00100111	1110001001	0001111001	D7.5	10100111	1110001010	0001111010
D8.1	00101000	1110011001	0001101001	D8.5	10101000	1110011010	0001101010
D9.1	00101001	1001011001	1001011001	D9.5	10101001	1001011010	1001011010
D10.1	00101010	0101011001	0101011001	D10.5	10101010	0101011010	0101011010
D11.1	00101011	1101001001	1101001001	D11.5	10101011	1101001010	1101001010
D12.1	00101100	0011011001	0011011001	D12.5	10101100	0011011010	0011011010
D13.1	00101101	1011001001	1011001001	D13.5	10101101	1011001010	1011001010
D14.1	00101110	0111001001	0111001001	D14.5	10101110	0111001010	0111001010
D15.1	00101111	0101111001	1010001001	D15.5	10101111	0101111010	1010001010
D16.1	00110000	0110111001	1001001001	D16.5	10110000	0110111010	1001001010
D17.1	00110001	1000111001	1000111001	D17.5	10110001	1000111010	1000111010
D18.1	00110010	0100111001	0100111001	D18.5	10110010	0100111010	0100111010
D19.1	00110011	1100101001	1100101001	D19.5	10110011	1100101010	1100101010
D20.1	00110100	0010111001	0010111001	D20.5	10110100	0010111010	0010111010
D21.1	00110101	1010101001	1010101001	D21.5	10110101	1010101010	1010101010
D22.1	00110110	0110101001	0110101001	D22.5	10110110	0110101010	0110101010
D23.1	00110111	1110101001	0001011001	D23.5	10110111	1110101010	0001011010
D24.1	00111000	1100111001	0011001001	D24.5	10111000	1100111010	0011001010
D25.1	00111001	1001101001	1001101001	D25.5	10111001	1001101010	1001101010
D26.1	00111010	0101101001	0101101001	D26.5	10111010	0101101010	0101101010
D27.1	00111011	1101101001	0010011001	D27.5	10111011	1101101010	0010011010
D28.1	00111100	0011101001	0011101001	D28.5	10111100	0011101010	0011101010
D29.1	00111101	1011101001	0100011001	D29.5	10111101	1011101010	0100011010
D30.1	00111110	0111101001	1000011001	D30.5	10111110	0111101010	1000011010
D31.1	00111111	1010111001	0101001001	D31.5	10111111	1010111010	0101001010
D0.2	01000000	1001110101	0110000101	D0.6	11000000	1001110110	0110000110

Data Byte	bits HGFEDCBA	RD- abcdeifghj	RD+ abcdeifghj	Data Byte	bits HGFEDCBA	RD- abcdeifghj	RD+ abcdeifghj
D1.2	01000001	0111010101	1000100101	D1.6	11000001	0111010110	1000100110
D2.2	01000010	1011010101	0100100101	D2.6	11000010	1011010110	0100100110
D3.2	01000011	1100010101	1100010101	D3.6	11000011	1100010110	1100010110
D4.2	01000100	1101010101	0010100101	D4.6	11000100	1101010110	0010100110
D5.2	01000101	1010010101	1010010101	D5.6	11000101	1010010110	1010010110
D6.2	01000110	0110010101	0110010101	D6.6	11000110	0110010110	0110010110
D7.2	01000111	1110000101	0001110101	D7.6	11000111	1110000110	0001110110
D8.2	01001000	1110010101	0001100101	D8.6	11001000	1110010110	0001100110
D9.2	01001001	1001010101	1001010101	D9.6	11001001	1001010110	1001010110
D10.2	01001010	0101010101	0101010101	D10.6	11001010	0101010110	0101010110
D11.2	01001011	1101000101	1101000101	D11.6	11001011	1101000110	1101000110
D12.2	01001100	0011010101	0011010101	D12.6	11001100	0011010110	0011010110
D13.2	01001101	1011000101	1011000101	D13.6	11001101	1011000110	1011000110
D14.2	01001110	0111000101	0111000101	D14.6	11001110	0111000110	0111000110
D15.2	01001111	0101110101	1010000101	D15.6	11001111	0101110110	1010000110
D16.2	01010000	0110110101	1001000101	D16.6	11010000	0110110110	1001000110
D17.2	01010001	1000110101	1000110101	D17.6	11010001	1000110110	1000110110
D18.2	01010010	0100110101	0100110101	D18.6	11010010	0100110110	0100110110
D19.2	01010011	1100100101	1100100101	D19.6	11010011	1100100110	1100100110
D20.2	01010100	0010110101	0010110101	D20.6	11010100	0010110110	0010110110
D21.2	01010101	1010100101	1010100101	D21.6	11010101	1010100110	1010100110
D22.2	01010110	0110100101	0110100101	D22.6	11010110	0110100110	0110100110
D23.2	01010111	1110100101	0001010101	D23.6	11010111	1110100110	0001010110
D24.2	01011000	1100110101	0011000101	D24.6	11011000	1100110110	0011000110
D25.2	01011001	1001100101	1001100101	D25.6	11011001	1001100110	1001100110
D26.2	01011010	0101100101	0101100101	D26.6	11011010	0101100110	0101100110
D27.2	01011011	1101100101	0010010101	D27.6	11011011	1101100110	0010010110
D28.2	01011100	0011100101	0011100101	D28.6	11011100	0011100110	0011100110
D29.2	01011101	1011100101	0100010101	D29.6	11011101	1011100110	0100010110
D30.2	01011110	0111100101	1000010101	D30.6	11011110	0111100110	1000010110
D31.2	01011111	1010110101	0101000101	D31.6	11011111	1010110110	0101000110
D0.3	01100000	1001110011	0110001100	D0.7	11100000	1001110001	0110001110
D1.3	01100001	0111010011	1000101100	D1.7	11100001	0111010001	1000101110
D2.3	01100010	1011010011	0100101100	D2.7	11100010	1011010001	0100101110
D3.3	01100011	1100011100	1100010011	D3.7	11100011	1100011110	1100010001
D4.3	01100100	1101010011	0010101100	D4.7	11100100	1101010001	0010101110
D5.3	01100101	1010011100	1010010011	D5.7	11100101	1010011110	1010010001
D6.3	01100110	0110011100	0110010011	D6.7	11100110	0110011110	0110010001

Data Byte	bits HGFEDCBA	RD- abcdeifghj	RD+ abcdeifghj	Data Byte	bits HGFEDCBA	RD- abcdeifghj	RD+ abcdeifghj
D7.3	01100111	1110001100	0001110011	D7.7	11100111	1110001110	0001110001
D8.3	01101000	1110010011	0001101100	D8.7	11101000	1110010001	0001101110
D9.3	01101001	1001011100	1001010011	D9.7	11101001	1001011110	1001010001
D10.3	01101010	0101011100	0101010011	D10.7	11101010	0101011110	0101010001
D11.3	01101011	1101001100	1101000011	D11.7	11101011	1101001110	1101001000
D12.3	01101100	0011011100	0011010011	D12.7	11101100	0011011110	0011010001
D13.3	01101101	1011001100	1011000011	D13.7	11101101	1011001110	1011001000
D14.3	01101110	0111001100	0111000011	D14.7	11101110	0111001110	0111001000
D15.3	01101111	0101110011	1010001100	D15.7	11101111	0101110001	1010001110
D16.3	01110000	0110110011	1001001100	D16.7	11110000	0110110001	1001001110
D17.3	01110001	1000111100	1000110011	D17.7	11110001	1000110111	1000110001
D18.3	01110010	0100111100	0100110011	D18.7	11110010	0100110111	0100110001
D19.3	01110011	1100101100	1100100011	D19.7	11110011	1100101110	1100100001
D20.3	01110100	0010111100	0010110011	D20.7	11110100	0010110111	0010110001
D21.3	01110101	1010101100	1010100011	D21.7	11110101	1010101110	1010100001
D22.3	01110110	0110101100	0110100011	D22.7	11110110	0110101110	0110100001
D23.3	01110111	1110100011	0001011100	D23.7	11110111	1110100001	0001011110
D24.3	01111000	1100110011	0011001100	D24.7	11111000	1100110001	0011001110
D25.3	01111001	1001101100	1001100011	D25.7	11111001	1001101110	1001100001
D26.3	01111010	0101101100	0101100011	D26.7	11111010	0101101110	0101100001
D27.3	01111011	1101100011	0010011100	D27.7	11111011	1101100001	0010011110
D28.3	01111100	0011101100	0011100011	D28.7	11111100	0011101110	0011100001
D29.3	01111101	1011100011	0100011100	D29.7	11111101	1011100001	0100011110
D30.3	01111110	0111100011	1000011100	D30.7	11111110	0111100001	1000011110
D31.3	01111111	1010110011	0101001100	D31.7	11111111	1010110001	0101001110

Table B.2: 8B10B coding table : data symbols.

Data Byte	bits HGFEDCBA	RD- abcdeifghj	RD+ abcdeifghj
K28.5	10111100	0011111010	1100000101
K28.7	11111100	0011111000	1100000111
K23.7	11110111	1110101000	0001010111
K27.7	11111011	1101101000	0010010111
K29.7	11111101	1011101000	0100010111
K30.7	11111110	0111101000	1000010111

Table B.3: 8B10B coding table : control symbols.

C

Abbreviations and Symbols

List of Abbreviations

AC	alternating current
ADC	analog-to-digital converter
AFE	analog frontend
AGC	automatic gain control
AOC	actice optical cable
AWG	arbitrary waveform generator
AWGN	additive white gaussian noise
BA	buffer amplifier
BER	bit error ratio
BSCA	backward space - center angle
btb	back-to-back
CORDIC	coordinate rotation digital computer
CYTOP	cyclic transparent optical polymer
DAC	digital-to-analog converter

DC	direct current
DD	decision directed
DFE	decision feedback equalization / equalizer
DFE (m, n)	decision feedback equalizer with m forward and n feedback taps
DLMS	delayed least mean squares
DMT	discrete multitone modulation
DSP	digital signal processing
DVD	digital versatile disk
ECOC	european conference on optical communications
EDC	electronic dispersion compensation
EFDM	explicit finite difference method
EMD	equilibrium mode distribution
FDM	finite difference method
FEC	forward error correction
FFE	feed-forward equalization / equalizer
FFE m	feed-forward equalizer with m taps
FFT	fast fourier transform
FIR	finite impulse response
FPGA	field programmable gate array
FSCA	forward space - center angle
FSE	fractionally-spaced equalization / equalizer
FWHM	full width at half maximum
GbE	Gigabit Ethernet
GI-MMF	graded-index glass multimode fiber
GI-POF	graded-index polymer optical fiber
GMII	gigabit media independent interface
HDMI	high definition multimedia interface
IC-POF	international conference on plastic optical fiber
IDF	Intel Developer Forum
IEC	international electro-technical commission
IEEE	institute of electrical and electronics engineers
IIR	infinite impulse response
IM/DD	intensity modulation / direct detection
INTERBUS	a field bus

ISI	inter-symbol interference
ISO	international organization for standardization
LAN	local area network
LD	laser diode
LED	light emitting diode
LMS	least mean squares
LP	low-pass
LRM	long reach multimode
MAC	media access control
MF	matched filter
MLSE	maximum likelihood sequence estimation
MMF	silica multi mode fiber
MMSE	minimum mean square error
MOST	media oriented system transport
MOST150	media oriented system transport 150 Mbit/s
MSE	mean squared error
NA	numerical aperture
NEP	noise equivalent power
OEIC	opto-electronic integrated circuits
OFC	optical fiber conference
OFDM	orthogonal frequency division multiplex
OM1 MMF	optical multimode 1 fiber
OM2 MMF	optical multimode 2 fiber
OMA	optical modulation amplitude
OOK	on-off-keying
OTA	operational transconductance amplifier
PAM	pulse amplitude modulation
PAM-4	4-level pulse amplitude modulation
PCB	printed circuit board
PD	photodiode
PF-GI-POF	perfluorinated graded-index polymer optical fiber
PHY	physical layer
PIN diode	positive intrinsic negative diode
PLL	phase locked loop

PMMA	poly-methyl-methacrylate (Plexiglas)
PMMA GI-POF	poly-methyl-methacrylate graded-index polymer optical fiber
PMMA SI-POF	poly-methyl-methacrylate step-index polymer optical fiber
POF	polymer optical fiber
PRBS	pseudo random binary sequence
PROFIBUS	process field bus
PRQS	pseudo random quaternary sequence
RC-LED	resonant-cavity light emitting diode
RC-lowpass	first order low-pass
RJ-45	registered jack with 8 pins
RMS	root mean square
RS	Reed Solomon
RX	receiver
SERCOS	serial realtime communication interface
SI-POF	step-index polymer optical fiber
SI-SMF	step-index single mode fiber
SNR	signal-to-noise power ratio
SSMF	standard single mode fiber
TF	transversal filter
TIA	trans-impedance amplifier
TX	transmitter
UV	ultra violet
VCSEL	vertical cavity surface emitting laser
VCXO	voltage controlled crystal oscillator
VGA	variable gain amplifier
ZF	zero-forcing

List of Symbols

a	fiber core radius
$\mathrm{bw}_{\mathrm{el}}$	electrical 3 dB bandwidth
$\mathbf{c}(k)$	equalizer coefficient vector at discrete time k
$c_{0,\mathrm{light}}$	speed of light in vacuum ($2.99792458 \cdot 10^8\,\mathrm{m\,s^{-1}}$)

C	channel capacity
$c(\theta)$	angle dependent coupling coefficient
c_m	coupling coefficient of the m-th mode
$D(\theta)$	angle dependent diffusion parameter
$d(\theta)$	penetration depth of the Goos-Haenchen effect
$e_{\mathrm{LMS}}(k)$	least-mean squares error signal at discrete time k
E_s	energy per modulation symbol
$e_{\mathrm{SaG}}(k)$	error signal at discrete time k for the Stop-and-Go algorithm
$e_{\mathrm{Sato}}(k)$	Sato error signal at discrete time k
$e(k)$	error signal at discrete time k for the (D)LMS
$\Delta f_{\mathrm{noise}}$	equivalent noise bandwidth
$G_{\mathrm{n}}(f)$	power spectral density of $n(t)$
$G_{\mathrm{noise}}(f)$	power spectral density of the distortions and the noise
$G_{\mathrm{r}}(f)$	power spectral density of $r(t)$
$G_{\mathrm{sig}}(f)$	signal power spectral density
$\underline{G}_{total}$	propagation matrix
$G_{\mathrm{x}}(f)$	power spectral density of $x(t)$
$H_k(z)$	transfer function of the goertzel algorithm
	for the k-th frequency component
$H_{\mathrm{opt}}(z_0, \omega)$	optical transfer function at a fiber length z_0
$h_{\mathrm{opt}}(z_0, t)$	optical impulse response at a fiber length z_0
$H_{\mathrm{rx}}(f)$	transfer function of the receiver
$h_{\mathrm{rx}}(t)$	impulse resonse of the receiver
$H_{\mathrm{total}}(f)$	transfer function of the complete transmission system
$H_{\mathrm{tx}}(f)$	transfer function of the transmitter
$h_{\mathrm{tx}}(t)$	impulse resonse of the transmitter
I_{bias}	bias current
$I_{\mathrm{drive}}(t)$	driving current signal
I_{mod}	modulation current
$I_{\mathrm{photo}}(t)$	photo current of the photo diode
I_{th}	threshold current
J	mean squared error
J_{min}	minimum mean squared error
$J_{\mathrm{min}}^{\mathrm{DFE}}$	minimum mean squared error of the DFE

$J_{\text{min}}^{\text{FFE}}$	minimum mean squared error of the FFE
J_{Sato}	cost function of the Sato algorithm
L_{core}	latency of the complete parallelized equalizer structure
M_{filt}	latency of the parallized FFE in number of clock cycles T_{DSP}
M_{modes}	total number of modes
NA	numerical aperture
n_{cladd}	refractive index fiber cladding
n_{core}	refractive index fiber core
N_{refl}	number of reflections
n_{RMS}	root mean square value of $n(t)$
N_0	noise spectral density
$n(r)$	refractive index profile function
$n(t)$	additive white gaussian noise signal
oSNR_{eq}	equivalent optical signal-to-noise power ratio
p_m	power in the m-th mode
P_{opt}	optical signal at the transmitter
$P_{\text{opt}}^{\text{rx}}$	optical signal at the receiver
P_{sig}	signal power
P_{signal}	signal power
P_{noise}	noise power
P_{x}	power of the $x(t)$
$p(\theta, z, t)$	continuous power distribution in the time domain
$P(\theta, z, \omega)$	continuous power distribution in the frequency domain
R	responsivity of the photo diode
r_{ic}	inner caustic radius
R_{refl}	refelction factor
r_{RMS}	root mean square value of $r(t)$
$r(t)$	bipolar received signal
SNR_{el}	electrical signal-to-noise power ratio
SNR_{norm}	normalized signal-to-noise power ratio
t	time variable
T_{bit}	bit length in time
T_{DSP}	FPGA digital signal processing clock cycle length
T_{symbol}	symbol length in time

t_{transit}	ray transit time
$\mathbf{u}(k)$	vector of samples within the tapped delay line of an equalizer at discrete time k
V_{cc}	supply voltage
v_{core}	velocity of light inside the fiber core
$v_k[n]$	intermediate result of the goertzel algorithm for the k-th frequency component at the sample index n
$V(\lambda)$	normalized frequency
W_N^k	complex phasor of the N point goertzel algorithm at the k-th frequency component
$x_e[n]$	input time samples of the goertzel algorithm
$\hat{x}_k$	estimate of the transmitted symbol x_k
x_{peak}	peak absolut value of $x(t)$
x_{RMS}	root mean square value of $x(t)$
$x(t)$	bipolar electrical current signal
$X[k]$	spectral component with frequency index k
$y_k[n]$	output result of the goertzel algorithm for the k-th frequency component at the sample index n
$y(t)$	noisy bipolar received signal
$Y(\omega)$	folded spectrum of the matched filter output
z_{even}	even symbols in the parallelized equalizer
z_k	output sample of an equalizer
z_{odd}	odd symbols in the parallelized equalizer
$\hat{z}_k$	decided symbol at discrete time k
z	spatial variable in fiber axis direction

α_{cladd}	attenuation of the fiber cladding material
α_{core}	attenuation of the fiber core material
α_{F}	overall fiber attenuation
$\alpha_{\text{GH}}(\theta)$	angle dependent attenuation of a mode due to the Goos-Haenchen effect
α_m	attenuation of the m-th mode
$\alpha_{\text{path}}(\theta)$	angle dependent attenuation of a mode due to path length
$\alpha_{\text{refl}}(\theta)$	angle dependent attenuation of a mode due to reflections
$\alpha(\theta)$	angle dependent attenuation of a mode

β	step-size parameter of the least-mean squares algorithm
γ_{Sato}	Sato constant
$\gamma_{\infty}^{\text{DFE}}$	signal-to-noise power ratio for the infinite long DFE
$\gamma_{\infty}^{\text{FFE}}$	signal-to-noise power ratio for the infinite long FFE
$\gamma_{\infty}^{\text{MF}}$	signal-to-noise power ratio for the matched filter
η_{mod}	modulation index
θ	angle of a mode with respect to the fiber axis
θ_c	critical angle
θ_m	angle of the m-th mode of a waveguide
θ_0	main incident angle
$\Delta\theta$	difference angle between neighboring modes
λ	wavelength
μ	crest factor of $x(t)$
$\mu_{\text{PAM}}(M)$	crest factor of M-ary PAM
σ_{beam}	standard deviation of the gaussian input beam power distribution
τ_{factor}	relative pulse broadening factor
τ_{max}	maximum ray transit time
τ_{min}	minimum ray transit time
τ_{rel}	relative mode delay
$\Delta\tau_{\text{transit}}$	maximum pulse broadening

Bibliography

[Agr02] G. P. Agrawal. *Fiber-optic communication systems*. John Wiley & Sons, Inc., New York, 3rd edition, 2002.

[AGSZ09] M. Atef, W. Gaberl, R. Swoboda, and H. Zimmermann. An integrated optical receiver for multilevel data communication over plastic optical fiber. In *Proc. NORCHIP*, pages 1–4, November 16–17, 2009.

[Ame92] William F. Ames. *Numerical Methods for Partial Differential Equations*. Academic Press, Inc., Boston, third edition, 1992.

[ASZ09] M. Atef, R. Swoboda, and H. Zimmermann. Optical receiver front-end for multilevel signalling. *Electronics Letters*, 45(2):121–122, January 2009.

[BC02] N. Benvenuto and G. Cherubini. *Algorithms for Communcations Systems and their applications*. John Wiley & Sons, 2002.

[BHC+06] F. Breyer, N. Hanik, C. Cvetkov, S. Randel, and B. Spinnler. Advanced simulation model of the impulse response of step-index polymer optical fiber. In *International Conference on Plastic Optical Fiber*, September 2006.

[BHLR07] F. Breyer, N. Hanik, S.C.J. Lee, and S. Randel. *POF Modelling: Theory, Measurement and Application*, chapter Getting the Impulse Response of SI-POF by Solving the Time-Dependent Power-Flow Equation using the Crank-Nicholson Scheme, pages 111–120. Books On Demand GmbH, 2007.

[BHRS06] F. Breyer, N. Hanik, S. Randel, and B. Spinnler. Investigations on electronic equalization for step-index polymer optical fiber systems. In *Annual Symposium of the IEEE/Leos Benelux Chapter*, December 2006.

[BLRH07a] F. Breyer, S.C.J. Lee, S. Randel, and N. Hanik. 10 Gbit/s transmission over 220 m perfluorinated graded-index polymer optical fiber using PAM-4

modulation and simple equalization schemes. In *International Conference on Plastic Optical Fibers*, September 2007.

[BLRH07b] F. Breyer, S.C.J. Lee, S. Randel, and N. Hanik. 1.25 Gbit/s transmission over up to 100 m standard 1 mm step-index polymer optical fibre using FFE or DFE equalisation schemes. In *European Conference on Optical Communications*, September 2007.

[BLRH07c] F. Breyer, S.C.J. Lee, S. Randel, and N. Hanik. 500-Mbit/s transmission over 50 m standard 1-mm step-index polymer optical fiber using PAM-4 modulation and simple equalization schemes. In *Ephotone One Summer School*, July 2007.

[BLRH08a] F. Breyer, S.C.J. Lee, S. Randel, and N. Hanik. Comparison of OOK- and PAM-4 modulation for 10 Gbit/s transmission over up to 300 m polymer optical fiber. In *Optical Fiber Communication Conference*, February 2008.

[BLRH08b] F. Breyer, S.C.J. Lee, S. Randel, and N. Hanik. PAM-4 signalling for Gigabit transmission over standard step-index polymer optical fiber. In *European Conference on Optical Communications*, September 2008.

[BLRH09] F. Breyer, S.C.J. Lee, S. Randel, and N. Hanik. Real-time Gigabit Ethernet transmission over up to 25 m step-index polymer optical fibre using LEDs and FPGA-based signal processing. In *European Conference on Optical Communications*, September 2009.

[BMH+07] F. Breyer, M. Moerz, N. Hanik, L. Li, S. Randel, and B. Spinnler. Analysis of electronic dispersion compensation for step-index polymer optical fiber by use of an advanced simulation model. *European Transactions on Telecommunications*, 18(8):881–886, 2007.

[BW70] M. Born and E. Wolf. *Principles of Optics*. Pergamon Press, Oxford, 1970.

[CBZ+06] J.E. Cunningham, D. Beckman, X. Zheng, D. Huang, T. Sze, and A. V. Krishnamoorthy. PAM-4 signaling over VCSELs with 0.13μm CMOS chip technology. *Optics Express*, 14(25):12028–12038, 2006.

[CLNC+09] D. F. Cardenas-Lopez, A. Nespola, S. Camatel, S. Abrate, and R. Gaudino. 100 Mb/s ethernet transmission over 275m of large core step index polymer optical fiber: Results from the POF-ALL european project. *IEEE/OSA Journal of Lightwave Technology*, 27(14):2908–2915, July 2009.

[CN47] J. Crank and P. Nicolson. A practical method for numerical evaluation of solutions of partial differential equations of the heat-conduction type. *Mathematical Proceedings of the Cambridge Philosophical Society*, 43(01):50–67, 1947.

[DeC05] C.M. DeCusatis. Fiber optic cable infrastructure and dispersion compensation for storage area networks. *IEEE Communications Magazine, IEEE*, 43:86–92, 2005.

[DS00] A. Djordjevich and S. Savovic. Investigations of mode coupling in step index plastic optical fibers using the power flow equation. *Photonics Technology Letters*, 12 (11):1489–1491, 2000.

[DS04] A. Djordjevich and S. Savovic. Numerical solution of the power flow equation in step-index plastic optical fibers. *Journal of the Optical Society of America B*, 21:1437–1442, 2004.

[ES07] D. Efinger and J. Speidel. A parallel equalizer for high-speed electronic dispersion compensation. In *European Conference on Optical Communications*, 2007.

[Fir] Firecomms. FC300R-120, available: http://www.firecomms.com/tech-rcled.html.

[FWrp] P.A. Franaszek and A.X. Widmer. Byte oriented DC-balanced (0,4) 8b/10b partitioned block transmission code, 1984, U.S. Patent 4,486,739 assigned to International Business Machines Corp.

[Gal68] R. Gallager. *Information Theory and Reliable Communication*. Wiley, 1968.

[GBB+07] R. Gaudino, G. Bosco, A. Bluschke, O. Hofmann, N. Kiss, M. Matthews, P. Rietzsch, S. Randel, S.C.J. Lee, and F. Breyer. On the ultimate capacity of SI-POF links and the use of OFDM: Recent results from the POF-ALL project. In *International Conference on Plastic Optical Fibers*, September 2007.

[GH47] F. Goos and H. Hänchen. Ein neuer und fundamentaler Versuch zur Totalreflexion. *Annalen der Physik*, 6(1):333–346, 1947.

[GHW92] R. D. Gitlin, J. F. Hayes, and S.B. Weinstein. *Data Communcations Principles*. Plenum Press, 1992.

[Glo72] D. Gloge. Optical power flow in multimode fibers. *Bell Systems Technical Journal*, 51:1767–1783, 1972.

[Glo73] D. Gloge. Impulse response of clad optical multimode fibers. *Bell Systems Technical Journal*, 53:801–816, 1973.

[Goe58] G. Goertzel. An algorithm for the evaluation of finite trigonometric series. *American Math*, 65:34–35, 1958.

[GPM75] W. A. Gambling, D. N. Payne, and H. Matsumura. Mode conversion coefficients in optical fibers. *Applied Optics*, 14, Issue 7:1538–1542, 1975.

[GVZL08] J. Gottschalk, J. Vinogradov, O. Ziemann, and O. Lednicky. Optimal equalizers for SI-POF and Gbps. In *International Conference on Polymer Optical Fibers*, 2008.

[GWW+99] G. Giaretta, W. White, M. Wegmueller, R.V. Yelamarty, and T. Onishi. 11 Gb/sec data transmission through 100 m of perfluorinated graded-index polymer optical fiber. In *Optical Fiber Communication Conference, PDP*, 1999.

[Hay02] S. Haykin. *Adaptive Filter Theory (4th ed.)*. Prentice Hall, 2002.

[iee02] IEEE standard for a high-performance serial bus - amendment 2. *IEEE Std 1394b-2002 (Amendment to IEEE Std 1394-1995)*, pages 1–369, 2002.

[iee06] IEEE standard for information technology telecommunications and information exchange between systems local and metropolitan area networks specific requirements part 3: Carrier sense multiple access with collision detection (CSMA/CD) access method and physical layer specifications amendment 2: Physical layer and management parameters for 10 Gb/s operation, type 10GBASE-LRM. *IEEE Std 802.3aq-2006 (Amendment to IEEE Std 802.3-2005)*, pages 1–48, 2006.

[Inc03] Scintera Networks Inc. Advanced signal processing platform. *White Paper*, 2003.

[INK+95] T. Ishigure, E. Nihei, Y. Koike, C.E. Forbes, L. LaNieve, R. Straff, and H.A. Deckers. Large-core, high-bandwidth polymer optical fiber for near infrared use. *Photonics Technology Letters*, 7(4):403–405, 1995.

[Kab83] P. Kabal. The stability of adaptive minimum mean square error equalizers using delayed adjustment. *IEEE Transactions on Communications*, 31(3):430–432, 1983.

[KB72] Kapany and Burke. *Optical Waveguides*. Academic Press, 1972.

[KFON81] T. Kaino, M. Fujiki, S. Oikawa, and Shigeo Nara. Low-loss plastic optical fibers. *Applied Optics*, 20(17):2886–2888, 1981.

[KK09] K. Koike and Y. Koike. Design of low-loss graded-index plastic optical fiber based on partially fluorinated methacrylate polymer. *IEEE/OSA Journal of Lightwave Technology*, 27(1):41–46, 2009.

[KP08] O. Kwon and C.-W. Park. Modification of RI profile for the reduction of bending lsss of a PMMA GI-POF. In *International Conference on Polymer Optical Fiber*, August 2008.

[LBC+09] S.C.J. Lee, F. Breyer, D. Cardenas, S. Randel, and A.M.J. Koonen. Real-time Gigabit DMT transmission over plastic optical fibre. *Electronics Letters*, 45(25):1342–1343, 2009.

[LBR+07a] S.C.J. Lee, F. Breyer, S. Randel, B. Spinnler, I.L. Lobato Polo, D. van den Borne, J. Zeng, E. de Man, H.P. van den Boom, and A.M. Koonen. 10.7 Gbit/s transmission over 220 m polymer optical fiber using maximum likelihood sequence estimation. In *Optical Fiber Communication Conference*, March 2007.

[LBR+07b] S.C.J. Lee, F. Breyer, S. Randel, J. Zeng, H.P. van den Boom, and A.M. Koonen. Discrete multi-tone modulation for low-cost and robust 10 Gb/s transmission over polymer optical fiber. In *European Conference on Optical Communications*, September 2007.

[LBR+08a] S.C.J. Lee, F. Breyer, S. Randel, H. van den Boom, and A.M.J. Koonen. Gigabit Ethernet transmission over standard step-index polymer optical fiber. In *International Conference on Polymer Optical Fiber*, August 2008.

[LBR+08b] S.C.J. Lee, F. Breyer, S. Randel, O. Ziemann, H.P. van den Boom, and A.M. Koonen. Low-cost and robust 1 GBit/s plastic optical fiber link based on light-emitting diode technology. In *Optical Fiber Communication Conference*, February 2008.

[LBR+09] S.C.J. Lee, F. Breyer, S. Randel, R. Gaudino, G. Bosco, A. Bluschke, M. Matthews, P. Rietzsch, R. Steglich, H. van den Boom, and A. Koonen. Discrete mutlitone modulation for maximizing transmission rate in step-index plastic optical fibers. *Journal of Lightwave Technology*, 27(11):1503–1513, 2009.

[Lee09] Jeffrey Lee. *Discrete Multitone Modulation for Short-Range Optical Communications*. Technical University Eindhoven, 2009.

[LM94] E.A. Lee and D.G. Messerschmitt. *Digital Communication (2nd Ed.)*. Kluwer Academic Publisher (Boston), 1994.

[LMOM05] J.D. Lambkin, B. McGarvey, M. O'Gorman, and T. Moriarty. RCLEDs for MOST and IDB 1394 automotive applications. In *International Conference on Polymer Optical Fiber*, 2005.

[Mar72] D. Marcuse. *Light Transmission Optics*. Van Nostrand, New York, 1972.

[Mc] MOST-cooperation. Media oriented system transport (MOST). *http://www.mostcooperation.com*.

[MDR+98] C. Mick, C. DiMinico, S. Raghavan, S. Rao, and M. Hatamian. 802.3ab - A tutorial presentation. *IEEE 802.3ab 1000BASE-T Task Force*, 1998.

[MJG+09] I. Mollers, D. Jager, R. Gaudino, A. Nocivelli, H. Kragl, O. Ziemann, N. Weber, T. Koonen, C. Lezzi, A. Bluschke, and S. Randel. Plastic optical fiber technology for reliable home networking: overview and results of the EU project POF-ALL. *Communications Magazine, IEEE*, 47(8):58–68, August 2009.

[MLGZ06] J. Mateo, M.A. Losada, I. Garces, and J. Zubia. Global characterization of optical power propagation in step-index plastic optical fibers. *Optics Express*, 14(20):9028–9035, 2006.

[MMR98] H. Meyr, M. Moeneclaey, and S.A. Rechtel. *Digital Communcation Receivers*. John Wiley & Sons, 1998.

[MS76] F.J. MacWilliams and N.J.A. Sloane. Pseudo-random sequences and arrays. *Proceedings of the IEEE*, 64(12):1715–1729, 1976.

[Opt] Optomedia. OM-Giga fiber specification, online. *http://www.optimedia.co.kr/ eng_optimedia_ main_b_01.htm*.

[PP87] G. Picchi and G Prati. Blind equalization and carrier recovery using a "stop-and-go" decision-directed algorithm. *Communications, IEEE Transactions on*, 35(9):877–887, 1987.

[PRK93] U. Paar, W. Ritter, and K.F. Klein. Excitation dependent losses in plastic optical fibers. *Proceedings of SPIE*, 1799:48–56, 1993.

[Pro01] J.G. Proakis. *Digitial Communications (4th ed.)*. McGraw-Hill, 2001.

[RJ77] M. Rousseau and L. Jeunhomme. Numerical solution of the coupled-power equation in step-index optical fibers. *IEEE Trans. on Microwave Theory and Techniques*, 25:577–585, 1977.

[RLB07] S. Randel, S.C.J. Lee, and F. Breyer. 1 Gbit/s transmission over POF using light-emitting diodes. In *International Conference on Plastic Optical Fibers*, September 2007.

[RLS+06] S. Randel, S.C.J. Lee, B. Spinnler, F. Breyer, H. Rohde, J. Walewski, A.M.J. Koonen, and A. Kirstaeter. 1 Gbit/s transmission with 6.3 bit/s/Hz spectral efficiency in a 100 m standard 1 mm step-index plastic optical fibre link using adaptive multiple sub-carrier modulation. In *Proc. European Conference on Optical Communications 2006, PD4.4.1*, Cannes, France, 2006.

[Sal73] J. Salz. Optimum mean-square decision feedback equalization. *The Bell System Tech. Journal*, 52(8):1341–1373, 1973.

[Sat75] Y. Sato. A method of self-recovering equalization for multilevel amplitude-modulation systems. *IEEE Transactions on Communications*, 23(6):679–682, June 1975.

[Sei98] Rich Seifert. *Gigabit Ethernet - Technology and Applications for High-Speed LANs*. Addison-Wesley, 1998.

[Sha48] C. E. Shannon. A mathematical theory of communication. *Bell System Technical Journal*, 27:379–423 and 623–656, July and October 1948.

[SL83] A.W. Snyder and J.D. Love. *Optical Waveguide Theory*. Chapman and Hall, 1983.

[SWC+92] E.F. Schubert, Y.-H. Wang, A.Y. Cho, L.-W. Tu, and G.J. Zydzik. Resonant cavity light emitting diode. *Applied Physics Letters*, 60:921–923, 1992.

[Vit67] A. J. Viterbi. Error bounds for convolutional codes and an asymptotic optimum decoding algorithm. *IEEE Trans. on Information Theory*, 13(4):260–269, 1967.

[Vol59] J. Volder. The CORDIC trigonometric computing technique. *IRE Transactions Electronic Computing*, EC-8:330–334, 1959.

[WF83] A. X. Widmer and P.A. Franaszek. A dc-balanced, partioned-block, 8B/10B transmission code. *IBM Journal of Research an Development - Communications Technology*, 27(5):40, 1983.

[WH31] N. Wiener and E. Hopf. On a class of singular integral equations. In *Prussian Acad. Math.Phys. Ser*, page 696, 1931.

[WH60] B. Widrow and M.E. Hoff. Adaptive switching circuits. In *IRE WESCON Convention Record*, pages 563–587, 1960.

[WMH+08] T. Wipiejewski, T. Moriarty, V. Hung, P. Doyle, G. Duggan, D. Barrow, B. Garvey, M. O'Gorman, T. Calvert, M. Maute, V. Gerhardt, and J.D. Lambkin. Gigabit/s in the home with plugless plastic optical fiber (POF) interconnencts. In *Electronics System-Integration Technology Conference (ETSC)*, pages 1263–1266, September 2008.

[YWB93] M. Yaseen, S.D. Walker, and R.J.S. Bates. 531-Mbit/s, 100-m all-plastic optical fiber data link for customer-premises network applications. In *Conference on Optical Fiber Communication/ International Conference on Integrated Optics and Optical Fiber Communication*, 1993.

[ZKZD08] O. Ziemann, J. Krauser, P. Zamzow, and W. Daum. *POF Handbook - Optical Short Range Transmission Systems, 2nd. Edition.* Springer-Verlag, 2008.